Thermo-mechanics of energy piles: fine-grained soils, cycles, and interfaces

Golchin, A.

Important note
To cite this publication, please use the final published version (if applicable).
Please check the document version above.

THERMO-MECHANICS OF ENERGY PILES:
FINE-GRAINED SOILS, CYCLES, AND INTERFACES

THERMO-MECHANICS OF ENERGY PILES: FINE-GRAINED SOILS, CYCLES, AND INTERFACES

Dissertation

for the purpose of obtaining the degree of doctor
at Delft University of Technology,
by the authority of the Rector Magnificus, Prof. dr. ir. T.H.J.J. van der Hagen,
chair of the Board for Doctorates,
to be defended publicly on 30 October 2023 at 17:30 o'clock

by

Ali GOLCHIN

Master of Science in Civil Engineering,
Shiraz University of Technology, Shiraz, Iran.

This dissertation has been approved by the promotors.

promotor: Prof. dr. P. J. Vardon
promotor: Prof. dr. M. A. Hicks

Composition of the doctoral committee:

Rector Magnificus,	chairperson
Prof. dr. P. J. Vardon,	Delft University of Technology, promotor
Prof. dr. M. A. Hicks,	Delft University of Technology, promotor

Independent members:

Prof. dr. A. Ferrari,	EPFL, Switzerland
Dr. D. Taborda,	Imperial College London, UK
Prof. dr. K. G. Gavin,	Delft University of Technology
Dr. F. Pisanò,	Delft University of Technology
Dr. D. V. Voskov,	Delft University of Technology
Prof. dr. T. J. Heimovaara,	Delft University of Technology, reserve member

To my wife Behnaz
and my parents Nahid & Ahmad

CONTENTS

SUMMARY

In the serviceability lifespan of thermo-active geo-structures such as energy-piles, soils surrounding these structures are exposed to a combination of mechanical and thermal loads. These loads are often complex (including cycles) and, depending on the state of the soils, the response of the surrounding soil to these loads may differ. Since the performance and safety of the soil-structure system directly depends of the response of the surrounding soil, it is important to understand and quantify the thermomechanical behaviour of soils. These objectives can be achieved by performing laboratory-scale element tests to gain knowledge on the fundamental response of the material and by developing numerical tools which can be used to simulate the complete soil–structure system under various complex load paths.

To date, many laboratory test have been conducted to study the thermomechanical behaviour of soils. A large portion of these tests have been triaxial tests and many thermomechanical constitutive models for soils are developed based on the phenomenological findings from these tests. While these models have been seen to be capable of capturing the general thermomechanical behaviour of soils, none have been formulated to ensure that they unconditionally satisfy the principles of thermodynamics. Therefore, under complex loading paths certain phenomena may not be captured/predicted, and other phenomena may be spuriously predicted. On the other hand, only a very limited number of tests have been conducted on soil-structure interfaces. Therefore the available knowledge on the thermomechanical behaviour of soil-structure interfaces until this time has been limited.

The objective of this thesis is to fill-in the gaps mentioned above by investigating and exploring the main mechanisms governing the thermomechancial behaviour of soils and soil-structure interfaces, as well as developing thermomechanical constitutive models constructed from a sound foundation (i.e. thermodynamics) and numerical algorithms that can be used in boundary-value solvers such as finite-element methods.

First, the phenomenological temperature effects observed in laboratory-scale tests are combined with principles of thermodynamics to develop a "*base*" thermomechanical constitutive model, defined in triaxial stress space, that can capture the main thermomechanical behaviour of fine-grained soils. This base model has a single flexibly shaped yield surface. The base model is then upgraded to a "*two surface/bubble*" thermomechanical model by introducing an additional yield surface. The additional yield surface translates within the admissible stress space via a temperature-dependent kinematic rule, which enables the model to capture additional thermomechanical features such as the shakedown behaviour of soils when subjected to thermal cycles, which the single yield surface constitutive model was not able to capture or predict.

The main value of constitutive models is achieved when they are efficiently embed within boundary-value solvers, such as a finite-element method solver. One such efficient method is to use the implicit stress integration scheme. However, many constitu-

tive models fail to converge within these schemes. One possible reason, as demonstrated in this thesis, is the existence of undesired elastic nuclei or domains with erratic divergence. A new yield function (which can also be used as a plastic potential function) is proposed, which is flexible and unique, and overcomes the aforementioned drawbacks. The single surface thermomechanical model (defined in triaxial space) is then modified by incorporating the newly proposed yield surface formulation with the addition of Lode angle dependency and generalisation to three-dimensional stress space, prior to being implemented in a finite-element context. Since the non-linear thermo-elastic relationships of the model were derived from a Gibbs-type energy potential, a new numerical algorithm was designed to accommodate this feature when implementing the model in a finite-element context using an implicit stress integration scheme.

The thermomechanical behaviour of soil-structure interfaces is experimentally investigated using a temperature-controlled direct shear apparatus. Several thermomechanical stress paths, with a wide ranges of stresses, temperatures and boundary conditions, analogous to those an interface element experiences in the serviceability life-time of an energy-pile, were designed and performed. Unique observations including the coupling effect of initial shear stress and thermal cycles were recorded, which enhanced the knowledge of thermoemchanical behaviour of soil-structure interfaces. The main impact on soil-concrete interfaces was seen to be the mechanical cyclic loads arising due to the heating and cooling of the concrete pile, rather than direct thermal impacts. Thermal creep was identified as a novel phenomen which had not been previously identified.

SAMENVATTING

In de bruikbaarheidslevensduur van thermo-actieve geostructuren, zoals energiepalen, worden de bodems rond deze structuren blootgesteld aan een combinatie van mechanische en thermische belastingen. Deze belastingen zijn vaak complex (inclusief cycli) en, afhankelijk van de toestand van de bodems, kan de reactie van de omringende bodem op deze belastingen verschillen. Aangezien de prestaties en veiligheid van het grondstructuursysteem direct afhangen van de reactie van de omringende grond, is het belangrijk om het thermomechanische gedrag van bodems te begrijpen en kwantificeren. Deze doelstellingen kunnen worden bereikt door het uitvoeren van laboratoriumschaal elementtesten om kennis te verwerven over de fundamentele respons van het materiaal en door het ontwikkelen van numerieke hulpmiddelen die kunnen worden gebruikt om het volledige grond-structuursysteem te simuleren onder verschillende complexe belastingpaden.

Tot op heden zijn er veel laboratoriumtesten uitgevoerd om het thermomechanische gedrag van bodems te bestuderen. Een groot deel van deze testen zijn triaxiale testen en veel thermomechanische constitutieve modellen voor bodems zijn ontwikkeld op basis van de fenomenologische bevindingen uit deze testen. Hoewel deze modellen over het algemeen in staat zijn gebleken om het thermomechanische gedrag van bodems vast te leggen, zijn er geen geformuleerd om ervoor te zorgen dat ze onvoorwaardelijk voldoen aan de principes van thermodynamica. Daarom kunnen bepaalde fenomenen onder complexe belastingpaden mogelijk niet worden vastgelegd / voorspeld, en kunnen andere fenomenen ten onrechte worden voorspeld. Aan de andere kant zijn er tot nu toe slechts een zeer beperkt aantal testen uitgevoerd op grond-structuurinterfaces. Daarom is de beschikbare kennis over het thermomechanische gedrag van de grondstructuurinterfaces tot nu toe beperkt geweest.

Het doel van dit proefschrift is om de hierboven genoemde hiaten op te vullen door het onderzoeken en verkennen van de belangrijkste mechanismen die het thermomechanische gedrag van bodems en grond-structuurinterfaces beheersen, en door het ontwikkelen van thermomechanische constitutieve modellen die zijn opgebouwd uit een degelijke basis (d.w.z. thermodynamica) en numerieke algoritmen die kunnen worden gebruikt in grenswaarde-oplossers zoals eindige-elementenmethoden.

Ten eerste worden de fenomenologische temperatuureffecten die in laboratoriumschaaltesten zijn waargenomen, gecombineerd met principes van thermodynamica om een "basis"thermomechanisch constitutief model te ontwikkelen, gedefinieerd in triaxiale spanningsruimte, dat het belangrijkste thermomechanische gedrag van fijnkorrelige bodems kan vastleggen. Dit basismodel heeft een enkel flexibel gevormd vloeigrensoppervlak. Het basismodel wordt vervolgens opgewaardeerd naar een "tweeoppervlak-/bel-thermomechanisch model door het introduceren van een extra vloeigrensoppervlak. Het extra vloeigrensoppervlak vertaalt zich binnen de toelaatbare spanningsruimte via een temperatuurafhankelijke kinematische regel, die het model in staat stelt om extra

thermomechanische eigenschappen vast te leggen, zoals het uitvlakgedrag (shakedown) van bodems bij blootstelling aan thermische cycli, wat het enkelvoudige vloeigrensoppervlak niet kon vastleggen of voorspellen.

De belangrijkste waarde van constitutieve modellen wordt bereikt wanneer ze efficiënt worden ingebed in grenswaarde-oplossers, zoals een eindige-elementenmethode-oplosser. Een dergelijke efficiënte methode is het gebruik van het impliciete stressintegratieschema. Veel constitutieve modellen slagen er echter in om binnen deze schema's samen te vallen. Een mogelijke reden, zoals in dit proefschrift wordt aangetoond, is het bestaan van ongewenste elastische kernen of domeinen met een chaotische divergentie. Er wordt een nieuwe vloeigrensfunctie voorgesteld (die ook kan worden gebruikt als plastisch potentieelfunctie), die flexibel en uniek is, en de eerder genoemde nadelen overwint. Het enkelvoudige oppervlakthermomechanische model (gedefinieerd in triaxiale ruimte) wordt vervolgens gewijzigd door het nieuw voorgestelde vloeigrensoppervlakformulering te incorporeren met de toevoeging van Lode-hoekafhankelijkheid en generalisatie naar driedimensionale spanningsruimte, voordat het in een eindige-elementencontext wordt geïmplementeerd. Aangezien de niet-lineaire thermo-elastische relaties van het model zijn afgeleid van een Gibbs-type energiepotentieel, is een nieuw numeriek algoritme ontworpen om deze functie te accommoderen bij het implementeren van het model in een eindige-elementencontext met behulp van een impliciet stressintegratieschema.

Het thermomechanische gedrag van grond-structuurinterfaces wordt experimenteel onderzocht met behulp van een temperatuurgeregelde direct-schuifapparatuur. Verschillende thermomechanische stresspaden, met een breed scala aan spanningen, temperaturen en randvoorwaarden, analoog aan die een interface-element ervaart in de bruikbaarheidslevensduur van een energiepaal, zijn ontworpen en uitgevoerd. Unieke waarnemingen, waaronder het koppelingeffect van initiële schuifspanning en thermische cycli, zijn vastgelegd, wat de kennis van het thermoemchanische gedrag van grond-structuurinterfaces heeft verbeterd. De belangrijkste impact op grond-betoninterfaces bleek te zijn de mechanische cyclische belastingen als gevolg van het verwarmen en koelen van de betonnen paal, in plaats van directe thermische impact. Thermische kruip werd geïdentificeerd als een nieuw fenomeen dat nog niet eerder was vastgesteld.

1

INTRODUCTION

1

1.1. INTRODUCTION

In recent decades, utilising thermal energy from the ground, as an almost unlimited source of heating and cooling, has gained attention. In deep geothermal energy projects, thermal energy is extracted from deep geological layers often several kilometres below the ground surface. However, the high costs of drilling technology and practical difficulties have restricted its implementation to large-scale applications [1]. Thus, due to their lower cost and reasonable long-term sustainability, shallow geothermal resources, mostly from soil layers, have become an interesting medium for extracting energy. Moreover, due to the initial lower temperatures, the ability to provide cooling, i.e., injecting energy, allows integration with newer better insulated buildings which require both heating and cooling. In contrast to deep geothermal systems, the application of shallow geothermal systems is feasible in a wide range of buildings, e.g., both residential and commercial buildings [2; 3], and in both small and large buildings. In addition, interest has globally been focused toward the so called "*nearly zero energy buildings*", with less energy consumption and low-carbon emissions, due to economical and environmental benefits [2].

At shallow depths below 5-10m (depending on the region) the Earth's temperature is reasonably stable, i.e., it does not vary over the course of a year, and can be used as a heat sink or as a source of energy [2]. Water can be circulated through heat exchanger pipes, where for shallow geothermal systems these are often closed, which are in turn in contact with the ground. The temperature in the ground is significantly lower than required for space or water heating and therefore heat pumps must be used. These systems are often called ground source heat pump (GSHP) systems. In a heating mode, the ground plays the role of the energy source from which thermal energy is extracted and transferred to the building (usually upgraded in temperature using a GSHP), while in a cooling mode the heat from the building is injected into the ground (which acts as a heat sink) [4]. By using these systems for both heating and cooling, thermal energy can be stored and the systems can be more efficient, i.e., they require less electrical input to the heat pump.

Energy-piles (also known as thermal-piles) are one of many kinds of GSHP systems. They are dual-purpose constructions, designed to bear the structural loads exerted from the building as their main purpose and to exchange heat with the ground as their secondary purpose. They are mostly made of concrete, which has a reasonably high heat capacity and thermal conductivity [5]. The heat exchangers with the ground are mostly U-tubes (plastic tubes in a U shape) inserted in the piles, in which a fluid circulates and carries the heat. A major advantage over other GSHP systems is that the installation of the ground heat exchangers is only fractionally more expensive than installing the foundation piles, although the impact on the structural performance must be quantified.

Though energy pile systems are gaining traction in certain countries, there is a general lack of recognised geotechnical design standards in most countries [4; 6]. Instead, the design processes largely rely on practical assessments and patterns derived from empirical data [7]. Often to compensate for this, a higher safety factor is used (in comparison to the design process of a regular pile) [4] to cover the possible detrimental effects of temperature variation. Although this approach would probably keep the design and construction safe, it could impose un-needed additional costs. To avoid this drawback, a clear understanding of the governing mechanisms occurring during the energy-pile life-

time is a must. Energy pile systems have a more complex soil-structure interaction in comparison to a regular pile. These complexities in behaviour are due to thermal effects on both the mechanical behaviour of the pile and the surrounding soil (which are cyclic on both a daily and annual basis), as well as their coupled effects.

1.2. CONCEPTUAL MODEL

Energy-piles are employed for the two main reasons of carrying mechanical loads and exchanging heat with the ground. The heat transfer results in changing temperature, which due to thermal expansion or contraction can cause changes in stresses and strains in the soil. Therefore, the stresses in the ground consist of both mechanical and thermally-induced stresses [8], as indicated in Figure 1.1. These stresses develop and act in combination with the ground and the pile. The resulting stresses can be studied separately as mechanical and thermally-induced stresses, and added together by using the superposition principle. The external load from the structure constructed on the pile, F (Figure 1.1a), is transferred to the pile and from the pile to the ground. As a result, by considering a pile element at the interface adjacent to a soil element, an axial stress σ_a as well as radial and hoop stresses (σ_r and σ_h) are applied to the pile element, due to Poisson's ratio and the restraints from the adjacent soil (Figure 1.1b). As the pile undergoes axial deformation (and possible changes in the radial and hoop stresses), the shear stress τ mobilises at the interface. As these elements are in stress equilibrium, stresses are transferred to the soil element at the interface.

When the heat exchange through the U-tubes initiates, the pile expands or contracts in all directions, depending on whether the pile heats up or cools down. By assuming the temperature is uniformly distributed radially and along the length of the pile, and considering if the pile would be completely free to deform (both radially and axially), no internal stresses would be generated inside the pile. However, depending on the soil state and boundary conditions, the pile may be (partially) constrained [8]. As a result, the portion of the volume expansion of the pile that is prevented produces internal stresses which are referred to as thermally-induced stresses. These stresses are (Figure 1.1c):

- σ_{Tap}, thermally-induced axial stress developed inside the pile. This stress is due to the restraint imposed by the surrounding soil in both the axial and radial directions and the possible restraint provided by the above structure.

- σ_{Tr}, thermally-induced radial stress developed at the interface. This stress is the result of prevention of radial displacements as well as to changes in the thermally-induced hoop stresses. Note that the radial displacements occur as a result of thermal expansion in the radial direction and the influence of Poisson's effect from constraining axial thermal expansion.

- σ_{Ts}, thermally-induced stress developed inside the soil. Depending on the soil's type and state, it may undergo both thermo-elastic expansion and permanent contraction during heating. When these volume changes are prevented, thermally-induced stresses are developed inside the soil element.

- σ_{Th}, thermally-induced hoop stress. A combination of radial and axial stress variations at different radii from the interface, as well as an irregular shape of the pile,

1

may produce hoop stresses perpendicular to both the axial and radial stresses.

- τ_T, thermally-induced shear stress. This stress is mobilised at the interface due to relative displacement between the pile and soil in contact, due to temperature variation and the combined effects of radial, hoop and axial stresses mobilised at the interface.

It should be noted that the above stresses are directly dependent on their interaction with each other and the level of restraint imposed by the ground. As an example, if the pile is installed in a stiff clayey-soil and the pile's radial expansion is confined, then a higher thermally-induced radial stress would be generated and, simultaneously, due to Poisson's ratio, higher thermally-induced axial stresses or strains (dependent on the axial restraints of the pile) are produced. This would also lead to differential displacement at the interface and thereby to the generation of shear stresses (τ_T).

The direction of the thermally-induced stresses depends on both the direction of heat transfer (heating or cooling) and the location of the element on the pile. For instance, the directions of the shear and axial stresses (σ_{Tap} and τ_T) at the pile during heating differ when the pile element is located above or below the null point (the point at which the axial stresses are zero, i.e., the point at which the direction of elongation changes). In addition, the direction of these stresses becomes opposite during cooling.

The magnitude of the stresses depends on the soil restraint imposed on the pile and the thermomechanical behaviour of the surrounding soil. For piles located in fine-grained (almost) normally-consolidated soils with a high plasticity-index, higher strains occur due to higher volume contraction during heating. In addition, soils may experience a reduction in shear strength as the temperature increases. For piles installed in such soils, larger relative displacements may be required to mobilise sufficient shear stress at the interface.

For a typical energy-pile, heating will be the primary use in the winter, resulting in cooling of the soil, whereas, in the summer, cooling will be used or the system will simply not be in operation; this will result in an annual cycle of temperatures and thermally-induced stresses. More minor cycles may be induced on a daily or weekly basis, but these will be of a significantly smaller magnitude.

(a)
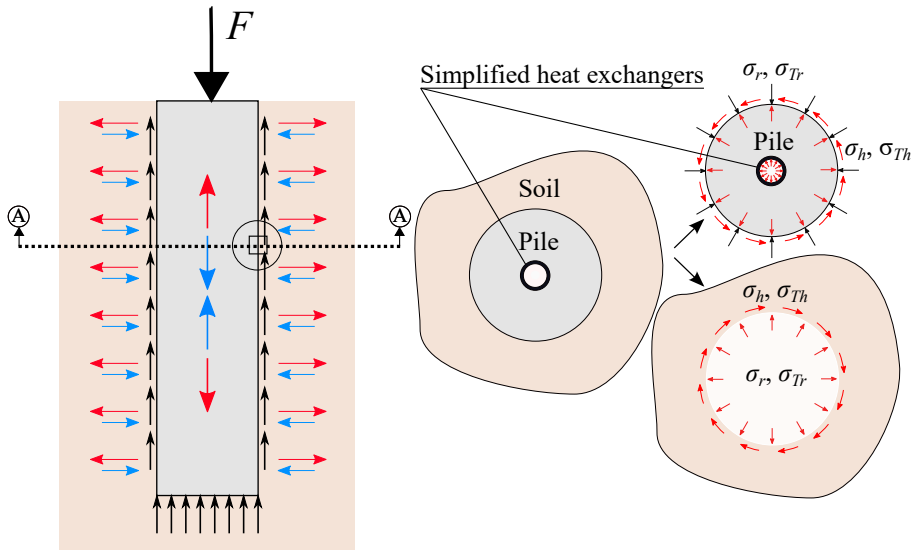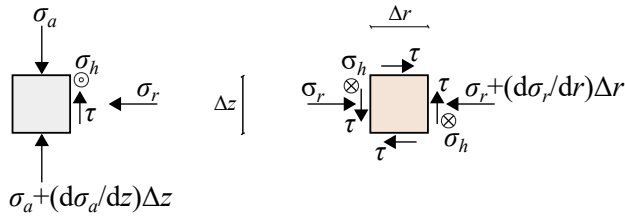
σ_a: Axial stress due to mechanical load
σ_r: Radial stress due to mechanical load
σ_h: Hoop stress due to mechanical load
τ: Shear stress mobilised at interface

(b)
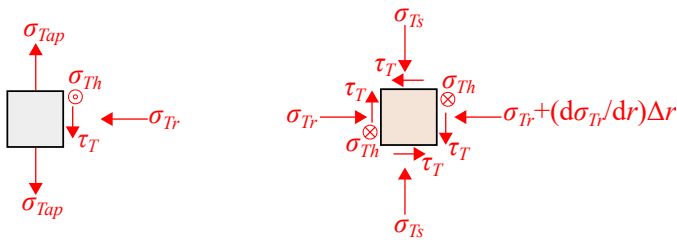
σ_{Tap}: Thermally-induced axial stress of the pile
σ_{Tr}: Thermally-induced radial stress
σ_{Ts}: Thermally-induced stress of the soil
σ_{Th}: Thermally-induced hoop stress
τ_T: Thermally-induced shear stress mobilised at the interface

(c)

Figure 1.1: (a) Stresses developed during the deployment of the energy pile; (b) mechanical stresses; (c) thermally-induced stresses

1.3. THERMOMECHANICAL BEHAVIOUR OF SOILS

In general, the thermomechanical behaviour of soils can mostly be categorised as thermally-induced volumetric and thermally-induced shear behaviour.

1.3.1. THERMALLY-INDUCED VOLUMETRIC BEHAVIOUR OF SOILS

FINE-GRAINED SOILS

The thermomechanical behaviour of fine-grained soils is highly dependent on the previous loading history. This can best be shown by the effect of the over-consolidation ratio (OCR) on its mechanical behaviour, which is defined as the ratio of the maximum mean effective stress experienced by the soil over the current mean effective stress. When a fine-grained soil is exposed to elevated temperatures, the volume of the soil has a tendancy to expand due to thermal elastic expansion; however, there is also the possibility of contraction, which is usually plastic and therefore permanent. Which process dominates the overall volume change of the soil directly depends on the OCR value. At low values of OCR (i.e., normally to slightly over-consolidated soils), permanent contraction is normally the dominant mechanism [9–14]. This behaviour is attributed to plastic yield of the soil due to soil particle rotation and rearrangement, similar in behaviour to when an additional compressive load is applied beyond the maximum mean effective stress experienced by the soil. At higher OCR values, permanent volume contraction decreases (or becomes zero) and thermo-elastic expansion becomes the dominant mechanism [10; 15].

COARSE-GRAINED SOILS

The volume change of sandy-soils has mostly been reported to be temperature-independent and has thus been neglected [16–18]. However, recent studies show that the temperature effect on the volumetric behaviour of sands is similar to clayey-soils, although its magnitude is smaller in comparison. The thermomechanical behaviour, similar to clays, is also dependent on loading history, although different mechanisms are involved which can often be described by confining pressure and void ratio (p and e). At low densities and high confining pressures (representing the wet side of the Critical State line), an increase in temperature leads to volume contraction, whereas, as the density increases or the confining pressure decreases, the behaviour would be mostly thermo-elastic expansion [19; 20]. Further increases in temperature are observed to result in the dominating mechanism asymptoting toward thermo-elastic expansion, independent of the soil's density.

1.3.2. THERMALLY-INDUCED SHEAR BEHAVIOUR OF SOILS

FINE-GRAINED SOILS

The thermally-induced shear behaviour of fine-grained soils depends directly on the soil's constituents and mineralogy. Thus, through an increase in temperature, the peak shear strength [10; 21–25], the stress ratio at the Critical State [22; 24; 26], and the elastic bulk and shear moduli [27] may increase, decrease or remain unchanged.

Coarse-grained soils

Most experimental results indicate a temperature-independency for the shear behaviour of coarse-grained soils [28–30]. However, a few studies show a reduction in the peak shear strength and secant modulus in dense sandy-soils as the temperature increases [20].

1.3.3. Behaviour of soils during heating-cooling cycles

When soils (both fine and coarse grained) are subjected to heating-cooling cycles, permanent volumetric strains can be produced which may accumulate [11; 17; 19; 25; 31; 32]. The highest strain produced normally results from the first cycle and additional strains become smaller as the number of cycles increases; this is known as hardening behaviour. Eventually, the soil reaches a thermally-stable condition in which further application of heating-cooling cycles would not develop permanent volumetric strains and the resultant volume change would only be due to thermo-elastic expansion.

1.3.4. Coupling behaviour

The volumetric behaviour has a strong impact on the shear behaviour in a system that has restraints. The shear stress on the pile's circumference directly depends on the applied normal stress. If the volume of a soil is reduced, the normal stress and consequently the shear strength are also reduced (in materials with frictional strength). Several coupling processes between the pile and the surrounding soil may result in volume reduction. When the soil is subjected to heating-cooling cycles, due to the hardening behaviour of soils the volume of a soil adjacent to the pile may decrease. The consecutive expansion-contraction of the pile, due to temperature variation, imposes mechanical cyclic shearing at the interface which also may result in volume reduction of the soil. Thus, settlement may occur as the shear strength and thereby bearing capacity reduce. Another key coupling is the ability of the soil to drain. In fully drained conditions, the soil is able to deform as described above. In fully undrained conditions, pore water pressures develop, due to both the thermal expansion/contraction of the water and the volumetric restraint provided by the water to the soil skeleton. In most cases, the soil is between these two states, and the behaviour therefore depends on the heating/cooling rate, the hydraulic conductivity and the drainage path.

1.3.5. Thermomechanical behaviour of soil-structure interfaces

Only a limited amount of research has been conducted on studying the thermomechanical behaviour of soils at the interface level with structures, e.g. concrete or steel. Experimental results show that the mechanical behaviour (shear and volumetric) of sand-interfaces is temperature independent [33–36]. However, the shear behaviour of clay-interfaces, similar to clayey samples in triaxial tests, shows various trends in response to thermal loads. As a result of an increase in temperature, the shear strength (or friction angle) of clay-interfaces may show a decrease [33] or remain unchanged [30; 36–38]. The adhesion of clay-interfaces demonstrated a OCR-dependency with respect to an increase in temperature. Thermomechanical tests on normally-consolidated or slightly-consolidated clay-interfaces showed an increase in adhesion [33; 34; 36], while over-consolidated clay-interfaces indicated a temperature-independency behaviour [30; 37].

1

1.4. MOTIVATION OF THE THESIS

This thesis aims to explain and quantify the governing mechanisms occurring during the performance of an energy-pile, with a focus on the behaviour of soils, which may impact the behaviour of an energy-pile (both settlements and bearing capacity). As explained in Section 1.2, soils experience a wide range of stresses (and strain levels) during the serviceability life-time of an energy-pile which can significantly affect its performance. The behaviour and performance of the energy-pile becomes even more complex when the mechanical behaviour of soils and soil-structure interfaces are also temperature dependent (Section 1.3). Therefore, in order to enable appropriate design decisions, accurate charactersation of the material behaviour and numerical models which incorporate this behaviour are required. The thesis consists of developing thermomechanical constitutive models and their implementation in a boundary-value solver (e.g. a finite-element method solver) as well as laboratory-scale direct shear tests. Since temperature has been shown to have noticeable effects on the behaviour of fine-grained soils (compared to coarse-grained soils), constitutive models were developed to capture the thermomechanical behaviour of fine-grained soils. Direct shear tests were performed on both fine-grained and coarse-grained soils to study the thermomechanical behaviour at the interface level due to the much more limited data available in the literature.

1.5. STRUCTURE OF THE THESIS

The remainder of the thesis is arranged into 7 further chapters, as follows:

In Chapter 2 a thermomechanical model using a flexible Modified Cam Clay (MCC) type single yield surface is presented which incorporates the major thermomechanical behaviour of fine-grained soils, observed when subjected to temperature variation. The model was developed based on the framework of Hyperelasticity-Hyperplasticity, to ensure its thermodynamical consistency, and thus a new rate of dissipation function was proposed. The performance of the model was also compared with laboratory test results which confirmed the capability of the model to capture the thermomechanical behaviour of soils. This was followed by proposing a descriptive micro-scale mechanism to explain how temperature affects the behaviour of fine-grained soils.

When numerically implementing constitutive models with flexible yield surfaces and plastic potentials (from which the plastic flow rule is obtained) using an implicit stress integration scheme, the numerical algorithm may fail to return the stress back onto the yield surface. This observation may be due to the existence of undesired elastic domains or domains with erratic and divergent gradients. In Chapter 3 a unique flexible MCC type yield function is proposed which addresses the aforementioned deficiencies by designing and implementing geometrical constraints for the yield function. As a result, the proposed yield function (or the plastic potential) is robust and efficient for return mapping algorithms used in implicit stress integration schemes.

Chapter 4 presents a numerical algorithm to implement the thermomechanical model developed in Chapter 2 when using a Gibbs energy potential (for deriving nonlinear thermo-elastic relationships), the flexible and robust yield function proposed in Chapter 3, and additional features such as Lode angle dependency, in a boundary-value solver (here, a finite-element method solver). Many features of the algorithm, includ-

ing accuracy, robustness, effectiveness and convergence were investigated. The performance of the thermomechanical model, implemented with this numerical algorithm in the DIANA FEA software, was thoroughly studied.

The thermomechanical model presented in Chapter 2 captures the majority of the thermomechanical behaviours of fine-grained soils. However, the model fails to predict the shakedown behaviour of soils when they are subjected to heating-cooling cycles. Therefore, a new thermomechanical constitutive model is developed in Chapter 5 to capture this type of behaviour. The model is formulated using two yield surfaces and, similar to the single-surface model developed in Chapter 2, it is developed within the framework of Hyperelasticity-Hyperplasticity. A new rate of dissipation potential is presented to capture the form of the yield function presented in Chapter 3. A temperature-dependent kinematic rule, developed within the context of thermodynamical constraints, was developed which allowed the inner yield surface to translate within the stress space. With these features the model was capable of capturing the hysteresis behaviour of soils during cyclic mechanical loadings and shakedown behaviour when they are subjected to heating-cooling cycles.

In Chapter 6 the thermomechanical behaviours of fine-grained soils (e.g. clays) and coarse-grained soils (e.g. sands) at the interface level with a concrete structure are investigated experimentally. Thermomechanical stress paths analogous to those that a soil element experiences during the short- and long-term operation of an energy-pile, at the interface level, were designed. These thermomechanical stress paths include monotonic and cyclic shearing at ambient temperature (20°C), elevated temperature (38°C) and reduced temperature (2°C), for the various boundary conditions of constant normal load (CNL), constant normal stiffness (CNS) and constant volume (CV).

Chapter 7 investigates experimentally the coupling effect of initial shear stress and thermal cycles on the thermomechanical behaviour of soils at the interface level with a concrete structure. The thermomechanical stress paths were designed to mimic soil-interface elements sheared, due to installation effects or pile elongation when subjected to daily and seasonal thermal cycles, prior to being subjected to thermal loads.

Finally, the thesis ends by synthesising the main conclusions from Chapters 2-7 and exploring the potential future research in Chapter 8.

Note that Chapters 2-7 are self-contained, as they have been or are in the process of being published as individual journal articles. As a result, there will be some repetition of fundamental concepts and literature reviews. Furthermore, notations were chosen to be simple and clear for each chapter rather than for the thesis as a whole; consequently, the notations may not be identical from chapter to chapter.

REFERENCES

[1] De Moel, M., Bach, P. M., Bouazza, A., Singh, R. M. and Sun, J. O. Technological advances and applications of geothermal energy pile foundations and their feasibility in Australia. *Renewable and Sustainable Energy Reviews*, 14(9):2683–2696, 2010.

[2] Laloui, L. and Rotta Loria, A. F. *Analysis and Design of Energy Geostructures: Theoretical essentials and practical application.* Academic Press, 2019.

1

[3] Yari, M., and Javani, N. Performance assessment of a horizontal-coil geothermal heat pump. *International Journal of Energy Research*, 31(3):288–299, 2007.

[4] Abuel-Naga, H. M., Raouf, A. M. I., Raouf, M. I. N. and Nasser, A. G. Energy piles: current state of knowledge and design challenges. *Environmental Geotechnics*, 2(4):195–210, 2015.

[5] Brandl, H. Energy foundations and other thermo-active ground structures. *Géotechnique*, 56(2):81–122, 2006.

[6] Peron, H., Knellwolf, C. and Laloui, L. A method for the geotechnical design of heat exchanger piles. *Geo-Frontiers*, page 470–479, 2011.

[7] Boennec, O. Piling on the energy. *Geodrilling International*, 150:25–28, 2009.

[8] Bourne-Webb, P. J., Amatya, B. and Soga, K. A framework for understanding energy pile behaviour. *Proceedings of the Institution of Civil Engineers - Geotechnical Engineering*, 166(2):170–177, 2013.

[9] Abuel-Naga, H. M., Bergado, D. T. and Bouazza, A. Thermally induced volume change and excess pore water pressure of soft Bangkok clay. *Engineering Geology*, 89:144–154, 2007.

[10] Cekerevac, C. and Laloui, L. Experimental study of thermal effects on the mechanical behaviour of a clay. *International Journal for Numerical and Analytical Methods in Geomechanics*, 28(3):209–228, 2004.

[11] Di Donna, A. and Laloui, L. Response of soil subjected to thermal cyclic loading: Experimental and constitutive study. *Engineering Geology*, 190:65–76, 2015.

[12] Sultan, N., Delage, P. and Cui, Y. J. Temperature effects on the volume change behaviour of Boom clay. *Engineering Geology*, 64:135–145, 2002.

[13] Towhata, I., Kuntiwattanaku, P., Seko, I. and Ohishi, K. Volume change of clays induced by heating as observed in consolidation tests. *Soils and Foundations*, 33(4):170–183, 1993.

[14] Uchaipichat, A. and Khalili, N. Experimental investigation of thermo-hydromechanical behaviour of an unsaturated silt. *Géotechnique*, 59(4):339–353, 2009.

[15] Khalili, N., Uchaipichat, A. and Javadi, A. A. Skeletal thermal expansion coefficient and thermo-hydro-mechanical constitutive relations for saturated homogeneous porous media. *Mechanics of Materials*, 42(6):593–598, 2010.

[16] Recordon„ E. Déformabilité des sols non saturés à diverses températures. *Revue Française de Géotechnique*, 65:37–56, 1993.

[17] Sadrekarimi, A. Effect of ambient temperature variation on triaxial shear testing of sands. *Geotechnical Testing Journal*, 39(4):20150160, 2016.

[18] Saix, C., Devillers, P. and El Youssoufi, M. S. Éléments de couplage thermomécanique dans la consolidation de sols non saturés. *Canadian Geotechnical Journal*, 37(2):308–317, 2000.

[19] Ng, C. W. W., Wang, S. H. and Zhou, C. Volume change behaviour of saturated sand under thermal cycles. *Géotechnique Letters*, 6(2):124–131, 2016.

[20] Liu, H., Liu, H., Xiao, Y. and McCartney, J. S. Effects of temperature on the shear strength of saturated sand. *Soils and Foundations*, 58(6):1326–1338, 2018.

[21] Abuel-Naga, H. M., Bergado, D. T. and Lim, B. F. Effect of temperature on shear strength and yielding behavior of soft Bangkok clay. *Soils and Foundations*, 47(3):423–436, 2007.

[22] Hueckel, T. and Baldi, G. Thermoplasticity of saturated clays: Experimental constitutive study. *Journal of Geotechnical Engineering*, 116(12):1778–1796, 1991.

[23] Hueckel, T., François, B. and Laloui, L. Explaining thermal failure in saturated clays. *Géotechnique*, 59(3):197–212, 2009.

[24] Kuntiwattanakul, P., Towhata, I., Ohishi, K. and Seko, I. Temperature effects on undrained shear characteristics of clay. *Soils and Foundations*, 35(1):147–162, 1995.

[25] Ng, C. W. W., Cheng, Q., Zhou, C. and Alonso, E. E. Volume changes of an unsaturated clay during heating and cooling. *Géotechnique Letters*, 6(3):192–198, 2016.

[26] Ghahremannejad, B. *Thermo-mechanical behaviour of two reconstituted clays*. PhD thesis, University of Sydney, 2003.

[27] Zhou, C., Xu, J. and Ng, C. W. W. Effects of temperature and suction on secant shear modulus of unsaturated soil. *Géotechnique Letters*, 5:123–128, 2015.

[28] Agar, J. G., Morgenstern, N. R. and Scott, J. D. Shear strength and stress-strain behaviour of Athabasca oil sand at elevated temperatures and pressures. *Canadian Geotechnical Journal*, 24(1):1–10, 1987.

[29] Graham, J., Alfaro, M. and Ferris, G. Compression and strength of dense sand at high pressures and elevated temperatures. *Canadian Geotechnical Journal*, 41(6):1206–1212, 2004.

[30] Yavari, N., Tang, A. M., Pereira, J. M. and Hassen, G. Effect of temperature on the shear strength of soils and the soil–structure interface. *Canadian Geotechnical Journal*, 53(7):1186–1194, 2016.

[31] Ng, C. W. W., Mu, Q. Y. and Zhou, C. Effects of specimen preparation method on the volume change of clay under cyclic thermal loads. *Géotechnique*, 69(2):146–150, 2019.

[32] Vega, A. and McCartney, J. S. Cyclic heating effects on thermal volume change of silt. *Environmental Geotechnics*, 2(5):257–268, 2015.

1

[33] Di Donna, A., Ferrari, A. and Laloui, L. Experimental investigations of the soil–concrete interface: Physical mechanisms, cyclic mobilization, and behaviour at different temperatures. *Canadian Geotechnical Journal*, 53(4):659–672, 2016.

[34] Wang, D., Lu, L. and Cui, P. Simulation of thermo-mechanical performance of pile geothermal heat exchanger (PGHE) considering temperature-depend interface behavior. *Applied Thermal Engineering*, 139:356–366, 2018.

[35] Vasilescu, A. R., Fauchille, A. L., Dano, C., Kotronis, P., Manirakiza, R. and Gotteland, P. Impact of temperature cycles at soil–concrete interface for energy piles. In *International Symposium on Energy Geotechnics*, pages 35–42. Springer, 2018.

[36] Maghsoodi, S., Cuisinier, O. and Masrouri, F. Thermal effects on mechanical behaviour of soil–structure interface. *Canadian Geotechnical Journal*, 57(1):32–47, 2020.

[37] Li, C., Kong, G., Liu, H. and Abuel-Naga, H. Effect of temperature on behaviour of red clay–structure interface. *Canadian Geotechnical Journal*, 56(1):126–134, 2019.

[38] Ravera, E., Sutman, M. and Laloui, L. Cyclic thermomechanical response of fine-grained soil–concrete interface for energy piles applications. *Canadian Geotechnical Journal*, 58(8):1216–1230, 2021.

2

A THERMO-MECHANICAL CONSTITUTIVE MODEL FOR FINE-GRAINED SOILS BASED ON THERMODYNAMICS

The formulation of a new thermo-mechanical constitutive model consistent with the principles of thermodynamics is presented. The model is capable of predicting rate-independent thermo-mechanical behaviour of fine-grained soils. The constitutive equations are derived by defining only a Gibbs-type free energy and a dissipation potential, in accordance with the hyperplasticity method. The addition of thermo-elasticity to the energy potential, and the embedding of the identified thermo-mechanical mechanisms into a newly proposed dissipation potential, enables the model to describe the thermo-mechanical behaviour. The proposed dissipation potential eliminates the application of shift stress which results in a simpler formulation in the context of hyperplasticity. The step-by-step procedure of deriving the equations, as well as a detailed analysis of the parameters of the model, is presented. The performance of the model is shown to be in good agreement with experimental data. A qualitative description of the possible micro-scale mechanisms for fine-grained soils, when subjected to temperature variation, is presented, as a step towards including the mechanisms in the formulation.

LIST OF SYMBOLS

Roman

$\mathbf{1}$	Identity tensor
A	Shape function for yield surface
α_k	Passive variables, $k = 1, 2, 3, \cdots$
B	Shape function for yield surface
C	Shape function for yield surface
CSL	Critical State Line
$\mathbf{C}^e$	Elastic compliance matrix
$\mathbf{D}^e$	Elastic stiffness matrix
d	Rate of mechanical dissipation function
d^t	Rate of total dissipation function
e	Void ratio
e_0	Initial void ratio
$\mathbf{e}^p$	Plastic deviatoric strain tensor
f	Helmholtz free energy potential
g	Gibbs free energy potential
g_1	Isothermal Gibbs free energy potential
$\bar{G}$	Maximum elastic shear modulus
h	Enthalpy
k_1, k_2	Functions
$\bar{K}$	Maximum elastic bulk modulus
l_1	Active variable
l_2	Conjugate of l_1
m	Power of p for bulk modulus
M	Critical State stress ratio
M_0	Critical State stress ratio at ambient temperature
n	Power of p for shear modulus
n_h	Order of an homogeneous function

Greek

α	Parameter related to the shape of the yield surface
α^*	Linear thermal expansion coefficient
$\boldsymbol{\alpha}_i$	Internal variables
β	Level of inclination of the yield surface
γ	Parameter related to the shape of the yield surface
$\boldsymbol{\varepsilon}$	Strain tensor
ε^p	Plastic strain tensor
$\dot{\boldsymbol{\varepsilon}}$	Strain increment tensor
ε_v	Total volumetric strain
ε_s	Total deviatoric strain
ε_v^e	Elastic volumetric strain
ε_s^e	Elastic deviatoric strain
$\dot{\varepsilon}_v^e$	Elastic volumetric strain increment
$\dot{\varepsilon}_s^e$	Elastic deviatoric strain increment
ε_v^p	Plastic volumetric strain
ε_s^p	Plastic deviatoric strain
$\dot{\varepsilon}_v^p$	Plastic volumetric strain increment
$\dot{\varepsilon}_s^p$	Plastic deviatoric strain increment
ε_v^T	Thermo-elastic volumetric strain
$\dot{\varepsilon}_v^T$	Thermo-elastic volumetric strain increment
η	Stress ratio
T	Absolute temperature
T_0	Initial absolute temperature
$\mathbf{T}_{,k}$	Thermal gradient
$\dot{T}$	Temperature increment
κ	Slope of unloading/reloading curve
λ	Slope of NCL

NCL	Normal Consolidation Line
OCR	Over Consolidation Ratio
p	Mean effective stress
p_0	Initial mean effective stress
p_c	Pre-consolidation pressure
p_{cT}	Apparent pre-consolidation pressure
$\dot{p}_{cT}$	Rate of change of the apparent pre-consolidation pressure
p_{ref}	Reference mean effective stress
PI	Plasticity index
q	Deviatoric stress
$\boldsymbol{q}$	Heat flux vector
q_0	Initial deviatoric stress
$\dot{Q}$	Heat supply
r	Homogeneous function
r_p	Plastic flow in p direction
r_q	Plastic flow in q direction
$\mathbf{r}$	Plastic flow direction
RH	Rotational hardening
s	Entropy
$\dot{s}$	Rate of change of entropy
$\mathbf{s}$	Deviatoric stress tensor
t	Thickness of hydrate layers
u	Internal energy potential
$\dot{u}$	Rate of change of internal energy
u_p	Pore water pressure
$\boldsymbol{\nu}$	Generalised dissipative velocities
w	Flow potential
$\dot{W}$	Work input
$\mathbf{x}$	State variables
y	Yield function in true stress space
y^d	Yield function in dissipative stress space
$\dot{y}$	Rate of change of the yield function
z	Force potential

$\dot{\Lambda}$	Plastic multiplier
μ	Thermal softening coefficient
π	Coefficient of Critical State stress ratio variation
Π_t	Total disjoining pressure
Π_e	Electrostatic disjoining pressure
Π_m	Molecular disjoining pressure
Π_s	Structural disjoining pressure
$\boldsymbol{\sigma}$	Total stress
$\dot{\boldsymbol{\sigma}}$	Stress increment tensor
$\boldsymbol{\sigma}'$	Effective stress
Υ	Scalar multiplier of χ
Υ'	Scalar multiplier
χ	Generalised dissipative force
χ_p	Mean generalised dissipative stress
χ_q	Deviatoric generalised dissipative stress
$\bar{\chi}$	Generalised stress
$\bar{\chi}_p$	Mean generalised stress
$\bar{\chi}_q$	Deviatoric dissipative stress

2.1. INTRODUCTION

A number of constitutive models have been developed to capture the thermo-mechanical behaviour of soils [1–17]. These models are mostly based on plasticity theory, and some are capable of capturing the general thermo-mechanical behaviour of soils with reasonable accuracy. However, mostly they do not follow the principles of thermodynamics; therefore, certain phenomena may not be captured/predicted and other phenomena may be spuriously predicted. For instance, Lashkari & Golchin [18] devised a stress path that formed a closed loop in the meridian stress space (p-q). They analyzed the responses stemming from a non-linear elasticity formula, which was created based on thermodynamic principles. This was subsequently compared with the responses from a variant without any underlying thermodynamic principles. While theoretically the elastic strains generated at the end of a closed-loop stress path should match the ones at its beginning (i.e., elastic responses should be stress-path independent), they demonstrated that only the elasticity derived from thermodynamics adhered to this concept. In contrast, the other formulation resulted in elastic strains that lacked physical justification or reasoning. However, not utilising thermodynamics principles allows observed behaviour to be relatively easily included in constitutive equations, and therefore can be used to reproduce observed behaviour well (e.g. [19]). As stress-paths become more complex (e.g. multi-physical processes or multi-directional cycles), or exceed bounds for which the models have been validated, it is certainly attractive to eliminate potential spurious non-thermodynamically consistent behaviour, which can accumulate with repeated loading [19].

The principles of thermodynamics are sufficient to develop a framework which accurately captures the behaviour of geomaterials [20; 21]. To do so, the identification of the governing mechanisms during the process and the assigning of appropriate variables that represent the system are required. A discussion on selecting these variables can be found in [22]. Several approaches exist that use the principles of thermodynamics to exploit constitutive equations (see [21–23], for example). In this chapter, a thermo-mechanical constitutive model is developed, based on the thermodynamically-consistent framework of hyperplasticity. Hyperplasticity theory was firstly developed by Collins & Houlsby [24], and combines and utilises the laws of thermodynamics through the application of Ziegler's hypothesis [25]. Thus, the derived constitutive equations satisfy the principles of thermodynamics and can be implemented with confidence into numerical simulations [20]. This approach has been used to capture the creep and freezing of soils ([26] and [27], respectively).

Note that the formulations presented here are in accordance with geotechnical conventions, where compressive stresses and contractive strains are considered to be positive and all stresses are effective stresses. In line with this context, the thermal expansion coefficient utilised in this chapter are presented with negative values.

2.2. THERMO-MECHANICAL BEHAVIOUR OF FINE-GRAINED SOILS

In general, the mechanical response of materials can be investigated in two distinct parts: the volumetric behaviour and the shear behaviour. Similarly, the effect of temper-

ature on the thermo-mechanical behaviour of soils can be split into thermally-induced volumetric and thermally-induced shear effects.

Normally and slightly over-consolidated clayey-soils (soils with low over-consolidation ratios) undergo permanent volumetric contraction when they are subjected to an increase in temperature [28–32]. As the over-consolidation ratio (OCR) increases, the severity of the thermally-induced volumetric contraction decreases and, at high OCRs, the thermo-mechanical behaviour transitions to volumetric expansion. This volumetric expansion is mostly reversible and is attributed to the thermo-elasticity of highly over-consolidated soils due to the volumetric expansion of soil particles without rearrangement [33].

Soils also show a reduction in yielding stress (represented by pre-consolidation pressure) at higher temperatures, when consolidated isotropically [28; 29; 32; 34]. Variation of the pre-consolidation pressure at different temperatures (p_{cT}), normalised by the pre-consolidation pressure at the ambient temperature (p_{cT0}), with respect to the subjected temperature difference, is shown in Figure 2.1 for different soils.

On the other hand, the shear behaviour of soils shows a range of behaviours as the temperature is elevated. Depending on the mineralogy and constituents of the soil, the peak shear strength and dilatancy may increase, remain unchanged, or decrease during heating [29; 35–39]. A similar result has also been reported for the stress ratio at Critical State conditions [29; 32; 34; 35; 40] (see Figure 2.2). A reduction or increase in the elastic shear modulus observed at elevated temperatures is another demonstration of mineralogy-dependency of the shear behaviour of soils [41].

Soils exhibit hardening behaviour during heating-cooling cycles [4; 39; 42; 43]. The oedometer test results for two different clays [28; 31], subjected to a heating-cooling cycle (heating followed by cooling), are presented in Figure 2.3. After the heating-cooling cycle, the void ratio reduces (permanent volumetric strains produce), leading toward a denser state. As a result, the pre-consolidation pressure increases and the elastic domain becomes bigger.

When soils are subjected to several thermal cycles, each cycle adds to the accumulated permanent volumetric strain. However, the amount of permanent strain in a cycle reduces with consecutive cycles, until a thermally stable condition is reached. In this condition, the permanent component of volumetric strain tends to zero and the behaviour becomes totally elastic, governed by the volumetric thermal expansion of soil grains.

The structure and chemical-reactivity potential of a soil are proven to significantly affect the intensity-level of thermally induced deformation during heating [30; 39; 43–45]. The plasticity index, PI, can be considered as an indication of the level of chemical-reactivity potential. As the PI increases, the soil is more susceptible to permanent volumetric reduction at elevated temperatures [4; 36]. Also, normally and slightly consolidated intact soils, with randomly distributed size and position of void spaces, are susceptible to higher volumetric contraction in comparison to remoulded soil specimens with uniformly distributed voids (both in size and position) [39].

2
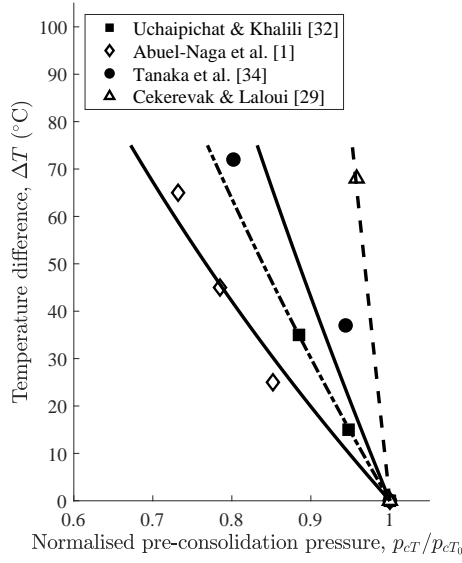
Figure 2.1: Reduction of the normalised pre-consolidation pressure with temperature difference ΔT°C
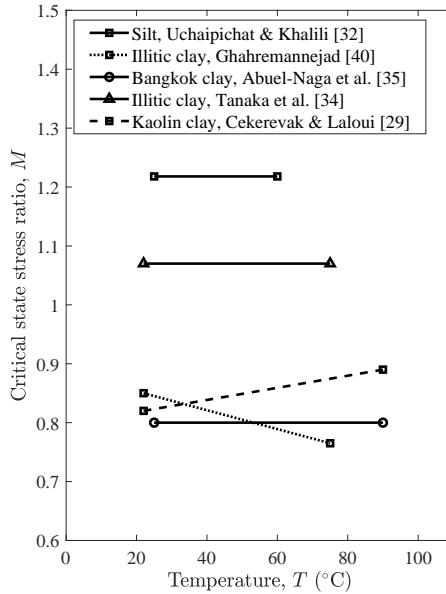
Figure 2.2: Variation of Critical State stress ratio, M, with temperature T°C
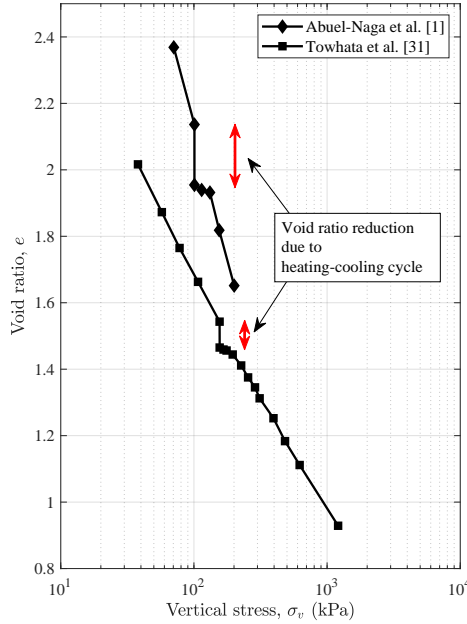
Figure 2.3: Hardening behaviour during heating-cooling cycle

2.3. FORMULATION OF THE THERMO-MECHANICAL MODEL

To capture the thermo-mechanical behaviour of soils, it is here proposed that the thermo-mechanical behaviour be defined using Terzaghi's effective stress, by embedding thermal mechanisms into the constitutive formulation. Terzaghi's [46] effective stress tensor is defined as:

$$\boldsymbol{\sigma}' = \boldsymbol{\sigma} - u_p \mathbf{1} \tag{2.1}$$

where $\boldsymbol{\sigma}$ and u_p are the total stress tensor and pore pressure, respectively and $\mathbf{1}$ is the second order identity tensor, and the effective stress is proven to be a thermodynamically consistent stress state variable that can reflect the mechanical behaviour of saturated soils [47]. From here on, all the stresses are effective. The employed continuum-scale thermo-mechanical mechanisms in this model, are outlined as follows:

- The position of the total (or permanent) volume variation due to change in the mean effective stress (p) line (often referred to as the normal consolidation line (NCL)) changes with temperature.

- The gradient of elastic and permanent volume variation due to changes in mean effective stress (p) are insensitive to temperature variation.

- The bounded size of the elastic domain changes as the temperature varies (Eq. (2.13)).

- The shear strength (i.e. the stress ratio) at the Critical State condition may change (increase, decrease or remain constant) as temperature varies (Eq. (2.12)).

- Thermal expansion of soil grains are thermo-elastic (Eq. (2.E.5)).

The components of the model, including elasticity, plasticity, and flow and hardening rules, are determined by specifying two potentials; namely, the Gibbs free energy potential and the rate of dissipation potential. The yield surface in the Meridian plane has an ellipsoid-type shape (demonstrated to be appropriate for geomaterials [48] and is defined by two parameters. It has the capability to rotate (be inclined with respect to the p-axis) and expand or shrink in the presence of isotropic hardening. The plastic flow (direction of the plastic strain increments) is non-associated, but without the necessity of defining a separate plastic potential as is the case in conventional plasticity models.

The major temperature effects on the mechanical behaviour of fine-grained soils, explained in Section 2.2, are associated with the irreversible response of the material. The variation of the apparent pre-consolidation pressure, p_{cT}, and the Critical State stress ratio, M, with temperature, respectively, represents the temperature influence on the variation of the yielding stress (initiation of irreversible response) and friction angle when the shear strength is fully mobilised (ultimate shear strength). Since the plasticity component of the constitutive equations are directly derived from the dissipation potential, it is logical to incorporate the identified thermo-mechanical mechanisms into the dissipation potential. By this, and with the addition of a volumetric thermal expansion component in the Gibbs free energy potential (to capture the thermo-elasticity), the temperature effects on both the volumetric and shear behaviours of soils are captured.

A new dissipation potential is proposed, which not only embeds the thermo-mechanical mechanisms, but also omits the utilisation of shift stresses during the conversion from dissipation space to true stress space (see Appendix 2.A); i.e., the addition of a kinematic hardening to shift the yield surface is excluded. Consequently, a simpler formulation is derived, which simplifies its numerical implementation in boundary value solvers such as the finite element and material point methods.

In the following, the procedure of deriving the complete constitutive formulation within the framework of hyperplasticty is presented. The current model is the first thermo-mechanical model for fine-grained soils developed by this framework. For completion, a description of the hyperplasticty approach is provided in Appendix 2.A.

2.3.1. ENERGY POTENTIAL INCLUDING TEMPERATURE EFFECTS

A Gibbs-type function is proposed for the free energy potential and is defined by true stress invariants in triaxial stress space (mean effective stress, $p = tr(\boldsymbol{\sigma})/3$ (kPa) and deviatoric stress, $q = (3/2\, \mathbf{s} : \mathbf{s})^{1/2}$ (kPa), where $\mathbf{s} = \boldsymbol{\sigma} - tr(\boldsymbol{\sigma})/3 : \mathbf{1}$ is the deviatoric stress tensor), internal variables (which here are only the plastic strain invariants; the plastic volumetric strain, $\varepsilon_v^p = tr(\boldsymbol{\varepsilon}^p)$, and the plastic deviatoric strain, $\varepsilon_s^p = (2/3\, \mathbf{e}^p : \mathbf{e}^p)^{1/2}$; $\mathbf{e}^p = \boldsymbol{\varepsilon}^p - tr(\boldsymbol{\varepsilon}^p)/3 : \mathbf{1}$, where $\boldsymbol{\varepsilon}^p$ and $\mathbf{e}^p$ are plastic strain and plastic deviatoric strain tensors, respectively), and the absolute temperature T(K), as the independent variables

$$g\left(p, q, \varepsilon_v^p, \varepsilon_s^p, T\right) = g_1\left(p, q\right) - p\varepsilon_v^p - q\varepsilon_s^p - 3\alpha^* p\left(T - T_0\right) \tag{2.2}$$

where α^* is the linear thermal expansion coefficient of the soil skeleton. The term $3\alpha^* p(T - T_0)$ represents the isotropic thermal volumetric expansion of the elasticity, due to temperature variation (thermo-elasticity). The linear thermal expansion coefficient α^* is considered constant, although its dependency on temperature, stress level and over-consolidation ratio has been addressed in literature. A constant value of α^*, with respect to both temperature and stress level, ensures thermodynamical consistency. Anisotropic terms for the thermal expansion coefficient for thermo-elasticity can be used if desired, although further experimental support is needed to define the appropriate terms.

The form of the energy potential in Eq. (2.2) leads to a "*decoupled*" material behaviour [24], through the terms $p\varepsilon_v^p$ and $q\varepsilon_s^p$, in which the elastic and plastic behaviours are independent of each other. Energy potentials incorporating elastic-plastic coupling can be found in the works of [18; 49; 50], which result in a complex elasticity formulation. For the sake of simplicity, and due to the lack of evidence linking the plasticity to the elasticity of fine-grained soils, decoupled behaviour is considered here. The term $g_1(p, q)$ is the free energy function for isothermal conditions, previously proposed by [51] for geo-materials, in which the elasticity component of the model (for isothermal conditions) is derived as

$$g_1(p, q) = -\frac{p^{2-m} - (2 - m)\, p\, p_0^{1-m}}{\bar{K}(2 - m)(1 - m)\, p_{ref}^{1-m}} - \frac{q^2}{6\bar{G} p_{ref}^{1-n} p^n} + \frac{q_0\,(2qp_0 - nq_0 p)}{6\bar{G} p_{ref}^{1-n} p_0^{1+n}} \tag{2.3}$$

where p_{ref} (kPa) is the reference pressure (here is 1 kPa); p_0 and q_0 are the initial values of the mean effective and deviatoric stresses, respectively; $\bar{K}$ and $\bar{G}$ are material constants, respectively related to the elastic bulk modulus and shear modulus; and m and n are constants representing the power dependence of the bulk and shear moduli, respectively, on the mean effective stress p. For the case when the bulk modulus is linearly proportional to p (for cases in which $m = 1$), the free energy is natural-log dependent on p

$$g_1(p, q) = -\frac{p}{\bar{K}}\left(\ln\left(\frac{p}{p_0}\right) - 1\right) - \frac{q^2}{6\bar{G} p_{ref}^{1-n} p^n} + \frac{q_0\,(2q - nq_0 p)}{6\bar{G} p_{ref}^{1-n} p_0^n} \tag{2.4}$$

Following Eq. (2.A.7), the total strains $(\varepsilon_v, \varepsilon_s)$, consisting of elastic $(\varepsilon_v^e, \varepsilon_s^e)$, thermo-elastic (ε_v^T), and thermo-plastic components $(\varepsilon_v^p, \varepsilon_s^p)$, are derived by differentiating the free energy potential (Eq. (2.2)) with respect to the stress components (p, q)

$$\varepsilon_v = -\frac{\partial g\left(p, q, \varepsilon_v^p, \varepsilon_s^p, T\right)}{\partial p} = -\frac{\partial g_1(p, q)}{\partial p} + 3\alpha^*\,(T - T_0) + \varepsilon_v^p = \varepsilon_v^e + \varepsilon_v^T + \varepsilon_v^p \tag{2.5}$$

$$\varepsilon_s = -\frac{\partial g\left(p, q, \varepsilon_v^p, \varepsilon_s^p, T\right)}{\partial q} = -\frac{\partial g_1(p, q)}{\partial q} + \varepsilon_s^p = \varepsilon_s^e + \varepsilon_s^p \tag{2.6}$$

Since the thermal expansion (i.e. the term $3\alpha^*\,(T - T_0)$ in Eq. (2.2)) is only defined for the volumetric part of the energy potential (isotropic term), the deviatoric thermo-elastic

strain is zero. In summary, the total strain can be rewritten in compact format as

$$\left\{ \begin{array}{c} \varepsilon_v \\ \varepsilon_s \end{array} \right\} = \left\{ \begin{array}{c} \varepsilon_v^e \\ \varepsilon_s^e \end{array} \right\} + \left\{ \begin{array}{c} \varepsilon_v^T \\ 0 \end{array} \right\} + \left\{ \begin{array}{c} \varepsilon_v^p \\ \varepsilon_s^p \end{array} \right\}$$

where $\varepsilon_v^e = -\frac{\partial g_1(p,q)}{\partial p}$; $\varepsilon_s^e = -\frac{\partial g_1(p,q)}{\partial q}$; $\varepsilon_v^T = 3\alpha^*(T - T_0)$

The generalised stresses (see Appendix 2.A), i.e. the derivative of the Gibbs free energy potential with respect to internal variables, are

$$\left\{ \begin{array}{c} \bar{\chi}_p \\ \bar{\chi}_q \end{array} \right\} = -\left\{ \begin{array}{c} \frac{\partial g}{\partial \varepsilon_v^p} \\ \frac{\partial g}{\partial \varepsilon_s^p} \end{array} \right\} = \left\{ \begin{array}{c} p \\ q \end{array} \right\} \tag{2.7}$$

2.3.2. RATE OF DISSIPATION POTENTIAL INCLUDING TEMPERATURE EFFECTS

In order to determine the plastic strains of a rate-independent material, the definition of an appropriate rate of dissipation potential function is required. Collins & Hilder [48] proposed a rate of dissipation potential for fine-grained soils and connected it to the conjugated energy potential through the shift stress. Here, a new rate of dissipation potential is presented whose novelty is twofold. Firstly, the dissipation function is defined in such a way so that the use of the shift stress is eliminated, while preserving the properties of the dissipation potential in [48] (with the advantage of a simpler formulation in comparison to the equations in [48]) and secondly, it incorporates the continuum-scale thermal mechanisms which are encapsulated in the apparent pre-consolidation pressure and Critical State stress ratio. The rate of dissipation function is defined as

$$d = C\left(\dot{\varepsilon}_v^p + \beta\dot{\varepsilon}_s^p\right) + \sqrt{A^2\left(\dot{\varepsilon}_v^p + \beta\dot{\varepsilon}_s^p\right)^2 + B^2\left(\dot{\varepsilon}_s^p\right)^2} \tag{2.8}$$

where $\dot{\varepsilon}_v^p$ and $\dot{\varepsilon}_s^p$ are plastic volumetric and deviatoric strain increments (as the generalised dissipative velocities, or the rate of change of internal variables in the case of rate-independent behaviour (see Appendix 2.A), respectively; and β represents the level of anisotropy by inclining the yield surface, with respect to the p-axis. A, B and C are functions defined by stress, history and shape parameter components, which define the shape and size of the yield function (to be determined later). Readers are referred to [48] for the procedure of determining the functions A and B. These two functions, with the newly defined function C, are defined as

$$A = \left(1 - \gamma\right)p + \frac{\gamma}{2}p_{cT} \tag{2.9}$$

$$B = M\left((1 - \alpha)p + \frac{\alpha\gamma}{2}p_{cT}\right) \tag{2.10}$$

$$C = \frac{\gamma}{2}p_{cT} \tag{2.11}$$

where α and γ are parameters that affect the shape of the yield surface. These two parameters provide the benefit of defining a single yield surface, resembling a Hvorslev-type surface for highly over-consolidated stress states and a cap-type surface for normally and lightly consolidated states. This can overcome the over-prediction of shear strength for highly over-consolidated soils that has been observed when using Modified Cam Clay-type models. M is the stress ratio at the Critical State. It has been seen in Figure 2.2 that M may change due to temperature variation. In this regard, a linear variation with temperature (as a first approximation) is considered

$$M = M_0 + \pi \, (T - T_0) \tag{2.12}$$

where π is the slope of the variation of M with respect to temperature T, and M_0 is the Critical State stress ratio at ambient temperature. The value of π depends on the mineralogy of the soil; M may increase or decrease with temperature, so that π may take positive or negative values, respectively, and in the case of temperature independency its value is zero.

p_{cT} is the apparent pre-consolidation pressure, which for the isothermal condition (no temperature variation) is similar to the formulation presented in [20; 52]. Here, the effect of temperature (see Figure 2.1) is included in the pre-consolidation pressure as follows

$$p_{cT} = p_r e^{\left(\frac{1+e_0}{\lambda-\kappa}\right)\varepsilon_v^p} \, e^{-\mu(T-T_0)} \tag{2.13}$$

where λ and κ are the slopes of the normal compression (NCL) and unloading lines in $\ln e$ (void ratio), versus $\ln p$ space, respectively; e_0 and T_0 are the initial void ratio and ambient absolute temperature, respectively; and μ is the coefficient of thermal softening/shrinkage, first presented by Cui et al. [3]. The apparent pre-consolidation pressure hardens isotropically with plastic volumetric strain (through the term $e^{((1+e_0)/(\lambda-\kappa))\varepsilon_v^p}$), while it (thermally) softens/shrinks with an increase in temperature (through the term $e^{-\mu(T-T_0)}$). Thermal softening/shrinkage influences the size of the elastic domain (reduces) and represents the thermal mechanism proposed for the volumetric part of the behaviour of soils.

Since the above rate of dissipation potential is defined for rate-independent materials, it is identical to the force potential z (see Appendix 2.A). Hence, the yield function (surface) can be derived, as defined by the generalised dissipative forces (or dissipative stresses in the case of rate-independent materials) which are determined as the derivation of the rate of dissipation potential function with respect to the rate of internal variables (Eq. (2.A.15)). The dissipative stresses are

$$\left\{ \begin{array}{c} \chi_p \\ \chi_q \end{array} \right\} = \left\{ \begin{array}{c} \frac{\partial d}{\partial \dot{\varepsilon}_v^p} \\ \frac{\partial d}{\partial \dot{\varepsilon}_s^p} \end{array} \right\} = \left\{ \begin{array}{c} C + \frac{A^2\left(\dot{\varepsilon}_v^p + \beta\dot{\varepsilon}_s^p\right)}{\sqrt{A^2\left(\dot{\varepsilon}_v^p+\beta\dot{\varepsilon}_s^p\right)^2 + B^2\left(\dot{\varepsilon}_s^p\right)^2}} \\ \beta C + \frac{B^2\dot{\varepsilon}_s^p + \beta A^2\left(\dot{\varepsilon}_v^p+\beta\dot{\varepsilon}_s^p\right)}{\sqrt{A^2\left(\dot{\varepsilon}_v^p+\beta\dot{\varepsilon}_s^p\right)^2 + B^2\left(\dot{\varepsilon}_s^p\right)^2}} \end{array} \right\} \tag{2.14}$$

The general procedure for deriving the yield surface for rate-independent materials, where the rate of dissipation potential is a first order homogeneous function of plastic

strain rates, is by invoking the Legendre-Fenchel transform on the rate of dissipation function, since the classical Legendre transform becomes degenerate [21]. However, this procedure can also be done in a simpler way. Any mathematical equation consisting of the dissipative stresses in Eq. (2.14) that equals to zero, represents the yield function. Hence, the yield function is

$$y^d = B^2 \left(\chi_p - C \right)^2 + A^2 \left(\chi_q - \beta \chi_p \right)^2 - A^2 B^2 = 0 \tag{2.15}$$

This form of yield function indicates an ellipsoid and is defined in dissipative stress space (χ_p, χ_q), rather than in conventional stress space (p, q). The yield function may be transferred to true stress space (see Appendix 2.A) by Ziegler's orthogonality condition.

2.3.3. TEMPERATURE DEPENDENT FLOW RULE

The flow of plastic strain increments is always normal to the yield surface (y^d) in dissipative stress space [20; 24], i.e., the flow rule is always associated in dissipative stress space. This can be mathematically shown as the derivative of the yield surface y^d (Eq. (2.15)) with respect to dissipative stresses as

$$\left\{ \begin{array}{c} \dot{\varepsilon}_v^p \\ \dot{\varepsilon}_s^p \end{array} \right\} = \dot{\Lambda} \left\{ \begin{array}{c} \frac{\partial y^d}{\partial \chi_p} \\ \frac{\partial y^d}{\partial \chi_q} \end{array} \right\} = 2\dot{\Lambda} \left\{ \begin{array}{c} B^2 \left(\chi_p - C \right) - \beta A^2 \left(\chi_q - \beta \chi_p \right) \\ A^2 \left(\chi_q - \beta \chi_p \right) \end{array} \right\} \tag{2.16}$$

where $\dot{\Lambda}$ is the plastic multiplier defining the plastic strain increment magnitude.

One of the useful assumptions implemented into hyperplasticity theory is Ziegler's orthogonality postulation (see Appendix 2.A), which is used to link the generalised stress (Eq. (2.7)) to the dissipative stress (Eq. (2.14)). By the use of Eq. (2.7) and Eq. (2.A.10), the generalised dissipative stress becomes

$$\left\{ \begin{array}{c} \chi_p \\ \chi_q \end{array} \right\} = \left\{ \begin{array}{c} p \\ q \end{array} \right\} \tag{2.17}$$

This outcome results in the definition of both the yield surface (Eq. (2.15)) and plastic flow (Eq. (2.16)) in conventional stress space (p,q), by substituting the dissipative stresses with generalised stresses (as in Eq. (2.17)). Consequently, the yield surface and plastic flow in terms of true stresses respectively become

$$y = B^2 \left(p - C \right)^2 + A^2 \left(q - \beta p \right)^2 - A^2 B^2 = 0 \tag{2.18}$$

$$\left\{ \begin{array}{c} \dot{\varepsilon}_v^p \\ \dot{\varepsilon}_s^p \end{array} \right\} = \dot{\Lambda} \left\{ \begin{array}{c} r_p \\ r_q \end{array} \right\} = 2\dot{\Lambda} \left\{ \begin{array}{c} B^2 \left(p - C \right) - \beta A^2 \left(q - \beta p \right) \\ A^2 \left(q - \beta p \right) \end{array} \right\} \tag{2.19}$$

It should be noted that the plastic flow in dissipative stress space (Eq. (2.16)) is associated to the yield surface y^d (Eq. (2.15)) with respect to the dissipative stresses χ_p and χ_q. However, the plastic flow in true stress space (Eq. (2.19)) becomes non-associated with respect to the yield surface y defined in true stress space (Eq. (2.18)). This is due to the

true stress-dependency of the dissipation function via functions A and B (see Eqs. (2.9)-(2.10)). Table 2.1 presents the yield surfaces defined in dissipative stress space and true stress space, along with their respective derivatives, and the flow rule in true stress space. The flow rule and normal to the yield surface (Eqs. (T-3) and (T-5), respectively) are different, as in true stress space the stress dependency of functions A and B are included in Eq. (T-5), whereas they are not in Eq. (T-3). An associated flow rule (in true stress space) would include this dependency, i.e. would follow Eq. (T-5); hence, Eq. (T-3) indicates the non-associativity of the plastic flow in true stress space. This is compatible with the findings of [21; 22], where it was shown that the non-associated flow rule for frictional materials (i.e. pressure-dependent materials such as geomaterials) is the result of the dependency of the rate of dissipation function to stresses.

The non-associated plastic flow presented above, unlikely classical plasticity theory, is derived without the necessity of introducing a separately defined plastic potential. Srinivasa [21] showed that for a rate of dissipation function defined by separable functions of stress and plastic strain increments, i.e., having the form of $d = d_1(\sigma) \, d_2(\dot{\varepsilon}^p)$, it is possible to derive the plastic potential (as well as the yield surface). Note that the rate of dissipation function adopted here (Eq. (2.8)) is not defined as a separable function. Thus, it may not be straightforward to determine the plastic potential in true stress space, although the plastic flow (Eq. (2.9) or Eq. (T-3)) is derived.

2.3.4. Temperature dependent hardening rules

In strain hardening hyperplasticity models, the hardening rules are specified by the potential functions. The proposed model consists of an isotropic hardening rule and may be extended to account for rotational hardening (though not covered here). The isotropic hardening is embedded through the way that the rate of dissipative function is defined, by making the rate of dissipative function dependent on internal variables (which here is the plastic volumetric strain).

Isotropic hardening

The apparent pre-consolidation pressure p_{cT} is the isotropic hardening variable of the model. It hardens by plastic volumetric strain increments (similar to the MCC family of models), while it softens/shrinks by an increase in temperature (Eq. (2.13)). By determining the rate of Eq. (2.13) (differentiation with respect to plastic volumetric strain ε_v^p, and absolute temperature T), the isotropic hardening is derived

$$\dot{p}_{cT} = \left(\frac{1 + e_0}{\lambda - \kappa} \dot{\varepsilon}_v^p - \mu \dot{T} \right) p_{cT} \tag{2.20}$$

2

Table 2.1: Comparison between the yield surface defined in dissipative stress space and that defined in true stress space, along with their respective normals, and the flow rule in true stress space

Yield surface defined in dissipative stress space (χ_p-χ_q) (Eq. (2.15))	Yield surface defined in true stress space (p-q) (Eq. (2.18))
$$y^d = B^2(\chi_p - C)^2 + A^2(\chi_q - \beta\chi_p)^2 - A^2B^2 = 0 \qquad \text{(T-1)}$$	$$y = B^2(p - C)^2 + A^2(q - \beta p)^2 - A^2B^2 = 0 \qquad \text{(T-4)}$$
Derivative of y^d with respect to dissipative stresses (χ_p-χ_q) (associated flow rule in dissipative stress space (Eq. (2.16)))	**Derivative of y with respect to true stresses (p-q) (normal to the yield surface)**
$$\left\{ \begin{array}{c} \frac{\partial y^d}{\partial \chi_p} \\ \frac{\partial y^d}{\partial \chi_q} \end{array} \right\}$$ $$= 2 \left\{ \begin{array}{c} B^2(\chi_p - C) - \beta A^2(\chi_q - \beta\chi_p) \\ A^2(\chi_q - \beta\chi_p) \end{array} \right\} \quad \text{(T-2)}$$	$$\left\{ \frac{\partial y}{\partial \boldsymbol{\sigma}} \right\} = \left\{ \begin{array}{c} \frac{\partial y}{\partial p} \\ \frac{\partial y}{\partial q} \end{array} \right\} = \left\{ \begin{array}{c} r_p + \frac{\partial y}{\partial A}\frac{\partial A}{\partial p} + \frac{\partial y}{\partial B}\frac{\partial B}{\partial p} \\ r_q + \frac{\partial y}{\partial A}\frac{\partial A}{\partial q} + \frac{\partial y}{\partial B}\frac{\partial B}{\partial q} \end{array} \right\} \quad \text{(T-5)}$$ where r_p and r_q are defined in (T-3)
Flow rule in true stress space (Eq. (2.19)) (by applying Zieglers postulation, Eq. (2.17), to the associated flow rule in dissipative stress space (T-2)) Ziegler's postulation and $\left\{ \begin{array}{c} \chi_p \\ \chi_q \end{array} \right\} = \left\{ \begin{array}{c} p \\ q \end{array} \right\}$ (Eq. (2.17)) $\rightarrow$ {Flow direction} $= \left\{ \begin{array}{c} r_p \\ r_q \end{array} \right\}$ $$= 2 \left\{ \begin{array}{c} B^2(p - C) - \beta A^2(q - \beta p) \\ A^2(q - \beta p) \end{array} \right\} \quad \text{(T-3)}$$	

ROTATIONAL HARDENING

Although various rotational hardening (RH) rules for clay constitutive models exist in literature [53–57], RH is not considered in this model. Several issues may arise regarding RH, so that its implementation should be considered with caution. For example, assigning RH may lead to a unique or non-unique anisotropic Critical State, which is a debatable issue [55]. Also, it may not be possible to determine a thermodynamically-consistent RH rule that is simultaneously compatible with currently accepted RH rules and criteria. This implies that further investigation is required to define an appropriate RH rule that is thermodynamically-consistent while matching with experimental data. However, here the yield surface is capable of being inclined in p-q stress space through the parameter β. This may be useful to capture the anisotropic shape of the yield surface for soils that have previously been anisotropically loaded, e.g. under K_0 conditions.

2.3.5. TEMPERATURE DEPENDENT PLASTIC MULTIPLIER

The last component of this model that needs to be determined is the plastic multiplier, representing the magnitude of the plastic strain increments. Eq. (2.18) can be written in the general form, $y = y\left(p, q, \varepsilon_v^p, T\right)$. The consistency condition can then be written as

$$\dot{y} = \left\{ \begin{array}{cc} \frac{\partial y}{\partial p} & \frac{\partial y}{\partial q} \end{array} \right\} \cdot \left\{ \begin{array}{c} \dot{p} \\ \dot{q} \end{array} \right\} + \left\{ \begin{array}{cc} \frac{\partial y}{\partial \varepsilon_v^p} & 0 \end{array} \right\} \cdot \left\{ \begin{array}{c} \dot{\varepsilon}_v^p \\ \dot{\varepsilon}_q^p \end{array} \right\} + \frac{\partial y}{\partial T} \dot{T} = 0 \qquad (2.21)$$

By substitution of Eq. (2.19) into Eq. (2.21), the plastic multiplier can be determined as

$$\dot{\Lambda} = -\frac{\left\{ \begin{array}{cc} \frac{\partial y}{\partial p} & \frac{\partial y}{\partial q} \end{array} \right\} \cdot \left\{ \begin{array}{c} \dot{p} \\ \dot{q} \end{array} \right\} + \frac{\partial y}{\partial T} \dot{T}}{\left\{ \begin{array}{cc} \frac{\partial y}{\partial \varepsilon_v^p} & 0 \end{array} \right\} \cdot \left\{ \begin{array}{c} r_p \\ r_q \end{array} \right\}} = -\frac{\left\{ \frac{\partial y}{\partial \boldsymbol{\sigma}} \right\}^{\mathrm{T}} \{\dot{\boldsymbol{\sigma}}\} + \frac{\partial y}{\partial T} \dot{T}}{\left\{ \frac{\partial y}{\partial \boldsymbol{\varepsilon}^p} \right\}^{\mathrm{T}} \{\mathbf{r}\}} \qquad (2.22)$$

The components of this formulation can be found in Appendix 2.D.

2.3.6. INCREMENTAL FORMULATION

For numerical analysis, an incremental relationship between stress and strain is mostly utilised. The incremental formulations can be derived based on stress or strain controlled conditions (as the input); both scenarios can be found in Appendix 2.E.

2.3.7. PARAMETERS OF THE MODEL

Depending on which energy potential for elasticity is chosen (Eq. (2.3) or Eq. (2.4)), the model is defined by 12 or 11 parameters, respectively. These parameters can be categorised in accordance to their role in the behaviour of the material; volumetric behaviour (elastic and plastic), shear behaviour (elastic and plastic), temperature impacts, and parameters related to the shape of the yield surface. The relevant parameters in each category and the required tests for determining them are summarised in Table 2.2. Rotation of the yield surface, controlled by β, is not considered ($\beta = 0$).

$\bar{K}$, $\bar{G}$, m and n are material constants related to elastic properties. $\bar{K}$ and $\bar{G}$ are attributed to the maximum values of the bulk and shear moduli of the soil, respectively.

They can be determined from the tangential values of the p-ε_v and q-ε_s curves, respectively, at low strain levels (representing the elastic region). These parameters can be measured from drained triaxial tests or more accurately from resonant and bender element tests. The parameters m and n are the powers related to p for the elastic bulk and shear moduli. In the case of $m = n = 1$, where the elastic bulk and shear moduli are linearly dependent on p, the number of parameters reduces to 10.

λ and κ are related to the volumetric behaviour of soils and are, respectively, the negative slopes of the normal compression and swelling lines in ln$e$-ln$p$ space, measured from isotropic triaxial (at $q = 0$) consolidation or oedometer tests.

M_0 is the stress ratio (q/p) at the Critical State condition at ambient temperature. It can be measured as the slope of a line passing through the final stress ratio of a soil monotonically loaded to the Critical State condition, e.g. as determined from both drained and undrained triaxial tests, and the origin ($p = q = 0$) in p-q stress space.

π can be determined as the ratio of the change in Critical State stress ratio to the change in temperature (from Eq. (2.12)), $\pi = \left(M_{T_2} - M_{T_2}\right)/(T_2 - T_1)$. Thus, triaxial tests at two temperatures would be sufficient. μ can be calculated from Eq. (2.13) as $\mu = -\ln\left(p_{cT}/p_c\right)/(T - T_0)$. Thus, by using 2 triaxial tests with equal pre-consolidation pressures at two different temperatures, the thermal softening coefficient may be determined.

As explained in Section 2.2, when fine-grained soils are subjected to heating-cooling cycles, they may show a hardening behaviour by undergoing permanent volumetric contraction until they reach a thermally-stable condition and further volumetric behaviour becomes thermally elastic. Therefore, any change in volumetric strain with respect to temperature (in T-ε_v space) is attributed to the volumetric thermal expansion coefficient, $3\alpha^*$, and can be approximated as $3\alpha^* = \Delta\varepsilon_v/\Delta T$, where $\Delta\varepsilon_v$ is the change in volumetric strain. A sample in a triaxial test setup subjected to equal-amplitude temperature cycles is sufficient; the test must be run until the cycles give converged results.

The yield surface of the model may be adjusted to different yield loci reported for a wide variety of soils via parameters α and γ. By trial and error, it is possible to match the desired shape of the yield surface. Typically, at least 3 triaxial tests are needed to determine the yield surface; one almost normally consolidated, one lightly over-consolidated and the third, highly over-consolidated.

2.4. FEATURES OF THE MODEL

One of the interesting features of the model is that a non-associated flow rule (Eq. (2.19)) is derived without the necessity to introduce an additional potential, e.g. the plastic potential as in conventional plasticity theory. Yield surfaces with different α values with $\gamma = 1$, as examples, are plotted with their corresponding plastic flow directions in Figure 2.4. It is obvious that in none of the cases (except for $\alpha = \gamma = 1$ in which the rate of dissipation function becomes stress independent) is the plastic flow direction perpendicular to the yield surface. This can be attributed to the presence of true stresses (p) in the rate of dissipation function (through the functions A and B in Eq. (2.8)). It should be noted that plastic flow is associated in dissipative stress space (χ_p, χ_q) (Eq. (2.16)). However, this feature is not transferred during the transition from dissipative stress space to true stress space, because of Ziegler's orthogonality condition. Note that, at the intersec-

Table 2.2: Parameters of the model

Categories		Parameters	Required tests
Volumetric behaviour	Elastic	$\bar{K}, m$	Resonant column test, bender element test or triaxial test
	Elastic	κ	Triaxial consolidation or oedometer tests
	Plastic	λ	Triaxial consolidation or oedometer tests
Shear behaviour	Elastic	$\bar{G}, n$	Resonant column test, bender element test or triaxial test
	Plastic	M_0	Triaxial test
Temperature impacts		π, μ, α^*	Series of temperature-controlled triaxial tests
Related to yield surface shape		α, γ	Series of triaxial tests

tion point of the yield surface with the CSL, the plastic flow is perpendicular to the yield surface and its components are only in the q-axis direction. This shows that the model is compatible with Critical State theory, which implies that at the Critical State condition, no plastic volumetric strains are produced due to the plastic flow direction being only in the direction of the q-axis.
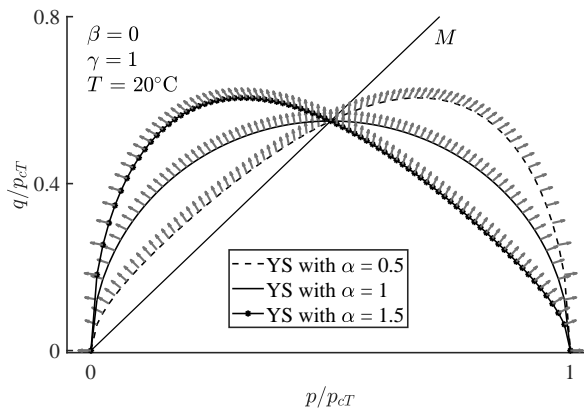
Figure 2.4: Plastic flow direction for three different yield surfaces

One of the distinguishing features of a constitutive equation derived by thermodynamics principles, in comparison with other fully phenomenological models (e.g. hypoelasticity), is that they ensure the satisfaction of thermodynamics laws. This feature is illustrated by two examples. Assume that an elastic material follows the closed stress

path (a)-(b)-(c)-(d)-(a) in triaxial stress space, as shown in Figure 2.5a, under isothermal conditions (constant temperature). This stress path is designed specifically to illustrate a reversible process, as the initial and end points of the loop coincide with each other. The material is firstly subjected to an increase in mean effective stress from point (a) to point (b), followed by an increase in deviatoric stress at constant p, up to point (c). Under constant deviatoric stress q from that point, the mean effective stress is reduced until point (d). In the final stage, the deviatoric stress is reduced in order that the stress state returns to its initial value at point (a). The corresponding mean effective stress versus volumetric strain and deviatoric stress versus deviatoric strain response for this stress path are depicted in Figure 2.5b and Figure 2.5c, respectively.
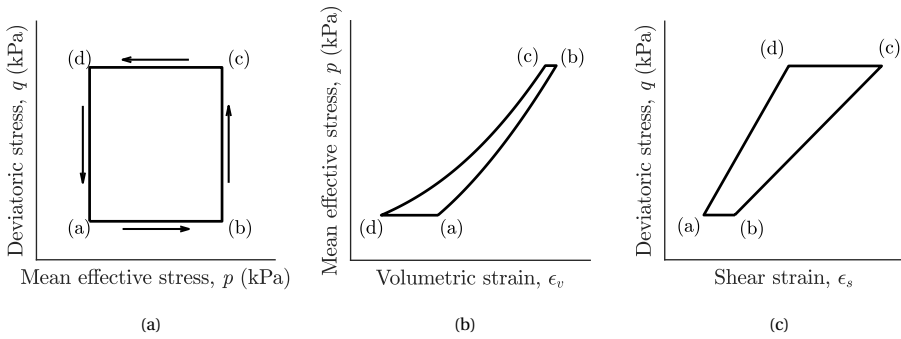
Figure 2.5: (a) Mechanical loop in elastic stress space; (b) mean effective stress vs. volumetric strain; (c) deviatoric stress vs. deviatoric strain
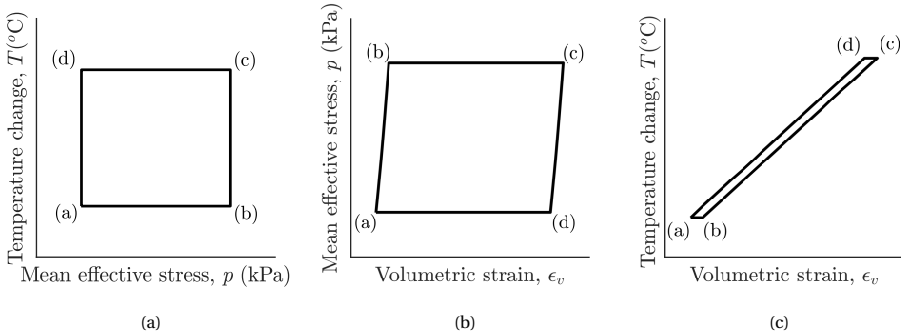
Figure 2.6: (a) Temperature loop in temperature vs. mean effective stress space; (b) mean effective stress vs. volumetric strain; (c) temperature vs. volumetric strain

The elastic properties of materials are in fact stress path independent, i.e., elasticity only depends on the final state of the material [52]. Hence, since the initial and final stress states (point (a) on the stress path) are identical, the initial and final states of the strains (both elastic volumetric and deviatoric strains in Figure 2.5b and Figure 2.5c) should be identical. As illustrated in Figure 2.5b and Figure 2.5c, this is indeed the case.

This behaviour represents the conservation of energy (first law of thermodynamics) during a reversible process and the model is capable of capturing this behaviour. On the other hand, non-linear fully phenomenological models (which are commonly used for soils) lack this principle, which may lead to strains which have no physical meaning. The hyperelasticity employed here overcomes this dilemma by using volumetric-deviatoric coupling terms. This means that volumetric behaviour affects deviatoric behaviour, as observed in geomaterials [52], and vice versa. However, these coupling terms are mostly ignored in models proposed for geomaterials, meaning that the volumetric and deviatoric behaviours are considered independent.

In the second example, an elastic material is subjected to stress and temperature variations, illustrated by the closed loop of points (a)-(b)-(c)-(d)-(a) in Figure 2.6a. From the initial state of stress and temperature represented by point (a), the mean effective stress under constant temperature is increase until the material is at a new stress state at point (b). The material is then heated under constant p to reach point (c). At this temperature the mean effective stress is reduced (to point (d)) and finally the material is cooled down at constant p to its initial state at point (a). The corresponding volumetric strain variation with mean effective stress p and temperature T are shown in Figure 2.6b and Figure 2.6c, respectively.

The closed loop T-p path represents a reversible process in which the behaviour is thermo-elastic. As seen in Figure 2.6b and Figure 2.6c, the material forms a closed loop for the corresponding p and T versus volumetric strain, in that the initial and final states are identical. This proves the thermodynamical consistency of the model, which is important for thermo-mechanical models when simulating change in volume of soils subjected to temperature variation, since the volume variation of over-consolidated soils during heating is considered a thermo-elastic response [58]. In literature, models exist in which the volumetric thermal expansion coefficient is related to the over-consolidation pressure or temperature (or both). Although this might appear satisfactory for predicting the behaviour, the models are not necessarily thermodynamically consistent. As a result, elastic strains can be produced where energy is lost.

2.5. TEMPERATURE EFFECTS

Figure 2.7 shows the three-dimensional yield surface (Eq. (2.18)) with respect to deviatoric stress q, mean effective stress p and temperature change ΔT°C, along with the corresponding parameter values used for the illustration. The yield surface is bounded at a pre-consolidation pressure (p_c) of 200 kPa at zero temperature change ($\Delta T = 0^\circ$C). As the temperature increases, the apparent pre-consolidation pressure (p_{cT}) decreases exponentially (according to Eq. (2.13)) which leads to a smaller yield surface. As the yield surface shrinks, the thermo-elastic domain (the area inside the yield surface) decreases. This means that for a material sheared in an over-consolidated and isotropic state (for example loading from $q = 0$ at $p = 100$ kPa in Figure 2.7), the yielding stress state is reached, i.e., the yield surface is encountered, at lower stress states when the material is at higher temperatures.

The parameter that controls the bounded size of the yield surface when the temperature changes, i.e., controls the curvature of the apparent pre-consolidation variation, is μ in Eq. (2.13), which is called the thermal softening parameter. Eq. (2.13) can also be

2

presented as $p_{cT} = p_c e^{-\mu(T-T_0)}$, where p_c is the pre-consolidation pressure at ambient temperature. By normalising the equation by p_c, the variation of μ due to change in temperature can be determined ($p_{cT}/p_c = e^{-\mu(T-T_0)}$). This variation for four different values is illustrated in Figure 2.8. As the value of μ increases, the yield surface shrinks faster in comparison with lower values when subjected to temperature increase. Note that this parameter is material specific and thus, depending on the soil type, the apparent pre-consolidation pressure can reduce dramatically (higher values of thermal softening parameter) or slightly as the temperature increases.
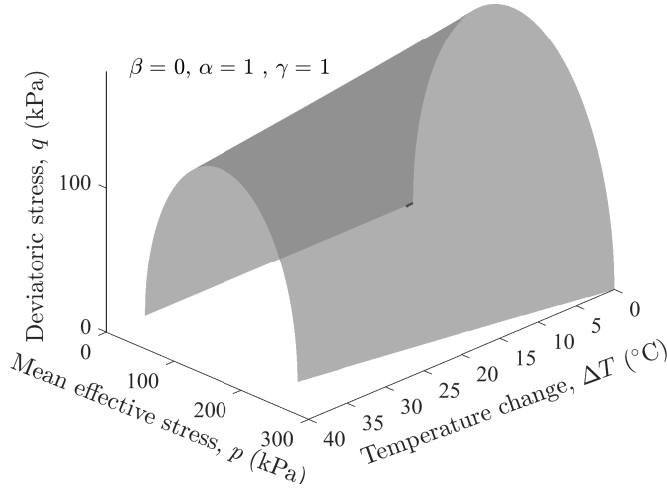
Figure 2.7: The yield surface in three dimensional p-q-T space

Depending on the constituents of the soil, the Critical State stress ratio M may increase or decrease as the temperature changes (Eq. (2.12)). This change is considered through the parameter π in Eq. (2.12) and its effect on the yield surface is presented in Figure 2.9. In this figure, the axes of deviatoric stress q and mean effective stress p are both normalised by the apparent pre-consolidation pressure p_{cT} to eliminate the thermal softening mechanism on the surface. Both positive and negative values can be assigned to π. Positive values of π result in a stretch in the minor axis (along the q-axis), i.e., an increase in size of the yield surface, while negative values cause a reduction in size.

In summary, the effect of temperature on the shear and volumetric behaviour of soils is incorporated by the addition of thermo-elasticity into the energy potential (Eq. (2.2)), a thermal softening mechanism (Eq. (2.13)), and a Critical State stress ratio variation with temperature (Eq. (2.12)) into the rate of dissipation function (Eq. (2.8)). Because all the constitutive equations are derived based on these two potentials, thermal effects are embedded into all the governing equations, including those for elasticity (Eq. (2.E.5)), plastic flow (Eq. (2.19)), plastic strain magnitude (plastic multiplier) (Eq. (2.22) or Eq. (2.E.8)), and the hardening rule (Eq. (2.20)), which implies that thermal effects are coupled with the mechanical behaviour of soils.
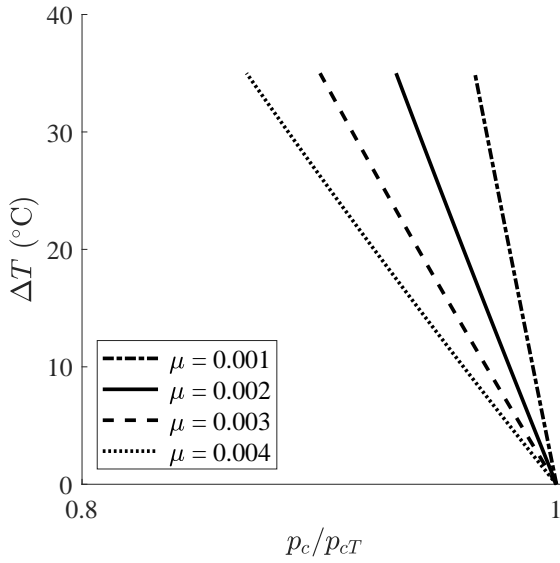
Figure 2.8: Effect of thermal softening/shrinkage parameter
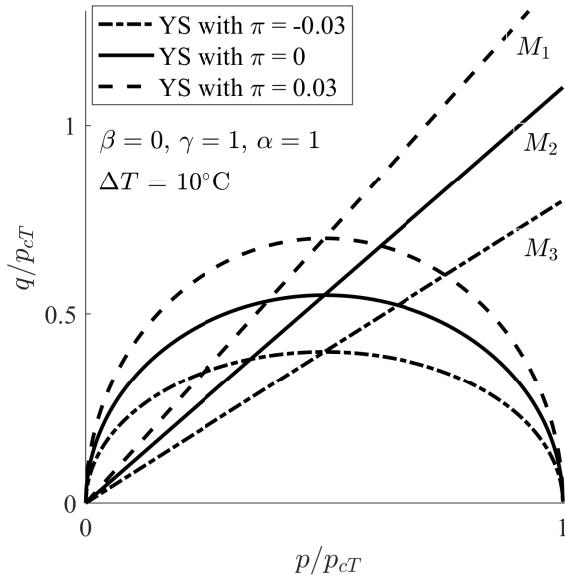
Figure 2.9: Effect of parameter π on the shape and size of the yield surface

2.6. MODEL PERFORMANCE

The performance of the model is validated by comparing simulations with a wide range of experimental data from oedometer and triaxial tests under drained and undrained conditions on different soil types. The tests cover a wide variety of stress paths and loading histories. The calibrated parameters used for the simulations are reported in Table 2.3.

TOWHATA ET AL. [31] TESTS

Towhata et al. [31] performed an oedometer test on a kaolinite clay and the void ratio variation with vertical stress is shown in Figure 2.10. First, the specimen was subjected to a vertical stress increase from 20 kPa to 160 kPa at a room temperature of 22°C. Next, with the vertical stress held constant at 160 kPa, the specimen was heated to 90°C and then cooled back to room temperature (22°C). This was followed by further compression with the vertical stress increasing to 1260 kPa at room temperature. During the heating-cooling cycle (22°C-90°C-22°C), the soil attained a denser state (observed via a void ratio reduction seen in Figure 2.10). As a result of the compression, the pre-consolidation pressure increased and the stress state of the soil changed from a normally-consolidated state to a slightly over-consolidated state. This is demonstrated by the bilinear response of the soil during the re-compression. On re-compressing the soil, starting from the vertical stress of 160 kPa, the initially stiffer response of the soil was due to elasticity and was therefore reversible. After reaching the new pre-consolidation pressure, irreversible behaviour was observed, as the response followed the normally consolidated line (for the ambient temperature).

The numerical simulation in Figure 2.10 captures the void ratio reduction during the thermal cycle, due to the thermal shrinkage mechanism of the elastic domain by Eq. (2.13). During heating, the apparent pre-consolidation tends to decrease due to the thermal softening mechanism. However, plastic volumetric strains are simultaneously produced which triggers the hardening mechanism. These two mechanisms compensate for each other, resulting in an unchanged apparent pre-consolidation pressure (at 90°C). During cooling, the apparent pre-consolidation pressure increases (hardening due to cooling, without any production of plastic volumetric strain) and the yield surface expands, resulting in the current stress state (vertical stress of 160 kPa) to be located inside the yield surface. Thus, further compression gives an elastic response, followed by elastoplastic response when the stress state reaches the yield surface. In conclusion, the model successfully captures the impact of a thermal cycle hardening mechanism exhibited by fine-grained soils.

Table 2.3: Summary of model parameters

Parameters	Towhata et al. [31]	Abuel-Naga et al. [1; 44]	Uchaipichat & Khalili [32]	Cekerevac & Laloui [29]	Ghahremannejad [40]	Graham et al. [59]; Tanaka et al. [34]
Soil name / type	Kaolinite clay	Bangkok clay	Silty soil	Kaolin clay	Illitic clay	Illitic clay
$\alpha(-)$	0.20	0.90	0.75	0.60	1.30	0.70
$\gamma(-)$	0.90	0.40	1.10	1.05	0.94	0.72
$\lambda(-)$	0.240	0.430	0.090	0.130	0.150	0.087
$\kappa(-)$	0.050	0.090	0.006	0.028	0.030	0.017
$M_0(-)$	0.750	0.80	1.218	0.820	0.850	1.070
$\bar{K}(-)$	38.0	17.5	75	500.0	$34.0(=1/\kappa)$	$59.0(=1/\kappa)$
$\bar{G}(-)$	80	15	170	700	150	20
$n(-)$	1.00	0.70	0.95	0.35	1.00	1.00
$m(-)$	1.00	1.00	0.85	0.70	1.00	1.00
$\alpha^*(1/K)$[1]	-3.1×10^{-6}	-3.1×10^{-6}	-3.4×10^{-5}	-1.8×10^{-4}	-3×10^{-5}	-1.5×10^{-4}
$\mu(1/K)$	5.95×10^{-3}	7.7×10^{-3}	3.4×10^{-3}	7.34×10^{-4}	9.09×10^{-4}	7×10^{-2}
$\pi(1/K)$	0	0	0	1.05×10^{-3}	-1.6×10^{-3}	0

[1]Note, the values of α^* have a range covering almost two orders of magnitude, which can be due to material differences or experimental calibration.
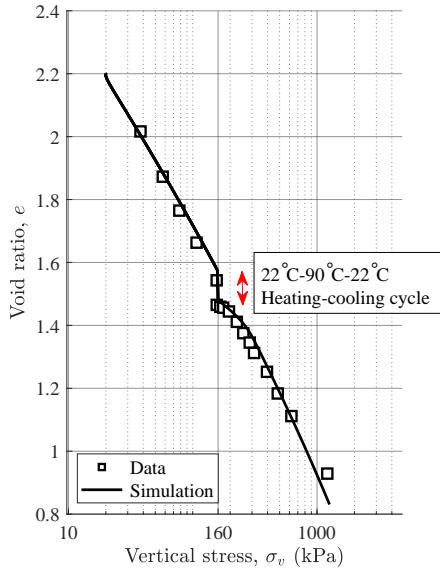
Figure 2.10: Comparison of void ratio vs. vertical stress predicted by model with experimental data of Towhata et al. [31]

ABUEL-NAGA ET AL. [1; 44] TESTS

Oedometer and triaxial compression tests on Bangkok clay, performed by Abuel-Naga et al. [1; 44], are presented in Figure 2.11 and Figure 2.12, respectively.

In Figure 2.11a, the void ratio variation with vertical stress, for Bangkok clay following a testing procedure similar to Towhata et al. [31], is presented. When the soil was subjected to a thermal cycle at the vertical stress of 100 kPa, the void ratio reduced (mostly due to permanent volumetric deformation). Again, the model results closely match the experimental results. As explained previously, this reduction of void ratio results in a slightly over-consolidated stress state. Abuel-Naga et al. [1], repeated the testing procedure for different vertical stresses (100, 200 and 300 kPa) and for a wide range of heating-cooling cycle magnitudes. The reported over-consolidated stress states attained after thermal cycles with respect to the thermal cycle amplitude are shown in Figure 2.11b. As expected, the larger the magnitude of the thermal cycle, the greater the over-consolidated state achieved, which implies a larger decrease in void ratio during the thermal cycle. The computed results are compared with the experimental data in Figure 2.11b, showing that the model is capable of capturing the heating-cooling hardening behaviour of soils. An interesting point that can be inferred from the experimental data is that the OCR values attained after each heating-cooling cycle are independent of the stress state (the vertical stress that the thermal cycle is applied), and this has also been well captured by the model.

Figure 2.12 shows the volumetric behaviour of the same soil in an isotropic compression test with triaxial apparatus, at three different temperatures of 25, 70 and 90°C.

2
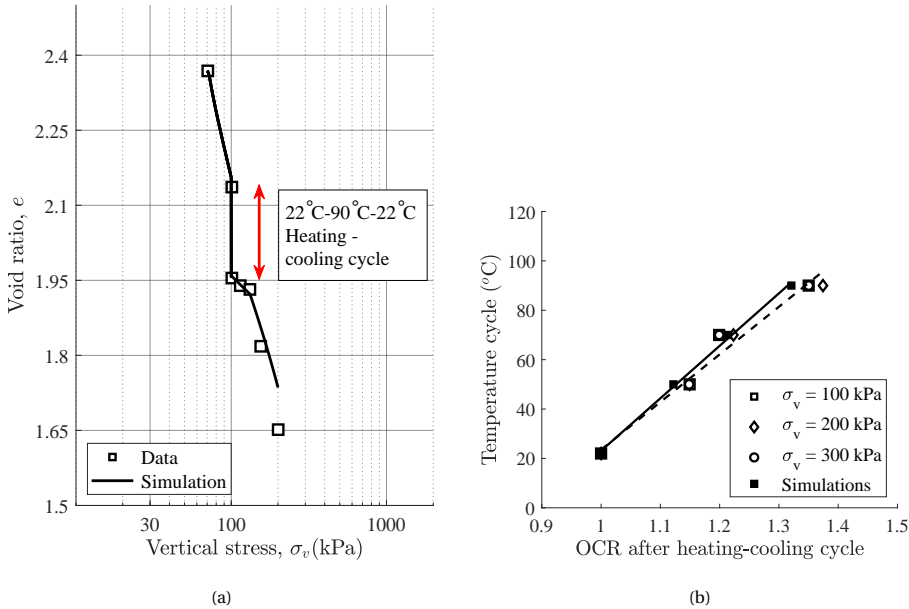
Figure 2.11: Comparison of model predictions with experimental data of Abuel-Naga et al. [1]: (a) void ratio vs. vertical stress; (b) attained OCR after thermal cycle vs. amplitude of the thermal cycle

At room temperature (25°C), samples were first isotropically compressed to a mean effective stress of 300 kPa and then unloaded to 25 kPa to attain an OCR of 12. Under drained conditions, the samples were then heated to the target temperature, followed by an isotropic re-compression to beyond 300 kPa. The model simulations are compared with the experimental data in Figure 2.12. Since the soil is initially highly over-consolidated, the initial response is elastic compression. For the sample at a temperature of 25°C, the response becomes elastoplastic at a stress state of 300 kPa. For samples compressed at elevated temperatures, the elastoplastic response is triggered at mean effective stresses lower than 300 kPa, due to the shrinkage of the yield surface due to the increase in temperature. The predictions of the model for all temperatures are satisfactory and capture well the difference in yield stress due to temperature difference.

UCHAIPICHAT & KHALILI [32] TESTS

In Uchaipichat & Khalili [32], the shear behaviour of a fully saturated silty soil under drained conditions was investigated at three temperatures (25, 40 and 60°C) and for three mean effective stresses (50, 100 and 150 kPa). Prior to shearing, all the samples were isotropically loaded to 200 kPa and unloaded to 50 kPa under isothermal conditions (constant temperature of 25°C). Hence, all samples had an initial pre-consolidation pressure of 200 kPa. The samples were then heated to the desired temperatures (25, 40 and 60°C) and sheared under drained conditions until failure. The experimental data and model predictions are presented in Figure 2.13. Figure 2.13a and Figure 2.13b show the yield surface at different soil temperatures, starting with the initial surface corre-
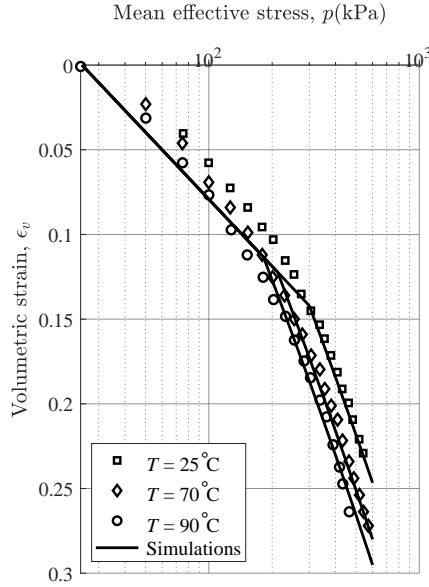
Figure 2.12: Comparison of model predictions of volumetric strain vs. mean effective stress, during isotropic compression at different temperatures, with experimental data of Abuel-Naga et al. [44]

sponding to a pre-consolidation of 200 kPa at 25°C, in p-q stress space and p-q-T space, respectively. From the laboratory data, it is obvious that, as the temperature increases, the yield surface shrinks in size and the pre-consolidation pressure decreases. The proposed model is capable of capturing both the shape of the yield surface and the yield surface shrinkage.

In Figure 2.13c, the shear stress versus shear strain and volumetric strain versus shear strain curves are shown. The predictions of the model are in good agreement with the experimental data for different over-consolidated states sheared at mean effective stresses of 150, 100 and 50 kPa. Changes in the Critical State stress ratio (M) have not been reported and the shear strengths of all samples sheared at identical mean effective stress reach the same ultimate value (Critical State), regardless of temperature effects. Therefore, $\pi = 0$ and the simulations are in agreement with the experimental data.

CEKEREVAC & LALOUI [29] TESTS

Cekerevac & Laloui [29] investigated the thermo-mechanical behaviour of a reconstituted kaolin clay under drained conditions. The samples at ambient temperature (22°C) were initially isotropically consolidated to 600 kPa and then unloaded to reach the desired over-consolidation ratio (1, 1.2, 1.5 and 2). Under drained conditions, the samples were heated to reach the desired temperatures (22 and 90°C). When the samples were equilibrated at the target temperatures, they were sheared until failure. The model predictions for the two temperatures are compared with the experimental data in Figure 2.14. The model predicts the deviatoric stresses and volumetric strains of the soil

with reasonable accuracy. It is worth noting that the critical state stress ratio had increased from 0.82 at 22°C to 0.89 at 90°C, which resulted in a higher ultimate shear stress (at the Critical State) at the elevated temperature in comparison with the ultimate shear stress at the ambient temperature, which is well captured by the model results.

GHAHREMANNEJAD [40] TESTS

Ghahremannejad [40] conducted a series of drained and undrained triaxial tests with different mechanical loading and heating stages on a normally consolidated illitic clay. From those tests, two undrained tests were selected for testing the model. In these experiments, in contrast to Uchaipichat & Khalili [32] and Cekerevac & Laloui [29], the soil was first heated to the desired temperature, and then isotropically compressed (to a mean effective stress of 400 kPa). With the temperature then kept constant, the specimens were sheared under undrained conditions. The test results for temperatures of 22°C and 75°C, along with the predictions of the model, are shown in Figure 2.15. Figure 2.15a, Figure 2.15b and Figure 2.15c, respectively, show the undrained stress path in p-q stress space, and the corresponding deviatoric stress and pore pressure versus deviatoric strain responses. The soil at a temperature of 75°C shows a softer behaviour than the soil at a temperature of 22°C, and its shear strength is lower at Critical State conditions. In other words, the Critical State stress ratio is decreased at elevated temperatures.

Comparison of the simulations with the experimental data (Figure 2.15) indicates that the current model successfully captures the softening behaviour of the soil at elevated temperatures, due to the temperature-dependent Critical State stress ratio controlled through the parameter π (Eq. (2.12)). Since the soil at the elevated temperature (75°C) was heated before being isotropically compressed, the thermal softening mechanism in Eq. (2.13) becomes deactivated (because $T = T_0$). Hence, the yield surface for any temperature (in this case, 22°C and 75°C) only expands isotropically due to compression and is bounded at 400 kPa. However, the size of the yield surface at $T = 75$°C is smaller than the size of the yield surface at $T = 22$°C due to the reduction of M at higher temperatures. As a result, the model predicts a softer response at elevated temperatures.

GRAHAM ET AL. [59] AND TANAKA ET AL. [34] TESTS

The undrained thermo-mechanical behaviour of a normally consolidated illitic clay was addressed in the work of Graham et al. [59] and Tanaka et al. [34]. The experimental results, including stress paths, shear stress evolution and pore water pressure changes during undrained shearing at two different temperatures, are shown in Figure 2.16. Prior to undrained shearing, the samples were isotropically consolidated to 1.5 MPa at room temperature (28°C) and subsequently heated to reach the desired temperatures (28 and 65°C). Due to the drained heating process, the samples attained different void ratios (due to the hardening mechanism) before the undrained shearing stage. The soil did not show any increase in the Critical State stress ratio (i.e. $\pi = 0$). The predictions of the model show good agreement with the laboratory data.

(a)

(b)

(c)
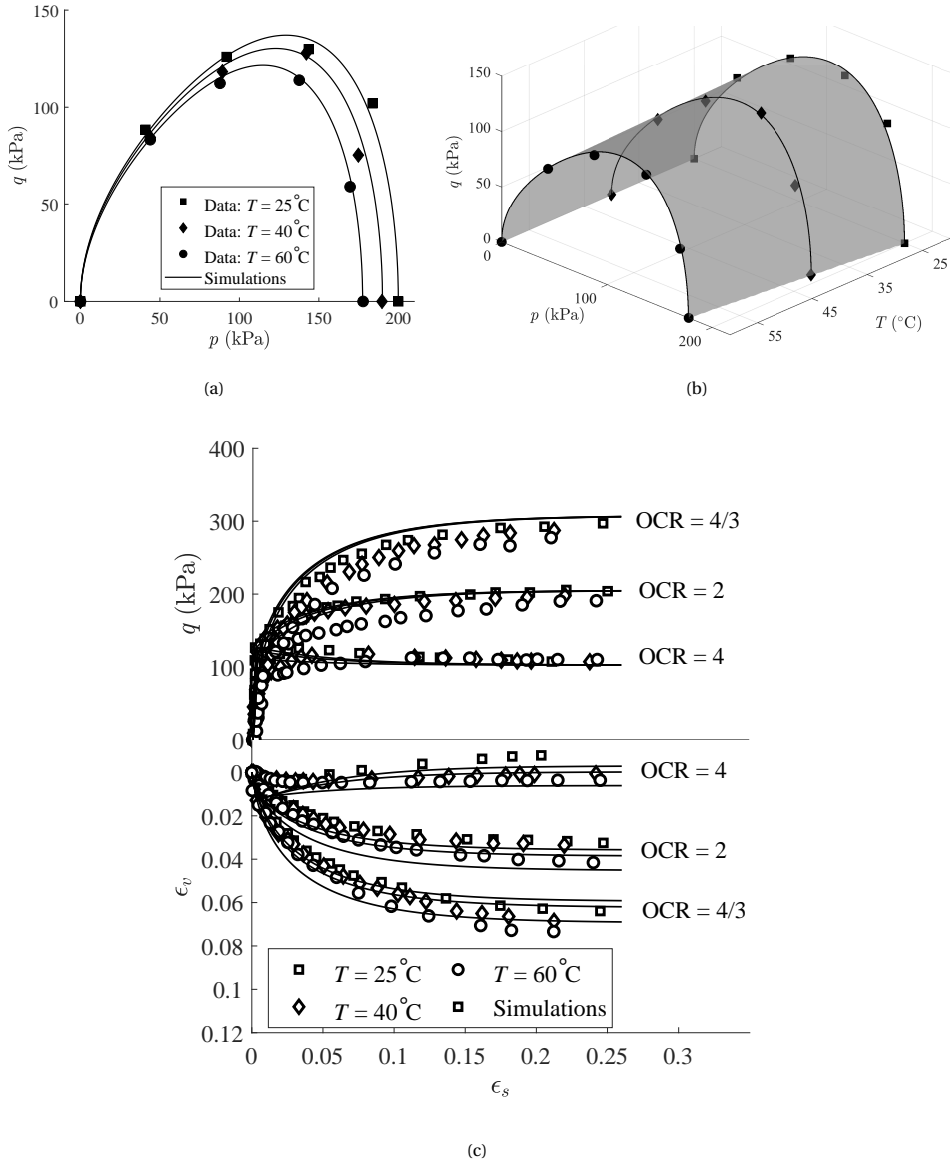
Figure 2.13: Comparison of model predictions with experimental data of Uchaipichat & Khalili [32]: (a) yield surfaces at different temperatures in p-q stress space; (b) yield surfaces at different temperatures in three dimensional p-q-T space; (c) deviatoric stress and volumetric strain vs. deviatoric strain at different OCRs

2
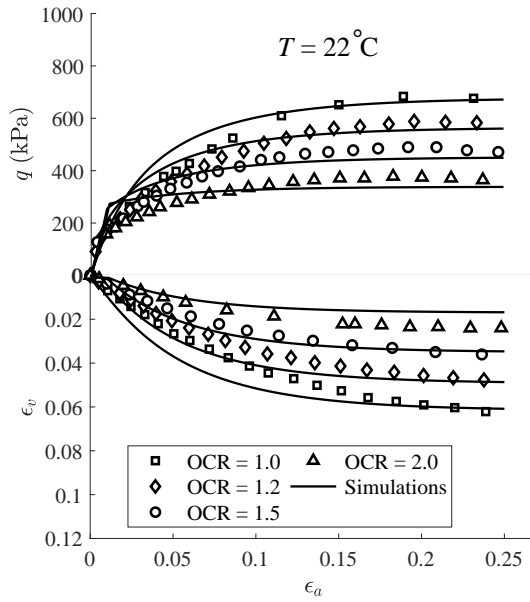
(a)
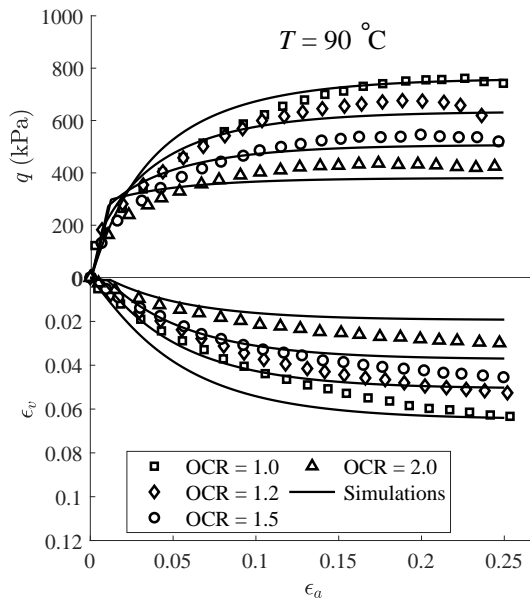
(b)

Figure 2.14: Comparison of model predictions of deviatoric stress and volumetric strain vs. axial strain at different OCRs with experimental data of Cekerevac & Laloui [29]: (a) at $T = 22°C$; (b) at $T = 90°C$

2
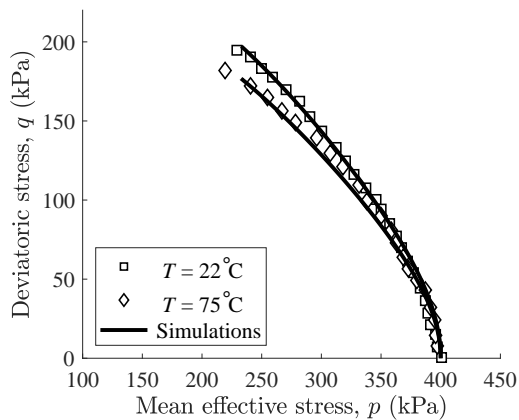
(a)
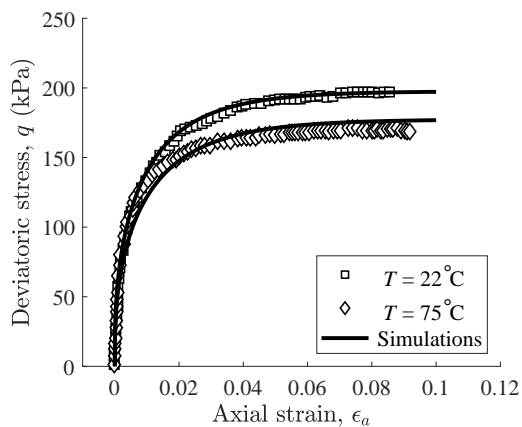
(b)
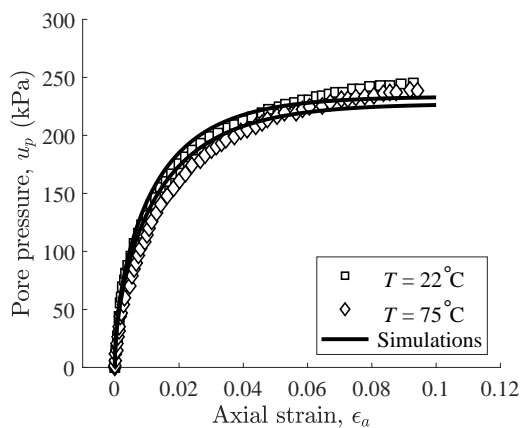
(c)

Figure 2.15: Comparison of model predictions with undrained experimental data of Ghahremannejad [40] at different temperatures; (a) stress path; (b) deviatoric stress vs. axial strain; (c) pore pressure vs. axial strain
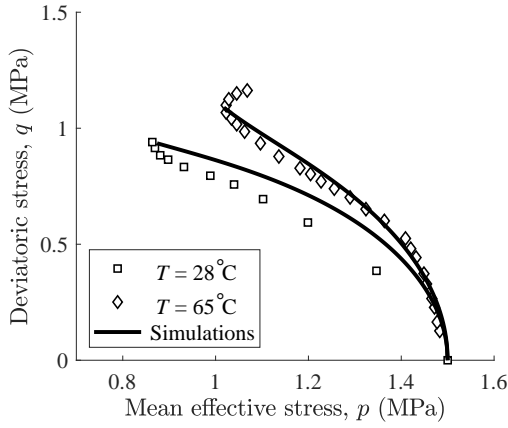
(a)
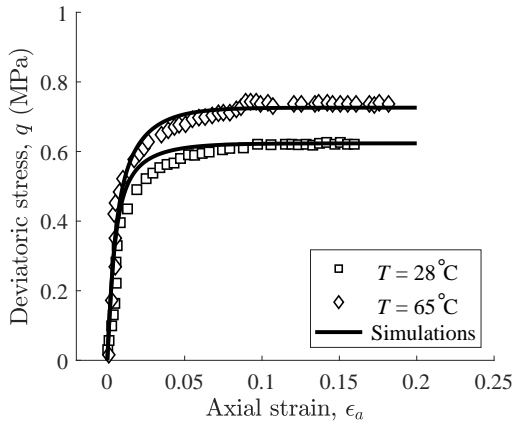
(b)
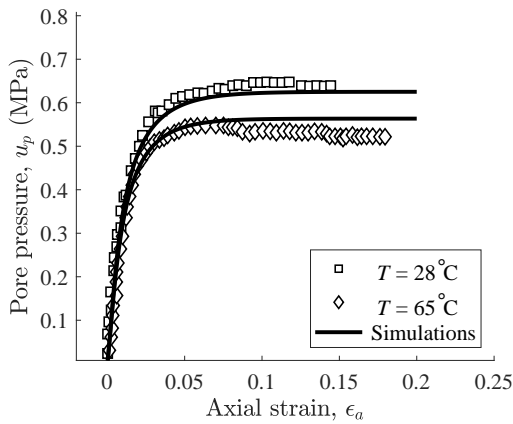
(c)

Figure 2.16: Comparison of model predictions with undrained experimental data of Graham et al. [59] and Tanaka et al. [34] at different temperatures; (a) stress paths; (b) deviatoric stress vs. axial strain; (c) pore pressure vs. axial strain

2.7. DISCUSSION: MICRO-MECHANICS, INTERNAL STRESSES, AND PHYSICOCHEMICAL PROCESSES DURING HEATING/COOLING

The thermo-chemo-hydro-mechanical behaviour of soils, especially fine-grained soils, are governed by the size of the particles and pore spaces between them, ranging from nano-metres to micro-metres. Thus, understanding the characterisation of fine grained soils, in a continuous manner, scaling from nano- to micro-metres is important to inform material models. Experimental techniques, such as neutron diffraction and nano-XCT, provide information about physicochemical processes occurring in such a scaling range. To implement such knowledge in a continuum scale constitutive model, an up-scaling approach is required. However, up-scaling methods are challenging and mostly not straightforward, in part due to identifying appropriate length scales that satisfactorily represents the physics of deformation of the material. Lack of identifying suitable length scales leads to lose of information when up-scaling is applied.

The impact of temperature in the energy and dissipation functions presented in this model is based upon phenomenological considerations in a thermodynamically consistent continuum approach. The step-by-step approach in the derivation is conducive to an approach also considering micro-structural aspects, as has been undertaken in other constitutive approaches (e.g. [60]). However, those approaches do not explicitly ensure the conservation of energy. This section attempts to qualitatively explain the processes that may occur during thermal loadings, in part to rationalise the choices made and, in part, as a first step towards a micro-mechanical model that is also consistent with thermodynamics principles.

Two main mechanisms have been proposed to understand some thermally-induced effects [43; 61]):

1. Difference in thermal volumetric expansion coefficients between soil particles and water: During heating of a saturated soil, because of the differences in thermal expansion coefficient between soil particles and water (the thermal expansion coefficient of water, depending on the mineralogy of the soil, is 8-15 times higher than that of soil particles), excess pore water pressure is generated. If drainage is allowed, consolidation occurs which can lead to permanent volume change (if the sample is confined and not heavily over-consolidated). However, if drainage is not allowed (undrained condition), there is no consolidation and thus the pore water pressure is retained.

2. Change in the viscosity of water: The second mechanism is attributed to the change (decrease) in the viscosity of water during heating and the thermal creep of soil particles. Reduction of the water viscosity results in easing of water flow through the void space. As the flow increases, consolidation increases which can eventually lead to plastic deformation.

Note that neither of the aforementioned mechanisms can explain the changes in shear or yielding behaviour. Various phenomena are described in the literature, where one of the major features which governs the mechanical behaviour of fine-grained soils, that

is the internal forces, have been ignored. Therefore, further investigation is required to understand the actual mechanisms occurring in the soil.

The surface area of fine-grained soils (like clays), in a specific mass of soil, are higher than for coarse-grained soils like sands [62]. These surfaces are mostly negatively-charged, which causes water molecules and cations to be adsorbed on the surface of the grain [62–64]. As a result, internal forces in the presence of external forces act between soil particles [63] and are called "*physicochemical internal forces*". These forces develop inside the soil mass and, depending on the source of the forces, may increase or decrease the internal energy of the soil. The major processes occurring inside the soil mass, which lead to the production of physicochemical forces, can be summarised as [63]

- Development of an electric double layer (EDL) and an electrostatic field of particles

- Occurrence of osmotic process

- Formation of thin water layers on soil particles (hydrate layers)

- Capillary menisci in unsaturated soils

- Concentration of ions in the liquid

and are shown schematically in Figure 2.17. In saturated soils (which are considered here), the effect of capillary menisci can be ignored. The stability of the soil mass is directly controlled by the balance between the attractive and repulsive forces generated during physicochemical processes. Attraction forces are due to Van der Waals forces between soil particles, whereas the repulsive forces are due to electrostatic interaction, due to the overlapping EDLs of particles and formation of adsorbed water films on the mineral surface of particles with specific structure.

The thermodynamic equilibrium between physicochemical forces (attractive and repulsive forces) leads to the development of thin hydrate films on the surface of the particle (Figure 2.17a), between any pair of particles in contact. Any change in the system, due to mechanical or thermal loads, disturbs the thermodynamic balance of the system and changes its energy level. As a result, the thickness of hydrate layers [63] changes and additional pressures are produced in the interphase liquid layer. This excess pressure is called the "*disjoining pressure*" $\Pi_t(t)$ and arises to counteract the imposed changes (because of mechanical and thermal loads) by keeping the soil-mass in equilibrium. The magnitude of the disjoining pressure is directly dependent on the thickness of the films, t, (i.e., on the level of overlapping of hydrate layers) and may attain positive or negative values (thickening or thinning of the layer, respectively). It should be noted that the strength and deformation properties of fine-grained soils are highly dependent on the disjoining pressure, resulting from physicochemical processes, of these hydrate films.

The total disjoining pressure due to different origins can be divided into three major independent sources which are additive [65]

$$\Pi_t(t) = \Pi_e + \Pi_m + \Pi_s \tag{2.23}$$

where Π_e, Π_m and Π_s are the respective electrostatic, molecular and structural components that act simultaneously with different governing laws.

Molecular forces (Van der Waals forces) are generated as the result of the molecular component of disjoining pressure Π_m. These forces act as attractive forces at the surface of the soil particle, which result in thinning of the hydrate layer. The magnitude of this force depends on the surface area of the soil particles.

The surfaces of clay particles are negatively charged, which in dry conditions (Figure 2.17b) are neutralised by cations adsorbed to the surface. In the presence of water (Figure 2.17c), hydration weakens the interaction of the surface and the cations, and water molecules replace a portion of the cations on the clay surface; consequently, a portion of cations remain adjacent to the surface and form the so-called "*adsorption*" or "*Schtern-Helmholtz layer*", while other cations diffuse from the surface and develop the "*external diffusive layer of cations*" or the "*Gui-Chapman*" layer, also known as the osmotic hydrate layer. Thus, a double electric layer with positive-electric charge is formed, with the latter layer being thicker than the former layer [63].

The diffusive layer provides a positive-electric field around the clay particles. In the case that the particles approach each other (due to mechanical loads), the positive-electric fields around the particles overlap (Figure 2.17d), which increases the cation concentration and consequently the electrical potential. This increase of cation concentration produces local osmotic pressures that force water to flow between particles and attempt to separate (disjoin) them. This is how the electric component of the disjoining pressure, Π_e, arises and contributes as repulsive forces [63].

The adsorption hydrate layer is strongly connected to the surface of the clay particles (the strength of adsorption depends on the mineralogy of the clay) and anisotropic stress states are formed inside it [63]. This anisotropic stress state and the adaption of water to the shape of the surface of the particle deforms the hydration bonds, which leads to a transformation of the structure of the water in the adsorbed film and imposes different properties compared to normal water. Increases in viscosity and the production of disjoining pressure are examples of different structural-mechanical properties of this hydrate layer [65–67]. Again, when the clay particles approach each other in a way that the adsorbed hydrate layers of particles overlap (Figure 2.17e), the layers start to be destroyed and the energy level increases, resulting in a thermodynamical imbalance. Consequently, disjoining pressure is developed to counteract the destruction of the hydrate layer and tends to separate particles. This repulsive pressure is called the structural-mechanical disjoining pressure Π_s [65; 68–70] and overall, depending on the mineralogy and shape of the particles, forms anisotropic stress-states with different mechanical properties inside the hydrate layer.

According to the disjoining pressure isotherm (the relationship between the force developed as the result of the total disjoining pressure, Π_t, and the thickness of hydrate films, t), two stable water layers, namely α- and β-films, may form on clay particle surfaces [65]. α-films are associated with thin layers with thicknesses around 10 nm, whereas β-films correspond to thick hydrate layers with thicknesses of nearly 100 nm.

The stability of β-films is dominated by electrostatic components of the disjoining pressure Π_e. Thus, they are highly sensitive to ion concentration surrounding the soil grains (in EDL and solvent) and show insensitivity to temperature variation [65; 68]. On
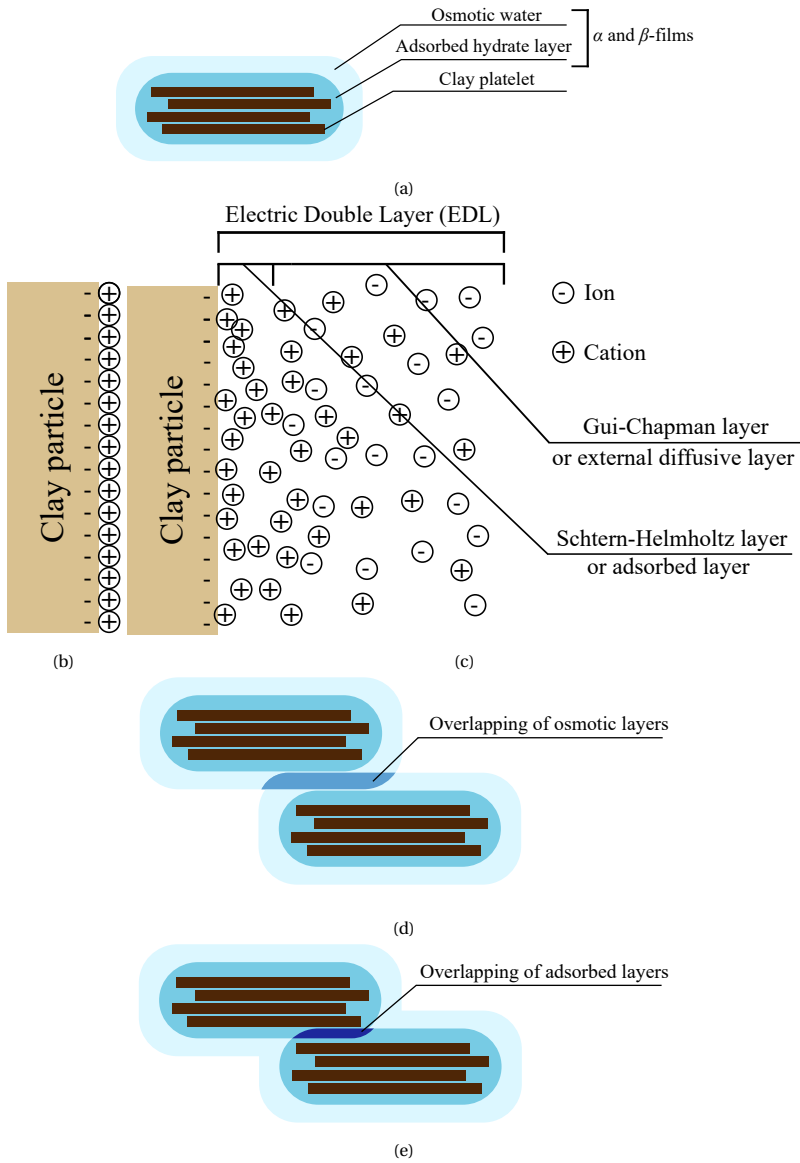
Figure 2.17: after [63]: (a): clay particle with different hydrate layers; (b): electric field of clay particle in dry condition; (c): electric field of clay particle in wet condition; (d): development of disjoining pressure during overlapping of osmotic layers; (e): development of disjoining pressure during overlapping of adsorbed layers

the other hand, α-films are mostly associated with the structural-mechanical component of the disjoining pressure Π_s. Therefore, the stability of these layers directly depends on the mineralogy and constituent properties of the clay particles and the hydrate layer. This hydrate layer shows a temperature-dependent behaviour, as it thins when the temperature increases and disappears at temperatures close to 65°C [65; 71]. Therefore, the impact of thermo-mechanisms on the mechanical behaviour of soils can be determined from the behaviour of this hydrate layer, when temperature varies. It should be noted that the β-films may break due to external mechanical loads. In this case, the disjoining pressure would develop only due to the overlapping of adsorbed layers and the structural component of the α-films governs its value.

The aforementioned physicochemical mechanisms may explain the thermo-mechanical behaviours observed in fine-grained soils. Soils with higher plasticity index PI have a higher level of chemical reactivity. Also, it has been observed that when the temperature is elevated, soils with a higher PI undergo higher thermally-induced volume changes compared to soils of a lower PI (demonstrated in Section 2.2). This may be attributed to α-films of different thicknesses, as, when the temperature of the soil mass increases, the α-film of soil particles with a higher PI becomes thinner. As a result, the water inside the hydrate layer squeezes out of the layer and elevates the pore pressure. Because of the volumetric reduction of soil grains due to thinning of the adsorbed hydrate layer (α-film) and excess pore water pressure generation, the (thermodynamically stable) state of the soil can be prone to moving to a thermodynamically unstable state. This means that during the transition from a thermodynamically stable condition to unstable condition, the stress state of the soil becomes closer to the maximum stress state that the soil has attained during its heating-loading history. This implies that the state of the soil becomes closer to yielding stress state. This behaviour has been introduced in Eq. (2.13), as it calculates a smaller elastic domain when temperature increases, i.e., the stress state becomes closer to the yielding stress state and a micro-structural formulation could be included here. When a thermodynamically unstable condition is reached, as the result of the excess pore pressure generation and volume reduction of soil particles (due to the thinning of hydrate layers), soil particles have a temporary freedom to rotate and reorient until they are positioned in a new thermodynamic equilibrium, with a higher contact area and a higher number of contacts with adjacent particles. This leads to an overall volume reduction, which has been observed when a soil is subjected to heating (as shown in Figure 2.3).

At the same time, due to change in the thickness of the hydration layer, new anisotropic stress states are generated inside the film to counteract the instability caused by temperature variation and to stabilise the soil particles at a new thermodynamic equilibrium. Consequently, new hydration bonds are formed and new structural-mechanical properties occur. The modification in structural-mechanical properties lead to different yield values (observed in Figure 2.1 and captured also by Eq. (2.13)) and shear properties (variation of Critical State stress ratio with temperature, Figure 2.2). Depending on the newly formed hydration bonds, the friction angle of soil particles may change (increase or decrease) or remain unchanged. This behaviour is encapsulated in Eq. (2.12), and could be updated with a micro-structural formulation, which well simulates the hardening and softening response of soils due to change in friction angle, when temperature

changes.

2.8. CONCLUSION

A constitutive model based on thermodynamics principles has been developed using the hyperplasticity framework. The formulation is based on a newly proposed Gibbs-type free energy and a newly proposed rate of dissipation potential function in which different thermo-mechanisms have been embedded. The model explicitly incorporates thermo-elasticity, pre-consolidation pressure and Critical State stress ratio as a function of temperature, to capture the thermo-mechanical behaviour of fine-grained soils. The model consists of 12 (or as few as 10 with some typical assumptions) parameters, which all have physical meaning and can be determined from conventional geotechnical laboratory tests. The model has been used to predict the thermo-mechanical behaviour of fine-grained soils and is shown to capture the observed temperature effects.

REFERENCES

[1] Abuel-Naga, H. M., Bergado, D. T., Bouazza, A. and Ramana, G. V. Volume change behaviour of saturated clays under drained heating conditions: Experimental results and constitutive modeling. *Canadian Geotechnical Journal*, 44(8):942–956, 2007.

[2] Cui, W., Potts, D. M., Zdravković, L., Gawecka, K. A. and Taborda, D. M. G. An alternative coupled thermo-hydro-mechanical finite element formulation for fully saturated soils. *Computers and Geotechnics*, 94:22–30, 2018.

[3] Cui, Y. J., Sultan, N. and Delage, P. A thermomechanical model for saturated clays. *Canadian Geotechnical Journal*, 37(3):607–620, 2000.

[4] Di Donna, A. and Laloui, L. Response of soil subjected to thermal cyclic loading: Experimental and constitutive study. *Engineering Geology*, 190:65–76, 2015.

[5] Hamidi, A., Tourchi, S. and Kardooni, F. A critical state based thermo-elasto-plastic constitutive model for structured clays. *Journal of Rock Mechanics and Geotechnical Engineering*, 9(6):1094–1103, 2017.

[6] Hamidi, A., Tourchi, S. and Khazaei, C. Thermomechanical constitutive model for saturated clays based on critical state theory. *International Journal of Geomechanics*, 15(1):04014038, 2015.

[7] Hong, P. Y., Pereira, J. M., Cui, Y. J. and Tang, A. M. A two-surface thermomechanical model for saturated clays. *International Journal for Numerical and Analytical Methods in Geomechanics*, 40(7):1059–1080, 2016.

[8] Laloui, L. and Cekerevac, C. Thermo-plasticity of clays: An isotropic yield mechanism. *Computers and Geotechnics*, 30(8):649–660, 2003.

[9] Laloui, L., Cekerevac, C. and François, B. Constitutive modelling of the thermo-plastic behaviour of soils. *Revue Européenne de Génie Civil*, 9(5-6):635–650, 2005.

2

[10] Laloui, L. and François, B. ACMEG-T: Soil thermoplasticity model. *Journal of Engineering Mechanics*, 135(9):932–944, 2009.

[11] Ma, Q. J. J., Ng, C. W. W., Mašín, D. and Zhou, C. An approach for modelling volume change of fine-grained soil subjected to thermal cycles. *Canadian Geotechnical Journal*, 54(6):896–901, 2017.

[12] Mašín, D. and Khalili, N. A thermo-mechanical model for variably saturated soils based on hypoplasticity. *International Journal for Numerical and Analytical Methods in Geomechanics*, 36(12):1461–1485, 2012.

[13] Xiong, Y., Ye, G., Zhu, H., Zhang, S. and Zhang, F. Thermo-elastoplastic constitutive model for unsaturated soils. *Acta Geotechnica*, 11(6):1287–1302, 2016.

[14] Yao, Y. P. and Zhou, A. N. Non-isothermal unified hardening model: A thermo-elasto-plastic model for clays. *Géotechnique*, 63(15):1328–1345, 2013.

[15] Zhou, C., Fong, K. Y. and Ng, C. W. W. A new bounding surface model for thermal cyclic behaviour. *International Journal for Numerical and Analytical Methods in Geomechanics*, 41(16):1656–1666, 2017.

[16] Zhou, C. and Ng, C. W. W. A thermomechanical model for saturated soil at small and large strains. *Canadian Geotechnical Journal*, 52(8):1101–1110, 2015.

[17] Zhou, C. and Ng, C. W. W. Simulating the cyclic behaviour of unsaturated soil at various temperatures using a bounding surface model. *Géotechnique*, 66(4):1–7, 2016.

[18] Lashkari, A. and Golchin, A. On the influence of elastic-plastic coupling on sands response. *Computers and Geotechnics*, 55:352–364, 2014.

[19] Einav, I. The unification of hypo-plastic and elasto-plastic theories. *International Journal of Solids and Structures*, 49(11):1305–1315, 2012.

[20] Houlsby, G. T. and Puzrin, A. M. *Principles of Hyperplasticity: An approach to plasticity theory based on thermodynamic principles.* Springer London, London, 2007.

[21] Srinivasa, A. R. Application of the maximum rate of dissipation criterion to dilatant, pressure dependent plasticity models. *International Journal of Engineering Science*, 48(11):1590–1603, 2010.

[22] Rajagopal, K. R. and Srinivasa, A. R. Some remarks and clarifications concerning the restrictions placed on thermodynamic processes. *International Journal of Engineering Science*, 140:26–34, 2019.

[23] Darabi, M. K., Abu Al-Rub, R. K. and Omidi, O. A thermodynamically consistent framework to derive local/nonlocal generalized nonassociative plasticity/viscoplasticity theories. *International Journal of Plasticity*, 110:19–37, 2018.

2

[24] Collins, I. F. and Houlsby, G. T. Application of thermomechanical principles to the modelling of geomaterials. In *Proceedings: Mathematical, Physical and Engineering Sciences, JSTOR*, volume 453, pages 1975–2001. 1997.

[25] Ziegler, H. *An introduction to thermomechanics*, volume 21. North-Holland Series in Applied Mathematics and Mechanics, Amsterdam, 1977.

[26] Aung, Y., Khabbaz, H. and Fatahi, B. Mixed hardening hyper-viscoplasticity model for soils incorporating non-linear creep rate–H-creep model. *International Journal of Plasticity*, 120:88–114, 2019.

[27] Lai, Y., Liao, M. and Hu, K. A constitutive model of frozen saline sandy soil based on energy dissipation theory. *International Journal of Plasticity*, 78:84–113, 2016.

[28] Abuel-Naga, H. M., Bergado, D. T. and Bouazza, A. Thermally induced volume change and excess pore water pressure of soft Bangkok clay. *Engineering Geology*, 89:144–154, 2007.

[29] Cekerevac, C. and Laloui, L. Experimental study of thermal effects on the mechanical behaviour of a clay. *International Journal for Numerical and Analytical Methods in Geomechanics*, 28(3):209–228, 2004.

[30] Sultan, N., Delage, P. and Cui, Y. J. Temperature effects on the volume change behaviour of Boom clay. *Engineering Geology*, 64:135–145, 2002.

[31] Towhata, I., Kuntiwattanaku, P., Seko, I. and Ohishi, K. Volume change of clays induced by heating as observed in consolidation tests. *Soils and Foundations*, 33(4):170–183, 1993.

[32] Uchaipichat, A. and Khalili, N. Experimental investigation of thermo-hydro-mechanical behaviour of an unsaturated silt. *Géotechnique*, 59(4):339–353, 2009.

[33] Khalili, N., Uchaipichat, A. and Javadi, A. A. Skeletal thermal expansion coefficient and thermo-hydro-mechanical constitutive relations for saturated homogeneous porous media. *Mechanics of Materials*, 42(6):593–598, 2010.

[34] Tanaka, N., Graham, J. and Crilly, T. Stress-strain behaviour of reconstituted illitic clay at different temperatures. *Engineering Geology*, 47(4):339–350, 1997.

[35] Abuel-Naga, H. M., Bergado, D. T. and Lim, B. F. Effect of temperature on shear strength and yielding behavior of soft Bangkok clay. *Soils and Foundations*, 47(3):423–436, 2007.

[36] Hueckel, T. and Baldi, G. Thermoplasticity of saturated clays: Experimental constitutive study. *Journal of geotechnical engineering*, 116(12):1778–1796, 1991.

[37] Hueckel, T., François, B. and Laloui, L. Explaining thermal failure in saturated clays. *Géotechnique*, 59(3):197–212, 2009.

[38] Kuntiwattanakul, P., Towhata, I., Ohishi, K. and Seko, I. Temperature effects on undrained shear characteristics of clay. *Soils and Foundations*, 35(1):147–162, 1995.

[39] Ng, C. W. W., Cheng, Q., Zhou, C. and Alonso, E. E. Volume changes of an unsaturated clay during heating and cooling. *Géotechnique Letters*, 6(3):192–198, 2016.

[40] Ghahremannejad, B. *Thermo-mechanical behaviour of two reconstituted clays.* PhD thesis, University of Sydney, 2003.

[41] Zhou, C., Xu, J. and Ng, C. W. W. Effects of temperature and suction on secant shear modulus of unsaturated soil. *Géotechnique Letters*, 5:123–128, 2015.

[42] Bai, B. and Su, Z. Thermal responses of saturated silty clay during repeated heating-cooling processes. *Transport in Porous Media*, 93(1):1–11, 2012.

[43] Vega, A. and McCartney, J. S. Cyclic heating effects on thermal volume change of silt. *Environmental Geotechnics*, 2(5):257–268, 2015.

[44] Abuel-Naga, H. M., Bergado, D. T., Ramana, G. V., Grino, L., Rujivipat, P. and Thet, Y. Experimental evaluation of engineering behavior of soft Bangkok clay under elevated temperature. *Journal of Geotechnical and Geoenvironmental Engineering*, 132(7):902–910, 2006.

[45] Laloui, L., Leroueil, S. and Chalindar, S. Modelling the combined effect of strain rate and temperature on one-dimensional compression of soils. *Canadian Geotechnical Journal*, 45(12):1765–1777, 2008.

[46] Terzaghi, K. *Erdbaumechanik auf Bodenphysikalischer Grundlage.* Deuticke, F., 1925.

[47] Houlsby, G. T. The work input to a granular material. *Géotechnique*, 47(1):193–196, 1997.

[48] Collins, I. F. and Hilder, T. A theoretical framework for constructing elastic/plastic constitutive models of triaxial tests. *International Journal for Numerical and Analytical Methods in Geomechanics*, 26(13):1313–1347, 2002.

[49] Collins, I. F. Associated and non-associated aspects of the constitutive laws for coupled elastic/plastic materials. *International Journal of Geomechanics*, 2(2):259–267, 2002.

[50] Golchin, A. and Lashkari, A. A critical state sand model with elastic-plastic coupling. *International Journal of Solids and Structures*, 51(15-16):2807–2825, 2014.

[51] Einav, I. and Puzrin, A. M. Pressure-dependent elasticity and energy conservation in elastoplastic models for soils. *Journal of Geotechnical and Geoenvironmental Engineering*, 130(1):81–92, 2004.

[52] Puzrin, A. M. *Constitutive Modelling in Geomechanics.* Springer, Berlin, Heidelberg, 2012.

[53] Coombs, W. M., Crouch, R. S. and Augarde, C. E. A unique Critical State two-surface hyperplasticity model for fine-grained particulate media. *Journal of the Mechanics and Physics of Solids*, 61(1):175–189, 2013.

[54] Dafalias, Y. F. and Taiebat, M. Anatomy of rotational hardening in clay plasticity. *Géotechnique*, 63(16):1406–1418, 2013.

[55] Dafalias, Y. F. and Taiebat, M. Rotational hardening with and without anisotropic fabric at critical state. *Géotechnique*, 64(6):507–511, 2014.

[56] Nieto-Leal, A., Kaliakin, V. N. and Mashayekhi, M. Improved rotational hardening rule for cohesive soils and definition of inherent anisotropy. *International Journal for Numerical and Analytical Methods in Geomechanics*, 42(3):469–487, 2018.

[57] Wheeler, S. J., Näätänen, A., Karstunen, M. and Lojander, M. An anisotropic elasto-plastic model for soft clays. *Canadian Geotechnical Journal*, 40(2):403–418, 2003.

[58] Hong, P. Y., Pereira, J. M., Tang, A. M. and Cui, Y. J. On some advanced thermo-mechanical models for saturated clays. *International Journal for Numerical and Analytical Methods in Geomechanics*, 37(17):2952–2971, 2013.

[59] Graham, J., Tanaka, N., Crilly, T. and Alfaro, M. Modified Cam-Clay modelling of temperature effects in clays. *Canadian Geotechnical Journal*, 38(3):608–621, 2001.

[60] Özdemir, I., Brekelmans, W. A. M. and Geers, M. G. D. Computational homogenization for the thermo-mechanical analysis of heterogeneous solids. *Computer Methods in Applied Mechanics and Engineering*, 198(3-4):602–613, 2008.

[61] Coccia, C. J. R. and McCartney, J. S. A thermo-hydro-mechanical true triaxial cell for evaluation of the impact of anisotropy on thermally induced volume changes in soils. *Geotechnical Testing Journal*, 35(2):103803, 2012.

[62] Mitchell, J. K. and Soga, K. *Fundamentals of soil behavior*. John Wiley & Sons, 2005.

[63] Osipov, V. I. *Physicochemical theory of effective stress in soils*, volume 41 of *SpringerBriefs in Earth Sciences*. Springer International Publishing, 2015.

[64] Sedighi, M. and Thomas, H. R. Micro porosity evolution in compacted swelling clays: A chemical approach. *Applied Clay Science*, 101:608–618, 2014.

[65] Deryaguin, B. V. and Churaev, N. V. *Wetting films*. Nauka, Moscow, 1984.

[66] Churaev, N. V., Sobolev, V. D. and Zorin, Z. M. Measurement of viscosity of liquids in quartz capilaries. In *Special discussion on Thin liquid films and boundary layers*, pages 213–220. Academic Press, New York, 1971.

[67] Zorin, Z. M., Sobolev, V. D. and Churaev, N. V. Variation of capillary pressure, surface tension, and liquid viscosity in quartz microcapillaries. In *Surface forces in thin films and disperse systems*. Nauka, Moscow, 1972.

[68] Deryaguin, B. V. *Theory of stability of colloids and thin films*. Nauka, Moscow, 1986.

[69] Deryaguin, B. V., Churaev, N. V. and Muller, V. M. *Surface forces*. Nauka, Moscow, 1985.

2

[70] Israelachvili, J. N. and Pashley, R. M. Molecular layering of water at surfaces and origin of repulsive hydration forces. *Nature*, 306(5940):249–250, 1983.

[71] Perevertaev, V. D. and Metsik, M. S. Investigation of water vapor adsorption on mica crystal surface. *Colloidal Journal*, 28(2):254–259, 1966.

[72] Brandl, H. Energy foundations and other thermo-active ground structures. *Géotechnique*, 56(2):81–122, 2006.

[73] Thomas, H. R., Vardon, P. J. and Cleall, P. J. Three-dimensional behaviour of a prototype radioactive waste repository in fractured granitic rock. *Canadian Geotechnical Journal*, 51(3):246–259, 2014.

[74] Bathe, K. J., Ramm, E. and Wilson, E. L. Finite element formulations for large deformation dynamic analysis. *International Journal for Numerical Methods in Engineering*, 9(2):353–386, 1975.

[75] Houlsby, G. T. Dissipation rate functions, pseudopotentials, potentials and yield surfaces. In Dewar, R. C., Lineweaver, C. H., Niven, R. K. and Regenauer-Lieb, K., editors, *Beyond the Second Law: Entropy Production and Non-equilibrium Systems*, pages 73–95. Springer, Berlin, Heidelberg, 2014.

[76] Houlsby, G. T. and Puzrin, A. M. Rate-dependent plasticity models derived from potential functions. *Journal of Rheology*, 46(1):113–126, 2002.

[77] Houlsby, G. T. and Puzrin, A. M. A thermomechanical framework for constitutive models for rate-independent dissipative materials. *International Journal of Plasticity*, 16(9):1017–1047, 2000.

[78] Houlsby, G. T., Amorosi, A. and Rojas, E. Elastic moduli of soils dependent on pressure: A hyperelastic formulation. *Géotechnique*, 55(5):383–392, 2005.

[79] Addison, S. R. Homogenous functions in thermodynamics. In *Proceedings Arkansas Academy of Science*, volume 45, pages 114–117, 1991.

APPENDIX

2.A. APPENDIX A: THERMODYNAMICS OF CONTINUA

This section explains the thermodynamics of continuum media and how the hyperplasticity framework uses the laws of thermodynamics to provide a platform for extracting the constitutive equations for different materials, including fine-grained soils. The formulations and notations in this section are in accordance with those in [20; 24; 52; 75–77]. The platform described in this section is used to derive the constitutive equations in Section 2.3.

For a system in a state of thermodynamic equilibrium, all laws of thermodynamics apply. The first and second laws introduce two properties of the system. From the first law, the law of energy conservation, a property named "*internal energy*" is defined, in which the total power input to the system (e.g. work input $\dot{W} = \boldsymbol{\sigma} : \dot{\boldsymbol{\varepsilon}}$, and heat supply or net heat flux $\dot{Q} = q_{,k}$) is identical to the rate of change of the internal energy of the system [20]

$$\dot{u} = \boldsymbol{\sigma} : \dot{\boldsymbol{\varepsilon}} - q_{,k} \tag{2.A.1}$$

where $\boldsymbol{\sigma}$, $\dot{\boldsymbol{\varepsilon}}$, $\boldsymbol{q}$ and $q_{,k}$ are the stress and strain increment tensors, heat flux vector and its spatial derivative (a scalar value), respectively. The comma in the subscript indicates spatial differentiation with respect to the k direction and the symbol ":" is the double contraction operator.

The second law of thermodynamics states that a property of the system called entropy s exists, in which its rate is non-negative [20]. This is best shown through the Clausius-Duhem inequality

$$\dot{s} \geq -\left(\frac{\boldsymbol{q}}{T}\right)_{,k} \tag{2.A.2}$$

where $\boldsymbol{q}/T$ is the entropy flux vector and T is the absolute temperature.

The above inequality can be rewritten as $\dot{s} + \left(\frac{\boldsymbol{q}}{T}\right)_{,k} = \dot{s} + \frac{q_{,k}}{T} - \frac{\boldsymbol{q}:\boldsymbol{T}_{,k}}{T^2} = \frac{d^t}{T} \geq 0$, where d^t is the rate of total dissipation and $\boldsymbol{T}_{,k}$ is the thermal gradient. Expanding this inequality and combining with the first law (Eq. (2.A.1)) (and eliminating the divergence of heat flux) results in

$$\dot{u} = \boldsymbol{\sigma} : \dot{\boldsymbol{\varepsilon}} + T\dot{s} - \frac{\boldsymbol{q}:\boldsymbol{T}_{,k}}{T} - d^t \tag{2.A.3}$$

where $-\frac{\boldsymbol{q}:\boldsymbol{T}_{,k}}{T}$ is the rate of thermal dissipation and the rest of the rate of dissipation $\left(d = d^t - \left(-\frac{\boldsymbol{q}:\boldsymbol{T}_{,k}}{T}\right)\right)$ is due to mechanical deformation (mechanical dissipation). It is logical to consider the thermal and mechanical dissipation processes independently. Since

the heat flux $\boldsymbol{q}$ and thermal gradient $T_{,k}$ have opposite signs, the rate of thermal dissipation quantity is always positive and already satisfies the second law of thermodynamics [20]. Hence, it can be excluded from the second law inequality which then requires the rate of mechanical dissipation to be non-negative. Thus, the first and second law of thermodynamics can be rewritten as

$$\text{First law:} \quad \dot{u} + d = \boldsymbol{\sigma} : \dot{\boldsymbol{\varepsilon}} + T\dot{s} \tag{2.A.4}$$

$$\text{Second law:} \quad T\dot{s} + q_{,k} = d \geq 0 \tag{2.A.5}$$

2.A.1. ENERGY FUNCTIONS OF DISSIPATIVE MATERIALS

Soils and geo-materials in general can be categorised as dissipative materials, in that they undergo irreversible processes and part of their mechanical deformation transforms to heat. In conventional thermodynamics, the internal energy is defined by a set of visible and measureable kinematic (strain-like) variables, such as strain tensor, as well as entropy s and internal variable α_i tensors [20; 52]. The essence of internal variables is essential to study the behaviour of dissipative materials and they encapsulate the history of the material behaviour due to irreversible processes [20].

The mechanical behaviour and properties of soils, e.g. bulk and shear modulus, are most conveniently characterised by stress rather than strain [51; 78]. Therefore, it is convenient to define a form of energy function defined by independent variables of (effective) stress $\boldsymbol{\sigma}$ (from here on, all the stresses are effective), absolute temperature T and internal variables α_i. Such an energy function is the Gibbs free energy, $g = g(\boldsymbol{\sigma}, T, \alpha_i)$. Invoking the Legendre transform (explained in Appendix 2.B) twice on the internal energy u, to interchange the role of strain with its work-conjugate stress $\boldsymbol{\sigma}$, and entropy s with absolute temperature T, the first law of thermodynamics (Eq. (2.A.4)) is revised in terms of state variables for the Gibbs free energy

$$\dot{g} + d = -\left(\dot{T}s + \dot{\boldsymbol{\sigma}} : \boldsymbol{\varepsilon}\right) \tag{2.A.6}$$

while the second law (Eq. (2.A.5)) remains unchanged.

Equating the rate (derivative with respect to time) of $g = g(\boldsymbol{\sigma}, T, \alpha_i)$ with Eq. (2.A.6) results in $\left(-\boldsymbol{\varepsilon} - \frac{\partial g}{\partial \boldsymbol{\sigma}}\right) : \dot{\boldsymbol{\sigma}} + \left(-s - \frac{\partial g}{\partial T}\right)\dot{T} + \left(-d - \frac{\partial g}{\partial \alpha_i} : \dot{\alpha}_i\right) = 0$. By assuming that the state variables of the energy function ($\boldsymbol{\sigma}$ and T) vary independently, it can be deduced that

$$\boldsymbol{\varepsilon} = -\frac{\partial g}{\partial \boldsymbol{\sigma}}, s = -\frac{\partial g}{\partial T}, -\frac{\partial g}{\partial \alpha_i} : \dot{\alpha}_i = d \geq 0 \tag{2.A.7}$$

By defining $-\frac{\partial g}{\partial \alpha_i}$ as the "*generalised stress tensor*", $\bar{\chi}$ [20], the rate of dissipation can be rewritten as

$$d = \bar{\chi} : \dot{\alpha}_i = \langle \bar{\chi}, \dot{\alpha}_i \rangle \geq 0 \tag{2.A.8}$$

where $\langle \rangle$ is the inner product operator.

Three important conclusions can be derived from this equation:

1. The presence of internal variables (e.g. α_i) in the energy functions is necessary for dissipative materials; otherwise the term $\partial g/\partial \alpha_i$ would be zero which results in zero dissipation and reversible behaviour, similar to the observed behaviour of elastic materials.

2. The dissipation should be a function of the rate of change of internal variables ($\dot{\alpha}_i$); i.e., it is enough and sufficient to define the rate of dissipation function only by the rate of change of internal variables ($d = d(\dot{\alpha}_i)$) [20].

3. The rate of dissipation function is the multiplication (inner product) of the derivative of the energy function with respect to the internal variable ($\partial g/\partial \alpha_i$) and its corresponding rate of change ($\dot{\alpha}_i$). This is similar to the properties of homogeneous functions (Appendix 2.C).

In summary, the rate of dissipation function should be homogeneous, non-negative and a function of the rate of internal variables.

2.A.2. RATE OF DISSIPATION FUNCTIONS

The rate of dissipation function of dissipative materials in general can be defined by "*generalised dissipative velocities,* $\boldsymbol{\nu}$", state variables $\mathbf{x}$, e.g. stress (or strain), and temperature T: $d = d(\mathbf{x}, \boldsymbol{\nu}, T) \geq 0$ [75]. Note that $\boldsymbol{\nu}$ and $\mathbf{x}$ can be either scalar or tensorial. Generalised dissipative velocities is a term that covers both the rate of change of internal variables (e.g. rate of plastic strains, $\dot{\alpha}_i$) and fluxes of various quantities (e.g. electrical charge). It can be proved that any thermodynamic function that is extensive (i.e. dependent on the size of the system) is an homogeneous function [79]. In addition, the dependence of the rate of dissipation function on the generalised dissipative velocities is enough to define the non-negative rate of dissipation function ($d = d(\boldsymbol{\nu})$). By considering these points and the fact that the rate of dissipation function is an homogeneous function, by writing Euler's theorem (Eq. (2.C.2)) for the rate of dissipation function d it can be concluded that

$$n_h d = \frac{\partial d}{\partial \boldsymbol{\nu}} : \boldsymbol{\nu} \tag{2.A.9}$$

where n_h is the order of homogeneity of the function (see Appendix 2.C).

2.A.3. HYPERPLASTICITY APPROACH

In hyperplasticity, the constitutive equations can be deduced by defining only the energy and rate of dissipation functions, without the need to add additional assumptions [20]. The thermodynamic work-conjugate of generalised velocities $\boldsymbol{\nu}$, is called "*generalised dissipative forces*", $\boldsymbol{\chi}$ (which, depending on $\boldsymbol{\nu}$, can be a scalar or a tensor). These work-conjugates are critical because the relationship between them and the generalised dissipative velocities determines the constitutive equations governing the behaviour of the material [75]. It is assumed that the rate of dissipation is a linear function of the generalised dissipative velocities $\boldsymbol{\nu}$, defined as $d = \boldsymbol{\chi} : \boldsymbol{\nu} = \langle \boldsymbol{\nu}, \boldsymbol{\chi} \rangle$, similar to Eq. (2.A.8). By comparing with Eq. (2.A.8) (since $\dot{\alpha}_i = \boldsymbol{\nu}$), the following result can be achieved

$$\bar{\chi} = \chi \tag{2.A.10}$$

This is a key element in hyperplasticity and is called Ziegler's orthogonality condition.

To determine the generalised dissipative forces $\boldsymbol{\chi}$, [25] postulated that the direction of $\partial d/\partial \boldsymbol{\nu}$ produces maximal entropy (or maximal dissipation rate). From the geometry point of view, this direction is normal to the dissipation. From the mathematical point of view, the generalised dissipative forces can then be determined as

$$\boldsymbol{\chi} = \Upsilon \frac{\partial d}{\partial \boldsymbol{\nu}} \tag{2.A.11}$$

where Υ is a scalar that represents the magnitude of the generalised dissipative forces. Substituting Eq. (2.A.11) into $d = \langle \boldsymbol{\nu}, \boldsymbol{\chi} \rangle$ results in

$$d = \Upsilon \left\langle \boldsymbol{\nu}, \frac{\partial d}{\partial \boldsymbol{\nu}} \right\rangle \tag{2.A.12}$$

By comparing the dissipation functions in Eqs. (2.A.9) and (2.A.12), it can be concluded that $\Upsilon = 1/n_h$. Thus, the assumed rate of dissipation function in the form of $d = \langle \boldsymbol{\nu}, \boldsymbol{\chi} \rangle$ is a homogeneous function of order n_h which is non-negative, which satisfies all the requirements of a rate of dissipation function. The generalised dissipative forces are then determined as

$$\boldsymbol{\chi} = \Upsilon \frac{\partial d}{\partial \boldsymbol{\nu}} = \frac{1}{n_h} \frac{\partial d}{\partial \boldsymbol{\nu}} \tag{2.A.13}$$

YIELD FUNCTION

By applying Eq. (2.B.1) on $d = \langle \boldsymbol{\nu}, \boldsymbol{\chi} \rangle$, it is possible to define

$$z(\mathbf{x}, \boldsymbol{\nu}, T) + w(\mathbf{x}, \boldsymbol{\chi}, T) = \langle \boldsymbol{\nu}, \boldsymbol{\chi} \rangle = d \tag{2.A.14}$$

where z and w are the force and flow potentials [20; 75], respectively. Thus, the following properties apply (in accordance with Eq. (2.B.2))

$$\boldsymbol{\chi} = \frac{\partial z(\mathbf{x}, \boldsymbol{\nu}, T)}{\partial \boldsymbol{\nu}}, \boldsymbol{\nu} = \frac{\partial w(\mathbf{x}, \boldsymbol{\chi}, T)}{\partial \boldsymbol{\chi}} \tag{2.A.15}$$

By comparing Eq. (2.A.15) with Eq. (2.A.13), it can be concluded that $\frac{\partial z}{\partial \boldsymbol{\nu}} = \frac{1}{n_h} \frac{\partial d}{\partial \boldsymbol{\nu}}$. For rate-independent materials, which are the motivation behind the model in this chapter, the rate of dissipation function is homogeneous of order one ($n_h = 1$), which yields $z = d$. Further substitution into Eq. (2.A.14) results in $w(\mathbf{x}, \boldsymbol{\chi}, T) = 0$, which means that the flow potential is always zero. In this case, it is possible to derive a function of the forces that is identically zero when yielding occurs

$$w(\mathbf{x}, \boldsymbol{\chi}, T) = \Upsilon' y(\mathbf{x}, \boldsymbol{\chi}, T) = 0 \tag{2.A.16}$$

where Υ' is a non-zero value. Thus, $y(\mathbf{x}, \boldsymbol{\chi}, T) = 0$, which is the yield function [20; 75; 76], defined in generalised force space (not in true stress space).

2.B. APPENDIX B: LEGENDRE TRANSFORM

The Legendre transform has a wide range of applications, especially in thermodynamics. As an example, this transform may be invoked to interchange between different types of energy function; internal energy (u), enthalpy (h), Helmholtz free energy (f), and Gibbs free energy (g). Another example is the interchange between the rate of dissipation and the yield functions for dissipative materials. Precisely, the purpose of this transform is to interchange the role of any independent variable of a function to its conjugate variable. Suppose that l_1 is an independent variable (active variable) of a set of variables that defines the function $k_1(l_1, a_1, a_2, a_3 \ldots)$. By Legendre transformation, the function k_1 is converted to the function k_2 which is defined by the same set of passive independent variables ($a_1, a_2, a_3, \ldots$); however, the active variable l_1 is replaced by its conjugate variable l_2, through application of the product-rule between the active variables ($\langle l_1, l_2 \rangle$). This can be mathematically shown as

$$k_1(l_1, a_1, a_2, a_3, \ldots) + k_2(l_2, a_1, a_2, a_3, \ldots) = \langle l_1, l_2 \rangle \tag{2.B.1}$$

where $\langle \rangle$ is the inner product operator. This transform can be applied to any set of independent variables.

One of the important features of the Legendre transform is that the properties of one function remain unchanged during the transformation and the properties are transferred to the other function. This means that, in the case of applying the Legendre transform on an energy function, using other types of energy function would lead to the same results. With the same reasoning, invoking the Legendre transform for the rate of dissipation function results in the interchangeable use of the yield function with the rate of dissipation function.

The Legendre transform provides two important properties; one is related to the active variable(s) and the other is related to the passive variable(s). It can be proven that the partial differential of each function with respect to its corresponding active variable is equal to their corresponding conjugates. This can be shown as

$$l_2 = \frac{\partial k_1(l_1, a_1, a_2, a_3, \ldots)}{\partial l_1}; \ l_1 = \frac{\partial k_2(l_2, a_1, a_2, a_3, \ldots)}{\partial l_2} \tag{2.B.2}$$

The partial differentials with respect to passive variables are identical for both functions

$$\frac{\partial k_1(l_1, a_1, a_2, a_3, \ldots)}{\partial a_i} = \frac{\partial k_2(l_2, a_1, a_2, a_3, \ldots)}{\partial a_i}; i = 1, 2, 3, \ldots \tag{2.B.3}$$

This equation is the transfer of the properties of k_1 to k_2.

2.C. APPENDIX C: PROPERTIES OF HOMOGENEOUS FUNCTIONS

A function $r(e)$ is homogeneous of degree n_h with respect to all the values of t if the following statement stands

$$r(te) = t^{n_h} r(e) \tag{2.C.1}$$

This definition can be generalised to any finite number of variables for the function. From the mathematical point of view, homogeneous functions possess a mapping (scaling) characteristic.

   One of the properties of an homogeneous function, which is extensively implemented in thermodynamics, is that Euler's theorem applies. According to this theorem, if a function r is defined by a variable e, and is homogeneous to degree n_h, then such a function can be written in terms of its partial derivatives with respect to e

$$n_h r(e) = \frac{\partial r(e)}{\partial e} e \tag{2.C.2}$$

2.D. APPENDIX D: COMPONENTS OF EQUATION (2.22)

The derivative components of the plastic multiplier in Eq. (2.22) are as follows

$$\{\mathbf{r}\} = \left\{ \begin{array}{c} r_p \\ r_q \end{array} \right\} = 2 \left\{ \begin{array}{c} B^2(p-C) - \beta A^2(q-\beta p) \\ A^2(q-\beta p) \end{array} \right\} \tag{2.D.1}$$

$$\left\{ \frac{\partial y}{\partial \boldsymbol{\sigma}} \right\} = \left\{ \begin{array}{c} \frac{\partial y}{\partial p} \\ \frac{\partial y}{\partial q} \end{array} \right\}$$
$$= 2 \left\{ \begin{array}{c} A(1-\gamma)\left((q-\beta p)^2 - B^2\right) + BM(1-\alpha)\left((p-C)^2 - A^2\right) + \left(B^2(p-C) - \beta A^2(q-\beta p)\right) \\ A^2(q-\beta p) \end{array} \right\} \tag{2.D.2}$$

$$\left\{ \frac{\partial y}{\partial \boldsymbol{\varepsilon}^p} \right\} = \left\{ \begin{array}{c} \frac{\partial y}{\partial \varepsilon_v^p} \\ \frac{\partial y}{\partial \varepsilon_s^p} \end{array} \right\}$$
$$= \left\{ \begin{array}{c} \left(\left(\frac{1+e_0}{\lambda - \kappa}\right) \gamma p_{cT}\right)\left(A\left((q-\beta p)^2 - B^2\right) + \alpha MB\left((p-C)^2 - A^2\right) - B^2(p-C)\right) \\ 0 \end{array} \right\} \tag{2.D.3}$$

$$\frac{\partial y}{\partial T} = \frac{\partial y}{\partial A}\frac{\partial A}{\partial p_{cT}}\frac{\partial p_{cT}}{\partial T} + \frac{\partial y}{\partial B}\frac{\partial B}{\partial p_{cT}}\frac{\partial p_{cT}}{\partial T} + \frac{\partial y}{\partial C}\frac{\partial C}{\partial p_{cT}}\frac{\partial p_{cT}}{\partial T} + \frac{\partial y}{\partial B}\frac{\partial B}{\partial M}\frac{\partial M}{\partial T} \rightarrow$$
$$\frac{\partial y}{\partial T} = \left(-\mu\gamma p_{cT}\right)\left(A\left((q-\beta p)^2 - B^2\right) + \alpha MB\left((p-C)^2 - A^2\right) - B^2(p-C)\right) ...$$
$$... + 2\pi B\left((p-C)^2 - A^2\right)\left((1-\alpha)p + \frac{\alpha\gamma}{2}p_{cT}\right) \tag{2.D.4}$$

2.E. APPENDIX E: TEMPERATURE DEPENDENT INCREMENTAL FORMULATIONS

2.E.1. STRESS-CONTROLLED INCREMENTAL FORMULATION

In a stress-controlled condition, stress increments are imposed to the system as inputs and the resulting strain increments are calculated. Most geotechnical numerical simulations, e.g. foundation analyses, come under this category.

The total strain increment can be determined by differentiating Eqs. (2.5) and (2.6)

$$\left\{ \begin{array}{c} \dot{\varepsilon}_v \\ \dot{\varepsilon}_s \end{array} \right\} = \left\{ \begin{array}{c} \dot{\varepsilon}_v^e \\ \dot{\varepsilon}_s^e \end{array} \right\} + \left\{ \begin{array}{c} \dot{\varepsilon}_v^T \\ 0 \end{array} \right\} + \left\{ \begin{array}{c} \dot{\varepsilon}_v^p \\ \dot{\varepsilon}_s^p \end{array} \right\} \tag{2.E.1}$$

where the elastic strains are

$$\dot{\varepsilon}_v^e = -\left(\frac{\partial^2 g_1(p,q)}{\partial p \partial p} \dot{p} + \frac{\partial^2 g_1(p,q)}{\partial p \partial q} \dot{q} \right)$$

$$\dot{\varepsilon}_s^e = -\left(\frac{\partial^2 g_1(p,q)}{\partial q \partial p} \dot{p} + \frac{\partial^2 g_1(p,q)}{\partial q \partial q} \dot{q} \right) \tag{2.E.2}$$

which can be rewritten in the compact form

$$\left\{ \begin{array}{c} \dot{\varepsilon}_v^e \\ \dot{\varepsilon}_s^e \end{array} \right\} = [\mathbf{C}^e] \left\{ \begin{array}{c} \dot{p} \\ \dot{q} \end{array} \right\} = -\left[\begin{array}{cc} \frac{\partial^2 g_1}{\partial p^2} & \frac{\partial^2 g_1}{\partial p \partial q} \\ \frac{\partial^2 g_1}{\partial q \partial p} & \frac{\partial^2 g_1}{\partial q^2} \end{array} \right] \left\{ \begin{array}{c} \dot{p} \\ \dot{q} \end{array} \right\}$$

where $[\mathbf{C}^e]$ is the elastic compliance (or flexibility) matrix. With respect to Eq. (2.3) or Eq. (2.4), the components of the elastic compliance matrix can be derived, respectively, as

$$[\mathbf{C}^e] = \frac{1}{3\bar{G}p_{ref} \left(\frac{p}{p_{ref}} \right)^n} \left[\begin{array}{cc} \left(\frac{3\bar{G}}{\bar{K}} \left(\frac{p}{p_{ref}} \right)^{n-m} + \bar{n}\eta^2 \right) & -n\eta \\ -n\eta & 1 \end{array} \right] ; \bar{n} = \frac{n(n+1)}{2} \tag{2.E.3}$$

$$[\mathbf{C}^e] = \frac{1}{3\bar{G}p_{ref} \left(\frac{p}{p_{ref}} \right)^n} \left[\begin{array}{cc} \left(\frac{3\bar{G}}{\bar{K}} \left(\frac{p}{p_{ref}} \right)^{n-1} + \bar{n}\eta^2 \right) & -n\eta \\ -n\eta & 1 \end{array} \right] \tag{2.E.4}$$

The thermo-elastic strain increment is

$$\dot{\varepsilon}_v^T = 3\alpha^* \dot{T} \tag{2.E.5}$$

The plastic strain increments, $\{\dot{\varepsilon}^p\} = \dot{\Lambda}\{\mathbf{r}\}$, are easily calculated by Eqs. (2.19) and (2.20). In summary, the total strain increments in a stress-controlled condition can be calculated as

$$\{\dot{\varepsilon}\} = [\mathbf{C}^e]\{\dot{\sigma}\} + 3\alpha^* \dot{T} + \dot{\Lambda}\{\mathbf{r}\} \tag{2.E.6}$$

2.E.2. STRAIN-CONTROLLED INCREMENTAL FORMULATION

In some geotechnical applications, e.g. triaxial soil element tests, strains are applied to the soil specimen and the stress increments are measured. This condition, where the total strain is the input and the stress increment is the measured output, is called the strain-controlled condition.

The plastic multiplier in Eq. (2.22) is determined for stress-controlled increments, which should be modified to be strain-increment dependent. Multiplying both sides of Eq. (2.E.6) by $\left(\left\{ \frac{\partial y}{\partial \sigma} \right\}^{\mathrm{T}} [\mathbf{C}^e]^{-1} \right)$ results in

$$\left\{ \frac{\partial y}{\partial \sigma} \right\}^{\mathrm{T}} \{\dot{\sigma}\} = \left\{ \frac{\partial y}{\partial \sigma} \right\}^{\mathrm{T}} [\mathbf{C}^e]^{-1} \{\dot{\varepsilon}\} - 3\alpha^* \left\{ \frac{\partial y}{\partial \sigma} \right\}^{\mathrm{T}} [\mathbf{C}^e]^{-1} \dot{T} - \dot{\Lambda} \left\{ \frac{\partial y}{\partial \sigma} \right\}^{\mathrm{T}} [\mathbf{C}^e]^{-1} \{\mathbf{r}\} \qquad (2.E.7)$$

Recalling the consistency condition (Eq. (2.21)) and comparing with Eq. (2.E.7), similar terms can be identified. By substituting and applying algebraic operations, the plastic multiplier defined by total strain increments can be determined

$$\dot{\Lambda} = \frac{\left\{ \frac{\partial y}{\partial \sigma} \right\}^{\mathrm{T}} [\mathbf{D}^e] \{\dot{\varepsilon}\} + \left(\frac{\partial y}{\partial T} - 3\alpha^* \left\{ \frac{\partial y}{\partial \sigma} \right\}^{\mathrm{T}} [\mathbf{D}^e] \right) \dot{T}}{\left\{ \frac{\partial y}{\partial \sigma} \right\}^{\mathrm{T}} [\mathbf{D}^e] \{\mathbf{r}\} - \left\{ \frac{\partial y}{\partial \varepsilon^p} \right\}^{\mathrm{T}} \{\mathbf{r}\}} \qquad (2.E.8)$$

where $[\mathbf{D}^e]$ is the elastic stiffness matrix and is the inverse of elastic flexibility matrix $[\mathbf{C}^e]$ (Eq. (2.E.3) and Eq. (2.E.4), respectively)

$$[\mathbf{D}^e] = [\mathbf{C}^e]^{-1} = \frac{3\bar{G}\bar{K}p_{ref}\left(\frac{p}{p_{ref}}\right)^m}{3\bar{G} + \underline{n}\eta^2 \bar{K}\left(\frac{p}{p_{ref}}\right)^{m-n}} \begin{bmatrix} 1 & n\eta \\ n\eta & \left(\frac{3\bar{G}}{\bar{K}}\left(\frac{p}{p_{ref}}\right)^{n-m} + \bar{n}\eta^2\right) \end{bmatrix}; \underline{n} = \frac{n(1-n)}{2} \qquad (2.E.9)$$

$$[\mathbf{D}^e] = \frac{3\bar{G}\bar{K}p}{3\bar{G} + \underline{n}\bar{K}\eta^2 \left(\frac{p}{p_{ref}}\right)^{1-n}} \begin{bmatrix} 1 & n\eta \\ n\eta & \left(\frac{3\bar{G}}{\bar{K}}\left(\frac{p}{p_{ref}}\right)^{n-1} + \bar{n}\eta^2\right) \end{bmatrix} \qquad (2.E.10)$$

By the use of Eq. (2.E.6), the stress increments can be calculated in accordance to strain increments

$$\{\dot{\sigma}\} = [\mathbf{D}^e] \left(\{\dot{\varepsilon}\} - \left\{ \begin{matrix} 3\alpha^* \\ 0 \end{matrix} \right\} \dot{T} - \dot{\Lambda}\{\mathbf{r}\} \right) \qquad (2.E.11)$$

where $[\mathbf{D}^e]$ and $\dot{\Lambda}$ are calculated respectively from Eq. (2.E.8) and Eq. (2.E.9) (or (2.E.10)).

3

A FLEXIBLE AND ROBUST YIELD FUNCTION FOR GEOMATERIALS

This chapter presents a new Modified Cam Clay (MCC) type yield function, that is designed for robust and efficient use with implicit stress integration algorithms. The proposed yield function attains non-elliptical (e.g. tear and bullet) shapes, as well as the typical elliptical shape of the MCC model. Like that of MCC, and unlike most other yield functions with non-elliptical shapes available in literature, it is non-singular and unique throughout stress space. The experimental yielding stresses of a wide range of geomaterials have been accurately simulated using the yield surface. The yield function can be used in constitutive models based on classical elasto-plasticity theory.

LIST OF SYMBOLS

3

Roman

$\mathbf{1}$	Second order identity tensor
A	Shape function for yield surface
B	Shape function for yield surface
C	Shape function for yield surface
CPPM	Closest point projection method
CS	Critical State
CSL	Critical State Line
$\mathbf{c}$	Fourth-order elastic compliance tensor
c	Centre of the yield surface
cv_1, cv_2	Co-vertexes of the yield surface
$\mathbf{D}^e$	Elastic stiffness tensor
$\mathbf{e}^e$	Elastic deviatoric strain tensor
G	Shear modulus
g	Plastic potential
h, h_1	Meridian functions of yield equation
$h_1{}', h_1{}''$	First and second derivative of h_1
$\mathbf{I}$	Fourth order identity tensor
$\mathbf{J}$	Jacobian matrix
K_0	Coefficient of earth pressure
k	Level set value
LAD	Lode angle dependency
MCC	Modified Cam Clay
M	Critical State stress ratio
M_c	Critical State stress ratio in compression

Greek

α	Parameter related to the shape of the yield surface
β	Level of inclination of the yield surface
γ	Parameter related to the shape of the yield surface
$\Delta\boldsymbol{\varepsilon}$	Strain increment tensor
$\Delta\varepsilon_{kk}^p$	Plastic volumetric strain increment
$\Delta\Lambda$	Increment of plastic multiplier
$\Delta\boldsymbol{\sigma}^{Predictor}$	Stress predictor increment tensor
$\Delta\boldsymbol{\sigma}^{Corrector}$	Stress corrector increment tensor
$\boldsymbol{\varepsilon}$	Strain tensor
$\boldsymbol{\varepsilon}^e$	Elastic strain tensor
$\boldsymbol{\varepsilon}^{e,trial}$	Elastic trial strain tensor
$\boldsymbol{\varepsilon}_n^e$	Elastic strain tensor at time step n
$\boldsymbol{\varepsilon}_{n+1}^e$	Elastic strain tensor at time step $n+1$
ε_v^e	Elastic volumetric strain
ε_v^p	Plastic volumetric strain
$\dot{\varepsilon}_v^p$	Rate of plastic volumetric strain
η	Stress ratio
η_{K_0}	Stress ratio at K_0 condition
θ	Lode angle
κ	Elastic compressibility index
λ	Elasto-plastic compressibility index
ζ	Lode angle dependent function
$\boldsymbol{\Pi}$	Residual vector
$\boldsymbol{\Pi}_1, \boldsymbol{\Pi}_2, \boldsymbol{\Pi}_3$	Residual equations

M_e	Critical State stress ratio in extension
NR_{it}	Number of iterations
$\hat{\mathbf{n}}$	Tensor of deviatoric direction
p	Mean effective stress
p_c^n	Pre-consolidation pressure at time step n
p_c^{n+1}	Pre-consolidation pressure at time step n+1
p_c	Pre-consolidation pressure
p_{cs}	Mean effective stress at Critical State
$\dot{p}_c$	Rate of change of the pre-consolidation pressure
p_r	Reference pressure
p^{trial}	Trial mean effective stress
p_{R1}, p_{R2}	Roots of R_1 and R_2
p_{R3}	Point of non-uniqueness (root of R_3)
p_{R4}	Point of singularity (root of R_4)
p_t	Tension pressure
$\mathbf{q}$	Hardening variables
q	Deviatoric stress
q_{cs}	Deviatoric stress at Critical State
q_t	Tensile strength
q^{trial}	Trial deviatoric stress
$R_{1,2,3,4}$	Geometrical constraint equations
$\mathbf{r}$	Plastic flow tensor
r	Spacing ratio
r_p	Plastic flow along the p-axis
r_q	Plastic flow along the q-axis
$\mathbf{s}$	Deviatoric stress tensor
t	Number of roots of the yield function
t_n	Time step n
t_{n+1}	Time step n+1
$\boldsymbol{v}$	Vector of increments
y	Yield surface
y^k	Yield function
z	Deviatoric function of yield equation

$\boldsymbol{\sigma}$	Effective stress tensor
$\boldsymbol{\sigma}^{trial}$	Trial stress tensor
$\boldsymbol{\sigma}_n$	Stress tensor at time step n
$\boldsymbol{\sigma}_{n+1}$	Stress tensor at time step n+1
ϕ_c	Friction angle

3

3.1. INTRODUCTION

To numerically simulate the mechanical performance of large-scale engineering infrastructures, constitutive equations that represent the mechanical behaviour of materials are used. These can be implemented in boundary-value solvers, such as the finite element method or the material point method, using several approaches (see [1–3] for detailed information), of which the most efficient belong to the implicit stress integration algorithm category [1; 3]. In this category, after the boundary-value solver has calculated a strain increment, a corresponding (trial) stress state is calculated and, when needed, this is mapped back onto the yield surface. More specifically, the trial stress state may temporarily go beyond the admissible stress states that are bounded by the yield surface. When this happens, the stress (located outside the yield surface) is returned back onto the yield surface using the plasticity component of the constitutive equations. This return mapping algorithm is generally an iterative procedure, with the stress being updated in each iteration. Usually, the return mapping procedure requires the first derivatives of the yield function and plastic potential with respect to the updated stress state. Therefore, it is essential for robust computation that computational methods employ a yield function (and plastic potential) that is defined uniquely in the entire stress space to ensure the updated stress is correctly mapped onto the yield surface [4]. Otherwise, this may result in limitations on the time/load steps used, or worse, to non-convergence or incorrect converged stresses which impairs the predictive capability of the constitutive equations [4].

Owing to a wide range of behaviours observed for geomaterials, researchers have paid particular attention to developing yield surfaces and plastic potentials with a variety of shapes in meridian and deviatoric stress space, in order to capture their behaviour as accurately as possible. Examples can be found in [5–15]. These constitutive equations have been derived from different theories, with classical plasticity and thermodynamics principles being commonly accepted examples.

As will be seen later, the Modified Cam Clay (MCC) [16] yield function and plastic potential are inherently robust and therefore highly suitable for implicit stress integration algorithms. However, although the MCC yield function therefore provides a suitable framework for developing constitutive equations, its elliptical surface does not represent the observed behaviour of many geomaterials. In fact, MCC has no flexibility to cope with experimentally determined loci of yield stress points with non-elliptical shapes (e.g. so-called tear, bullet and egg shapes). Many alternative surfaces can be found in the literature that have addressed this limitation (see for example [5; 7; 11–13; 17]). However, most of them have non-unique elastic domains, i.e., locations in stress space outside the intended elastic domain where the yield function value implies elasticity, a so-called undesired (false) elastic domain or nucleus. This was investigated by Coombs & Crouch [18] for the yield surface proposed by Collins & Hilder [11]. One may use the convexification technique to overcome this problem by developing an alternative formulation of the yield function which resembles and preserves the non-elliptical shape of the yield surface at all values; for example, Stupkiewicz et al. [19] used such an approach to extend the formulation of a previously proposed yield surface [13]. Moreover, Panteghini & Lagioia [20] corrected the undesired elastic domain of a distorted MCC-type yield surface with a single shape-parameter via a convexification technique [21], to develop a fully

convex and unique yield function expression. However, in both of these works, the analytical expression for the yield function is complex and the approach they pursue may not be practical or convenient for all yield surfaces, as imaginary solutions may arise.

In this chapter, a new yield function is proposed which has the flexibility of attaining non-elliptical shapes. As for MCC, it is robust for implicit stress integration algorithms, without having the shortcomings of false elastic domains, singularities or erratic gradients in meridian stress space. Note that the formulations presented are in accordance with geotechnical conventions, where compressive stresses and contractive strains are considered to be positive.

3.2. Requirements of the yield function

Yield surface functions are generally defined by the effective stress tensor, $\boldsymbol{\sigma}$, and hardening variables, $\mathbf{q}$, which may be tensors (such as kinematic hardening variables) or scalars (e.g. isotropic hardening variables). Here, as is common in geotechnical engineering, yield surfaces defined in meridian stress space, i.e. by stress invariants p and q (respectively, the mean effective stress, $p = tr(\boldsymbol{\sigma})/3$ (kPa) and deviatoric stress, $q = (3/2\ \mathbf{s}:\mathbf{s})^{1/2}$ (kPa), where $\mathbf{s} = \boldsymbol{\sigma} - tr(\boldsymbol{\sigma})/3 : \mathbf{1}$ is the deviatoric stress tensor and $\mathbf{1}$ is the second order identity tensor), and specifically those with isotropic hardening, defined by a pre-consolidation pressure p_c, are considered. This is particularly relevant for history dependent materials such as soils. A function y is defined which is used to control the constitutive behaviour. Hereafter, the terms yield surface and yield function are distinguished by level sets of y [4]. The yield surface is defined by the level set "*zero*", i.e., $y(\boldsymbol{\sigma},\mathbf{q}) = 0$ and the yield function is defined for "*non-zero*" level sets, i.e., $y^k(\boldsymbol{\sigma},\mathbf{q}) = k$ where $k > 0$.

In elasto-plasticity, a yield surface is employed to divide the stress space into three regions [4]:

1. stresses inside the yield surface, that represent the elastic domain, $y < 0$;

2. stress states on the yield surface, $y = 0$, that undergo elasto-plastic deformation;

3. inadmissible stresses outside the yield surface, which satisfy $y > 0$.

Yield surfaces should uniquely define the admissible/elastic stress space ($y \le 0$), i.e., there should only be one yield surface. Moreover, the yield surface is required to be convex over its admissible stress space, which means that stresses cannot go outside the yield surface from one point inside the yield surface to another point inside the yield surface. When the yield surface is implemented in a boundary-value solver with an implicit stress updating procedure, additional restrictions for the yield function are needed.

When used in boundary-value solvers, usually a so-called return mapping procedure is used in order to correctly calculate the stress and hardening parameters associated with a certain strain (increment) (see Figure 3.1). Here, a closest point projection method (CPPM) is employed as the return mapping approach, where it is assumed that for a time interval $[t_n, t_{n+1}]$, at time step n, the stress tensor, $\boldsymbol{\sigma}_n$, strain tensor, $\boldsymbol{\varepsilon}_n$, hardening variables, $\mathbf{q}_n$, and yield surface (y_n), are converged and defined, and that the stress state is located on the yield surface. To calculate the corresponding variables at time step $n+1$, the return mapping technique applies two steps: (i) by the use of the total strain

increment (obtained from the boundary-value solver), $\Delta\varepsilon$, an incremental stress predictor, $\Delta\boldsymbol{\sigma}^{predictor}$, is calculated, assuming only elastic behaviour. Consequently, the trial stress is calculated ($\boldsymbol{\sigma}^{trial} = \boldsymbol{\sigma}_n + \Delta\boldsymbol{\sigma}^{predictor}$); (ii) when $\boldsymbol{\sigma}^{trial}$ goes beyond the yield surface (i.e. $y > 0$), the stress state must be corrected (mapped) back onto the yield surface. This is performed by the application of a stress increment corrector, $\Delta\boldsymbol{\sigma}^{corrector}$. In this step, the plastic behaviour is estimated, giving a new prediction of the updated stress, the yield surface and the hardening variables. This may be done iteratively, in order to return the new stress ($\boldsymbol{\sigma}_{n+1}$) onto the updated yield surface (y_{n+1}), updated via its hardening variables (such as p_c). As a result of step (i), $\boldsymbol{\sigma}^{trial}$ sits on a non-zero level set of the yield function (i.e. $y(\boldsymbol{\sigma}^{trial}) > 0$), and $\Delta\boldsymbol{\sigma}^{corrector}$ in step (ii) is typically calculated iteratively by using the first and second derivatives of the yield function ($y^j{}_{n+1}, j = 1, 2, 3, \ldots$) (in the case of an associated flow rule) or plastic potential function ($g^j{}_{n+1}, j = 1, 2, 3, \ldots$) at every state that the return path experiences. To have a correct return mapping path, the yield function ($y^k(\boldsymbol{\sigma},\mathbf{q}) = k$) should meet the criteria considered for the yield surface ($y = 0$), including uniqueness and convexity. It should be noted that these restrictions are due to numerical implementation considerations and not material behaviour/energy considerations. Moreover, even if the yield surface satisfies these conditions, it is not automatic that the yield function also satisfies them. It is also possible to have mathematical expressions that provide the same yield surface but very different yield functions in terms of their level set variation.

The majority of this chapter focuses on the uniqueness of yield functions and how to develop a robust and efficient form for implicit stress updating algorithms. Non-uniqueness may appear from several sources. Three of these are identified and their detrimental consequences summarised below:

1. Non-unique elastic domains: in the stress space outside the desired yield surface ($y(\boldsymbol{\sigma},\mathbf{q}) = 0$) it may be possible to identify domains where the condition $y > 0$ is not satisfied, i.e., the yield surface defines two (or more) enclosed areas where the condition $y < 0$ is satisfied; this is a so-called false (undesired) elastic domain or nucleus (Figure 3.2a). Potentially, this means that the stress predictor could move the trial stress into the false elastic domain; then the behaviour is falsely predicted to be elastic, and consequently would not trigger the return mapping procedures and, therefore, not calculate plasticity, material hardening or the return to the yield surface.

2. Singularity: in the stress space outside the yield surface, the yield function or its derivatives may not be mathematically defined, which is hereafter called a "*singularity*" (Figure 3.2b). As a result, there are sudden changes in the behaviour of the yield function (i.e., discontinuities), for example in its gradients, resulting in divergence of the solution.

3. Erratic gradients: in the stress space outside the yield surface, high curvatures of the yield function may be observed (Figure 3.2c), even though it is mathematically defined at those stress states (in contrast to singularity points). In these regions, convergence can be difficult.
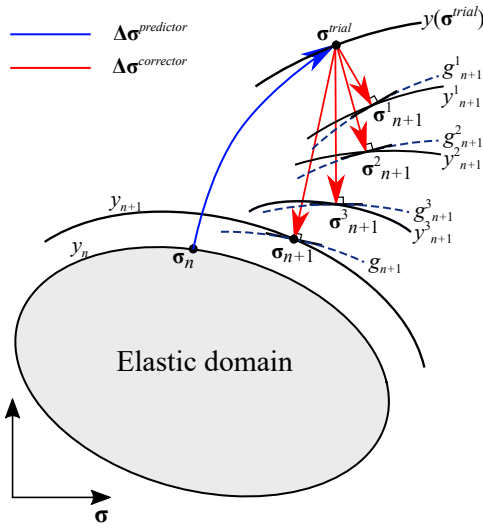
Figure 3.1: CPPM return mapping technique in implicit stress integration approach
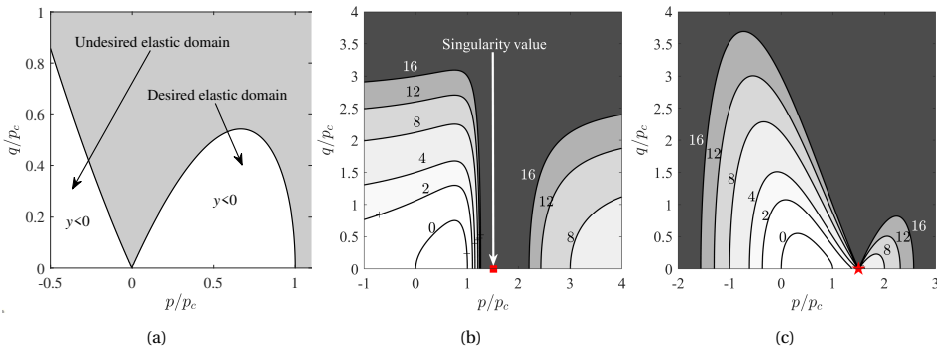
Figure 3.2: Sources of non-uniqueness of yield functions: (a) undesired elastic domain (false elastic nucleus) (yield function of [13]); (b) singularity and discontinuity in the gradient for same level sets (yield function of [11]); (c) high curvature of the yield function (yield function of [11])

Other issues, including local minima (the stress state getting trapped and being unable to return to the yield surface), also result in an inefficient stress integration algorithm. Although these issues are not covered in this chapter, they may be linked to the sources of non-uniqueness mentioned above and these issues may be solved by following the approach proposed here.

3.3. ANALYSIS OF FLEXIBLE ELLIPTICAL YIELD FUNCTIONS

Many constitutive modelling approaches and yield surfaces have been proposed for geomaterials. Collins & Hilder [11], using the principles of thermodynamics, derived a family of isotropic yield surfaces for geomaterials (readers may refer to [11; 22] for detailed

descriptions of the derivation procedure). These yield surfaces have a quadratic-type formulation, similar to that of an ellipse

$$y = \frac{(p-C)^2}{A^2} + \frac{q^2}{B^2} - 1 = 0 \tag{3.1a}$$

or, alternatively, in the form

$$y = B^2 (p - C + A)(p - C - A) + A^2 q^2 = 0 \tag{3.1b}$$

Both these forms will be used later to identify the geometrical constraints required to formulate a unique and non-singular yield surface. Eq. (3.1) is the zero level set of the general yield function (y^k)

$$y^k = \frac{(p-C)^2}{A^2} + \frac{q^2}{B^2} - 1 = k \tag{3.2a}$$

$$y^k = B^2 \left(p - C - \sqrt{1+k}A\right)\left(p - C + \sqrt{1+k}A\right) + A^2 q^2 = 0 \tag{3.2b}$$

where $k \geq 0$ represents the level set of interest.

A and B are, respectively, the semi-major and semi-minor axes of the yield surface (Figure 3.3) and C controls the horizontal distance (or shift) between the semi-minor axis of the surface and the origin (denoted by point O in Figure 3.3). All the surfaces in Figure 3.3 are bounded on the hydrostatic axis at p_c (the pre-consolidation pressure) and the centre of the surface (point c) is obtained as the intersection of the semi-major and semi-minor axes. A_1, is the horizontal distance of the centre of the yield surface from the tensile apex (which is here coincident with the origin, so that $A_1 = C$), whereas A_2 is the horizontal distance between the centre of the yield surface and the compression apex of the yield surface (p_c). Hence the sum of A_1 and A_2 is the size of the major axis of the yield surface (i.e., $A_1 + A_2 = p_c$). For an ellipse (Figure 3.3a), it holds that $C/(A_1 + A_2) = 0.5$ (i.e., $A_1/A_2 = 1$) and the gradients (demonstrated by red arrows) at the co-vertexes (shown by cv_1 and cv_2) are zero with respect to the p-axis. Flexible non-elliptical shapes can be formed by several approaches. Here, two of those possible methods are discussed.

The first method fixes the semi-minor axis on the p-axis in the same place as an ellipse (i.e. $A_1 = A_2$) (Figure 3.3a) and at this point the yield surface is inclined to the p-axis. Two such surfaces are depicted in Figure 3.3b and Figure 3.3c. Note that, for these surfaces, the gradients with respect to the p-axis at points cv_1 and cv_2 are non-zero (in contrast to the ellipse). In the second approach, the location of the minor-axis on the p-axis is changed compared to an ellipse (and the gradient at this point is maintained at zero). This implies that the ratio of A_1/A_2 changes with respect to elliptical shapes (i.e. $A_1/A_2 \neq 1$). Figure 3.3d and Figure 3.3e, respectively, illustrate yield surfaces with $A_1/A_2 < 1$ and $A_1/A_2 > 1$, that have been developed via this approach. For these surfaces, similar to an ellipse, the gradients at points cv_1 and cv_2 are zero with respect to the p-axis. A combination of these two methods may also be employed to develop non-elliptical surfaces of an appropriate form to present the material under consideration.
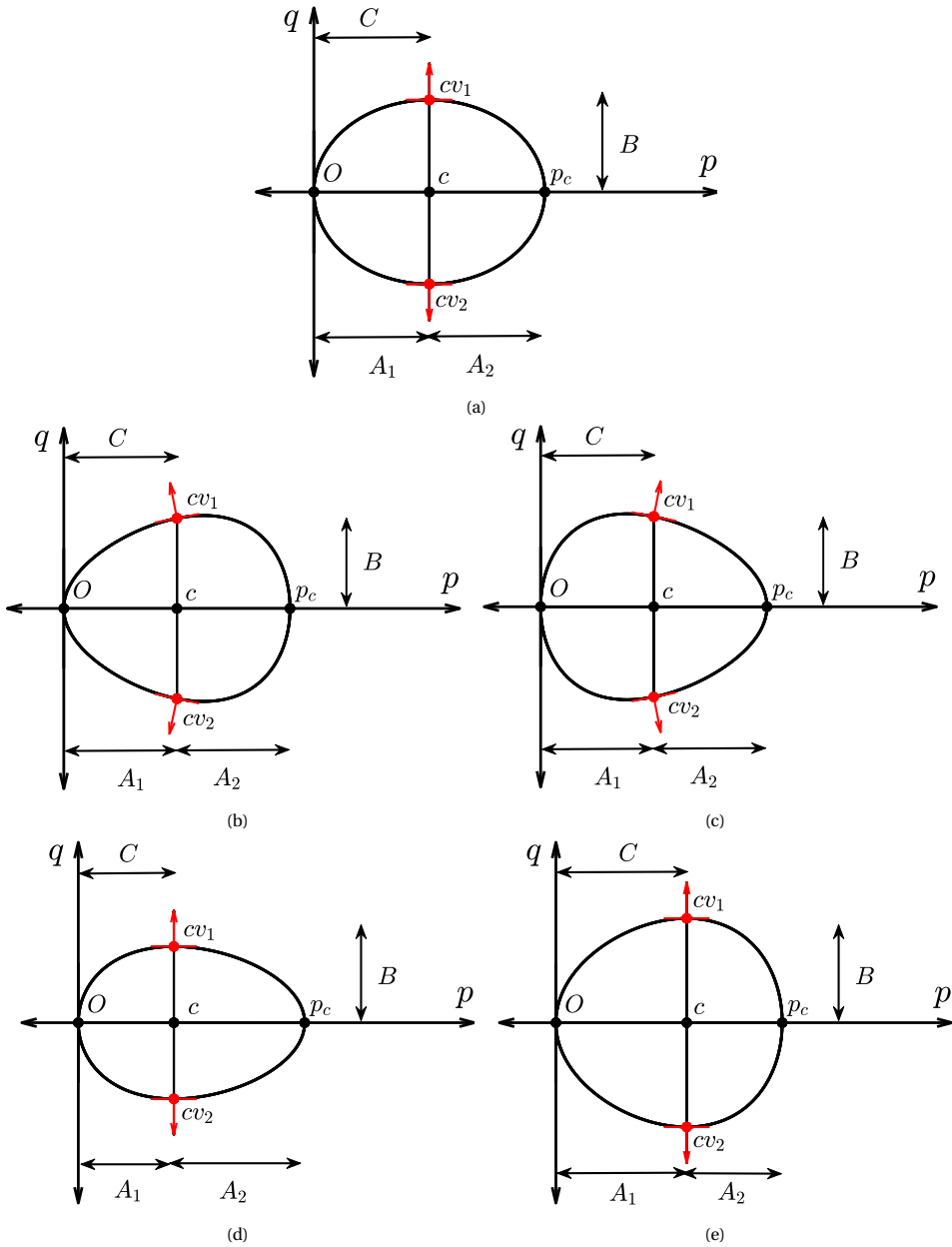
Figure 3.3: Definition of A, B and C for yield surfaces: (a), (b) and (c) $C/(A_1 + A_2) = 0.5$; (d) $C/(A_1 + A_2) < 0.5$; (e) $C/(A_1 + A_2) > 0.5$.

To mathematically incorporate these surfaces in Eq. (3.1), A, B and C are defined in terms of stress invariants (for example, the hydrostatic pressure p) and hardening variables (for example, the pre-consolidation pressure p_c), i.e., $A = A(p, p_c)$, $B = B(p, p_c)$ and

$C = C(p_c)$. Therefore, hereafter they are called "*stress-like functions*". Note that the value of $A = A(p, p_c)$ varies between A_1 and A_2 depending on p. By modifying the definition of the stress-like functions (A, B and C) and using the general quadratic-form of the yield surface presented in Eq. (3.1), non-elliptical (flexible) MCC-type yield surfaces compatible with the observed yielding stresses in geomaterials have been proposed [5; 11; 12]. These models employ two-parameter (α and γ) functions to define A, B and C, in order to form "*tear*" and "*bullet*" shape MCC-type surfaces. The functions for four yield surfaces of the MCC-type family, applicable to soils with zero tensile strength, are summarised in Table 3.1. Regardless of the different formulations proposed for these functions, they all comply to certain geometrical restrictions. Assuming an isotropic yield surface, the yield surface at zero deviatoric stress, q, should be defined at two points, $(p, q) = (-p_t, 0)$ and $(p, q) = (p_c, 0)$, where p_c and p_t are, respectively, the compression and tensile apex of the yield surface along the hydrostatic axis (p-axis), and $p_t = 0$ for soils. Substitution of these two points in Eq. (3.1) results in

$$A(0, p_c) = C \tag{3.3}$$

$$A(p_c, p_c) = p_c - C \tag{3.4}$$

Eq. (3.3) is equal to A_1 in Figure 3.3 and shows that the functions A and C are inter-related in such a way that function C is the same as function A when the dependency on p is omitted. Thus, they have similar signs. In addition, Eq. (3.4) represents A_2 in Figure 3.3.

Assuming that C represents the hydrostatic pressure at Critical State (CS) conditions, i.e.

$$C = p_{cs} \tag{3.5}$$

where subscript "cs" indicates a CS-related variable, the third geometrical constraint is then derived by considering that the yield surface is required to be defined at $(p, q) = (p_{cs}, q_{cs}) = (p_{cs}, Mp_{cs})$

$$B(p_{cs}, p_c) = Mp_{cs} \tag{3.6}$$

where M is the CS stress ratio (the gradient of the CS Line (CSL) in p-q stress space). By substituting Eq. (3.5) in Eq. (3.6) and combining Eq. (3.3) with Eq. (3.4), the following relations are extracted

$$A(0, p_c) = C \tag{3.7a}$$

$$A(0, p_c) + A(p_c, p_c) = p_c \tag{3.7b}$$

$$B(C, p_c) = MC \tag{3.7c}$$

Note that the dependency of function B on function C (and consequently on function A) in Eq. (3.7c) demonstrates how the stress-like functions are linked. The above criteria provide a general method to define stress-like functions in order to develop non-elliptical (flexible) MCC-type yield surfaces; i.e., any proposed stress-like functions that

satisfy these conditions result in a flexible MCC-type yield surface in meridian stress space (see the stress-like functions for several MCC-type yield surfaces presented in Table 3.1).

Note that Eq. (3.1) can easily be extended to account for the influence of the third invariant, the Lode angle θ, by multiplying the function B with an appropriate Lode angle dependent (LAD) function $\zeta(\theta)$

$$y = \frac{(p-C)^2}{A^2} + \frac{q^2}{\zeta^2 B^2} - 1 = 0 \tag{3.8a}$$

or, alternatively, in the form

$$y = \zeta^2 B^2 (p - C + A)(p - C - A) + A^2 q^2 = 0 \tag{3.8b}$$

A number of these LAD functions are reported in [13; 23–25]. Since these functions are independent of p and p_c, the generality of the above approach is not compromised. Since the focus of this chapter specifically concerns numerical deficiencies in the meridian plane, the incorporation of a LAD function into the yield surface is hereafter ignored.

3.3.1. ANALYSIS OF THE MODIFIED CAM-CLAY (MCC) MODEL
To use the same yield surface as in the Modified Cam Clay (MCC) model, the functions A, C and B are defined as $A = C = p_c/2$ and $B = Mp_c/2$, respectively. Thus, for the MCC model the yield surface (Eq. (3.1)) becomes

$$y = \frac{(p - p_c/2)^2}{(p_c/2)^2} + \frac{q^2}{(Mp_c/2)^2} - 1 = 0 \tag{3.9a}$$

or

$$y = M^2 p (p - p_c) + q^2 = 0 \tag{3.9b}$$

Level sets of the MCC yield function in normalised meridian stress space are shown in Figure 3.4a. All the level sets are defined in meridian (p, q) stress space and are concentric with respect to the yield surface, i.e., transformations of the yield surface by an increase in the yield function have the same shape. In addition, the yield function at any level set has identical properties, such as identical gradients. Since the MCC yield surface is unique and convex, its level sets ($k > 0$) also adhere to these properties and are ensured to be unique and convex, as is obvious from Figure 3.4a. It can also be inferred from Figure 3.4a that, during the return mapping procedure of an implicit stress integration approach, any stress state outside the MCC yield surface (resulting from the stress predictor) can be correctly returned back onto the yield surface. This is because, during the return mapping, the stress will be located on surfaces that all have their gradients towards the yield surface ($y = 0$).

3.3.2. ANALYSIS OF THE GENERAL FORMULATION OF THE YIELD FUNCTION (EQ. (3.2)) AND NON-ELLIPTICAL MCC-TYPE MODELS

The stress-like functions of the MCC and three flexible MCC-type yield surfaces [5; 11; 12] are presented in Table 3.1. The functions A, B and C defined for MCC are independent of the stress invariants p and q (see Table 3.1). On the other hand, for the other three yield functions, the shape parameters α and γ are related to p to form non-elliptical MCC-type surfaces. It should be noted that by assigning specific values for the shape parameters, the dependency of these functions on p can be eliminated to resemble the MCC yield function. The respective shape parameters for the yield functions from [11], [12] and [5] are $(\alpha, \gamma) = (1, 1)$, $(\alpha, \gamma) = (1, 0)$ and $(\alpha, \gamma) = (1/2, 0)$ to recover the MCC yield surface.

The level set contours of these four yield surfaces are illustrated in Figure 3.4. It is observed that all the yield functions (except for MCC) have either singularities or are non-unique for some level sets. Although the defined stress-like functions result in a unique yield surface (for a specifically defined range of α and γ), the yield functions lose their uniqueness or may be undefined for a specific value of p (due to singularity) at non-zero level sets (see Figure 3.4). These drawbacks can be investigated in the roots and singularity points of the general yield function equation (Eq. (3.2a)) and will be explored in the following subsections.

The general formulation of the yield function, Eq. (3.2a), may have several roots in meridian stress space (p, q), i.e., on the p-axis (when $q = 0$). The roots are values of p that satisfy the following three equations

$$R_1 : \ p - C - \sqrt{1 + k} A \left(p, p_c \right) = 0 \tag{3.10a}$$

$$R_2 : \ p - C + \sqrt{1 + k} A \left(p, p_c \right) = 0 \tag{3.10b}$$

$$R_3 : \ B \left(p, p_c \right) = 0 \tag{3.10c}$$

The roots corresponding to R_1, R_2 and R_3 (obtained from Eq. (3.10)) for each yield function [5; 11; 12] are presented in Table 3.1 and are shown, respectively, by solid circle, open circle and red star in Figure 3.4.

3.3.3. UNIQUENESS

By substituting A, B and C for the MCC yield function in Eq. (3.10), the yield surface ($\gamma = 0$ and $k = 0$) intersects the p-axis at two points; $(p, q) = (0, 0)$ and $(p, q) = (p_c, 0)$. These points can easily be determined by considering $q = 0$ in the yield function. In other words, the yield surface in meridian stress space has only two roots (the roots of R_1 and R_2 in Eq. (3.10a) and Eq. (3.10b)). Since the function B is independent of p, R_3 has no root, which keeps the total number of roots of the yield surface function as two. When the roots of the yield function at non-zero level sets (for a given k) in meridian stress space are analysed (by solving for p at a given $k > 0$), again only two roots, $(p, q) = (p_c(1 - \sqrt{(1 + k)})/2, 0)$ and $(p, q) = (p_c(1 + \sqrt{(1 + k)})/2, 0)$, are obtained (shown by the solid and open circles in Figure 3.4).

Table 3.1: Different yield surface formulations.

	MCC	Collins & Hilder [11]	Chen & Yang [12]	Zhang et al. [5]
Function A	$\frac{p_c}{2}$	$(1-\gamma)p + \gamma\frac{p_c}{2}$	$\frac{p_c}{2}$	$p_c\sqrt{\alpha^2 + (1-2\alpha)\frac{p}{p_c}}$
Function B	$M\frac{p_c}{2}$	$M\left((1-\alpha)p + \alpha\gamma\frac{p_c}{2}\right)$	$M\frac{p_c}{2}\left(\alpha + \gamma(1-\alpha)\frac{p}{p_c}\right)$	$Mp_c\sqrt{\alpha^2(1-\gamma) + \alpha\gamma\frac{p}{p_c}}$
Function C	$\frac{p_c}{2}$	$\gamma\frac{p_c}{2}$	$\frac{p_c}{2}$	αp_c
Roots of the yield function of the form Eq. (3.2b)	$R_1: p_{R_1} = \left(1+\sqrt{1+k}\right)\frac{p_c}{2}$ $R_2: p_{R_2} = \left(1-\sqrt{1+k}\right)\frac{p_c}{2}$ $R_3: \text{N.A.}$	$R_1: p_{R_1} = \frac{\gamma\left(1+\sqrt{1+k}\right)}{1-(1-\gamma)\sqrt{1+k}}\frac{p_c}{2}$ $R_2: p_{R_2} = \frac{\gamma\left(1-\sqrt{1+k}\right)}{1+(1-\gamma)\sqrt{1+k}}\frac{p_c}{2}$ $R_3: p_{R_3} = -\frac{\alpha\gamma}{(1-\alpha)}\frac{p_c}{2}$	$R_1: p_{R_1} = \left(1+\sqrt{1+k}\right)\frac{p_c}{2}$ $R_2: p_{R_2} = \left(1-\sqrt{1+k}\right)\frac{p_c}{2}$ $R_3: p_{R_3} = -\frac{\alpha}{\gamma(1-\alpha)}\frac{p_c}{2}$	$R_1: p_{R_1} = \left(z + (z^2 + 4\alpha^2 k)^{1/2}\right)\frac{p_c}{2}$ $R_2: p_{R_2} = \left(z - (z^2 + 4\alpha^2 k)^{1/2}\right)\frac{p_c}{2}$ $z = 1 + (1-2\alpha)k$ $R_3: p_{R_3} = -\frac{\alpha(1-\gamma)}{\gamma}p_c$
Root of function A	$R_4: \text{N.A.}$	$R_4: p_{R_4} = -\frac{\gamma}{(1-\gamma)}\frac{p_c}{2}$	$R_4: \text{N.A.}$	$R_4: p_{R_4} = -\frac{\alpha^2}{(1-2\alpha)}p_c$
No. of roots of Eq. (3.2b)	2	2-3	2-3	2-3
Uniqueness	Yes	No (due to p_{R3})	No (due to p_{R3})	No (due to p_{R3})
Singularity	No	Yes (due to p_{R4})	No	Yes (due to p_{R4})

Note: N.A. stands for not applicable

For the other three yield functions, by substituting the stress-like functions in Eq. (3.10), the roots of the yield function for a given k are extracted (see Table 3.1). Since these functions are defined by p and p_c, there is a possibility that the number of roots (t) for Eq. (3.2b) can exceed two. In fact, t roots (in Eq. (3.2b)) enclose the meridian stress space with $t-1$ domain(s) and each domain represents an elastic domain (bounded by a yield surface). For the MCC yield function, $t = 2$ and, therefore, the number of elastic domains is one. However, for the other yield functions, $t \geq 2$ (due to the root of R_3) and, as a result, there are one ($t = 2$) or more ($t > 2$) elastic domains, which means that it may be possible to identify the existence of at least one false (undesired) elastic nucleus, indicating a loss of uniqueness. It is therefore concluded that, to avoid false elastic nuclei, it is required to keep the number of roots of the yield function Eq. (3.2b) (for a given level set k) equal to two ($t = 2$).

3.3.4. SINGULARITY (DISCONTINUITY)

By substituting $q = 0$ in Eq. (3.2a), the yield function reduces to $y^k = (p - C)^2/A^2 - (1 + k) = 0$. This function is not defined when $A = 0$, i.e., at p values that fulfil

$$R_4 : \quad A(p, p_c) = 0 \tag{3.11}$$

At these values of p, the yield function is undefined (as indicated by the solid red squares in Figure 3.4), thereby causing a sudden change in behaviour such as gradients, i.e., resulting in a discontinuity. This type of behaviour is due to the lack of a fully defined yield function in meridian stress space. Of the four yield functions investigated, only the yield functions of MCC and [12] have no singularities (see Table 3.1).

3.3.5. OBSERVATIONS AND CONCLUSIONS

From the above analysis of both forms of the general yield function (Eq. (3.2a) and Eq. (3.2b)), the following observations are made:

- To form a non-elliptical MCC-type yield surface, the functions A or B (or both) should be a function of p, and controlled via shape parameters such as α and/or γ.

- The yield function is required to be defined for all values of its shape parameters.

- To preserve the uniqueness of the admissible elastic region in stress space, the number of roots (t) of the yield function Eq. (3.2b), obtained from Eq. (3.10), is required to be equal to two.

- To avoid singularities (discontinuity), the yield function Eq. (3.2a) should be defined for all stresses in meridian stress space.
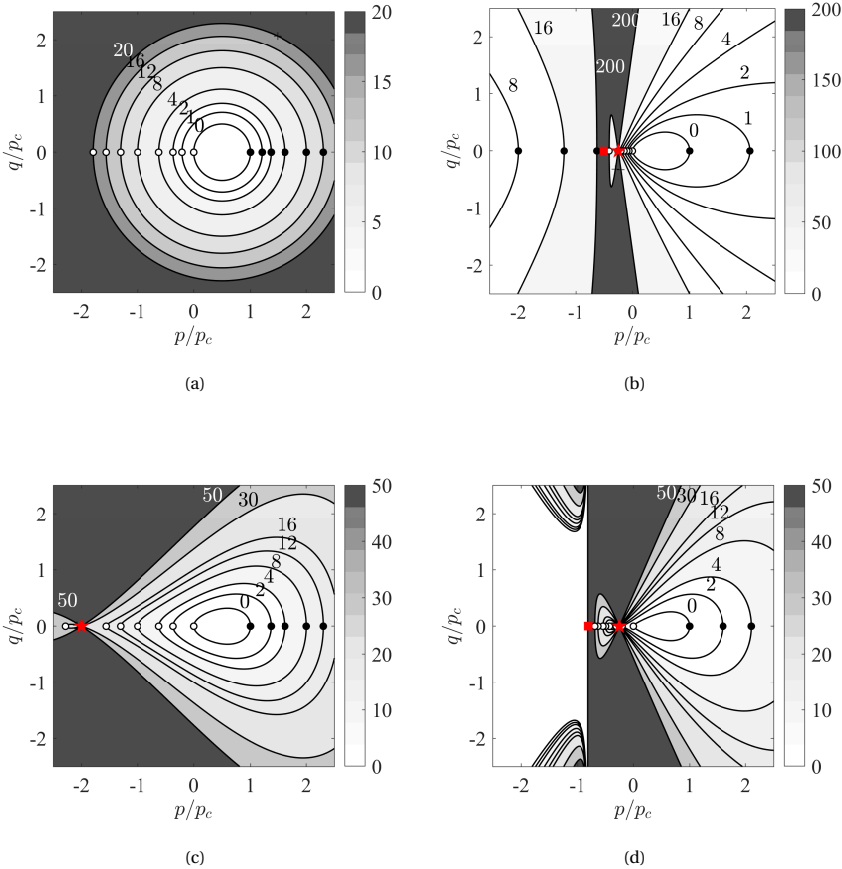
Figure 3.4: Level sets of (a) MCC; (b) Collins & Hilder [11] with $\alpha = 0.5$ and $\gamma = 0.5$; (c) Chen & Yang [12] with $\alpha = 0.5$ and $\gamma = 0.5$; (d) Zhang et al. [5] with $\alpha = 0.4$ and $\gamma = 0.8$. Solid circle, open circle, red star and red square represent, respectively, the roots of R_1, R_2, R_3, and R_4 and, for all yield functions, $M = 1.0$.

3.4. PROPOSED YIELD SURFACE

A countless number of equations can be defined for stress-like functions to form non-elliptical MCC-type yield functions. By accounting for the observations reported in Section 3.3.5, general geometric constraints are designed which result in the development of a non-elliptical MCC-type yield function that is unique and non-singular, and is robust for a return-mapping technique using the implicit stress integration approach. Two shape parameters, α and γ, are used to define the A, B and C functions, following existing methods. Moreover, an additional parameter, β, which represents the back-stress, is introduced, allowing the yield surface (and its non-zero level sets) to be sheared/distorted with respect to the p-axis. The yield surface is described by a quadratic-type expression

which is derived from a thermodynamic basis by defining an appropriate dissipation function (see [11; 22; 26] for the derivation of a quadratic-type yield surface with β). The yield surface can therefore be incorporated into constitutive models which have either a thermodynamic or a phenomenological basis. The modified yield surface and yield function are respectively expressed as

$$y = \frac{(p-C)^2}{A^2} + \frac{(q-\beta p)^2}{B^2} - 1 = 0 \tag{3.12a}$$

or

$$y = B^2 (p-C+A)(p-C-A) + A^2 (q-\beta p)^2 = 0 \tag{3.12b}$$

and

$$y^k = \frac{(p-C)^2}{A^2} + \frac{(q-\beta p)^2}{B^2} - 1 = k \tag{3.13a}$$

or

$$y^k = B^2 \left(p-C+\sqrt{1+k}A\right)\left(p-C-\sqrt{1+k}A\right) + A^2 (q-\beta p)^2 = 0 \tag{3.13b}$$

The roots of Eq. (3.13b), when $q = 0$ and $\beta \neq 0$, are

$$R_1 : \ p - C - \sqrt{1+k}A(p,p_c) = 0 \tag{3.14a}$$

$$R_2 : \ p - C + \sqrt{1+k}A(p,p_c) = 0 \tag{3.14b}$$

$$R_3 : \ B(p,p_c) = 0 \tag{3.14c}$$

$$R_4 : \ A(p,p_c) = 0 \tag{3.14d}$$

3.4.1. GEOMETRICAL CONSTRAINTS

As observed in Section 3.3, in order to avoid singularities and to preserve uniqueness, a yield function in the form of Eq. (3.13b) is required to have only two roots (for a given level set k) on the hydrostatic axis (p-axis) and a yield function in the form of Eq. (3.13a) is required to be defined over the entire meridian stress space. However, from Eq. (3.14c) and Eq. (3.14d), it is shown that there is the possibility to have more than two roots in Eq. (3.13b), and/or to have discontinuities in Eq. (3.13a). Note that, amongst these roots, level set values (k) are only incorporated within the roots R_1 and R_2. To overcome these discrepancies, the general strategy (followed here) is to define functions A and B individually so as to have no roots on the p-axis. In this way, the roots R_3 and R_4 in Eq. (3.14c) and Eq. (3.14d), respectively, are directly eliminated and the other two roots corresponding to R_1 and R_2 (for $k = 0$) satisfy the Eq. (3.7a) and Eq. (3.7b) criteria.

Functions A and B are defined using the shape parameters γ and α, respectively, and are proposed to have the following general forms

$$A(p,p_c) = \frac{p_c}{\pi} \arctan\left(\gamma\left(a_1 - \frac{p}{p_c}\right)\right) + \frac{p_c}{2} \tag{3.15}$$

$$B(p, p_c) = b_1 \exp\left(\alpha \frac{p}{p_c}\right) \tag{3.16}$$

These functions are specifically selected in order to have no roots (no intersection with the p-axis) and to be always positive, i.e., $A, B \in (0, \infty)$. The parameters a_1 and b_1 are determined by satisfying the criteria in Eq. (3.7), which leads to the stress-like functions being defined as

$$A(p, p_c) = \frac{p_c}{2\pi}\left(2\arctan\left(\frac{\gamma(p_c - 2p)}{2p_c}\right) + \pi\right) \tag{3.17}$$

$$B(p, p_c) = MC \exp\left(\frac{\alpha(p - C)}{p_c}\right) \tag{3.18}$$

$$C = \frac{p_c}{2\pi}\left(2\arctan\left(\frac{\gamma}{2}\right) + \pi\right) \tag{3.19}$$

The MCC yield function is retrieved by setting $\alpha = \gamma = 0$.

The variation of functions A and B for different values of α and γ are presented in Figure 3.5a and Figure 3.5b, respectively. As can be seen, these functions are always positive, regardless of the (positive or negative) values assigned to the shape parameters. In addition, the stress-like functions asymptote toward zero when p, depending on the value of α and γ, approaches $\pm\infty$, but never intersect with the p-axis. This ensures that the functions do not have any roots, thereby avoiding the possibility of non-uniqueness or singularities. Furthermore, R_1 and R_2 (for $k = 0$) in Eq. (3.14a) and Eq. (3.14b), for three different γ, are depicted in Figure 3.5c, showing that, independently of γ, R_1 and R_2 have only one root on the hydrostatic axis (p-axis), intersecting at $(p, q) = (p_c, 0)$ and $(p, q) = (0, 0)$ (the origin), respectively. This is similar to the MCC yield surface, but, for different values of α and γ, giving non-elliptical (flexible) MCC-type surfaces.

3.4.2. CONVEXITY AND RANGE OF SHAPE PARAMETERS α AND γ

The quadratic yield surface (yield function with level set of zero), Eq. (3.12a), with the addition of a LAD function, can be re-written as

$$y = -\sqrt{B^2\left(1 - \frac{(p - C)^2}{A^2}\right)} + \frac{(q - \beta p)}{\zeta(\theta)} = h(p) + z((q - \beta p), \theta) \tag{3.20}$$

Eq. (3.20) demonstrates the formulation of the yield surface that is divided into two separate functions defined in the meridian, $h(p)$, and deviatoric, $z((q - \beta p), \theta)$, planes. Note that $(q - \beta p)$ is the radius of the yield surface, at a shear level of β, in the deviatoric plane. For such yield surfaces that are distinguished by meridian and deviatoric functions, through the use of the theorem of convex analysis [27], Bigoni & Piccolroaz [13] demonstrated that the convexity of the yield surface can be separately investigated in meridian and deviatoric stress spaces; i.e., convexity of the functions, $h(p)$ and $z((q - \beta p), \theta)$, implies that the yield surface is also convex. Note that the convexity of the deviatoric

function, $z((q - \beta p), \theta)$, is directly related to the form of the LAD function, $\zeta(\theta)$. When convex LAD functions such as those proposed in [13; 23–25] are used, the convexity of the yield surface in deviatoric space is ensured and, consequently, the convexity of the yield surface reduces to the convexity of the meridian function. Here, the convexity in meridian stress space is considered, as it relates to the main topic of this chapter.

The convexity of the meridian function, $h(p)$ (Eq. (3.20)), is satisfied when $h''(p) \geq 0$. $h(p)$ can be rewritten as $h(p) = -\sqrt{h_1(p)}$, where

$$h_1(p) = B^2 \left(1 - \frac{(p - C)^2}{A^2}\right) \tag{3.21a}$$

Consequently, the convexity of the meridian function results in a condition that satisfies

$$\left(h_1'(p)\right)^2 - 2 h_1(p) h_1''(p) \geq 0 \tag{3.21b}$$

where $h_1'(p)$ and $h_1''(p)$ are, respectively, the first and second derivatives of the function $h_1(p)$ with respect to p. Although the yield surface is defined for the entire range of values of α and γ, it is only convex if a certain combination of these parameters is used and it is possible to determine these ranges by applying the convexity criterion (Eq. (3.21b)), which for the current yield surface is shown in Figure 3.6. In practice, the non-elliptical yielding stresses in geomaterials can be captured by using $-2 \leq \alpha, \gamma \leq 2$. The convexity of the yield surface over this range of shape parameters is shown in Figure 3.6b. Note that the above analysis is limited to the convexity of the yield surface (yield function at the level set of zero). The convexity of the yield function for a non-zero level set is investigated in Section 3.7.

(a)

(b)

(c)
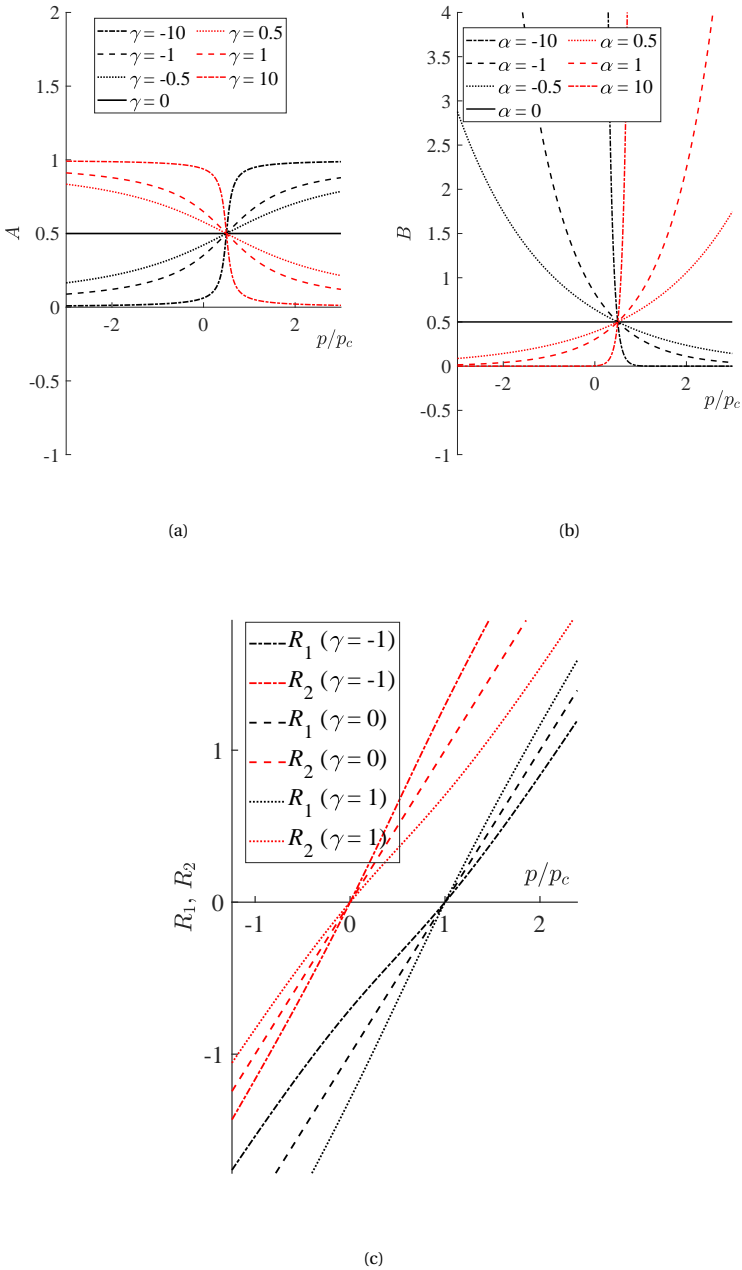
Figure 3.5: (a) Variation of function A with γ; (b) variation of function B with α; (c) variation of R_1 and R_2 in Eq. (3.10a) with γ
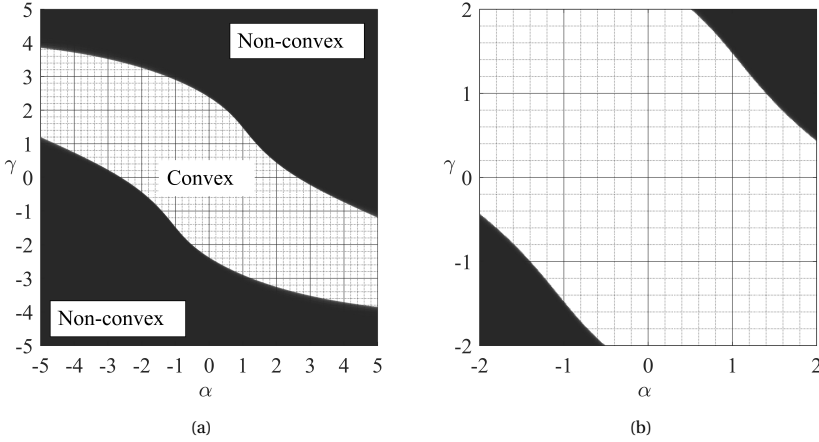
Figure 3.6: Ranges of combined α and γ resulting in convex and non-convex surfaces ($k = 0$), for (a) $-5 \le \alpha$, $\gamma \le 5$; (b) $-2 \le \alpha$, $\gamma \le 2$

3.4.3. EXTENSION OF FORMULATION TO ACCOUNT FOR TENSILE STRENGTH

Geomaterials, such as sandstones and concrete, in general may have tensile strength, i.e., at zero mean effective stress, $p = 0$, the material has a shear strength of q_t. Alternatively, the tensile strength can be characterised by a corresponding tensile pressure, p_t; i.e., the decompression pressure (initial isotropic pressure) is shifted from $(p, q) = (0,0)$ to $(p, q) = (-p_t, 0)$. The stress-like functions can be modified to extend the formulation to account for tensile strength. Hence, the yield surface should intersect the p-axis at $p = -p_t$ and $p = p_c$. By applying the aforementioned conditions in Eq. (3.12a), Eq. (3.7) becomes

$$A(-p_t, p_c) = C + p_t \tag{3.22a}$$

$$A(p_c, p_c) = p_c - C \tag{3.22b}$$

$$B(p_{cs}, p_c) = M p_{cs} \tag{3.22c}$$

Furthermore, substituting Eq. (3.5) in Eq. (3.22c) and combining Eq. (3.22a) with Eq. (3.22b) results in

$$A(-p_t, p_c) = C + p_t \tag{3.23a}$$

$$A(-p_t, p_c) + A(p_c, p_c) = p_c + p_t \tag{3.23b}$$

$$B(C, p_c) = MC \tag{3.23c}$$

To account for p_t in functions A and B, the approach of Bigoni & Piccolroaz [13] is followed, where the normalised pressure term (p/p_c) is replaced by $(p + p_t)/(p_c + p_t)$. Then, by satisfying the criteria in Eq. (3.23), functions A, B and C are modified to

$$A\left(p, p_c, p_t\right) = \frac{\left(p_c + p_t\right)}{2\pi}\left(2\arctan\left(\frac{\gamma\left(p_c - p_t - 2p\right)}{2p_c}\right) + \pi\right)$$

(3.24)

$$B\left(p, p_c, p_t\right) = MC\exp\left(\frac{\alpha\left(p - C\right)}{p_c + p_t}\right)$$

(3.25)

$$C\left(p_c, p_t\right) = \left(\frac{p_c + p_t}{\pi}\right)\arctan\left(\frac{\gamma}{2}\right) + \left(\frac{p_c - p_t}{2}\right)$$

(3.26)

The tensile strength, q_t, can be determined by substituting $p = 0$ in Eq. (3.12a).

3.4.4. PARAMETRIC STUDY OF THE PROPOSED YIELD FUNCTION

The results of a sensitivity analysis of the parameters on the yield surface, Eq. (3.12), and level set contours of the yield function, Eq. (3.13), defined by Eqs. (3.24)-(3.26), are shown in Figure 3.7 to Figure 3.9.

In geomechanics, the ratio of the mean effective stress at the CS condition, p_{cs}, to the over-consolidation pressure, p_c, is often used to calibrate the yield surface. This ratio, r, is called the "*spacing ratio*" [11; 17] and, by using Eq. (3.5) and Eq. (3.19), it is calculated as

$$r = \frac{p_{cs}}{p_c} = \frac{1}{2\pi}\left(2\arctan\left(\frac{\gamma}{2}\right) + \pi\right)$$

(3.27)

As the spacing ratio is determined from experimental data, Eq. (3.27) can be used to calibrate the shape parameter γ as

$$\gamma = 2\tan\left(\pi\left(r - \frac{1}{2}\right)\right)$$

(3.28)

The effect of the shape parameter γ on the yield surface with $\alpha = 0$ is demonstrated in normalised stress space $(p/p_c, q/p_c)$ in Figure 3.7a. In the figure $\beta = p_t = 0$, and the intersection of the CS stress ratio (M) with the yield surfaces are indicated by red dots and their corresponding p/p_c represents the normalised mean effective stress at the CS (p_{cs}/p_c), i.e., indicating the spacing ratio, r. As the parameter γ increases, r increases, as shown by Eq. (3.27). In addition, the yield surface is stretched with respect to the q-axis as γ increases, which means the material can withstand more deviatoric stress for a given p.

Figure 3.7b shows how the yield function changes as the shape parameter α varies. At constant spacing ratio, r (or rather, constant γ; see Eq. (3.28)), the yield surface attains a tear shape for $\alpha \neq 0$. This is shown for $r = 0.5$ ($\gamma = 0$) in Figure 3.7b, where the yield surface curvature changes with respect to the CS stress point, $(p, q) = (p_{cs}, q_{cs})$.

In Figure 3.8 the level sets of the proposed yield function for a range of shape parameters α and γ are plotted. Figure 3.8e with $\alpha = \gamma = 0$ resembles the MCC model, in which all the level sets intersect the hydrostatic axis (p-axis) at two points. With the new formulations defined for the stress-like functions (Eqs. (3.24)-(3.26)), which have no singularities or roots, the level sets of the proposed yield surface with different shape parameters α and γ, similar to MCC, intersect the p-axis at two points, i.e., the yield function for a given k has only two roots. Therefore, the yield function is defined over the entire domain of p (i.e. there is no singularity) and does not produce any undesired (false) elastic nuclei.

The CS stress ratio, M, indicates the ultimate strength of the material and controls the size of the yield surface along the q-axis. In terms of the CS friction angle of the material, ϕ_c, this parameter can be determined on the compression and extension sides, respectively, as

$$M_c = \frac{6\sin\phi_c}{3 - \sin\phi_c}; \qquad M_e = \frac{6\sin\phi_c}{3 + \sin\phi_c} \qquad (3.29)$$

The change in the shape of the yield surface, as parameter M varies, is depicted in Figure 3.9a for yield surfaces with $(\alpha, \gamma, \beta) = (0.5, 0.5, 0)$. It is observed that, as M increases, the size of the yield surface increases, i.e., the yield surface stretches along the q-axis while the p value of the intersection point of the yield surface with the CSL (shown by red dots) remains unchanged. Moreover, the level sets of the yield function (Figure 3.9b) indicate that the uniqueness of the yield function is preserved as M changes.

Geomaterials, such as sands and clays, may be consolidated under K_0 conditions (i.e. anisotropically consolidated), where the yield surface (and plastic potential) have been observed to be inclined along a non-zero stress ratio ($\eta \neq 0$). It is important to capture this feature of geomaterials, as their mechanical behaviour may be significantly influenced by it. The yield surface (Eq. (3.12)) can be sheared/distorted with respect to the p-axis by the parameter β and a suitable hardening rule can be assigned for it during plastic deformation. β may be related to K_0 by [8]

$$\beta = \frac{3\left(1 - \eta_{K_0}\right)}{1 + 2\eta_{K_0}} \qquad (3.30)$$

where η_{K_0} is the stress ratio at K_0 conditions. Shearing/distorting of yield surfaces with shape parameters $(\alpha, \gamma) = (0.5, 0.5)$, for $\beta = 0, 0.3, 0.6$ and 0.9, as well as the original CSL, are plotted in Figure 3.9c. As the shearing/distortion level (β) increases, the intersection point of the yield surface with the CSL changes. This implies that the CS may not remain unique. However, one may follow the approach of Coombs [10] to relate the shape parameters, α and γ, to β to develop a unique CS yield surface (see Appendix 3.A). Note that the uniqueness of the CSL does not place any requirements on the yield surface formulation, although some formulations of the CSL utilise features of the yield surface. The influence of β on the level sets of the proposed yield function is investigated in Figure 3.9d. The level sets of the yield function with shape parameters $(\alpha, \gamma) = (0.5, 0.5)$ and $\beta = 0.3$ (in Figure 3.9d) indicate that the proposed yield function maintains its uniqueness as β is varied and does not produce false elastic nuclei or singularities.

(a)

(b)
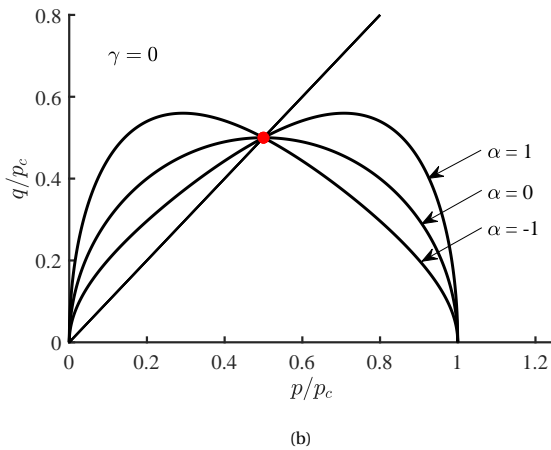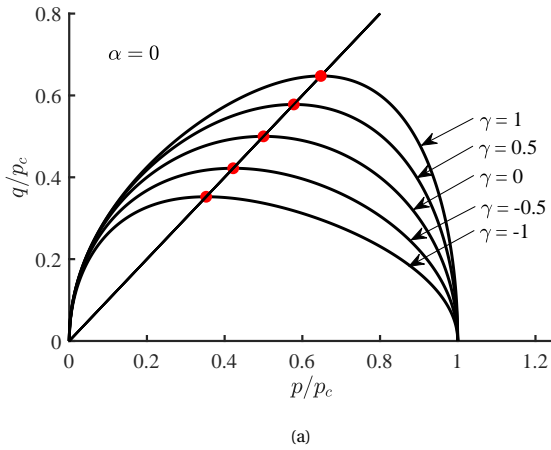
Figure 3.7: Effect of shape parameters on the yield surface for (a) γ; (b) α

The influence of parameter p_t on yield surfaces with shape parameters $(\alpha, \gamma, \beta) = (0.5, 0.5, 0)$ is presented in Figure 3.9e. The yield surface stretches along the p-axis by increasing p_t, whereas it shrinks along the q-axis; i.e., the yield surface flattens as p_t increases. The level sets of the yield surface, for the same shape parameters and $|p_t/p_c| = 0.3$ (in Figure 3.9f), indicate that the uniqueness is not lost as p_t varies.
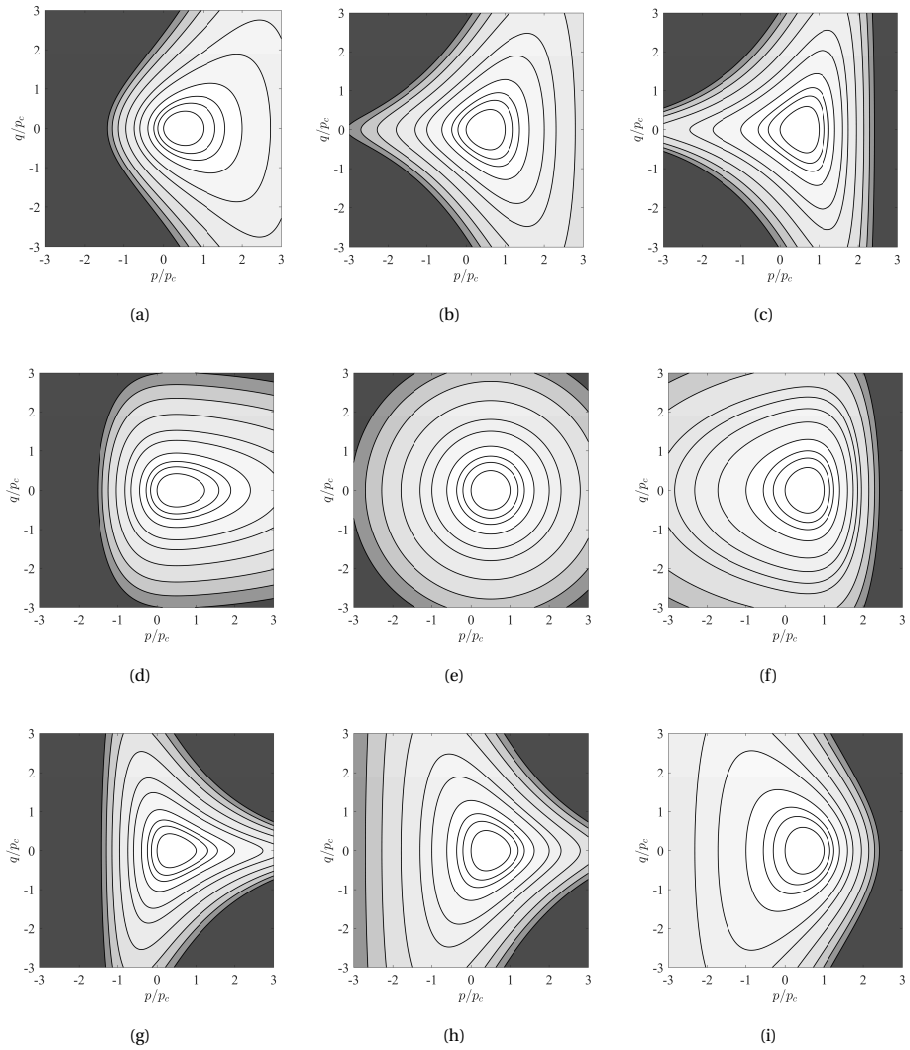
Figure 3.8: Level sets of the proposed yield function for different shape parameters α and γ (for level set contours [0, 1, 2, 4, 8, 12, 20, 30, 40, 50])
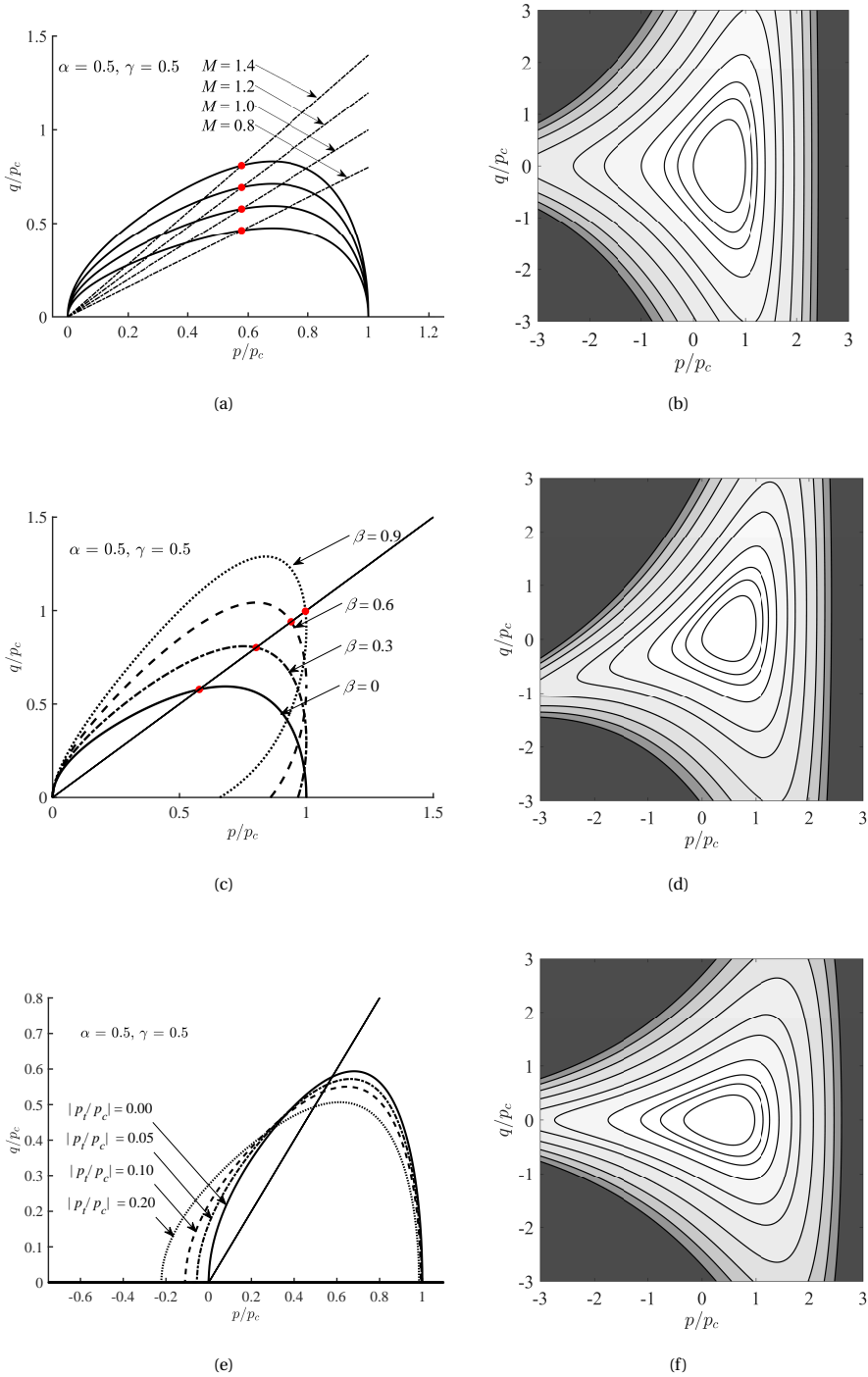
Figure 3.9: Effect of various parameters on yield surfaces with $\alpha = \gamma = 0.5$; (a) effect of parameter M; (b) level sets of the yield function with $M = 1.25$; (c) effect of parameter β; (d) level sets of the yield function with $\beta = 0.3$; (e) effect of parameter p_t; (f) level sets of the yield function with $|p_t/p_c| = 0.3$. The contours corresponds to level sets [0, 1, 2, 4, 8, 12, 20, 30, 40, 50].

Table 3.2: Model parameters (taken from [18]).

Parameter	Symbol	Value
Elastic compressibility index	κ	0.00729 (-)
Shear modulus	G	18 (MPa)
Elasto-plastic compressibility index	λ	0.0447 (-)
Critical State Line gradient in p-q stress space	M	0.9635 (-)
Reference pressure	p_r	100 (kPa)

3.5. EFFICIENCY AND ROBUSTNESS

This section aims to demonstrate the advantages that the proposed yield surface brings in implicit stress integration algorithms. Therefore, some comparative numerical investigations are presented using MCC, the models of Collins & Hilder [11], Chen & Yang [12] and Zhang et al. [5], and the proposed model. These analyses consider stress changes as might be experienced, for example, due to loading of a soil layer near the ground surface, for a soil close to normally consolidated conditions as might be modelled with a relatively small yield surface. The applied loads may cause large strain increments and, when these are passed to a constitutive model, trial stresses are computed that may be a few times bigger than the hydrostatic extent of the yield surface. All of the yield equations were integrated via an implicit CPP algorithm and common constitutive components, including (hyper)elasticity, isotropic hardening rule and the assumption of associated plastic flow, were used. The complete set of constitutive equations and the numerical implementation are provided in Appendix 3.B. For two types of tear-shape yield surfaces, the stress update algorithm using isotropic non-linear and linear elasticity was subjected to various trial stress states and the number of iterations to find the updated stress state were recorded. The yield surface includes hardening, whilst remaining pinned at the origin of p-q stress space. The model's hardening law is based on the MCC volumetric hardening relationship, such that

$$\dot{p}_c = \frac{p_c}{\lambda - \kappa} \dot{\varepsilon}_v^p \tag{3.31}$$

where λ and κ are the bi-logarithmic elasto-plastic and elastic compressibility indices, respectively, and $\dot{\varepsilon}_v^p$ is the rate of plastic volumetric straining. Common material parameters based on Lower Cromer Till are provided in Table 3.2.

The shape parameters to form two types of tear-shape surfaces, for each of the yield equations of Collins & Hilder [11], Chen & Yang [12], Zhang et al. [5], and the proposed form are presented in Table 3.3. The shape parameters for the models of Chen & Yang [12], Zhang et al. [5] and the proposed form were determined via regression analysis to provide a best fit to Collins & Hilder [11]. For Sections 3.5.1 and 3.5.2, the major axis of each yield surface is aligned with the p axis (that is, $\beta = 0$). Analyses involving return mapping when $\beta \neq 0$ are investigated in Section 3.5.3.

Table 3.3: Shape parameters to form different tear-shape yield surfaces.

Yield surface	Tear-shape yield surface type I	Tear-shape yield surface type II
Collins & Hilder [11]	$\alpha = 1.00$, $\gamma = 1.50$	$\alpha = 1.27$, $\gamma = 0.82$
Chen & Yang [12]	$\alpha = 0.64$, $\gamma = 4.07$	$\alpha = 1.18$, $\gamma = 4.46$
Zhang et al. [5]	$\alpha = 0.74$, $\gamma = 0.21$	$\alpha = 0.41$, $\gamma = -0.43$
Proposed form	$\alpha = 0.09$, $\gamma = 2.00$	$\alpha = -0.58$, $\gamma = -0.60$

3.5.1. Iteration-stress maps for non-linear elasticity

For non-linear (hyper)elasticity, the Cauchy stress (σ) is linked to the elastic strains, ε^e, via

$$\sigma = p_r \left(\frac{\varepsilon^e_v}{\kappa} \right) \mathbf{1} + 2G\mathbf{e}^e \tag{3.32}$$

where $\mathbf{e}^e$ is the elastic deviatoric strain, $\mathbf{e}^e = \varepsilon^e - \frac{1}{3}\varepsilon^e_v\mathbf{1}$, ε^e_v is the elastic volumetric strain, G is the shear modulus and p_r is the reference pressure.

The trial states were related to the hydrostatic extent of the yield surface, p_c, such that the following region of stress space was explored

$$\frac{p^{trial}}{p_c} \in [0,2] \quad \text{and} \quad \frac{q^{trial}}{p_c} \in [0,1.5] \tag{3.33}$$

where they were applied from the same starting stress state, $(p,q) = (p_c/2, 0)$, for all the models. The strain increment to cause these elastic trial states was determined and applied in a single step. The number of iterations for each of the trial states is shown in Figure 3.10, for the two series of tear-shape yield surfaces and the MCC model. A total of 120,400 trial states were explored for each model.

Table 3.4 gives the maximum and total number of iterations, and the number of points that failed to converge (i.e. hit the maximum number of iterations, which was set to 25 for this analysis) for the MCC model and for the four other yield equations forming tear-shape surfaces. The table also provides the number of elasto-plastic trial states (i.e., those trial states that were outside the yield surface and required iterations to update the stress state), and the average number of iterations for the elasto-plastic stress updates.

Tear-shape type I yield surface analysis

For trial stresses with $p/p_c > 1.5$, the yield function proposed by Collins & Hilder [11] encountered difficulties to return back to the yield surface and 10,081 points failed to converge, as shown by the red points in Figure 3.10b, and it is this region that caused the average number of iterations to be double that of the MCC model. The model of Zhang et al. [5] predicts the lowest number of elasto-plastic states (47,423) compared to other models, and is nearly half of those predicted by Collins & Hilder [11], Chen & Yang [12] and the proposed yield equation. This is due to the false elastic region when $p/p_c > 1.15$ (Figure 3.10f). The model utilising the Chen & Yang [12] yield equation, although on average requiring a lower number of iterations for elasto-plastic states to converge, struggles to converge for trial stress states around $p/p_c = 0$ and $q/p_c = 1.5$ (Figure 3.10d),

or failed to converge (one failure point). The proposed form on average requires only one more iteration than the MCC model, despite having far more control over the shape of the yield envelope, and all the trial states converged.

TEAR-SHAPE TYPE II YIELD SURFACE ANALYSIS

Figure 3.10c shows the contours of number of iterations required to return the trial stress back onto the yield surface of Collins & Hilder [11]. For trial stresses with $p/p_c > 1.5$, the model faced difficulties to converge and, 157 points failed to return to the yield surface. Similar behaviour is observed for the model of Chen & Yang [12] (Figure 3.10e) where 319 trial stresses did not converge. The model of Zhang et al. [5] performed the worst, with some trial stresses falsely predicted to be in an elastic domain (false elastic domain indicated in Figure 3.10g), and 557 points failed to converge. The proposed yield surface performed the best, as all the trial stresses were converged within a maximum of 9 iterations. The total number of iterations required for all trial stresses to return to the yield surface using this yield function (667,343) were nearly 20% less compared to those of Collins & Hilder [11] and Chen & Yang [12], which required 816,518 and 802,520 iterations, respectively. Compared to the MCC model, on average one extra iteration is required to return all of the trial stresses.
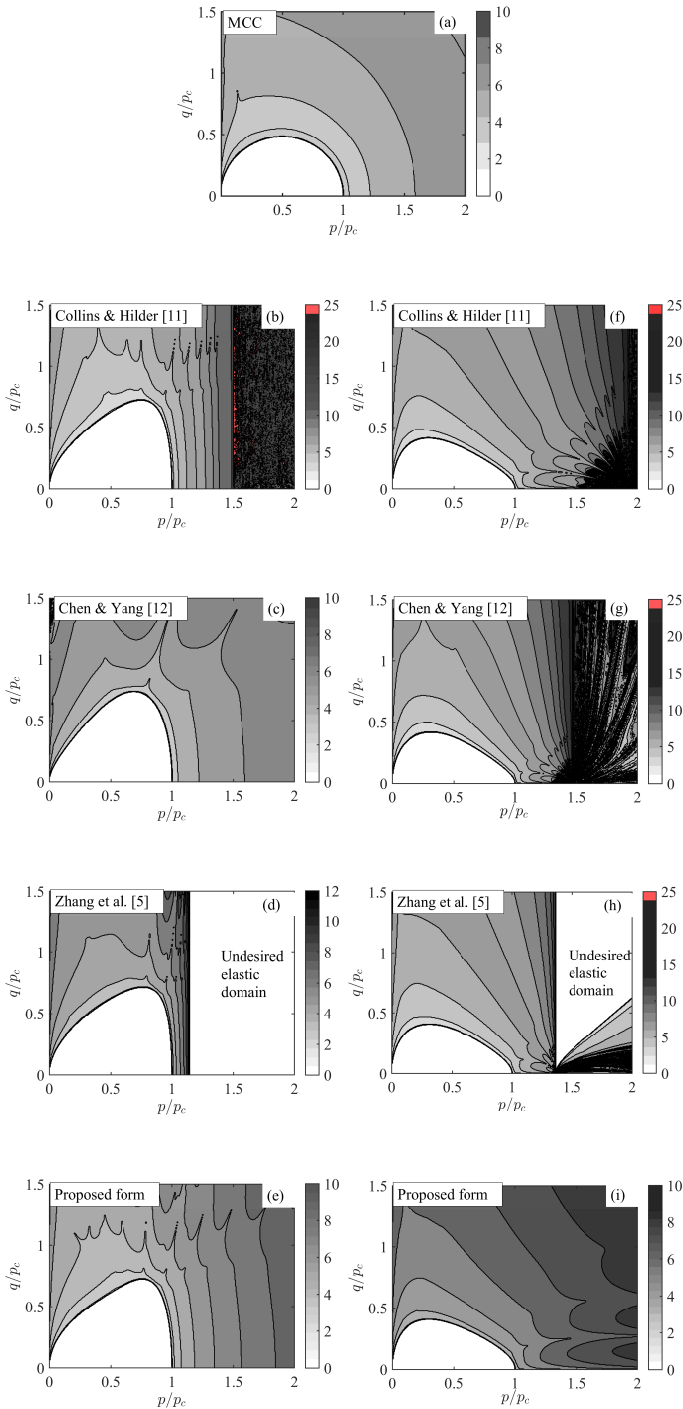
Figure 3.10: Number of iterations in the stress update algorithm for various trial stress locations, for various yield surfaces and non-linear elasticity: (b), (c), (d) and (e), tear-shape type I yield surface; (f), (g), (h) and (i), tear-shape type II yield surface.

Table 3.4: Stress-space iterations for non-linear elasticity: maximum and total number of iterations, number of points that failed to converge (hit the maximum number of iterations), number of elasto-plastic points (trial states outside the yield surface with $y > 0$) and average number of iterations for elasto-plastic points. The maximum number of iterations was set to 25.

Yield surface	Max (NR_{it})	$\sum (NR_{it})$	Number of failed	$y > 0$	Average NR_{it}
MCC	7	553,100	0	105,176	5.26
Yield surface/ tear-shape type I					
Collins & Hilder [11]	25	1,067,544	10,081	99,238	10.76
Chen & Yang [12]	25	525,433	1	99,604	5.28
Zhang et al. [5]	13	239,716	0	47,423	5.06
Proposed form	10	631,188	0	99,290	6.36
Yield surface/ tear-shape type II					
Collins & Hilder [11]	25	816,518	157	108,545	7.52
Chen & Yang [12]	25	802,520	319	108,532	7.39
Zhang et al. [5]	25	491,685	557	79,060	6.22
Proposed form	9	667,343	0	108,438	6.15

3.5.2. ITERATION-STRESS MAPS FOR LINEAR ELASTICITY

Here, the previous analysis is repeated but with a linear elastic formulation (that allows negative p values for trial states to be explored). The Cauchy stress is obtained from

$$\boldsymbol{\sigma} = \mathbf{D}^e \boldsymbol{\varepsilon}^e \quad \text{where} \quad \mathbf{D}^e = \left(\frac{p_r}{\kappa} - \frac{2G}{3} \right) (\mathbf{1} \otimes \mathbf{1}) + 2G\mathbf{I} \tag{3.34}$$

and $\mathbf{I}$ is the forth-order identity tensor. The following region of p-q stress space was explored

$$\frac{p^{trial}}{p_c} \in [-1, 2] \quad \text{and} \quad \frac{q^{trial}}{p_c} \in [0, 1.5] \tag{3.35}$$

with a total of 180,900 equally distributed trial states. The strain increment to cause these elastic trial states (starting from $(p, q) = (p_c/2, 0)$) was determined and applied in a single step. The number of iterations for each of the trial states is shown in Figure 3.11, for the MCC model and for the four other yield surfaces for the two different tear-shape surfaces (with the same shape parameters as analysed for the return mapping using non-linear elasticity).

Table 3.5 gives the corresponding results of Table 3.4, including the maximum and total number of iterations, the number of points that failed to converge, the number of elasto-plastic trial states, and the average number of iterations for elasto-plastic stress updates, for the five yield equations and linear elasticity. Only those models using MCC and the yield function proposed in this chapter converged for all the trial stresses. Note that the model utilising the proposed yield equation only required, on average, 1 additional iteration compared to the MCC model.

TEAR-SHAPE TYPE I YIELD SURFACE ANALYSIS

It can been seen from Figure 3.11b that the yield equation of Collins & Hilder [11] failed to converge for some trial states at $p/p_c < -0.5$, and for all trial stresses at $p/p_c > 1.5$ (a total

Table 3.5: Stress-space iterations for linear elasticity: maximum and total number of iterations, number of points that failed to converge (hit the maximum number of iterations), number of elasto-plastic points (trial states outside the yield surface with $y > 0$) and average number of iterations for elasto-plastic points. The maximum number of iterations was set to 25.

Yield surface	Max (NR_{it})	$\sum (NR_{it})$	Number of failed	$y > 0$	Average NR_{it}
MCC	8	929,318	0	165,676	5.51
Yield surface/ tear-shape type I					
Collins & Hilder [11]	25	1,631,974	33,792	159,738	10.22
Chen & Yan [12]	25	1,075,455	330	160,104	6.72
Zhang et al. [5]	25	597,369	542	107,923	5.54
Proposed form	9	954,118	0	159,790	5.97
Yield surface/ tear-shape type II					
Collins & Hilder [11]	25	1,400,135	14,249	169,044	8.28
Chen & Yang [12]	25	1,224,038	1,004	169,039	7.24
Zhang et al. [5]	25	917,895	2,244	135,646	6.77
Proposed form	9	1,085,935	0	168,937	6.43

number of 33,792 points shown by the red region). Although the model of Chen & Yang [12] performed relatively well using non-linear elasticity (Figure 3.10d), the model using linear elasticity struggled to converge for trial states at $p/p_c < -0.5$ and failed to converge for 330 trial stresses. The model of Zhang et al. [5] contains a spurious $y < 0$ region when $p/p_c > 1.5$, as indicated in Figure 3.11f. Although the yield equation of Zhang et al. [5] has the lowest number of total iterations, this is a spurious result because the yield equation incorrectly predicts that a number of trial states are in a (false) elastic region of stress space (this point is explained in more detail below). In addition, for some trial stresses at $-1.00 \leq p/p_c \leq -0.75$ (542 points) the model was not able to converge.

Figure 3.12a shows the distribution of the number of iterations within the stress update algorithm for the MCC model and for the four other models of tear-shape type I, in terms of the proportion of the total number of trial stress states. For example, for the MCC model around 37% of the trial states require 6 iterations to converge. Figure 3.12b shows the normalised cumulative distribution, which indicates the total proportion of trial states equal to or below the given number of iterations for each of the models. It is clear from the cumulative distribution (Figure 3.12b) that the Zhang et al. [5] model spuriously predicts around 40% of the trial states as being within the yield surface, even though the actual percentage is around 12%, due to an additional region where $y < 0$ for normalised pressures above $p/p_c \approx 1.1$, as shown in Figure 3.12d. It is also clear from Figure 3.12b that around 20% of the trial states struggle to converge for the Collins & Hilder [11] model, as demonstrated by the step in the cumulative distribution curve for this model when the number of iterations equals 25. Comparing the Chen & Yang [12] model with that proposed in this chapter (Figure 3.12b), the proposed formulation has a shorter tail, with 99% of states converging within 9 iterations, whereas the Chen & Yang [12] model requires 18 iterations before 99% of the states have converged and only 88% have converged within 9 iterations.

TEAR-SHAPE TYPE II YIELD SURFACE ANALYSIS

14,249 trial stresses at $-1.00 \le p/p_c \le -0.75$ failed to converge for the yield equation of Collins & Hilder [11] (shown in red in Figure 3.11c) and, consequently, this increased the average number of iterations to 8.28. The model of Chen & Yang [12] faced difficulties in converging with trial stresses at $p/p_c > 1.5$ and $p/p_c < -1.0$ (Figure 3.11e), resulting in 1,004 non-converged stresses. For the studied stress space, two undesired elastic regions were identified for the model of Zhang et al. [5], where trial stresses were not returned back on to the yield surface (Figure 3.12d). This is also demonstrated in Figure 3.12d where 25% of trial stresses were identified to remain in the elastic domain, while the MCC model showed approximately 8.5% of trial stresses were located inside the yield surface. Moreover, 2,244 trial stresses were not returned back on to the yield surface. The proposed yield surface only required 8 iterations to converge for more than 96% of all the trial stresses (Figure 3.12d) and 9 iterations for all of the trial states to converge.

3.5.3. ITERATION-STRESS MAPS FOR THE PROPOSED YIELD SURFACE AT SHEARED/DISTORTED STATES

In Sections 3.5.1 and 3.5.2, the analysis of returned mapping stresses were limited to isotropic yield surfaces where $\beta = 0$. Here, to further demonstrate the robustness of the proposed yield surface for implicit stress integration algorithms, the convergence of trial stresses when the yield surface is sheared at $\beta = 0.0$, $\beta = 0.1$, $\beta = 0.3$, $\beta = 0.5$ and $\beta = 0.7$ for two types of tear-shape yield surface are investigated. The same material properties as reported in Table 3.2 and non-linear elasticity are used. The iteration-stress maps are shown in Figure 3.13. The shape parameters for the tear-shape type I yield surface analysed in Figure 3.13a to Figure 3.13i are $\alpha = \gamma = 0.5$, and for the tear-shape type II yield surface in Figure 3.13b to Figure 3.13j they are $\alpha = \gamma = -0.5$. Detailed analysis, including the distribution and normalised cumulative distribution of the number of iterations are presented in Figure 3.14 for both types of tear-shape yield surface.

For both types of tear-shape yield surface sheared at various β values, all the trial stresses were converged with a maximum of 8 iterations; the only exception was for the tear-shape type II yield surface with $\beta = 0$, where 9 iterations were needed to return less than 3% of trial stresses back on to the yield surface (Figure 3.14d). Moreover, most of the trial stresses were mapped on to the yield surface in 6 iterations for both types of tear-shape surface. Note that the number of elasto-plastic points reduced as β increased. This is because the yield surface bounds a larger portion of the stress space as it shears-off the p-axis.

In conclusion, while other flexible yield surfaces studied in this work have either singularities which result in difficulties in returning trial stresses back on to the yield surface, or have false elastic nuclei, the proposed yield surface is unique, without any singularities, and is demonstrated to be robust for implicit stress integration algorithms for different types of tear-shapes and levels of shearing/distortion.

Figure 3.11: Number of iterations in the stress update algorithm for various trial stress locations, for various yield surfaces and linear elasticity: (b), (c), (d) and (e), tear-shape type I yield surface; (f), (g), (h) and (i), tear-shape type II yield surface.

(a)

(b)

(c)

(d)
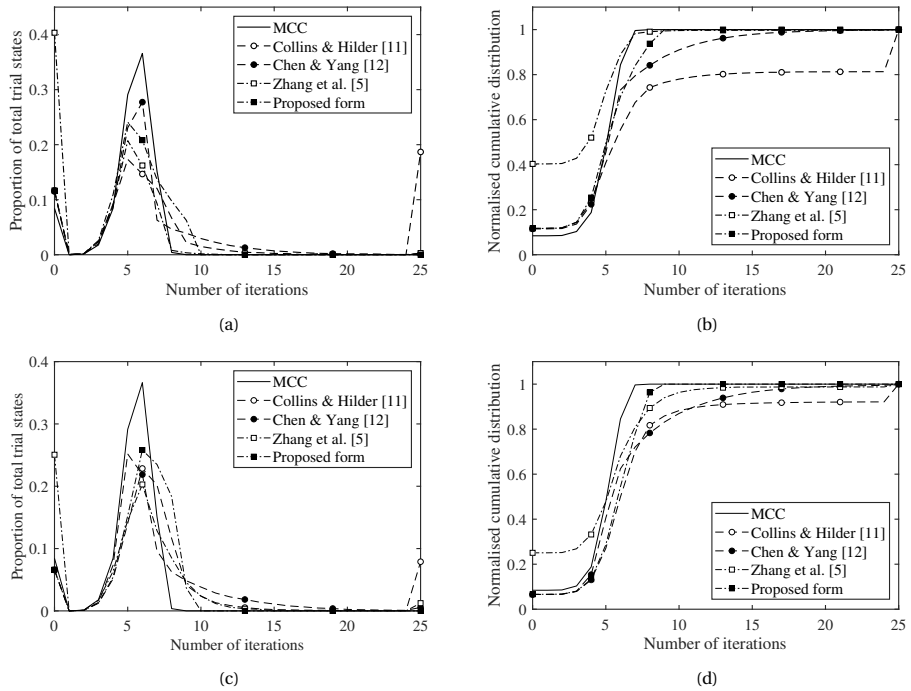
Figure 3.12: Distribution of number of iterations for linear elasticity in terms of the proportion of the total trial states for a given number of iterations and normalised cumulative distribution for: (a) and (b), tear-shape type I yield surface; (c) and (d), tear-shape type II yield surface.
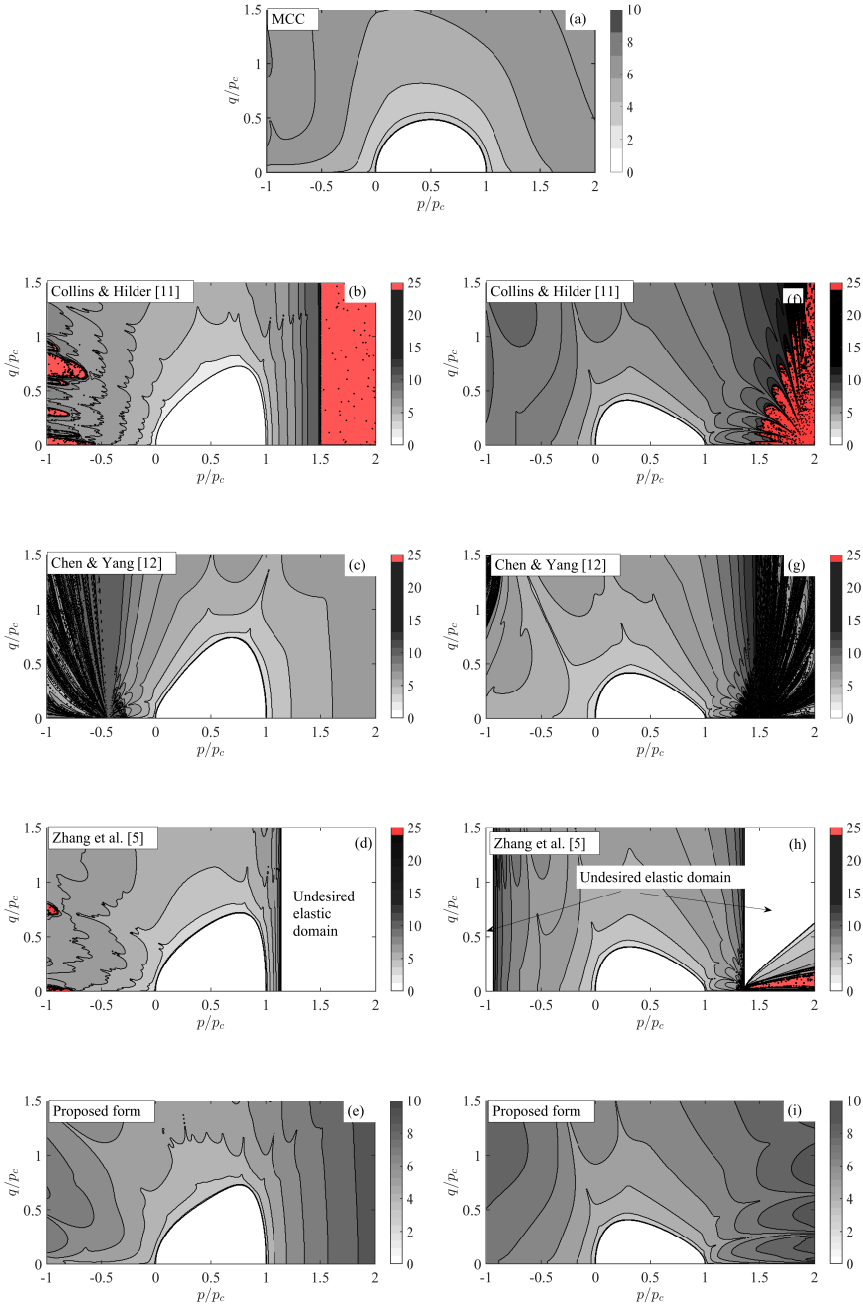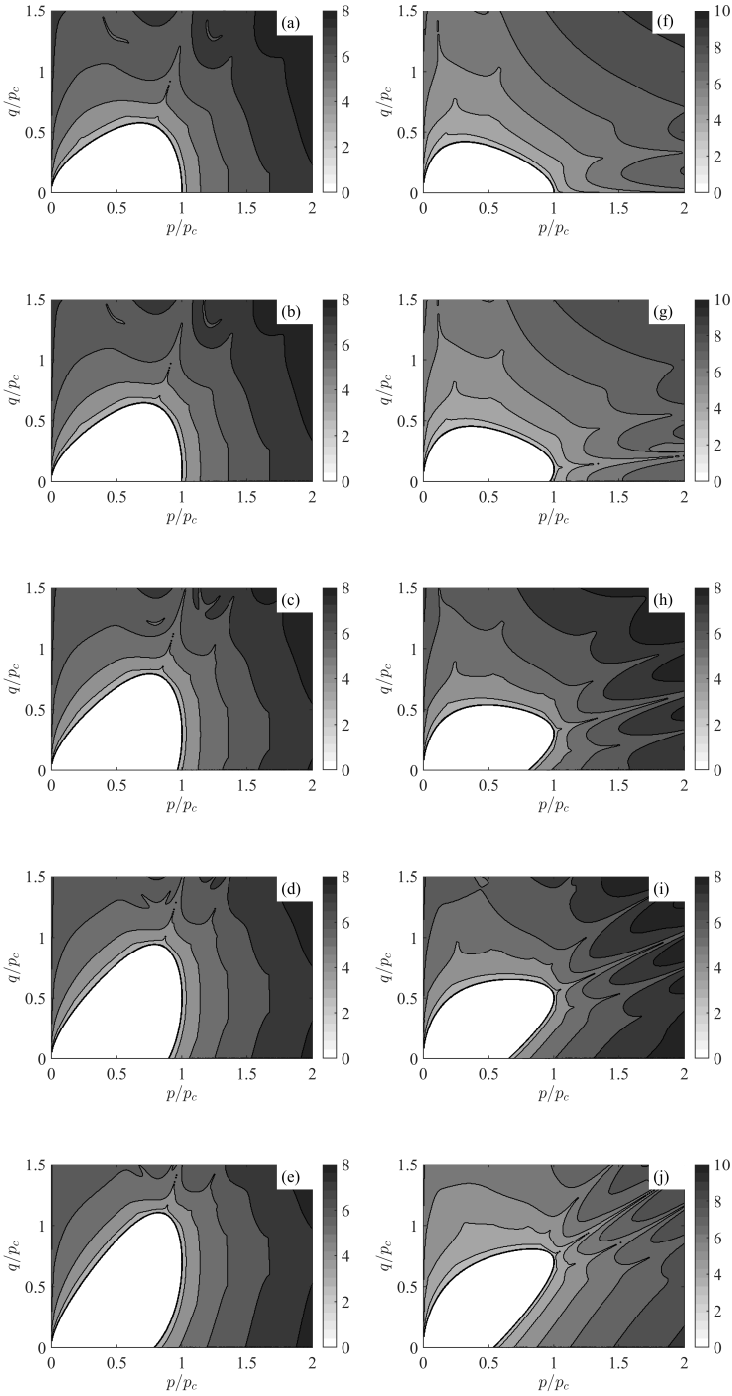
Figure 3.13: Number of iterations in the stress update algorithm for various trial stress locations, using linear elasticity and for two types of tear-shape yield surfaces ((a)-(e), type I; (f)-(j), type II) using the proposed yield equation, sheared at: (a),(f) $\beta = 0.0$; (b),(g) $\beta = 0.1$; (c),(h) $\beta = 0.3$; (d),(i) $\beta = 0.5$; (e),(j) $\beta = 0.7$.
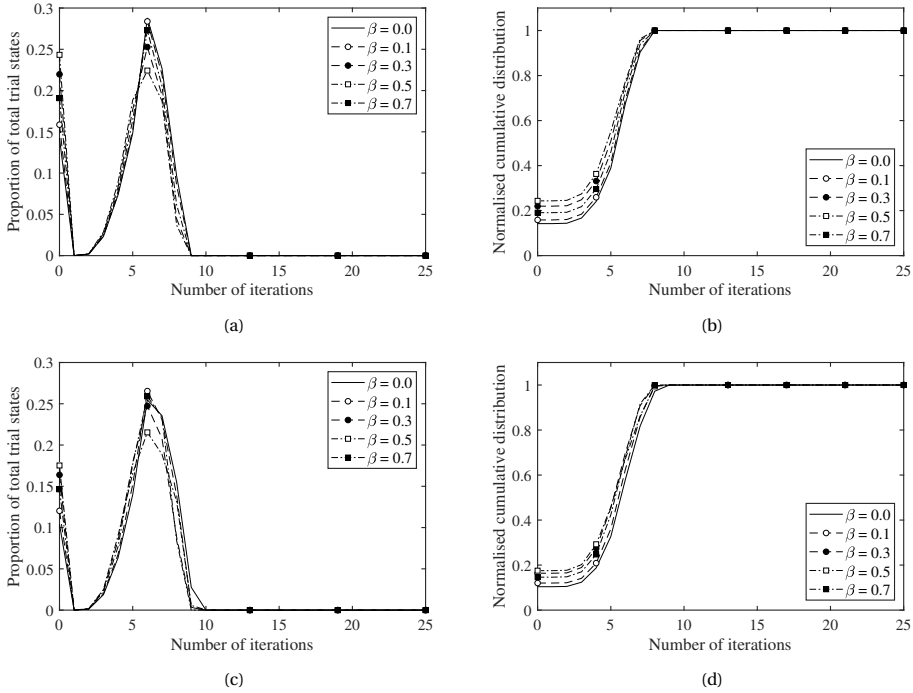
Figure 3.14: Distribution of number of iterations for linear elasticity in terms of the proportion of the total trial states for a given number of iterations and normalised cumulative distribution for: (a) and (b), tear-shape type I yield surface; (c) and (d), tear-shape type II yield surface, sheared at $\beta = 0.0$, $\beta = 0.1$, $\beta = 0.3$, $\beta = 0.5$, and $\beta = 0.7$.

3.6. COMPARISON WITH EXPERIMENTAL DATA

The applicability of the proposed yield surface to resemble the yield stress points of a wide range of geomaterials, including clays, sands, carbonate sand, sandstones and gravel, are investigated here. The calibrated parameters for examples of each geomaterial are presented in Table 3.6.

The yield stresses of two clays, namely Boom Clay [28] and Bothkennar Clay [29], along with the calibrated yield surfaces, are presented in Figure 3.15a and Figure 3.15b, respectively. The natural Boom Clay samples were initially compressed isotropically to 9 MPa, followed by isotropic unloading to form samples with a wide range of over-consolidation ratios. Then, the samples were sheared under drained triaxial stress paths. The yield stresses were calculated as the intersection of bilinear tangents to the ε_v-ln$p$ curves. For Bothkennar Clay [29], undisturbed samples were consolidated under K_0 conditions to resemble in-situ stress states, and then unloaded along the same stress path to form over-consolidated states. Triaxial drained probing tests were then performed and the yield stresses were calculated as the intersection of bilinear tangents of the p-ε_v and q-ε_s curves. It can be seen that the proposed non-elliptical yield surfaces successfully capture the yield stresses of both Boom Clay and Bothkennar Clay, which have respec-

Table 3.6: Calibrated yield surface parameters for the selected sets of experimental data.

Parameters	α	γ	β	M_c/M_e	p_c	p_t
Boom Clay [28]	1.8	-1.7	0	0.87/N.A.	9 (MPa)	0 (MPa)
Bothkennar Clay [29]	0	-0.2	0.5	1.3/1.3	51 (kPa)	0 (kPa)
Decomposed granite sand [30]	0.35	-0.1	0	0.68/N.A.	600 (kPa)	0 (kPa)
Aio Sand [31]	1	-0.7	0.5	1.015/1.015	1065 (kPa)	0 (kPa)
Carbonate sand [32]	0.8	-0.53	0	0.9/N.A.	1	0
Rothbach Sandstone [33; 34]	1	-0.65	0	1.25/N.A.	250 (MPa)	7 (MPa)
Darley Sandstone [33; 34]	0.95	-0.4	0	1.53/N.A.	380 (MPa)	5 (MPa)
Pancrudo Slate gravel [35]	0.45	1.8	0	2.00/N.A.	1	0

Note: N.A. stands for not applicable

tively been isotropically and anisotropically loaded.

In Figure 3.15c, fully-saturated sand samples collected from a decomposed granite deposit were isotropically consolidated to 600 kPa and then unloaded isotropically to attain different over-consolidated stress states [30]. Then, the samples were subjected to drained triaxial shear stress paths and the yield stresses were measured by an acoustic emission technique. In this approach, the onset of plastic deformation, i.e. the yield stress, was detected from the sounds produced by the sliding of grains during shearing. The calibrated yield surface fits the experimental data with a good accuracy.

Fully-saturated dense Aio Sand [31] samples (Figure 3.15d) were loaded and unloaded anisotropically, and then subjected to several drained triaxial stress paths to determine the yield stress points. The yield stresses form a non-symmetric and non-elliptical shape which the proposed yield surface captures accurately with the calibrated parameters.

Many offshore-related structures are constructed on carbonate sands. These geo-materials exhibit distinctive behaviour, as they have a similar volumetric behaviour to fine-grained soils (e.g. clay) while their shear behaviour follows that of sands [36]. This feature is mainly due to carbonate sands being formed from the skeletal remains of marine organisms. The yield stress points and the calibrated yield surface are presented in Figure 3.15e, which shows the capability of the proposed yield surface to bound the non-elliptical shape of the experimental data.

The effectiveness of the proposed yield surface to represent the onset of shear compaction of sandstones is demonstrated for Rothbach Sandstone and Darley Dale Sandstone [33; 34] in Figure 3.15f and Figure 3.15g, respectively. The experimental data form non-elliptical envelopes that indicate the initiation of compaction during shearing. These envelopes are well presented by the calibrated yield surface. It should be noted that tensile pressures have been accounted for in simulating the yield surfaces.

Alonso et al. [35] determined the yield loci of Panncrudo Slate gravel by performing a single multistage triaxial test. The yield locus in normalised stress space is presented in Figure 3.15h. The yield stress points form a non-elliptical yield surface, for which the proposed yield function captures its curvature by its calibrated parameters.

3
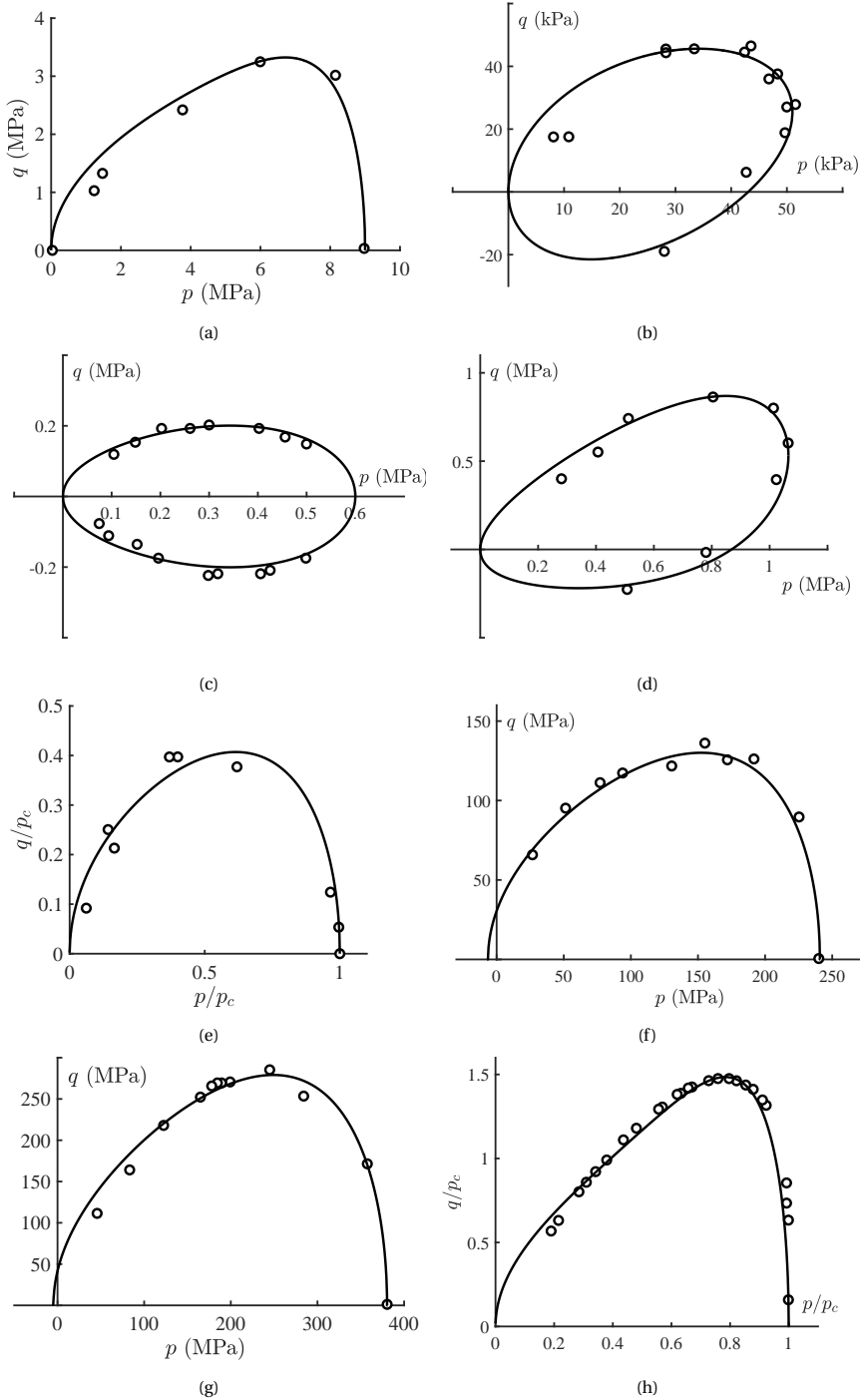
Figure 3.15: Comparison of the yield surface with experimental yielding stresses for: (a) Boom clay [28]; (b) Bothkennar clay [29]; (c) decompose granite sand [30]; (d) Aio sand [31]; (e) carbonate sand [32]; data taken from [36]; (f) Rothbach sandstone [33; 34]; (g) Darley Dale sandstone [33; 34]; (h) Pancrudo slate gravel [35].

3.7. Discussion on the potential loss of simple convexity at higher level sets

The uniqueness of the proposed yield function has been proven and demonstrated in Sections 3.4 and 3.5. By referring to level set contours, for example in Figure 3.8c, one may argue that for non-zero value shape parameters, the convexity of the yield function may be lost as the level sets increase; i.e., although the yield surface is (simply) convex, an increase of the curvature of the yield surface at a higher level set may result in non-convexity (so that the yield function cannot be considered to be fully convex). For example, the range of shape parameters resulting in convex surfaces at level set $k = 30$ is shown in Figure 3.16, where, compared to Figure 3.6 for $k = 0$, a narrower range is indicated.

3
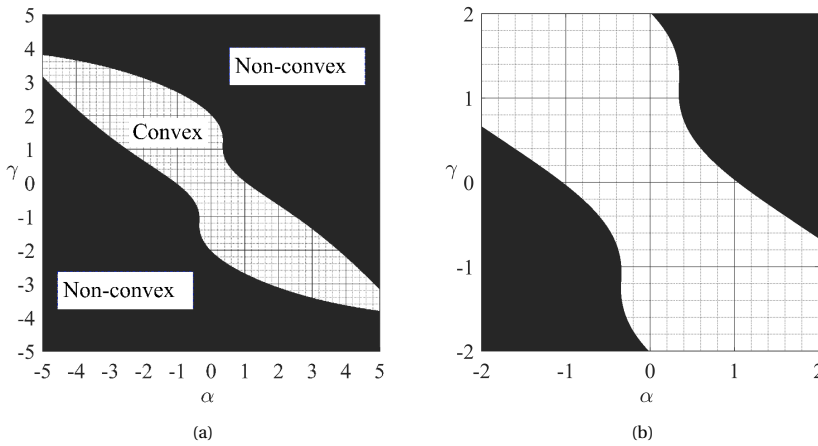
Figure 3.16: Ranges of combined α and γ resulting in convex and non-convex surfaces ($k = 30$) for: (a) $-5 \leq \alpha$, $\gamma \leq 5$; (b) $-2 \leq \alpha$, $\gamma \leq 2$

The loss of convexity does not affect the ability of the return mapping algorithm for the proposed yield function. In fact, it is still robust and is generally efficient, although the level of efficiency is likely to be reduced. Here, to demonstrate the robustness of the yield function for an implicit stress integration approach, a return mapping analysis for large strain increments is investigated.

For the simulations, the material parameters $G = 55$ (MPa), $\lambda = 0.05$, $\kappa = 0.01$, and shape parameters $\alpha = \gamma = 0.5$ were used, and p_c and β were respectively set to 200 kPa and 0.5. A linear elasticity and associated plastic flow constitutive behaviour, similar to Section 3.5.2, were considered. Starting from an isotropic stress state at the reference pressure, $(p, q) = (p_r, 0)$, the model was subjected to trial stresses (in a single step) which were related to the hydrostatic extent of the yield surface, p_c, such that a large region $p^{trial}/p_c \in [0, 5]$ and $q^{trial}/p_c \in [0, 5]$ in the stress space (p-q) was explored (with p^{trial} and q^{trial} being as large as 1000 kPa).

The level sets of the yield surface up to 1000, in the studied stress space, are shown

in Figure 3.17a and the map of the number of iterations to return the trial stresses back on to the yield surface is presented in Figure 3.17b. It is obvious that for the considered shape parameters ($\alpha = \gamma = 0.5$), as the level sets of the yield function increase, they become more non-convex. However, as can be seen in Figure 3.17b, even for large trial stresses that sit on such non-convex level sets, they are returned back on to the yield surface with an increased number of iterations (although all trial stresses are converged within a maximum of 13 iterations).

(a)   (b)
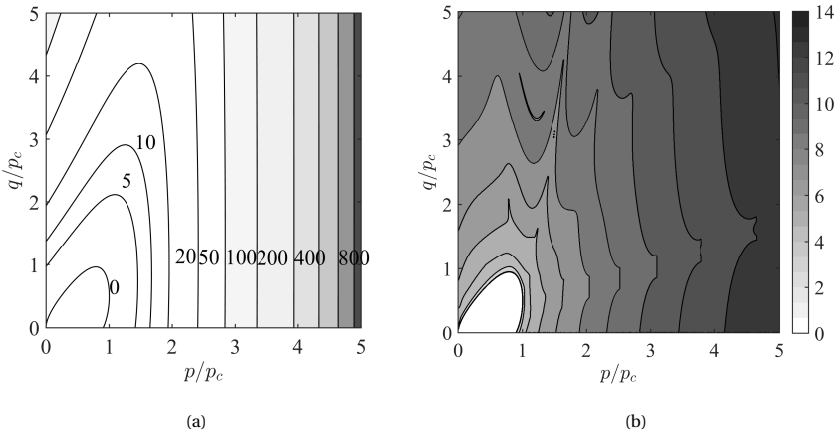
Figure 3.17: (a) Level sets; (b) number of iterations in the stress update algorithm for various trial stress locations, using linear elasticity with the proposed yield function ($\alpha = \gamma = \beta = 0.5$) in normalised stress space.

The implicit stress integration is an iterative procedure in which, in each iteration, the updated stress converges toward the solution that satisfies the CPP energy equation by using the gradients of the yield surface at that stress value. This means that, in each iteration, the updated stress sits on a lower level set with a lower curvature intensity, and eventually returns back onto the yield function with a level set of zero. Because the intensity level of the curvature of the yield surface reduces iteratively, convexity is retrieved as the level sets reduce. Therefore, the iteration solution of the implicit stress integration algorithm ensures the correct returning path of the updated stress onto the yield surface. Thus, the proposed yield function, while not being fully convex (with respect to non-zero level sets), facilitates reliable return mapping paths for the trial stress.

3.8. CONCLUSION

A new yield function is proposed for geomaterials which is non-singular and uniquely defined in meridian stress space, and is therefore suitable and robust for implicit stress integration algorithms. The components and possible roots of the general yield function in meridian stress space were analysed in depth, and geometrical constraints are designed in such a way that the yield function preserves its uniqueness and non-singularity at any level set (value). Compared with other yield surfaces studied here, the proposed form of the yield function presented in this chapter is robust and efficient for return

mapping for large strain increments. It does not have undesired elastic domains, and therefore avoids the possible prediction of spurious false elastic behaviour or domains with erratic and divergent gradients, which could have resulted in a high number of iterations required to return stress states back onto the yield surface. Moreover, the yield function can attain elliptical and a wide range of non-elliptical shapes compatible with the experimental data of geomaterials available in literature.

REFERENCES

[1] Anandarajah, A. *Computational methods in elasticity and plasticity*. Springer New York, 2010.

[2] Simo, J. C. and Hughes, T. J. R. *Computational inelasticity*. Springer-Verlag, New York, 1998.

[3] Borja, R. I. *Plasticity, modeling and computation*. Springer, Berlin, Heidelberg, 2013.

[4] Brannon, R. M. and Leelavanichkul, S. A multi-stage return algorithm for solving the classical damage component of constitutive models for rocks, ceramics, and other rock-like media. *International Journal of Fracture*, 163:133–149, 2010.

[5] Zhang, Z., Chen, Y. and Huang, Z. A novel constitutive model for geomaterials in hyperplasticity. *Computers and Geotechnics*, 98:102–113, 2018.

[6] Sivasithamparam, N. and Castro, J. An anisotropic elastoplastic model for soft clays based on logarithmic contractancy. *International Journal of Numerical and Analytical Methods in Geomechanics*, 40:596–621, 2016.

[7] Mortara, G. A new yield criterion for soils with embedded tension cut-off. *Meccanica*, 54:683–696, 2019.

[8] Ling, H. I., Yue, D., Kaliakin, V. N. and Themelis, N. J. Anisotropic elastoplastic bounding surface model for cohesive soils. *Journal of Engineering Mechanics*, 128:748–758, 2002.

[9] Karrech, A., Regenauer-Lieb, K. and Poulet, T. A damaged visco-plasticity model for pressure and temperature sensitive geomaterial. *International Journal of Engineering Science*, 49:1141–1150, 2011.

[10] Coombs, W. M. Continuously unique anisotropic critical state hyperplasticity. *International Journal of Numerical and Analytical Methods in Geomechanics*, 41:578–601, 2017.

[11] Collins, I. F. and Hilder, T. A theoretical framework for constructing elastic/plastic constitutive models of triaxial tests. *International Journal of Numerical and Analytical Methods in Geomechanics*, 26:1313–1347, 2002.

[12] Chen, Y. N. and Yang, Z. X. A family of improved yield surfaces and their application in modeling of isotropically over-consolidated clays. *Computers and Geotechnics*, 90:133–143, 2017.

[13] Bigoni, D. and Piccolroaz, A. Yield criteria for quasibrittle and frictional materials. *International Journal of Solids and Structures*, 41:2855–2878, 2004.

[14] Mir, A., Nguyen, G. D. and Sheikh, A. A thermodynamics-based model for brittle to ductile behaviour and localised failure of porous rocks. *International Journal of Solids and Structures*, 152:161–184, 2018.

[15] Lagioia, R., Puzrin, A. M. and Potts, D. M. A new versatile expression for yield and plastic potential surfaces. *Computers and Geotechnics*, 19(3):171–191, 1996.

[16] Roscoe, K. H. and Burland, J. B. On the generalized stress strain behaviour of 'wet' clay. In Heyman, J. and Leckie, F. A., editors, *Engineering Plasticity*, pages 535–609. Cambridge University Press, 1968.

[17] Yu, H. S. S. CASM: A unified state parameter model for clay and sand. *International Journal of Numerical and Analytical Methods in Geomechanics*, 22:621–653, 1998.

[18] Coombs, W. M. and Crouch, R. S. Algorithmic issues for three-invariant hyperplastic Critical State models. *Computer Methods in Applied Mechanics and Engineering*, 200:2297–2318, 2011.

[19] Stupkiewicz, S., Denzer, R., Piccolroaz, A. and Bigoni, D. Implicit yield function formulation for granular and rock-like materials. *Computational Mechanics*, 54:1163–1173, 2014.

[20] Panteghini, A. and Lagioia, R. An extended modified Cam-Clay yield surface for arbitrary meridional and deviatoric shapes retaining full convexity and double homothety. *Géotechnique*, 68:590–601, 2018.

[21] Panteghini, A. and Lagioia, R. An approach for providing quasi-convexity to yield functions and a generalized implicit integration scheme for isotropic constitutive models based on 2 unknowns. *International Journal of Numerical and Analytical Methods in Geomechanics*, 42:829–855, 2018.

[22] Golchin, A., Vardon, P. J. and Hicks, M. A. A thermo-mechanical constitutive model for fine-grained soils based on thermodynamics. *International Journal of Engineering Science*, 174:103579, 2022.

[23] Sheng, D., Sloan, S. W. and Yu, H. S. Aspects of finite element implementation of critical state models. *Computers and Geotechnics*, 26:185–196, 2000.

[24] Gudehus, G. Elastoplastische stoffgleichungen fur trockenen sand. *Ingenieur-Archiv*, 42(3):151–169, 1973.

[25] Zienkiewicz, O. C. and Pande, G. N. Some useful forms of isotropic yield surfaces for soil and rock mechanics. In *Gudehus, G. (ed.) Finite Elements in Geomechanics*, pages 179–190, London, 1977. Wiley.

[26] Coombs, W. M., Crouch, R. S. and Augarde, C. E. A unique Critical State two-surface hyperplasticity model for fine-grained particulate media. *Journal of the Mechanics and Physics of Solids*, 61:175–189, 2013.

[27] Ekeland, I. and Témam, R. Convex analysis and variational problems. *Classics in Applied Mathematics*, 1976.

[28] Sultan, N., Cui, Y. J. and Delage, P. Yielding and plastic behaviour of Boom clay. *Géotechnique*, 60:657–666, 2010.

[29] Smith, P. R., Jardine, R. J. and Hight, D. W. The yielding of Bothkennar clay. *Géotechnique.*, 42:257–274, 1992.

[30] Tanimoto, K. and Tanaka, Y. Yielding of soil as determined by acoustic emission. *Soils and Foundations*, 26:69–80, 1986.

[31] Yasufuku, N., Murata, H., and Hyodo, M. Yield characteristics of anisotropically consolidated sand under low and high stresses. *Soils and Foundations*, 31:95–109, 1991.

[32] Huang, J. T. *The effects of density and cementation on cemented sands*. PhD thesis, University of Sydney, 1994.

[33] Baud, P., Klein, E., and Wong, T. F. Compaction localization in porous sandstones: Spatial evolution of damage and acoustic emission activity. *Journal of Structural Geology*, 26:603–624, 2004.

[34] Wong, T. F., Baud P., and Klein, E. Localized failure modes in a compactant porous rock. *Geophysical Research Letters*, 28:2521–2524, 2001.

[35] Alonso, E. E., Romero, E. E. and Ortega, E. Yielding of rockfill in relative humidity-controlled triaxial experiments. *Acta Geotechnica*, 11:455–477, 2016.

[36] Islam, M. K., Carter, J. P. and Airey, D. W. Comparison of the yield locus and stress-dilatancy function of some critical state constitutive models with experimental data for carbonate sand. *Journal of the Institution of Engineers*, 84:267–274, 2004.

3

APPENDIX

3.A. APPENDIX A: UNIQUE CRITICAL STATE

When the yield surface (Eq. (3.12)) is sheared/distorted in the deviatoric direction via parameter β, the position of the CS surface (corresponding to isochoric flow) changes and becomes dependent on the degree of shearing/distortion of the yield surface. With the following general approach, it is possible to obtain conditions where isochoric plastic flow remains constant throughout the shearing/distortion process, which hereby is referred to as the "*unique Critical State*".

For such conditions, it is required that at any level of shearing/distortion, p_{cs}/p_c remains constant and $q_{cs}/p_{cs} = M\zeta(\theta)$ holds valid, where p_{cs} and q_{sc} are the hydrostatic pressure and deviatoric stress at CS conditions, respectively. The plastic flows along the p-axis (r_p) and q-axis (r_q) are derived as

$$r_p = \frac{\partial g}{\partial p}; \quad r_q = \frac{\partial g}{\partial q} \tag{3.A.1}$$

where g is the plastic flow potential. Assuming that g has a similar formulation to Eq. (3.12) with stress-like functions (A, B and C) defined via Eqs. (3.17)-(3.19), equating r_p to zero ($r_p = 0$), which resembles the CS conditions (zero plastic volumetric strain increments), results in function B being defined by functions A and C and the variable β

$$B_g^2 = B_g\left(A, C, \beta\right) \tag{3.A.2}$$

where B_g represents the function B obtained from criteria applied to the plastic potential, g.

By using Eq. (3.12), it is possible to obtain an alternative form for function B

$$B_y^2 = \frac{A^2 \left(q - \beta p\right)^2}{\left(A - C + p\right)\left(A + C - p\right)} \tag{3.A.3}$$

where B_y represents the function B obtained from the yield surface, y.

Note that functions A and C are defined by the shape parameter γ (as well as by p and p_c) (Eqs. (3.17) and (3.19), respectively) while function B is defined by α and γ (Eq. (3.18)). Equating B_g to B_y eliminates parameter α and results in an equation that can be solved to obtain parameter γ with respect to p_{cs}, p_c and β.

Once γ is obtained from the above procedure, α can be determined via Eq. (3.A.2).

3.B. APPENDIX B: NUMERICAL IMPLEMENTATION

Here, a fully implicit backward Euler stress integration scheme is provided for the constitutive relationships presented in Section 3.5. Constitutive variables defined at time t

and $t + \Delta t$ are indicated, respectively, by n and $n+1$. Formulations presented here are in accordance with geotechnical conventions, where compressive stresses and contractive strains are considered to be positive and all the stresses are effective. Scalars and tensors are denoted with italic and bold letters, respectively. The notations $(\bullet : \bullet)$ and $(\bullet \otimes \bullet)$, respectively, demonstrate the double contraction and tensor product, and $\|\bullet\|$ and $tr(\bullet)$ represent the absolute value and trace functions, respectively.

The implicit integration of Eq. (3.31) results in

$$p_c^{n+1} = p_c^n \exp\left(\frac{\Delta\varepsilon_{kk}^p}{\lambda - \kappa}\right) \tag{3.B.1}$$

where $\Delta\varepsilon_{kk}^p$ is the plastic volumetric strain increment, determined as

$$\Delta\varepsilon_{kk}^p = \Delta\Lambda\, tr(\mathbf{r}) = \Delta\Lambda r_p \tag{3.B.2}$$

$\Delta\Lambda$ is the plastic multiplier increment and $\mathbf{r}$ is the plastic flow direction tensor, which for an associated flow rule is the derivative of the yield surface with respect to the stress tensor

$$\mathbf{r} = \frac{\partial y}{\partial\boldsymbol{\sigma}} \tag{3.B.3}$$

Three residual equations, corresponding to the state variable (here it is the strain tensor, ε), hardening variable (here it is the pre-consolidation pressure, p_c) and consistency condition, are defined as

$$\boldsymbol{\Pi}_1 = \boldsymbol{\varepsilon}_{n+1}^e - \boldsymbol{\varepsilon}^{e,trial} + \Delta\Lambda\mathbf{r} \tag{3.B.4}$$

$$\Pi_2 = \frac{p_c^{n+1}}{p_c^n} - \exp\left(\frac{\Delta\varepsilon_{kk}^p}{\lambda - \kappa}\right) \tag{3.B.5}$$

$$\Pi_3 = y \tag{3.B.6}$$

where $\boldsymbol{\varepsilon}^{e,trial}$ is the trial strain tensor, defined as

$$\boldsymbol{\varepsilon}^{e,trial} = \boldsymbol{\varepsilon}_n^e + \Delta\boldsymbol{\varepsilon} \tag{3.B.7}$$

where $\Delta\boldsymbol{\varepsilon}$ is the strain increment tensor.

These residual equations are explicitly functions of p_c and $\Delta\Lambda$, and implicitly of $\boldsymbol{\sigma}$ (stress tensor). In the implicit stress integration scheme, these residual equations are minimised via a linearisation technique; that is, the Taylor expansion of the residual equations with respect to unknown variables at time $t + \Delta t$ ($\boldsymbol{\sigma}$, p_c and $\Delta\Lambda$)

$$\begin{aligned}
\boldsymbol{\Pi}_1 + \frac{\partial\boldsymbol{\Pi}_1}{\partial\boldsymbol{\sigma}_{n+1}}\delta\boldsymbol{\sigma} + \frac{\partial\boldsymbol{\Pi}_1}{\partial p_c^{n+1}}\delta p_c + \frac{\partial\boldsymbol{\Pi}_1}{\partial\Delta\Lambda}\delta\Lambda &= 0 \\
\Pi_2 + \frac{\partial\Pi_2}{\partial\boldsymbol{\sigma}_{n+1}}\delta\boldsymbol{\sigma} + \frac{\partial\Pi_2}{\partial p_c^{n+1}}\delta p_c + \frac{\partial\Pi_2}{\partial\Delta\Lambda}\delta\Lambda &= 0 \\
\Pi_3 + \frac{\partial\Pi_3}{\partial\boldsymbol{\sigma}_{n+1}}\delta\boldsymbol{\sigma} + \frac{\partial\Pi_3}{\partial p_c^{n+1}}\delta p_c + \frac{\partial\Pi_3}{\partial\Delta\Lambda}\delta\Lambda &= 0
\end{aligned} \tag{3.B.8}$$

which can be written in compact form as $\mathbf{J} \cdot \boldsymbol{v} = \boldsymbol{\Pi}$, where $\mathbf{J}$, $\boldsymbol{v}$ and $\boldsymbol{\Pi}$ are, respectively, the Jacobian matrix, and the increments of the unknown and residual vectors, defined as

$$\mathbf{J} = \begin{bmatrix} \dfrac{\partial \boldsymbol{\Pi}_1}{\partial \boldsymbol{\sigma}_{n+1}} & \dfrac{\partial \boldsymbol{\Pi}_1}{\partial p_c^{n+1}} & \dfrac{\partial \boldsymbol{\Pi}_1}{\partial \Delta\Lambda} \\[2mm] \dfrac{\partial \Pi_2}{\partial \boldsymbol{\sigma}_{n+1}} & \dfrac{\partial \Pi_2}{\partial p_c^{n+1}} & \dfrac{\partial \Pi_2}{\partial \Delta\Lambda} \\[2mm] \dfrac{\partial \Pi_3}{\partial \boldsymbol{\sigma}_{n+1}} & \dfrac{\partial \Pi_3}{\partial p_c^{n+1}} & \dfrac{\partial \Pi_3}{\partial \Delta\Lambda} \end{bmatrix} \tag{3.B.9}$$

$$\boldsymbol{v} = \left\{ \begin{array}{ccc} \delta\boldsymbol{\sigma}_{n+1} & \delta p_c^{n+1} & \delta\Delta\Lambda \end{array} \right\}^{\mathrm{T}} \tag{3.B.10}$$

$$\boldsymbol{\Pi} = -\left\{ \begin{array}{ccc} \boldsymbol{\Pi}_1 & \Pi_2 & \Pi_3 \end{array} \right\}^{\mathrm{T}} \tag{3.B.11}$$

The unknown increments at each iteration are solved as

$$\boldsymbol{v} = \mathbf{J}^{-1} \cdot \boldsymbol{\Pi} \tag{3.B.12}$$

and are added to the previous increment values. The iteration procedure continues until the residual values are within an acceptable tolerance range. The components of the Jacobian matrix are

$$\frac{\partial \boldsymbol{\Pi}_1}{\partial \boldsymbol{\sigma}_{n+1}} = \frac{\partial \varepsilon_{n+1}^e}{\partial \boldsymbol{\sigma}_{n+1}} + \Delta\Lambda \frac{\partial \mathbf{r}}{\partial \boldsymbol{\sigma}_{n+1}} \tag{3.B.13}$$

$$\frac{\partial \boldsymbol{\Pi}_1}{\partial p_c^{n+1}} = \Delta\Lambda \frac{\partial \mathbf{r}}{\partial p_c^{n+1}} \tag{3.B.14}$$

$$\frac{\partial \boldsymbol{\Pi}_1}{\partial \Delta\Lambda} = \mathbf{r} \tag{3.B.15}$$

$$\frac{\partial \Pi_2}{\partial \boldsymbol{\sigma}_{n+1}} = -\frac{\Delta\Lambda}{\lambda - \kappa} \frac{\partial r_p}{\partial \boldsymbol{\sigma}_{n+1}} \exp\left(\frac{\Delta\varepsilon_{kk}^p}{\lambda - \kappa}\right) \tag{3.B.16}$$

$$\frac{\partial \Pi_2}{\partial p_c^{n+1}} = \frac{1}{p_c^n} - \frac{\Delta\Lambda}{\lambda - \kappa} \frac{\partial r_p}{\partial p_c^{n+1}} \exp\left(\frac{\Delta\varepsilon_{kk}^p}{\lambda - \kappa}\right) \tag{3.B.17}$$

$$\frac{\partial \Pi_2}{\partial \Delta\Lambda} - \frac{r_p}{\lambda - \kappa} \exp\left(\frac{\Delta\varepsilon_{kk}^p}{\lambda - \kappa}\right) \tag{3.B.18}$$

$$\frac{\partial \Pi_3}{\partial \boldsymbol{\sigma}_{n+1}} = \frac{\partial y}{\partial \boldsymbol{\sigma}_{n+1}} \tag{3.B.19}$$

$$\frac{\partial \Pi_3}{\partial p_c^{n+1}} = \frac{\partial y}{\partial p_c} \tag{3.B.20}$$

$$\frac{\partial \Pi_3}{\partial \Delta \Lambda} = 0 \tag{3.B.21}$$

$$\frac{\partial \varepsilon_{n+1}^e}{\partial \sigma_{n+1}} = \mathbf{c} \tag{3.B.22}$$

where **c** is the fourth-order elastic compliance tensor, and is the inverse of the elastic stiffness tensor for non-linear and linear elastic constitutive relations.

Considering an associated flow rule (Eq. (3.B.3)), the first and second derivatives of the yield function are required to obtain Eq. (3.B.13) to Eq. (3.B.20).
The derivative of the yield surface with respect to p_c is

$$\frac{\partial y}{\partial p_c} = \frac{\partial y}{\partial A}\frac{\partial A}{\partial p_c} + \frac{\partial y}{\partial B}\frac{\partial B}{\partial p_c} + \frac{\partial y}{\partial C}\frac{\partial C}{\partial p_c} \tag{3.B.23a}$$

where

$$\frac{\partial y}{\partial A} = -2\frac{(p-C)^2}{A^3} \tag{3.B.23b}$$

$$\frac{\partial y}{\partial B} = -2\frac{(q-\beta p)^2}{B^3} \tag{3.B.23c}$$

$$\frac{\partial y}{\partial C} = -2\frac{(p-C)}{A^2} \tag{3.B.23d}$$

For an associated flow rule

$$\mathbf{r} = \frac{\partial y}{\partial \sigma} = r_p\frac{\partial p}{\partial \sigma} + r_q\frac{\partial q}{\partial \sigma} = \frac{1}{3}r_p\mathbf{1} + \sqrt{\frac{3}{2}}r_q\hat{\mathbf{n}} \tag{3.B.24a}$$

$$r_p = \frac{\partial y}{\partial p} = 2\left(\frac{A^*}{A^3} - \frac{B^*}{B^3}\right) \tag{3.B.24b}$$

$$r_q = \frac{\partial y}{\partial q} = \frac{2(q-\beta p)}{B^2} \tag{3.B.24c}$$

$$\hat{\mathbf{n}} = \frac{\mathbf{s}}{\|\mathbf{s}\|} = \frac{\mathbf{s}}{(\mathbf{s}:\mathbf{s})^{\frac{1}{2}}} = \sqrt{\frac{3}{2}}\frac{\mathbf{s}}{q} \tag{3.B.24d}$$

where

$$A^* = A(p - C) - \frac{\partial A}{\partial p}(p - C)^2 \tag{3.B.24e}$$

$$B^* = \beta B(q - \beta p) + \frac{\partial B}{\partial p}(q - \beta p)^2 \tag{3.B.24f}$$

The derivative of the flow rule with respect to the stress tensor is

$$\frac{\partial \mathbf{r}}{\partial \boldsymbol{\sigma}} = \frac{1}{3}\frac{\partial r_p}{\partial \boldsymbol{\sigma}}\mathbf{1} + \sqrt{\frac{3}{2}}\frac{\partial r_q}{\partial \boldsymbol{\sigma}}\hat{\mathbf{n}} + \sqrt{\frac{3}{2}}r_q\frac{\partial \hat{\mathbf{n}}}{\partial \boldsymbol{\sigma}} \tag{3.B.25a}$$

$$\frac{\partial r_p}{\partial \boldsymbol{\sigma}} = \frac{1}{3}\frac{\partial r_p}{\partial p}\mathbf{1} + \sqrt{\frac{3}{2}}\frac{\partial r_p}{\partial q}\hat{\mathbf{n}} \tag{3.B.25b}$$

$$\frac{\partial r_q}{\partial \boldsymbol{\sigma}} = \frac{1}{3}\frac{\partial r_q}{\partial p}\mathbf{1} + \sqrt{\frac{3}{2}}\frac{\partial r_q}{\partial q}\hat{\mathbf{n}} \tag{3.B.25c}$$

$$\frac{\partial \hat{\mathbf{n}}}{\partial \boldsymbol{\sigma}} = \sqrt{\frac{3}{2}}\frac{1}{q}\left(\mathbf{I} - \frac{1}{3}\mathbf{1} \otimes \mathbf{1} - \hat{\mathbf{n}} \otimes \hat{\mathbf{n}}\right) \tag{3.B.25d}$$

where

$$\frac{\partial r_p}{\partial p} = 2\left(\frac{1}{A^6}\left(\frac{\partial A^*}{\partial p}A^3 - 3A^2\frac{\partial A}{\partial p}A^*\right) - \frac{1}{B^6}\left(\frac{\partial B^*}{\partial p}B^3 - 3B^2\frac{\partial B}{\partial p}B^*\right)\right) \tag{3.B.25e}$$

$$\frac{\partial r_p}{\partial q} = -\frac{2}{B^3}\frac{\partial B^*}{\partial q} \tag{3.B.25f}$$

$$\frac{\partial r_q}{\partial p} = -\frac{2}{B^3}\left(\beta B + 2\frac{\partial B}{\partial p}(q - \beta p)\right) \tag{3.B.25g}$$

$$\frac{\partial r_q}{\partial q} = \frac{2}{B^2} \tag{3.B.25h}$$

$$\frac{\partial A^*}{\partial p} = A - \frac{\partial^2 A}{\partial p^2}(p - C)^2 - \frac{\partial A}{\partial p}(p - C) \tag{3.B.25i}$$

$$\frac{\partial B^*}{\partial p} = -\beta^2 B + \frac{\partial^2 B}{\partial p^2}(q - \beta p)^2 - \beta\frac{\partial B}{\partial p}(q - \beta p) \tag{3.B.25j}$$

$$\frac{\partial B^*}{\partial q} = \beta B + 2\frac{\partial B}{\partial p}\left(q - \beta p\right) \tag{3.B.25k}$$

The derivative of the flow rule with respect to p_c is

$$\frac{\partial \mathbf{r}}{\partial p_c} = \frac{1}{3}\frac{\partial r_p}{\partial p_c}\mathbf{1} + \sqrt{\frac{3}{2}}\frac{\partial r_q}{\partial p_c}\hat{\mathbf{n}} \tag{3.B.26a}$$

$$\frac{\partial r_p}{\partial p_c} = 2\left(\frac{1}{A^6}\left(\frac{\partial A^*}{\partial p_c}A^3 - 3A^2\frac{\partial A}{\partial p_c}A^*\right) - \frac{1}{B^6}\left(\frac{\partial B^*}{\partial p_c}B^3 - 3B^2\frac{\partial B}{\partial p_c}B^*\right)\right) \tag{3.B.26b}$$

$$\frac{\partial r_q}{\partial p_c} = -4\frac{\left(q - \beta p\right)}{B^3}\frac{\partial B}{\partial p_c} \tag{3.B.26c}$$

where

$$\frac{\partial A^*}{\partial p_c} = \frac{\partial A}{\partial p_c}\left(p - C\right) - \frac{\partial C}{\partial p_c}A - \frac{\partial^2 A}{\partial p \partial p_c}\left(p - C\right)^2 + 2\frac{\partial A}{\partial p}\frac{\partial C}{\partial p_c}\left(p - C\right) \tag{3.B.26d}$$

$$\frac{\partial B^*}{\partial p_c} = \beta\frac{\partial B}{\partial p_c}\left(q - \beta p\right) + \frac{\partial^2 B}{\partial p \partial p_c}\left(q - \beta p\right)^2 \tag{3.B.26e}$$

Different constitutive models are distinguished by the first and second derivatives of the stress-like functions. The following are used for the studied yield surfaces

	MCC	Collins & Hilder [11]	Chen & Yang [12]	Zhang et al. [5]
Function A	$\frac{p_c}{2}$	$\left(1 - \gamma\right)p + \gamma\frac{p_c}{2}$	$\frac{p_c}{2}$	$p_c\sqrt{\alpha^2 + \left(1 - 2\alpha\right)\frac{p}{p_c}}$
Function B	$M\frac{p_c}{2}$	$M\left(\left(1 - \alpha\right)p + \alpha\gamma\frac{p_c}{2}\right)$	$M\frac{p_c}{2}\left(\alpha + \gamma\left(1 - \alpha\right)\frac{p}{p_c}\right)$	$Mp_c\sqrt{\alpha^2\left(1 - \gamma\right) + \alpha\gamma\frac{p}{p_c}}$
Function C	$\frac{p_c}{2}$	$\gamma\frac{p_c}{2}$	$\frac{p_c}{2}$	αp_c
$\partial A/\partial p$	0	$1 - \gamma$	0	$\frac{1 - 2\alpha}{2}\frac{p_c}{A}$
$\partial^2 A/\partial p^2$	0	0	0	$-\frac{\left(\partial A/\partial p\right)^2}{A}$
$\partial B/\partial p$	0	$M\left(1 - \alpha\right)$	$M\frac{\gamma\left(1 - \alpha\right)}{2}$	$M^2\frac{\alpha\gamma}{2}\frac{p_c}{B}$
$\partial^2 B/\partial p^2$	0	0	0	$-\frac{\left(\partial B/\partial p\right)^2}{B}$
$\partial A/\partial p_c$	$\frac{1}{2}$	$\frac{\gamma}{2}$	$\frac{1}{2}$	$\frac{A}{p_c} - \left(1 - 2\alpha\right)\frac{p}{p_c}$
$\partial^2 A/\partial p \partial p_c$	0	0	0	$\frac{\partial A/\partial p}{p_c}$
$\partial B/\partial p_c$	$\frac{M}{2}$	$M\frac{\alpha\gamma}{2}$	$M\frac{\alpha}{2}$	$\frac{B}{p_c} - M\alpha\gamma\frac{p}{p_c}$
$\partial^2 B/\partial p \partial p_c$	0	0	0	$\frac{\partial B/\partial p}{p_c}$
$\partial C/\partial p_c$	$\frac{1}{2}$	$\frac{\gamma}{2}$	$\frac{1}{2}$	α

For the proposed yield surface, the derivatives are

$\partial A/\partial p$	$\partial^2 A/\partial p^2$	$\partial B/\partial p$	$\partial^2 B/\partial p^2$
$-\frac{\gamma}{\pi}\left(1+\gamma^2\left(\frac{1}{2}-\frac{p}{p_c}\right)^2\right)^{-1}$	$-2\pi\frac{\gamma}{p_c}\left(\frac{1}{2}-\frac{p}{p_c}\right)\left(\frac{\partial A}{\partial p}\right)^2$	$\alpha\frac{B}{p_c}$	$\frac{\partial B/\partial p}{B}$

$\partial A/\partial p_c$	$\partial B/\partial p_c$	$\partial C/\partial p_c$	$\partial B/\partial C$
$\frac{A}{p_c}-\frac{p}{p_c}\frac{\partial A}{\partial p}$	$-\alpha\frac{B}{p_c}\frac{p-C}{p_c}+\frac{\partial B}{\partial C}\frac{\partial C}{\partial p_c}$	$\frac{C}{p_c}$	$B\left(\frac{1}{C}-\frac{\alpha}{p_c}\right)$

$\partial^2 A/\partial p\partial p_c$	$\partial^2 B/\partial p\partial p_c$		
$-2\pi\gamma\left(\frac{\partial A}{\partial p}\right)^2\left(\frac{1}{2}-\frac{p}{p_c}\right)\frac{p}{(p_c)^2}$	$\frac{\alpha}{p_c}\left(\frac{\partial B}{\partial p_c}-\frac{B}{p_c}\right)$		

3

4

NUMERICAL IMPLEMENTATION OF A HYPERPLASTIC THERMOMECHANICAL CONSTITUTIVE MODEL BASED ON GIBBS ENERGY POTENTIAL

The numerical implementation of a thermomechanical constitutive model for fine-grained soils based on the thermodynamical framework of hyperelasticity-hyperplasticity is presented. A new implicit stress integration technique for constitutive models compatible with elasticity derived from Gibbs (complementary) energy potential is designed and used for implementing the thermomechanical model, developed in Chapter 2, in the DIANA FEA finite element boundary-value solver. The accuracy, robustness, effectiveness and convergence of the stress integration algorithm of the thermomechanical constitutive model is studied. Triaxial and oedometer tests on soils subjected to various thermomechanical stress paths, are modelled in DIANA FEA and many features of fine-grained soils such as non-linear elasticity, flexible yield surface, non-associated flow rule, Lode angle dependency, thermo-elastic expansion, thermal shrinkage of the yield surface and temperature-dependent Critical State stress ratio are thoroughly investigated.

LIST OF SYMBOLS

Roman		Greek	
$\mathbf{1}$	Kronecker tensor	$\boldsymbol{\alpha}$	Internal variables
A	Stress-like function	α	Parameter related to the shape of the yield surface
$\mathbf{B}$	Strain-displacement matrix	α^*	Linear thermal expansion coefficient
B	Stress-like function	γ	Parameter related to the shape of the yield surface
BVS	Boundary-value solver	$\Delta\varepsilon$	Increment of total strain tensor
C	Stress-like function	$\Delta\varepsilon^e$	Increment of elastic strain tensor
CSL	Critical State Line		
$\mathbf{C}^e$	Elastic compliance matrix	$\Delta\varepsilon^p$	Increment of plastic strain tensor
$\mathbf{D}$	Elasto-plastic continuum tangent tensor	$\Delta\varepsilon^p_{kk}$	Plastic volumetric strain increment
$\mathbf{D}^e$	Elastic stiffness matrix	$\Delta\varepsilon^{Therm}$	Increment of thermo-elastic strain tensor
$\mathbf{D}_O$	Consistent tangent operator	$\Delta\sigma$	Increment of stress tensor
d	Rate of dissipation potential function	$\Delta\Lambda$	Increment of plastic multiplier
e	Enthalpy	ΔT	Temperature increment
e_0	Initial void ratio	Δt	Time increment
$\mathbf{e}^{e,trial}$	Elastic trial deviatoric strain tensor	ε	Strain tensor
$\mathbf{e}^p$	Plastic deviatoric strain tensor	ε_n	Strain tensor at time t
$\boldsymbol{F}_{int}$	Unknown internal nodal force	ε^e	Elastic strain tensor
f	Helmholtz free energy potential	$\varepsilon_n^{e,trial}$	Elastic trial strain tensor
g	Gibbs energy potential	ε_n^e	Elastic strain tensor at time t
g_1	Gibbs free energy potential at isothermal conditions	ε_{n+1}^e	Elastic strain tensor at time $t+1$
$\bar{G}$	Material parameter related to elastic shear modulus	ε^p	Plastic strain tensor
h	Helmholtz free energy potential	ε^{Therm}	Thermo-elastic strain tensor
$\mathbf{I}$	Fourth-order identity tensor	$\dot{\varepsilon}$	Rate of total strain tensor
$\mathbf{J}$	Jacobian matrix	$\dot{\varepsilon}^e$	Rate of elastic strain tensor

J	Second stress invariant	$\dot{\boldsymbol{\varepsilon}}^p$	Rate of plastic strain tensor
$\dot{J}$	Rate of second stress invariant	$\dot{\boldsymbol{\varepsilon}}^{Therm}$	Rate of thermo-elastic strain tensor
$\mathbf{K}$	Global stiffness matrix	$\varepsilon_1, \varepsilon_2, \varepsilon_3$	Principle strains
$\bar{K}$	Material parameter related to elastic bulk modulus	ε_v	Total volumetric strain
$\mathbf{k}_i$	Stiffness matrix of element i	ε_s	Total deviatoric strain
LAD	Lode angle dependency	ε_v^e	Elastic volumetric strain
MCC	Modified Cam-Clay	$\varepsilon_v^{e,trial}$	Elastic trial volumetric strain
$\bar{M}$	Critical State stress ratio	ε_s^e	Elastic deviatoric strain
M_c	Critical State stress ratio in compression mode of loading	$\varepsilon_s^{e,trial}$	Elastic trial deviatoric strain
M_{c0}	Critical State stress ratio in compression mode of loading at ambient temperature	$\dot{\varepsilon}_v^e$	Rate of elastic volumetric strain
M_{e0}	Critical State stress ratio in extension mode of loading at ambient temperature	$\dot{\varepsilon}_s^e$	Rate of elastic deviatoric strain
NOI	Number of iterations	ε_v^p	Plastic volumetric strain
N–R	Newton-Raphson	ε_s^p	Plastic deviatoric strain
N_E	Number of elements	$\dot{\varepsilon}_v^p$	Rate of plastic volumetric strain
n	Parameter of pressure dependency of elastic moduli	$\dot{\varepsilon}_s^p$	Rate of plastic deviatoric strain
$\hat{\mathbf{n}}$	Tensor of direction of deviatoric component of stress and strain tensors	ε_v^T	Thermo-elastic volumetric strain
OCR	Over consolidation ratio	$\dot{\varepsilon}_v^T$	Rate of thermo-elastic volumetric strain
$\boldsymbol{P}$	Global external nodal force	θ	Lode angle
p	Mean effective stress	$\dot{\theta}$	Rate of Lode angle
p^{trial}	Trial hydrostatic pressure	κ	Elastic compressibility index
p_a	Reference hydrostatic pressure	λ	Elasto-plastic compressibility index
p_{c0}	Pre-consolidation pressure	$\dot{\Lambda}$	Plastic multiplier
p_{cT}	Apparent pre-consolidation pressure	μ_0	Thermal softening coefficient
p_{cT}^n	Apparent pre-consolidation pressure at time t	ζ	LAD function
p_{cT}^{n+1}	Apparent pre-consolidation pressure at time $t+1$	π^*	Coefficient of Critical State stress ratio variation with temperature
$\dot{p}_{cT}$	Rate of change of the apparent pre-consolidation pressure	ρ^*	Proportion of stress ratio at Critical State conditions in extension mode of loading over compression mode of loading at ambient temperature

q	Deviatoric stress	$\boldsymbol{\sigma}$	Cauchy stress tensor
q^{trial}	Trial deviatoric stress	$\boldsymbol{\sigma}_n$	Cauchy stress tensor at time t
q_y	Deviatoric yield stress	$\boldsymbol{\sigma}_{n+1}$	Cauchy stress tensor at time $t+1$
$\boldsymbol{q}$	Heat flux vector	$\boldsymbol{\sigma}_e$	Exact return stress tensor
q_0	Initial deviatoric stress	$\boldsymbol{\sigma}_r$	Return stress tensor
$\boldsymbol{R}$	Vector of residuals	$\boldsymbol{\sigma}^{est}$	Estimated stress tensor
$\boldsymbol{R}_1$	Residual equation for the state variable	$\boldsymbol{\sigma}^{trial}$	Trial stress tensor
R_2	Residual equation for the hardening variable	$\boldsymbol{\sigma}^*$	Stress tensor at the end of iteration
R_3	Residual equation for the consistency variable	$\dot{\boldsymbol{\sigma}}$	Stress rate tensor
$\boldsymbol{r}$	Plastic flow tensor	$\sigma_1, \sigma_2, \sigma_3$	Principle stresses
$\boldsymbol{r}^d$	Plastic flow tensor in dissipative stress space	σ_v	Vertical stress
r_p	Plastic flow in p direction	χ	Generalised dissipative stress tensor
r_p^d	Plastic flow in p direction in dissipative stress space	χ_p	Mean generalised dissipative stress
r_q	Plastic flow in q direction	χ_q	Deviatoric generalised dissipative stress
r_q^d	Plastic flow in q direction in dissipative stress space	$\bar{\chi}$	Generalised stress tensor
S	Third stress invariant	$\bar{\chi}_p$	Mean generalised stress
$\dot{S}$	Rate of third stress invariant	$\bar{\chi}_q$	Deviatoric dissipative stress
$\boldsymbol{s}$	Deviatoric stress tensor	Ω_i	Domain of element i
T	Current absolute temperature		
T_0	Initial absolute temperature		
T_n	Absolute temperature at time t		
T_{n+1}	Absolute temperature at time $t+1$		
$\dot{T}$	Rate of temperature		
t	Time step		
tol	Tolerance		
$\boldsymbol{u}$	Global unknown nodal displacement		
u	Internal energy potential		
$\dot{u}$	Rate of change of internal energy		
$\boldsymbol{v}$	Vector of unknown variables		
w^p	Dissipated work		
y	Yield function in true stress space		
y^d	Yield function in dissipative stress space		
$\dot{y}$	Rate of change of the yield function		

4.1. INTRODUCTION

Boundary-Value Solvers (BVS) efficiently provide approximate solutions for displacements and forces by solving a set of mathematical equations for problems dealing with complexities in geometry and loading configurations, as well as material behaviour. The finite element method is one such numerical tool. At the heart of these equations are material constitutive relations, which significantly influence the accuracy and rationality of numerical outcomes. For materials whose behaviours are non-linear and dependent on the history of loading (i.e., stress-path dependent), constitutive relationships need to be integrated for BVS using numerical algorithms [1].

Many thermo-active geo-structures such as energy-piles, heat storage tanks, thermal retaining walls, pipelines and thermal quay walls, exchange temperature with the ground and consequently may impose thermal loads to the soil adjacent to these structures [2]. Such loads have been proven to influence the mechanical behaviour of fine-grained soils and, therefore, it is essential to use constitutive models that account for those soil behaviours in numerical simulations. Based on plasticity theory (or its variants), a number of thermo-mechanical models had been developed in past decades and were successful, with reasonable accuracy, in capturing the major effects of temperature on the mechanical behaviour of soils observed in laboratory soil element tests [3–11]. In most of these models, however, thermodynamic restrictions (principles of thermodynamics) may not unconditionally be satisfied. Thus, certain fundamental material behaviour may not be captured/predicted and other phenomena may be spuriously predicted [12].

In addition, it had been demonstrated that the elastic moduli of soils are non-linearly proportional to hydrostatic pressure [13–16] and, as such, this effect should be included in constitutive equations to achieve results with a high or reasonable accuracy.

In Chapter 2 a thermomechanical constitutive model for fine-grained soils was developed using the (hyperelasticity-) hyperplasticity framework proposed by [17], in which thermodynamic principles were satisfied unconditionally. The definitions of an energy potential (e.g. Gibbs energy potential) and a rate of dissipation potential were sufficient to derive all the components of the model, including (non-linear) elasticity relationships, yield surface, plastic flow and hardening rules, similar to a classical elasto-plastic model [12]. Note that some soil models adhered to the first law of thermodynamics (conservation of energy) by combining hyperelasticity with classical plasticity theory to formulate the entire constitutive relationship [18–22]. In these models, a Helmholtz energy (strain energy) potential or a Gibbs energy (complementary energy) potential was usually introduced to derive the elastic constitutive relationships.

One method to implement constitutive relationships in a BVS is to use *"elastic predictor-plastic corrector"* techniques within an implicit stress integration scheme [1; 23; 24]. In these approaches, the algorithm is first subjected to a trial elastic solution (elastic predictor) as the result of a strain increment. When the elastic predictor fails to satisfy the yield criterion (when the trial stress lays outside the yield surface), the algorithm returns the trial stress back on to the yield surface by correcting the stress value in an iterative procedure which generates plastic strains and the evolution of any hardening variables. These approaches have been widely used for implementing hyperplasticity models and classical plasticity models with hyperelastic constitutive relations derived

from the definition of Helmholtz free energy potentials in a BVS (see [21; 22] for models with linear elastic (stress independent elasticity), and [1; 25–31] for models incorporating non-linear elasticity). In these models, however, elastic moduli were formulated in terms of strains, and thus they are inconvenient when compared with laboratory data (where elastic moduli are mostly formulated in terms of stress). Alternatively, by employing a Gibbs energy potential, elastic moduli can be defined in terms containing stresses and this is the approach adopted in this chapter. To the best knowledge of the author, elastic predictor-plastic corrector methods in an implicit stress integration scheme have not been developed for models having elasticity formulations derived via a Gibbs energy potential. The novelty of this chapter lies in developing such an algorithm. The constitutive equations of the thermomechanical hyperplasticity model developed in Chapter 2, with non-linear elasticity formulations extracted from a Gibbs energy potential, were used to develop the algorithm and can easily be generalised for other Gibbs-type elasticity formulations.

The formulations presented here are in accordance with geotechnical conventions, where compressive stresses and contractive strains are considered to be positive and all the stresses are effective. In line with this context, the thermal expansion coefficient utilised in this chapter are presented with negative values. Scalars and vectors are denoted with italic and bold-italic letters, respectively; tensors and matrices are denoted with bold letters. The notations $(\bullet : \bullet)$ and $(\bullet \otimes \bullet)$, respectively, denote the double contraction and tensor product, and $\| \bullet \|$ and $tr(\bullet)$ represent the norm and trace function, respectively.

4.2. BACKGROUND

Any continuum medium should satisfy a series of principles such as conservation of mass, linear momentum, conservation of energy, virtual work and so on. [1; 24]. A combination of different principles may be employed to develop finite element equations for a mechanical boundary value problem. Considering the problem as static (neglecting the dynamic components) and applying the principle of virtual work [1] (or the weak form of the momentum balance equation [24]) to a continuum leads to a set of equations which need to be solved for nodal unknowns:

$$F_{INT} = P \tag{4.1}$$

where F_{INT} is the unknown internal nodal force vector and P is the global external nodal force vector. Note that Eq. (4.1) is applicable for both linear and non-linear systems. This equation represents the discretised version of the momentum equation for a medium that is discretised into elements by nodes. F_{INT} and P are determined by assembling the contributions of individual elements which are determined at the Gaussian points (quadrature points). For linear problems, the internal nodal force can be determined as

$$F_{INT} = \mathbf{K}u \tag{4.2}$$

where $\mathbf{K}$ and u are the global stiffness matrix and the global (unknown) nodal displacement vector, respectively. In general, Eq. (4.2) is nonlinear and dependent on the history of loading (and displacement). Consequently, an iterative algorithm such as the Newton-Raphson (N-R) method is required to solve the global finite element problem (Eq. (4.1)).

The global stiffness matrix **K** is established by assembling the stiffness matrices $\mathbf{k}_i$ of all the elements:

$$\mathbf{K} = \underset{i=1}{\overset{N_E}{\mathbf{A}}} \mathbf{k}_i = \underset{i=1}{\overset{N_E}{\mathbf{A}}} \int_{\Omega_i} \mathbf{B}^{\mathrm{T}} \mathbf{D}_O \mathbf{B} \, dv \tag{4.3}$$

where i is the number of the corresponding element; $\mathbf{A}$ represents the assembly operator; Ω_i represents the domain of element i; N_E is the number of elements; **B** is the strain-displacement matrix (i.e., connecting the displacement vector $\boldsymbol{u}$ to the strain vector $\boldsymbol{\varepsilon}$); and $\mathbf{D}_O$ is the material stiffness matrix (for elastic materials) or the consistent tangent operator (for elasto-plastic materials) of the element and is defined as the derivative of the stress increment tensor, $\Delta\boldsymbol{\sigma}$, with respect to the strain increment tensor, $\Delta\varepsilon$:

$$\mathbf{D}_O = \frac{\partial \Delta\boldsymbol{\sigma}}{\partial \Delta\varepsilon} \tag{4.4}$$

which represents a linearisation of the constitutive relation (the relationship between stress and strain). The use of the tangent operator to assemble the global stiffness matrix provides consistency in a N-R algorithmic solution (e.g. the global finite element iteration) and ensures asymptotic quadratic convergence [24].

Laboratory soil element tests have demonstrated that the mechanical behaviour of geomaterials, e.g. soils, is dependent on the history of loading which has been experienced by the material (stress path dependency). To capture this behaviour, elasto-plastic constitutive relationships at continuum level are inevitably developed in rate form, in which the stress rate tensor, $\dot{\boldsymbol{\sigma}}$, and the strain rate tensor, $\dot{\varepsilon}$, are related by

$$\dot{\boldsymbol{\sigma}} = \mathbf{D}\dot{\varepsilon} \tag{4.5}$$

where **D** is the elasto-plastic continuum tangent tensor. Note that the tangent operator $\mathbf{D}_O$ (Eq. (4.4)) is in general, different from the continuum tangent **D**; $\mathbf{D}_O$ plays a similar role as **D**, but for a discretised domain (of a continuum medium).

After the system of governing equations (Eq. (4.1)) is evaluated (also known as the global iteration), the elasto-plastic rate equation (Eq. (4.5)) needs to be integrated at the Gaussian points (local integration), to ensure that all state variables are consistently solved. Any resulting imbalanced forces can be solved via iteration of the solution procedure. An updated tangent operator ($\mathbf{D}_O$) for the next step is then needed for the global iteration procedure using the N-R approach.

Solutions at the local (Gaussian point) level are necessary for solving the boundary-value problem (global system) and these significantly affect its robustness, accuracy, efficiency and convergence [32]. Stress integration schemes are broadly categorised as explicit, implicit or closed-form methods. The last approach is only applicable for simple constitutive relations, and is thus not considered here. In the explicit approach (e.g. the forward-Euler method), stress integration algorithms are formulated based on the conditions at time step t (i.e., at the start of the strain increment). The trial stress is estimated via the applied strain increment and the elastic stiffness tensor at time t, and when the stress state goes beyond the admissible stress domain (outside the yield surface), it is returned back on to the yield surface by the evolution of plastic strains. This procedure

is completed in a single iteration. The main advantages of this approach are its simplicity to implement and its applicability to almost all constitutive equations. However, the consistency condition is not enforced at the end of the solution and therefore the updated stress may deviate from the exact solution [1; 32]. Another drawback of this approach is the relatively low accuracy. Subjecting the stress integration algorithm to a relatively small strain increment may control this shortcoming. However, computational costs will increase, which may affect the efficiency of the overall BVS solution. In addition, the use of the tangent operator derived from this approach does not result in asymptotic quadratic convergence of the global iteration, which also influences the efficiency of the boundary-value problem solver.

Stress-updating algorithms developed via an implicit scheme (e.g. backward-Euler method) are formulated based on updated stresses at time step $t + \Delta t$. Solutions are usually determined by minimising the appropriately-defined residual equations in an acceptable tolerance range via iteration. Geometrically, this approach means that, when the trial stress resulting from the strain increment goes outside the yield surface, it is pulled-back on to the yield surface by iteratively updating the state variables (stresses and strains) and hardening rules of the material. One of the advantages of this approach is that the consistency condition is enforced (within the specified tolerance) at the end of the solution, which ensures that the stress is eventually returned back on to the yield surface. Hence, accurate results are obtained even for relatively large strain increments (improving the efficiency on the boundary-value problem). In addition to high accuracy, a quadratic convergence asymptote is ensured. However, using this approach requires the calculation of the derivatives of the flow rule and the hardening rules, as well as the second derivatives of the plastic potential surface with respect to their unknowns. Consequently, this approach may not be suitable for models with complex constitutive relations. Moreover, this method may encounter convergence difficulties when unsuitable forms of yield functions and flow directions are utilised. A number of sources causing these difficulties are explained in Chapter 3, for example, yield functions that have erratic gradients, or false elastic nuclei in stress space (see Chapter 3 for more details).

4.3. THERMOMECHANICAL CONSTITUTIVE MODEL

Hyperplasticity is a continuum plasticity approach which ensures that the constitutive relations satisfy the principles of thermodynamics (First and Second laws of thermodynamics) [12; 17]. Specifying an energy potential and a rate of dissipation potential is sufficient to extract the entire constitutive components of a rate-independent material, including the yield surface, elasticity relationships, plastic flow and hardening rules. In Chapter 2 a thermomechanical constitutive model within this framework was presented by defining a complementary energy potential, also known as Gibbs energy potential, and a rate of dissipation potential that accounted for temperature effects on the mechanical behaviour of fine-grained soils. Consequently, all the constituents of that model were temperature dependent. While keeping the general formulation similar to that in Chapter 2, here the energy potential at isothermal conditions and the rate of dissipation function used in that work are updated to use the flexible and robust yield surface proposed in Chapter 3, and to include Lode angle dependency on the yield surface and flow rule.

Geomaterials have often been demonstrated to have yield surfaces that are non-elliptical in shape. To add flexibility to the yield surface to enable non-elliptical forms, the stress-like functions proposed in Chapter 3 (and discussed later) are used in the definition of the rate of dissipation potential. The resulting yield surface was shown to be uniquely defined in stress space, without having false elastic nuclei or erratic gradients, unlike other hyperplasticity-based constitutive models [33–36]. The constitutive relations are presented here briefly.

Constitutive equations, in general, can be defined by state variables of stress, $\boldsymbol{\sigma}$, strain, $\boldsymbol{\varepsilon}$, absolute temperature, T, entropy, s, and internal variables, $\boldsymbol{\alpha}$. Depending on which set of state variables are selected as independent variables, a scalar energy potential can be defined in the form of either an internal energy potential, $u(\boldsymbol{\varepsilon}, \boldsymbol{\alpha}, s)$, Helmholtz free energy potential, $h(\boldsymbol{\varepsilon}, \boldsymbol{\alpha}, T)$, Gibbs energy potential, $g(\boldsymbol{\sigma}, \boldsymbol{\alpha}, T)$, or enthalpy, $e(\boldsymbol{\sigma}, \boldsymbol{\alpha}, s)$. Note that strain and entropy are thermodynamically conjugate pairs to stress and temperature, respectively, and vice-versa (i.e., $(\boldsymbol{\varepsilon} \leftrightarrow \boldsymbol{\sigma})$ and $(s \leftrightarrow T)$). Therefore, it is possible to interchange from one energy potential to another type via Legendre transformation and by altering the role of independent variables to their corresponding thermodynamic conjugate pairs. Helmholtz free energy and Gibbs energy are the two commonly used energy potentials to develop constitutive models for geomaterials. In this work, a Gibbs energy potential is used. The main advantage is that the elastic constitutive relationships are defined in terms of stresses (for example, the hydrostatic pressure dependency of elastic moduli).

The Gibbs energy potential is defined by temperature, stress invariants and plastic strain invariants (as the internal variables) as

$$g\left(p, q, \varepsilon_v^p, \varepsilon_s^p, T\right) = g_1\left(p, q\right) - p\varepsilon_v^p - q\varepsilon_s^p - 3\alpha^* p\left(T - T_0\right) \tag{4.6}$$

where p, q, ε_v^p and ε_s^p are the hydrostatic pressure (mean effective stress), deviatoric stress, plastic volumetric strain and plastic deviatoric strain, respectively, as defined in Table 4.1 ; T_0, T and $3\alpha^*$ are the initial temperature (K), current temperature (K), and the volumetric thermal expansion coefficient, respectively.

Table 4.1: Definition of invariants of stress and plastic strain tensors

Stress related invariants		Strain related invariants	
Hydrostatic pressure (kPa)	$p = tr(\boldsymbol{\sigma})/3$	Plastic volumetric strain	$\varepsilon_v^p = tr(\boldsymbol{\varepsilon}^p)$
Deviatoric stress (kPa)	$q = (3/2\, \mathbf{s}:\mathbf{s})^{1/2}$	Plastic deviatoric strain	$\varepsilon_s^p = (2/3\, \mathbf{e}^p:\mathbf{e}^p)^{1/2}$
Lode angle (°)	$\theta = \frac{1}{3}\sin^{-1}\left[\frac{3\sqrt{3}}{2}\left(\frac{S}{J}\right)^3\right]; -\frac{\pi}{6} \leq \theta \leq \frac{\pi}{6}$		
where $\boldsymbol{\sigma}$: Cauchy stress tensor; $\mathbf{s}$: Deviatoric stress tensor, $\mathbf{s} = \boldsymbol{\sigma} - p\mathbf{1}$; $\mathbf{1}$: Second-order identity tensor; $J = q/\sqrt{3}$; $S = \left(\frac{1}{3}S_{ij}S_{jp}S_{pi}\right)^{1/3}$; $\boldsymbol{\varepsilon}^p$: Plastic strain tensor; $\mathbf{e}^p$: Plastic deviatoric strain, $\mathbf{e}^p = \boldsymbol{\varepsilon}^p - \left(\varepsilon_v^p/3\right)\mathbf{1}$			

Eq. (4.6) leads to constitutive relationships of decoupled materials, where the total strain can be divided into elastic and plastic components. The Gibbs energy potential

for elastic-plastic coupling materials can be found in the works of [12; 19; 20]. g_1 is Gibbs energy potential under isothermal conditions, proposed by [37], as

$$g_1 = -\frac{p_0^{2-n}}{\bar{K}(2-n)(1-n)p_a^{1-n}} - \frac{p}{\bar{K}(1-n)}; n \neq 1 \tag{4.7a}$$

$$g_1 = -\frac{1}{\bar{K}}\left(\ln\left(\frac{p}{p_a}\right) - 1\right) - \frac{q^2}{6\bar{G}p}; n = 1 \tag{4.7b}$$

where $p_0 = \sqrt{p^2 + \frac{\bar{K}(1-n)}{3\bar{G}}q^2}$; p_a is the reference hydrostatic pressure (here equal to atmospheric pressure 101 kPa); $\bar{K}$ and $\bar{G}$ are material constants related to the elastic bulk and elastic shear moduli respectively; n is the parameter indicating (hydrostatic) pressure dependency of the elastic moduli.

The total strain tensor is determined by differentiating the complementary energy potential with respect to the stress tensor:

$$\varepsilon = -\frac{\partial g}{\partial \boldsymbol{\sigma}} = -\frac{\partial g_1}{\partial \boldsymbol{\sigma}} + \alpha^*(T - T_0)\mathbf{1} + \varepsilon^e + \varepsilon^{Therm} + \varepsilon^p \tag{4.8}$$

where ε^e , ε^{Therm} and ε^p are the isothermal elastic, thermo-elastic and plastic components of the total strain, respectively.

The generalised stress, $\bar{\chi}$, is defined as the derivative of the energy potential with respect to the internal variables (here plastic strains):

$$\bar{\chi} = -\frac{\partial g}{\partial \varepsilon^p} \tag{4.9a}$$

where the mean and deviatoric components are

$$\bar{\chi}_p = -\frac{\partial g}{\partial \varepsilon_v^p} = p \tag{4.9b}$$

$$\bar{\chi}_q = -\frac{\partial g}{\partial \varepsilon_s^p} = q \tag{4.9c}$$

For rate-independent materials (considered here), the rate of the dissipation potential function is a first order homogenous function of the rate of internal variables. For the current model, this potential is expressed by the invariants of the rate of the internal variables, temperature, and stress invariants:

$$d = C\dot{\varepsilon}_v^p + \sqrt{A^2\left(\dot{\varepsilon}_v^p\right)^2 + B^2\left(\dot{\varepsilon}_v^p\right)^2} \tag{4.10}$$

where A, B and C are stress-like functions containing the temperature and stress invariants (explained later). Note that temperature effects and Lode angle dependency (LAD) are implicitly incorporated in these functions.

The generalised dissipative stress, χ, is the derivative of the rate of dissipation potential with respect to the rate of the internal variable:

$$\chi = \frac{\partial d}{\partial \dot{\varepsilon}^p} \tag{4.11a}$$

where the mean and deviatoric components are

$$\chi_p = \frac{\partial d}{\partial \dot{\varepsilon}_v^p} = C + \frac{A^2 \dot{\varepsilon}_v^p}{\sqrt{A^2 \left(\dot{\varepsilon}_v^p\right)^2 + B^2 \left(\dot{\varepsilon}_v^p\right)^2}} = C + \frac{A^2 \dot{\varepsilon}_v^p}{d - C\dot{\varepsilon}_v^p} \tag{4.11b}$$

$$\chi_p = \frac{\partial d}{\partial \dot{\varepsilon}_s^p} = \frac{B^2 \dot{\varepsilon}_v^p}{\sqrt{A^2 \left(\dot{\varepsilon}_v^p\right)^2 + B^2 \left(\dot{\varepsilon}_s^p\right)^2}} = \frac{B^2 \dot{\varepsilon}_s^p}{d - C\dot{\varepsilon}_v^p} \tag{4.11c}$$

The yield function (surface) of a rate-independent material is generally determined by invoking the Legendre-Fenchel transform on the rate of dissipation potential [12]. However, eliminating d between Eqs. (4.11b) and (4.11c) results in an equation, defined by terms consisting of dissipative stress invariants, which represents the yield surface

$$y^d = \frac{\left(\chi_p - C\right)^2}{A^2} + \frac{\left(\chi_q\right)^2}{B^2} - 1 = 0 \tag{4.12}$$

which forms an ellipse in χ_p-χ_q space (dissipative stress space). The plastic flow tensor ($\mathbf{r}^d$) is normal (associated) to y^d with respect to dissipative stresses [17]:

$$\mathbf{r}^d = \frac{\partial y^d}{\partial \chi} \tag{4.13a}$$

where the mean and deviatoric components are defined as

$$r_p^d = \frac{\partial y^d}{\partial \chi_p} = \frac{2\left(\chi_p - C\right)}{A^2} \tag{4.13b}$$

$$r_q^d = \frac{\partial y^d}{\partial \chi_q} = \frac{2\left(\chi_q\right)}{B^2} \tag{4.13c}$$

When the deformation of a material is accompanied by irreversibility, the second law of thermodynamics states that the energy of the material is dissipating and its rate is always positive. In hyperplasticity theory this notion is satisfied by using Ziegler's hypothesis [38], which postulates that dissipation (or production of entropy) is maximised when $\bar{\chi} = \chi$. By utilising this hypothesis, the yield surface (Eq. (4.10)) and plastic flow (Eq. (4.13)), defined in dissipative stress space, are transformed to true stress space:

$$y = \frac{\left(p - C\right)^2}{A^2} + \frac{q^2}{B^2} - 1 \tag{4.14}$$

$$r_p = \frac{2(p - C)}{A^2} \tag{4.15a}$$

$$r_q = \frac{2q}{B^2} \tag{4.15b}$$

Note that the flow rule (Eq. (4.13)) is normal to the yield surface (Eq. (4.10))) in dissipative stress space (χ_p-χ_q). However, this often does not remain valid in true stress space (p-q), due to the stress-dependency of functions A, B and C (see below and Chapter 2 for more details).

4.3.1. STRESS-LIKE FUNCTIONS A, B AND C

Most geomaterials have yield surfaces that are enclosed and non-elliptical in shape. Eq. (4.14) represents the general equation of an ellipse. Flexible yield surfaces, i.e., yield surfaces with distorted and non-elliptical shapes, can be formed by defining stress-dependent functions within the yield surface function, i.e. the stress-like functions A, B and C in Eq. (4.14). Several of these functions can be found in literature (e.g. [33–36]). However, in Chapter 3 it was shown that most of these functions, despite providing flexibility for the yield surface, have difficulties when numerically implemented in implicit stress integration approaches. Implicit stress integration algorithms using these stress-like functions suffered in terms of robustness and convergence, due to false elastic nuclei and erratic gradients of the yield functions when the stress state of the material lays outside the yield surface. Here, the stress-like functions proposed in Chapter 3 are used, which, in addition to providing flexibility for the yield surface were proven to be robust for applications in an implicit stress integration algorithm:

$$A(p, p_{cT}) = \frac{p_{cT}}{2\pi} \left(2\arctan \left(\gamma \left(\frac{1}{2} - \frac{p}{p_{cT}} \right) \right) + \pi \right) \tag{4.16a}$$

$$B(p, p_{cT}) = \bar{M} C \exp \left(\frac{\alpha(p - c)}{p_{cT}} \right) \tag{4.16b}$$

$$C(p_{cT}) = \frac{p_{cT}}{2\pi} \left(2\arctan \left(\frac{\gamma}{2} \right) + \pi \right) \tag{4.16c}$$

where $-1 \leq \alpha \leq 1$ and $-1 \leq \gamma \leq 1$ are shape parameters and $\bar{M}$ is the stress ratio at Critical State conditions. Note that the Modified Cam-Clay (MCC) yield surface is recovered when $\alpha = \gamma = 0$. Laboratory soil element tests demonstrated that the yield surface is smaller at higher temperatures [39–43]. To take this phenomenological observation into account, the apparent pre-consolidation pressure, p_{cT}, is defined to reduce with temperature, while it hardens with plastic volumetric strain similar to the MCC model:

$$p_{cT} = p_{c0} \exp \left(\frac{1 + e_0}{\lambda - \kappa} \varepsilon_v^p \right) \exp \left(-\mu(T - T_0) \right) \tag{4.17}$$

where p_{c0} is the initial pre-consolidation pressure; λ and κ are the bi-logarithmic elasto-plastic and elastic compressibility indices, respectively; e_0 is the initial void ratio; μ_0 is the coefficient of thermal shrinkage of the yield surface.

It has been demonstrated that, depending on their constituents and mineralogy, the stress ratio at Critical State conditions of fine-grained soils, e.g. clays and silts, varies with temperature (i.e., it may increase, decrease or remain unchanged) [44–47]. To account for this observation, as well as Lode angle dependency (LAD) on the yield surface, the approach of [30] is followed here where $\bar{M}$ is defined as

$$\bar{M} = \zeta(\theta) M_c = \zeta(\theta)(M_{c0} + \pi^*(T - T_0)) \tag{4.18}$$

where M_c and M_{c0} are the stress ratios at Critical State conditions in compression loading ($\theta = \pi/6$; θ is the Lode angle, see Table 4.1) at the current and the ambient temperatures ($T = T_0$), respectively, π^* is the gradient of the variation of $\bar{M}$ with temperature, and ζ is the LAD function. Several LAD functions can be found in the literature, e.g., [48–51]. Here, the LAD function proposed by [50] is used:

$$\zeta(\theta, \rho^*) = \left(\frac{2(\rho^*)^4}{1 + (\rho^*)^4 - \left(1 - (\rho^*)^4\right)\sin 3\theta} \right)^{\frac{1}{4}} \tag{4.19}$$

where $\rho^* = M_{e0}/M_{c0}$ and M_{e0} is the stress ratio at Critical State conditions in extension loading ($\theta = -\pi/6$) at the ambient temperature ($T = T_0$). The aforementioned LAD function results in a convex yield surface in deviatoric stress space (e.g. π-plane), for $\rho^* \leq 0.6$, corresponding to friction angles less than 48.6° [50].

The flexibility of the yield surface is demonstrated in principle stress space (σ_1-σ_2-σ_3) in Figure 4.1. For $\alpha = \gamma = 0$ (Figure 4.1b) the yield surface attains the MCC model with a Lode angle dependent shape in the deviatoric plane ($\rho^* = 0.8$). The yield surface using $\alpha = \gamma = -0.5$ (Figure 4.1a) is stretched along the hydrostatic axis (σ_1-σ_2-σ_3) and attains a bullet-shape, while using shape parameters $\alpha = \gamma = 0.5$ the yield surface is flattened along the hydrostatic axis and forms a droplet shape. Figure 4.2 shows the three-dimensional yield surface in p-q-ΔT space. The yield surface is bounded at p_{cT} and, according to Eq.4.17, it shrinks with respect to temperature increase and expands due to cooling.
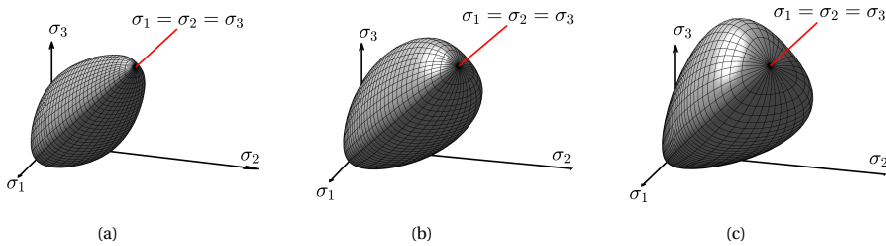

Figure 4.1: Yield surface in principle stress space with $M_c = 1.00$ and $\rho^* = 0.8$ and different shape parameters (a) $\alpha = \gamma = -0.5$; (b) $\alpha = \gamma = 0$ (MCC); (c) $\alpha = \gamma = 0.5$

Plastic flow directions for the studied yield surfaces in Figure 4.1 are presented in Figure 4.3 in p-q stress space and in deviatoric stress space at $p/p_{cT} = 0.4$ (cross section A-A). In general, the flow rule (Eq. (4.15)) is non-associated in p-q space due to the stress-dependency of the stress-like functions (Eq. (4.16)); this is demonstrated in Figure 4.3a and Figure 4.3e for yield surfaces using $\alpha = \gamma = -0.5$ and $\alpha = \gamma = 0.5$, respectively. For the MCC model, the stress-dependent terms in the functions A and B drop out and the rate of dissipation potential becomes stress-independent. Thus, the flow rule becomes associated (Figure 4.3c).
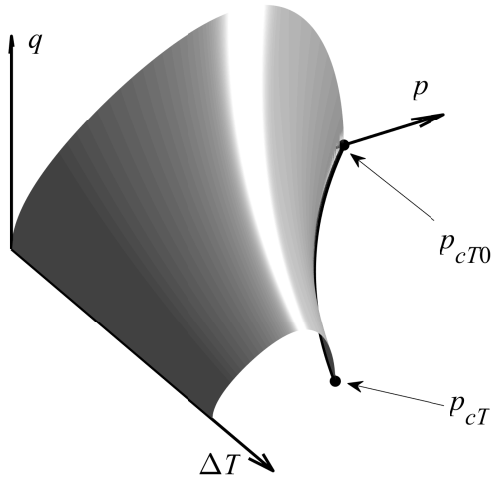

Figure 4.2: Yield surface in p-q-ΔT space with $M_c = 1.00$, $\mu_0 = 0.001$, $\pi^* = 0$ and $\alpha = \gamma = 0.5$
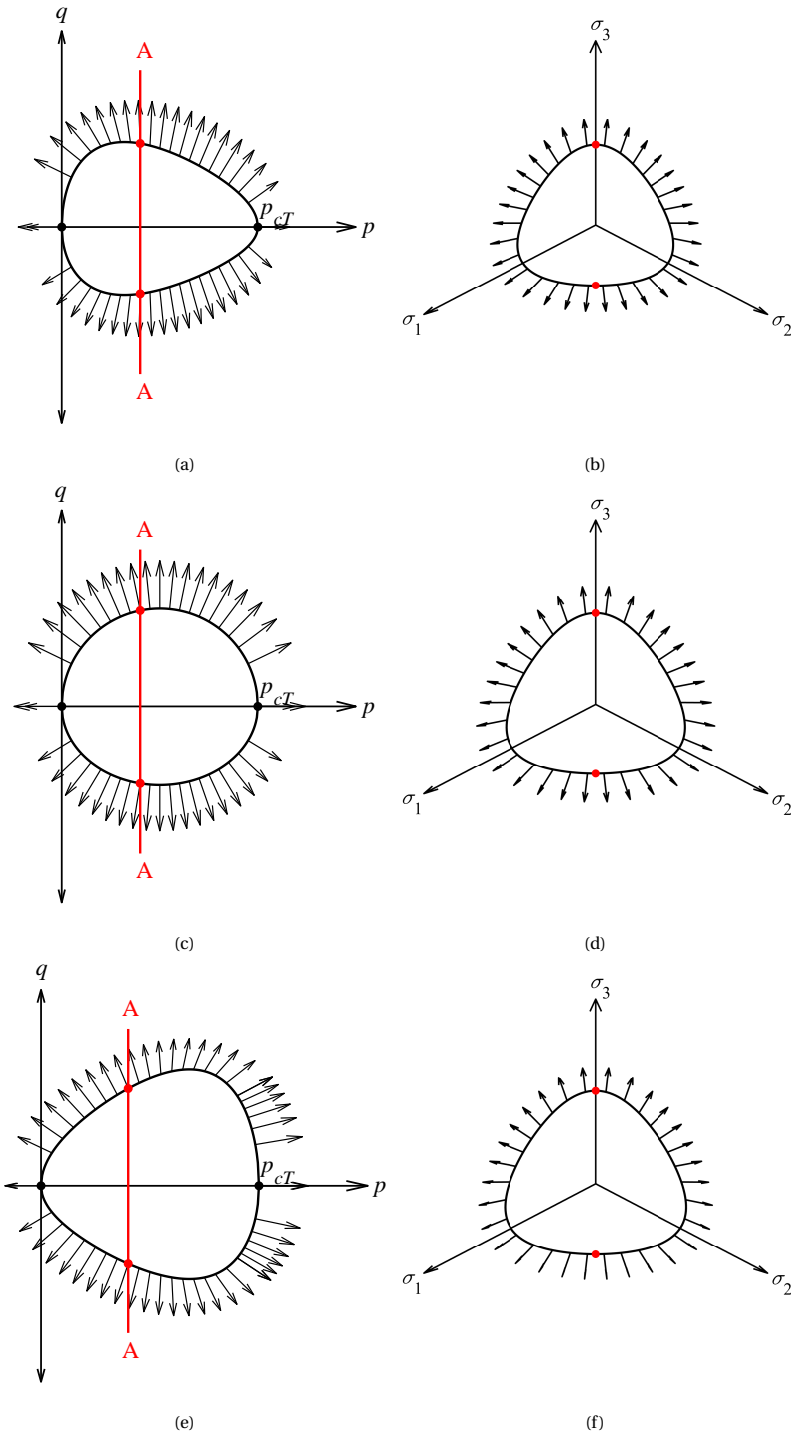
Figure 4.3: Flow rule in p-q stress space and in the deviatoric plane at $p/p_{cT} = 0.4$ (cross section A-A), for yield surfaces using $M_c = 1.00$ and $\rho^* = 0.8$ and different shape parameters (a) and (b) $\alpha = \gamma = -0.5$; (c) and (d) $\alpha = \gamma = 0$ (MCC); (e) and (f) $\alpha = \gamma = 0.5$

4.3.2. RATE FORM OF ELASTO-PLASTIC RELATIONSHIPS

The isotropic hardening rule of the model is the rate of Eq. (4.17):

$$\dot{p}_{cT} = \left(\frac{1+e_0}{\lambda - \kappa} \dot{\varepsilon}_v^p - \mu_0 \dot{T} \right) p_{cT} \tag{4.20}$$

The rate of the total strain tensor (Eq. (4.8)) is

$$\dot{\varepsilon} = \dot{\varepsilon}^e + \dot{\varepsilon}^{Therm} + \dot{\varepsilon}^p \tag{4.21}$$

where

$$\dot{\varepsilon}^e = -\frac{\partial^2 g_1}{\partial \dot{\sigma}^2} : \dot{\varepsilon} = \left[\mathbf{C}^e \right] : \dot{\sigma} \tag{4.22a}$$

$$\dot{\varepsilon}^{Therm} = \alpha^* \dot{T} \mathbf{1} \tag{4.22b}$$

$$\dot{\varepsilon}^p = \dot{\Lambda} \mathbf{r} \tag{4.22c}$$

where $[\mathbf{C}^e]$ is the forth-order elastic compliance tensor and $\dot{\Lambda}$ is the plastic multiplier, derived from the consistency condition ($\dot{y} = 0$) as

$$\dot{\Lambda} = -\frac{\left\{ \frac{\partial y}{\partial \sigma} \right\}^{\mathrm{T}} [\mathbf{D}^e] \left\{ \dot{\varepsilon} - \dot{\varepsilon}^{Therm} \right\} + \frac{\partial y}{\partial T} \dot{T}}{\left\{ \frac{\partial y}{\partial \varepsilon^p} \right\}^{\mathrm{T}} \{\mathbf{r}\} - \left\{ \frac{\partial y}{\partial \sigma} \right\}^{\mathrm{T}} [\mathbf{D}^e] \{\mathbf{r}\}} \tag{4.23}$$

where $[\mathbf{D}^e]$ is the forth-order elastic stiffness tensor, which is the inverse of $[\mathbf{C}^e]$ (i.e., $[\mathbf{D}^e] = [\mathbf{C}^e]^{-1}$).

4.4. IMPLICIT STRESS INTEGRATION (LOCAL INTEGRATION)

The stress integration is split into two parts, i.e. an elastic predictor and a plastic corrector. A first estimation of the trial stress (elastic predictor) is calculated using the elastic trial strain. Whenever the stress is identified to be outside the yield domain, it is returned back on to the yield surface iteratively via the development of plastic strain (the plastic corrector). Within a typical time step between times t and $t + \Delta t$, where Δt is the time increment, it is assumed that the state variables (e.g. stress and strain), hardening variables (here the apparent pre-consolidation pressure p_{cT}) and the absolute temperature at time t (hereafter variables at time t are indicated with n) are converged and known (i.e., the values of σ_n, ε_n, P_{cT}^n and T_n are known), and the strain and temperature increments ($\Delta \varepsilon_n$ and ΔT) are given from the BVS (global iteration). Then, the objective is to find the state variable (stress) and the hardening variable (pre-consolidation pressure) at time $t + \Delta t$ (i.e., to find the values of σ_{n+1} and P_{cT}^{n+1}). Note that when the behaviour is elasto-plastic, these variables are implicitly or explicitly dependent on the magnitude of the plastic multiplier increment (also known as the consistency variable), $\Delta \Lambda$, which also has an unknown value. Therefore, there are three unknown values that need to be calculated (σ_{n+1}, P_{cT} and $\Delta \Lambda$). The general method of developing an implicit stress integration algorithm consisting of three unknown variables, is to find three residual equations

and to minimise them simultaneously using an iterative approach such as the Newton-Raphson method. These residual equations are defined for the state variable (stress or strain), hardening variable and consistency variable.

When the elasticity relationships are derived based on a Helmholtz (strain) energy potential, the stress can be directly derived as

$$\boldsymbol{\sigma} = \frac{\partial h(\boldsymbol{\varepsilon})}{\partial \boldsymbol{\varepsilon}} \tag{4.24}$$

and is defined by strain-dependent terms. Therefore, it is possible to define the yield function and plastic flow in strain space by substituting Eq. (4.24). For the majority of constitutive models found in literature that use Helmholtz (strain) energy potential to derive elasticity relationships, strain is considered as the state variable to derive the residual equation for the state variable and consists of expressions defined by strain. However, as will be shown later, for elasticity relationships which are derived based on the Gibbs energy potential, the strain is considered to define the residual equation but is defined by terms containing stresses.

4.4.1. RESIDUAL EQUATION FOR THE STATE VARIABLE

Integrating the rate form of the total strain (Eq. (4.21)) over a time interval of $[t_n, t_{n+1}] = [t, t + \Delta t]$ results in

$$\int_t^{t+\Delta t} \dot{\boldsymbol{\varepsilon}} \, dt = \int_t^{t+\Delta t} \dot{\boldsymbol{\varepsilon}}^e \, dt + \int_t^{t+\Delta t} \dot{\boldsymbol{\varepsilon}}^{Therm} \, dt + \int_t^{t+\Delta t} \dot{\boldsymbol{\varepsilon}}^p \, dt \tag{4.25a}$$

or

$$\Delta \boldsymbol{\varepsilon} = \Delta \boldsymbol{\varepsilon}^e + \Delta \boldsymbol{\varepsilon}^{Therm} + \Delta \boldsymbol{\varepsilon}^p \tag{4.25b}$$

The temperature increment is a known value at the beginning of the integration and is passed from the global integration (finite element domain) to local integration (material model). Therefore, $\Delta \boldsymbol{\varepsilon}^{Therm}$ is calculated, based on Eq. (4.22b), as

$$\Delta \boldsymbol{\varepsilon}^{Therm} = \alpha^* \Delta T \mathbf{1} \tag{4.26}$$

The plastic strain increment ($\Delta \boldsymbol{\varepsilon}^p$) can be approximated, based on Eq. (4.22c), as

$$\Delta \boldsymbol{\varepsilon}^p \approx \Delta \Lambda \mathbf{r} \left(\boldsymbol{\sigma}_{n+1}, p_{cT}^{n+1} \right) \tag{4.27}$$

Note that integration over $\mathbf{r}$ is neglected. The advantage of this assumption is achieving accurate results with using a less complicated formulation [1].

The elastic strain increment is defined as

$$\Delta \boldsymbol{\varepsilon}^e = \boldsymbol{\varepsilon}_{n+1}^e - \boldsymbol{\varepsilon}_n^e \tag{4.28}$$

where $\boldsymbol{\varepsilon}_n^e$ is the elastic strain at time t and is a known value. By using Eq. (4.8), the elastic strain at time $t + \Delta t$, ($\boldsymbol{\varepsilon}_{n+1}^e$) is determined as

$$\boldsymbol{\varepsilon}_{n+1}^e = -\frac{\partial g_1 (\boldsymbol{\sigma}_{n+1})}{\partial \boldsymbol{\sigma}_{n+1}} \tag{4.29}$$

Substituting Eqs. (4.27), (4.28) and (4.29) in Eq. (4.25b), results in

$$\underbrace{-\frac{\partial g_1(\boldsymbol{\sigma}_{n+1})}{\partial \boldsymbol{\sigma}_{n+1}} + \Delta\Lambda \mathbf{r}\left(\boldsymbol{\sigma}_{n+1}, p_{cT}^{n+1}\right)}_{\text{unknown terms}} - \underbrace{\left(\varepsilon_n^e + \Delta\varepsilon - \Delta\varepsilon^{Therm}\right)}_{\text{known terms}} = 0 \qquad (4.30)$$

Eq. (4.30) can be split into terms with known variables ($\varepsilon_n^e + \Delta\varepsilon - \Delta\varepsilon^{Therm}$) and terms which are functions of unknown variables ($\boldsymbol{\sigma}_{n+1}$, p_{cT}^{n+1}, and $\Delta\Lambda$). Here, the summation of known variables is referred to as the elastic trial strain:

$$\varepsilon^{e,trial} = \varepsilon_n^e + \Delta\varepsilon - \Delta\varepsilon^{Therm} \qquad (4.31)$$

Whereas the trial strain remains unchanged, the unknown variables ($\boldsymbol{\sigma}_{n+1}$, p_{cT}^{n+1}, and $\Delta\Lambda$) are update iteratively to fulfil Eq. (4.30) within an accepted tolerance value. Thus, a tensor residual equation for the state variable can be defined as

$$\mathbf{R}_1 = \varepsilon_{n+1}^e + \Delta\Lambda \mathbf{r} - \varepsilon^{e,trial} = -\frac{\partial g_1}{\partial \boldsymbol{\sigma}_{n+1}} + \Delta\Lambda \mathbf{r} - \varepsilon^{e,trial} \qquad (4.32)$$

Substituting the updated values for $\boldsymbol{\sigma}_{n+1}$, p_{cT}^{n+1} and $\Delta\Lambda$ (that are obtained at the end of the iteration procedure) in Eq. (4.32) results in an approximate solution for Eq. (4.30).

4.4.2. RESIDUAL EQUATION FOR THE HARDENING VARIABLE

The only hardening variable in the model is the apparent pre-consolidation pressure, where its rate form is presented in Eq. (4.20). Considering the fact that the temperature increment is known, integrating Eq. (4.20) over a time interval of $[t_n, t_{n+1}] = [t, t + \Delta t]$ results in

$$\int_t^{t+\Delta t} \frac{\dot{p}_{cT}}{p_{cT}} \, dt = \frac{1 + e_0}{\lambda - \kappa} \int_t^{t+\Delta t} \dot{\varepsilon}_v^p \, dt - \mu_0 \int_t^{t+\Delta t} \dot{T} \, dt \qquad (4.33a)$$

$$p_{cT}^{n+1} = p_{cT}^n \exp\left(\frac{1 + e_0}{\lambda - \kappa} \Delta\varepsilon_{kk}^p - \mu_0 \Delta T\right) \qquad (4.33b)$$

where ε_{kk}^p ($k = 1, 2, 3$) is the plastic volumetric strain increment, determined as

$$\varepsilon_{kk}^p = \Delta\Lambda \, tr\left(\mathbf{r}\left(\boldsymbol{\sigma}_{n+1}, p_{cT}^{n+1}\right)\right) = \Delta\Lambda r_p\left(\boldsymbol{\sigma}_{n+1}, p_{cT}^{n+1}\right) \qquad (4.34)$$

The terms in Eq. (4.33b) update at each iteration, in accordance with the unknown variables $\boldsymbol{\sigma}_{n+1}$, p_{cT}^{n+1} and $\Delta\Lambda$. Therefore, the difference between the terms on the left and the right sides yields a residual value which needs to be minimised. Note that the residual equation for the state variable (strain), Eq. (4.32), is non-dimensional (as well as the residual equation of the consistency condition, Eq. (4.37)). To avoid the dominancy of large values of p_{cT}^{n+1} in comparison to other residual equations in the iteration process, Eq. (4.33) is normalised by p_{cT}^n. Consequently, the second residual equation is obtained as

$$R_2 = \frac{p_{cT}^{n+1}}{p_{cT}^n} - \exp\left(\frac{1 + e_0}{\lambda - \kappa} \Delta\varepsilon_{kk}^p - \mu_0 \Delta T\right) \qquad (4.35)$$

4.4.3. RESIDUAL EQUATION BASED ON THE CONSISTENCY CONDITION

As mentioned in Section 4.2, one of the advantageous of implicit stress integration approaches is that the stress state is forced to return back on to the yield surface, which implies that

$$y\left(\boldsymbol{\sigma}_{n+1}, p_{cT}^{n+1}\right) = 0 \tag{4.36}$$

The yield criterion for stress states outside the yield domain attains a non-zero and positive value (i.e. $y > 0$). Thus, it is required for y to asymptote toward zero (minimised) iteratively using the updated values of $\boldsymbol{\sigma}_{n+1}$ and p_{cT}^{n+1}. This criterion forms the third residual equation:

$$R_3 = y\left(\boldsymbol{\sigma}_{n+1}, p_{cT}^{n+1}\right) \tag{4.37}$$

4.4.4. LINEARISATION OF THE RESIDUAL EQUATIONS

The residual equations (Eqs. (4.32), (4.35) and (4.37)) need to be minimised and solved simultaneously. Linearisation is a technique that facilitates this process and involves Taylor's expansion of the residual equations with respect to the unknowns at time t_{n+1}:

$$\ell\mathbf{R}_1 = \mathbf{R}_1 + \frac{\partial \mathbf{R}_1}{\partial \boldsymbol{\sigma}_{n+1}}\delta\boldsymbol{\sigma} + \frac{\partial \mathbf{R}_1}{\partial p_{cT}^{n+1}}\delta p_{cT} + \frac{\partial \mathbf{R}_1}{\partial \Delta\Lambda}\delta\Delta\Lambda = 0$$

$$\ell R_2 = R_2 + \frac{\partial R_2}{\partial \boldsymbol{\sigma}_{n+1}}\delta\boldsymbol{\sigma} + \frac{\partial R_2}{\partial p_{cT}^{n+1}}\delta p_{cT} + \frac{\partial R_2}{\partial \Delta\Lambda}\delta\Delta\Lambda = 0 \tag{4.38a}$$

$$\ell R_3 = R_3 + \frac{\partial R_3}{\partial \boldsymbol{\sigma}_{n+1}}\delta\boldsymbol{\sigma} + \frac{\partial R_3}{\partial p_{cT}^{n+1}}\delta p_{cT} + \frac{\partial R_3}{\partial \Delta\Lambda}\delta\Delta\Lambda = 0$$

where ℓ and δ represent, respectively, the linearisation operator and the increment. Note that differentiation with respect to known values (the values at step n or values determined by known increments of $\Delta\varepsilon$ and ΔT) drop out. Eq. (4.38a) can be written in compact form as $\mathbf{J} \cdot \boldsymbol{v} = \boldsymbol{R}$, where $\mathbf{J}$, $\boldsymbol{v}$ and $\boldsymbol{R}$ are, respectively, the Jacobian matrix, vector of increments of unknown variables and residual vector, defined as

$$\mathbf{J} = \begin{bmatrix} \frac{\partial \mathbf{R}_1}{\partial \boldsymbol{\sigma}_{n+1}} & \frac{\partial \mathbf{R}_1}{\partial p_{cT}^{n+1}} & \frac{\partial \mathbf{R}_1}{\partial \Delta\Lambda} \\ \frac{\partial R_2}{\partial \boldsymbol{\sigma}_{n+1}} & \frac{\partial R_2}{\partial p_{cT}^{n+1}} & \frac{\partial R_2}{\partial \Delta\Lambda} \\ \frac{\partial R_3}{\partial \boldsymbol{\sigma}_{n+1}} & \frac{\partial R_3}{\partial p_{cT}^{n+1}} & \frac{\partial R_3}{\partial \Delta\Lambda} \end{bmatrix} = \begin{bmatrix} \mathbf{A} & \mathbf{B} & \mathbf{F} \\ \mathbf{H}^{\mathrm{T}} & \omega & \rho \\ \mathbf{E}^{\mathrm{T}} & \varpi & \vartheta \end{bmatrix} \tag{4.38b}$$

$$\boldsymbol{v} = \left\{\delta\boldsymbol{\varepsilon}_{n+1} \ \delta p_{cT}^{n+1} \ \delta\Delta\Lambda\right\}^{\mathrm{T}} \tag{4.38c}$$

$$\boldsymbol{R} = -\left\{\mathbf{R}_1 \ R_2 \ R_3\right\}^{\mathrm{T}} \tag{4.38d}$$

where $\mathbf{A}$, $\mathbf{B}$, $\mathbf{F}$, $\mathbf{H}$, $\mathbf{E}$, ω, ρ, ϖ, and ϑ are the coefficients of derivatives defined in Appendix 4.B. The unknown increments at each iteration are solved as

$$\boldsymbol{v} = \mathbf{J}^{-1} \cdot \boldsymbol{R} \tag{4.39}$$

and are added to the values obtained in the previous iteration. The iteration procedure continues until the residual values are within an acceptable tolerance range (e.g. 10^{-6}).

Instead of using Eq. (4.39) to calculate the updated unknown increments, which requires the calculation of the inverse of the Jacobian matrix ($\mathbf{J}^{-1}$), it is possible to calculate the unknown increments using a closed-form formulation. This is beneficial for obtaining a closed-form formulation for the tangent operator. Eq. (4.38a) can be re-written by using Eq. (4.38b) as

$$\mathbf{A}\delta\boldsymbol{\sigma} + \mathbf{B}\delta p_{cT} + \mathbf{F}\delta\Delta\Lambda = -\mathbf{R}_1 \tag{4.40a}$$

$$\mathbf{H}^{\mathrm{T}}\delta\boldsymbol{\sigma} + \omega\delta p_{cT} + \rho\delta\Delta\Lambda = -R_2 \tag{4.40b}$$

$$\mathbf{E}^{\mathrm{T}}\delta\boldsymbol{\sigma} + \varpi\delta p_{cT} = -R_3 \tag{4.40c}$$

From Eq. (4.40b), the increment of the hardening variable, δp_{cT}, is determined:

$$\delta p_{cT} = -\frac{1}{\omega}\left\{R_2 + \rho\delta\Delta\Lambda + \mathbf{H}^{\mathrm{T}}\delta\boldsymbol{\sigma}\right\} \tag{4.41}$$

The stress increment, $\delta\boldsymbol{\sigma}$, is determined by substituting Eq. (4.41) in Eq. (4.40a):

$$\delta\boldsymbol{\sigma} = \mathbf{W}\left\{-\mathbf{R}_1 + \frac{R_2}{\omega}\mathbf{B} - \bar{\mathbf{r}}^*\delta\Delta\Lambda\right\} \tag{4.42a}$$

where

$$\mathbf{W} = \left[\mathbf{A} - \frac{1}{\omega}\mathbf{B}\mathbf{H}^{\mathrm{T}}\right]^{-1} \tag{4.42b}$$

$$\bar{\mathbf{r}}^* = \mathbf{F} - \frac{\rho}{\omega}\mathbf{B} \tag{4.42c}$$

Substituting Eqs. (4.41) and (4.42a) in Eq. (4.40c), the increment of the plastic multiplier is calculated as

$$\delta\Delta\Lambda = \frac{R_3 - \bar{\boldsymbol{\zeta}}^{\mathrm{T}}\mathbf{W}\mathbf{R}_1 + \bar{x}R_2\bar{\boldsymbol{\zeta}}^{\mathrm{T}}\mathbf{W}\mathbf{B} - \bar{x}\varpi R_2}{\bar{x}\varpi\rho + \bar{\boldsymbol{\zeta}}^{\mathrm{T}}\mathbf{W}\bar{\mathbf{r}}^*} \tag{4.43a}$$

where

$$\bar{\boldsymbol{\zeta}}^{\mathrm{T}} = \mathbf{E}^{\mathrm{T}} - \frac{\varpi}{\omega}\mathbf{H}^{\mathrm{T}} \tag{4.43b}$$

$$\bar{x} = 1/\omega \tag{4.43c}$$

The increment of the hardening variable is then determined in a straightforward manner via Eq. (4.40c) as

$$\delta p_{cT} = -\frac{1}{\varpi}\left(R_3 + \mathbf{E}^{\mathrm{T}}\delta\boldsymbol{\sigma}\right) \tag{4.44}$$

The steps of the stress integration algorithm are summarised in Box 4.1.

Box 4.1: Description of the steps for developing the implicit stress integration algorithm (continued on next page)

1. Update the temperature (known value)

$$T_{n+1} = t_n + \Delta T$$

- Compute the thermo-elastic strain via Eq. (4.26)

- Compute the Critical State stress ratio via Eq. (4.18)

2. Compute the elastic trial strain tensor, $\varepsilon^{e,trial}$, via Eq. (4.31)

- Calculate the volumetric and deviatoric invariants of the elastic trial strain using

$$\varepsilon_v^{e,trial} = tr\left(\varepsilon^{e,trial}\right)$$
$$\varepsilon_s^{e,trial} = \sqrt{2/3}\left(\mathbf{e}^{e,trial} : \mathbf{e}^{e,trial}\right)^{1/2}$$
$$\mathbf{e}^{e,trial} = \varepsilon^{e,trial} - tr\left(\varepsilon^{e,trial}\right)/3 : \mathbf{1}$$

3. Estimate the trial stress (elastic predictor)

- Estimate the hydrostatic pressure, p^{trial}, and the deviatoric trial stresses, q^{trial}, via Eqs. (4.F.3a) and (4.F.3b) in Appendix 4.F (or alternatively Eqs. (4.F.4a) and (4.F.4b)), respectively

- Determine the direction of the deviatoric part of the trial stress by considering that the deviatoric strain and deviatoric stress tensors are coaxial (see Appendix 4.E)

$$\hat{\mathbf{n}} = \frac{\mathbf{e}^{e,trial}}{\|\mathbf{e}^{e,trial}\|} = \sqrt{\frac{2}{3}}\frac{\mathbf{e}^{e,trial}}{\varepsilon_s^{e,trial}}$$

- Determine the trial stress tensor via

$$\boldsymbol{\sigma}^{trial} = p^{trial}\mathbf{1} + \sqrt{\frac{2}{3}}q^{trial}\hat{\mathbf{n}}$$

4. Set the initial values of variables by assuming elastic conditions

- The apparent pre-consolidation pressure is set to its value at time step t ($p_{cT} = p_{cT}^n$)

- The increment of plastic multiplier is set to zero ($\Delta\Lambda = 0$)

5. Check the yield condition via Eq. (4.14) with the estimated trial stress

- If $y\left(\boldsymbol{\sigma}^{trial}\right) < 0$, then

i. $\sigma_{n+1} = \sigma^{trial}$; $p_{cT}^{n+1} = p_{cT}^{n}$; $\Delta\Lambda = 0$

ii. Set the tangent operator stiffness matrix equal to elastic tangent stiffness, Eq. (4.E.11) in Appendix 4.E

- If $y(\sigma^{trial}) \geq 0$, then: iteration process

i. While $|\boldsymbol{R}| \leq$ tol $(= 10^{-6})$ (residuals are not in the range of accepted tolerance)

❖ Compute the invariants of the trial stress σ^{trial}

❖ Compute the flow rule and derivatives with respect to the trial stress σ^{trial} and p_{cT}

❖ Calculate the residuals via Eqs. (4.32), (4.35) and (4.37)

❖ Calculate the increments of unknowns via Eqs. (4.42), (4.43) and (4.44)

❖ Update the unknowns
$\sigma_{i+1} = \sigma_i + \delta\sigma$; $(p_{cT})_{i+1} = (p_{cT})_i + \delta p_{cT}$; $\Delta\Lambda_{i+1} = \Delta\Lambda_i + \delta\Delta\Lambda$
where i is the iteration number

ii. Update σ, p_{cT} and $\Delta\Lambda$, based on the values calculated in the last iteration that was converged

iii. Calculate the tangent operator stiffness matrix, Eq. (4.48)

4.4.5. TANGENT OPERATOR STIFFNESS MATRIX

During the iteration procedure, the residuals (Eqs. (4.32), (4.35) and (4.37)) asymptote toward zero (i.e. converging). When the variables are converged (i.e., within a set tolerance range), Eqs. (4.30), (4.33b) and (4.37) are approximated; i.e.

$$-\frac{\partial g_1(\sigma_{n+1})}{\partial(\sigma_{n+1})} + \Delta\Lambda\mathbf{r}(\sigma_{n+1}, p_{cT}^{n+1}) - \left(\varepsilon_n^e + \Delta\varepsilon - \varepsilon^{Therm}\right) \approx 0 \tag{4.45a}$$

$$\frac{p_{cT}^{n+1}}{p_{cT}^{n}} - \exp\left(\frac{1+e_0}{\lambda-\kappa}\Delta\varepsilon_{kk}^p - \mu_0\Delta T\right) \approx 0 \tag{4.45b}$$

$$y\left(\sigma_{n+1}, p_{cT}^{n+1}\right) \approx 0 \tag{4.45c}$$

These equations are defined by terms including variables σ_{n+1}, p_{cT}^{n+1} and $\Delta\Lambda$. Taking the time derivative (rate) of these equations with respect to their variables and linearising, yields a set of equations similar to Eq. (4.38a):

$$\hat{\mathbf{A}}\delta\sigma + \hat{\mathbf{B}}\delta p_{cT} + \hat{\mathbf{F}}\delta\Lambda = \delta\varepsilon \tag{4.46a}$$

$$\hat{\mathbf{H}}^{\mathrm{T}} \delta \boldsymbol{\sigma} + \hat{\omega} \delta p_{cT} + \hat{\rho} \delta \Lambda = 0 \tag{4.46b}$$

$$\hat{\mathbf{E}} \delta \boldsymbol{\sigma} + \hat{\bar{\omega}} \delta p_{cT} = 0 \tag{4.46c}$$

where, by using the coefficients defined in Eq. (4.38b), it follows that

$$\hat{\mathbf{A}} = \mathbf{A}; \quad \hat{\mathbf{B}} = \mathbf{B}; \quad \hat{\mathbf{F}} = \mathbf{F}; \quad \hat{\mathbf{H}}^{\mathrm{T}} = \mathbf{H}^{\mathrm{T}}; \quad \hat{\omega} = \omega \quad \hat{\rho} = \rho; \quad \hat{\mathbf{E}}^{\mathrm{T}} = \mathbf{E}^{\mathrm{T}}; \quad \hat{\bar{\omega}} = \bar{\omega} \tag{4.46d}$$

Note that the known terms, such as the variables at step n and the thermo-elastic strain increment ($\Delta \varepsilon^{Therm}$), are known values and do not vary over time, whereas the strain tensor increment, $\Delta \varepsilon$, is treated as a variable, where $\partial \Delta \varepsilon / \partial t = \partial \varepsilon$. Following a similar approach as those of determining the increments of unknown variables (i.e., Eqs. (4.42), (4.44) and (4.43)), the estimated stress tensor increment and plastic multiplier increment are

$$\delta \boldsymbol{\sigma} = \mathbf{W} \left\{ \delta \varepsilon - \bar{\mathbf{r}}^{*} \delta \Lambda \right\} \tag{4.47a}$$

$$\delta \Lambda = \frac{\bar{\boldsymbol{\zeta}}^{\mathrm{T}} \mathbf{W}}{\bar{x} \bar{\omega} \rho + \bar{\boldsymbol{\zeta}}^{\mathrm{T}} \mathbf{W} \bar{\mathbf{r}}^{*}} \delta \varepsilon \tag{4.47b}$$

Further, substituting Eq. (4.47b) in Eq. (4.47a) results in a formulation which represents the tangent operator stiffness matrix:

$$\delta \boldsymbol{\sigma} = \left\{ \mathbf{W} - \mathbf{W} \frac{\boldsymbol{\zeta}^{\mathrm{T}} \mathbf{W} \bar{\mathbf{r}}^{*}}{\bar{x} \bar{\omega} \rho + \bar{\boldsymbol{\zeta}}^{\mathrm{T}} \mathbf{W} \bar{\mathbf{r}}^{*}} \right\} \delta \varepsilon = \mathbf{D}_{O} \delta \varepsilon \tag{4.48}$$

4.5. ACCURACY, ROBUSTNESS AND EFFECTIVENESS OF THE STRESS INTEGRATION ALGORITHM

To demonstrate the robustness and effectiveness of the proposed stress integration algorithm, several aspects were investigated, including the shape of the yield surface, number of iterations required for the algorithm to return the stress back on to the yield surface (iteration-stress map) for trial stresses varying in magnitude and direction, and Gudehus plots which demonstrate the stress response when the algorithm is subjected to strain probes. In addition, iso-error plots for yield surfaces with different shape parameters subjected to trial stresses varying in magnitude and direction were analysed to assess the accuracy of the proposed algorithm.

4.5.1. FORM OF THE YIELD SURFACE

The influence of the form of the yield function was investigated in Chapter 3. It was demonstrated that the form of the yield function significantly affects the efficiency and robustness of the implicit stress integration algorithm, mostly due to false elastic nuclei and erratic gradients (singularities). The level sets of the normalised yield function given in Eq. (4.14) with the proposed stress-like functions (Eq. (4.16)) for a range of shape parameters α and γ are shown in normalised stress space in Figure 4.4. It is observed that

the normalised form of the yield function has no false elastic nuclei or erratic gradients, and thus is very suitable for implicit stress integration algorithms (see Chapter 3 for more details).
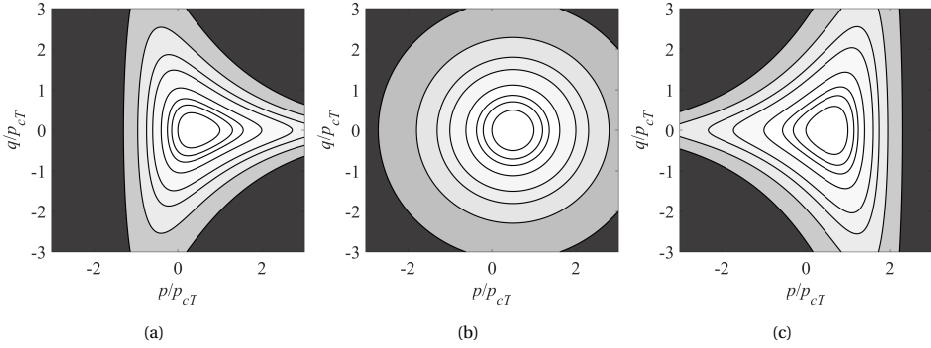

Figure 4.4: Level sets (contours) of the yield function ([0, 1, 2, 4, 8, 12, 20, 40] from inside to outside) using Eq. (4.14) for different shape parameters (a) $\alpha = \gamma = -0.5$; (b) $\alpha = \gamma = 0$ (MCC); (c) $\alpha = \gamma = 0.5$

4.5.2. ITERATION-STRESS MAPS

Starting from an isotropic stress state at the reference pressure, $(p, q) = (p_a, 0)$, and considering isothermal conditions (no temperature variation), the model was subjected to several trial stresses which were related to the hydrostatic extent of the yield surface, p_{cT}, such that the region $p^{trial}/p_{cT} \in [0, 3]$ and $q^{trial}/p_{cT} \in [0, 3]$ in meridian stress space (p-q) was explored. The following parameters where used for the simulations: $\bar{K} = 700$, $\bar{G} = 200$, $n = 0.5$, $\lambda = 0.20$, $\kappa = 0.09$, $M_{c0} = 1.05$, $\rho^* = 0.8$, and p_{cT} was set to 200 kPa. The strain increments inducing these trial stresses were determined and applied in a single step. The number of iterations (NOI) required to converge the trial stresses, i.e., to return them back on to the yield surface by using the stress integration algorithm, were measured and are plotted in Figure 4.5 for three yield surfaces with shape parameters $\alpha = \gamma = -0.5$, $\alpha = \gamma = 0$ and $\alpha = \gamma = 0.5$ (similar to the yield surfaces/functions in Figure 4.1 and Figure 4.4). Note that the maximum allowed NOI was set to 25.

From Figure 4.5, it was observed that for all yield surfaces the NOIs were less than 11, i.e., all the trial stresses were returned back on to the yield surface. It is seen, as expected, that the larger the trial stresses applied (in terms of magnitude), the higher the NOI required for convergence. The MCC model ($\alpha = \gamma = 0$) had the lowest NOI (Figure 4.5b); the trial stresses in the studied stress domain were mostly converged within 7 iterations (8 iterations were required only for trial stresses close to $p^{trial}/p_{cT} = 3$ and $q^{trial}/p_{cT} = 3$). Yield surfaces with $\alpha = \gamma = -0.5$ and $\alpha = \gamma = 0.5$ had, respectively, higher curvature (gradients) near the compression apex (i.e. $p = p_{cT}$) and decompression apex (i.e. at the origin, $p = 0$). The former yield surface required a maximum of 11 iterations to converge trial stresses (close to $p^{trial}/p_{cT} = 3$ and $q^{trial}/p_{cT} = 3$), while all the trial stresses investigated for the latter yield surface were returned back on to the surface with a maximum of 9 iterations.

4.5.3. GUDEHUS PLOTS

It is essential that the return mapping algorithm can return trial stresses, induced by strain increments, at any location and direction in three-dimensional stress space. The following example demonstrates the robustness of the stress integration algorithm to address this necessity. The parameters of the model were set to $\alpha = \gamma = 1.0$, $n = 0.5$, $\lambda = 0.21$, $\kappa = 0.02$, $M_{c0} = 0.8$, $\rho^* = 0.8$, and the hydrostatic extent of the yield surface was set to $p_{cT} = 200$ kPa.

64 locations on the yield surface (total number of clouds), defined in principle stress space (σ_1-σ_2-σ_3), were randomly selected to check the robustness of the return mapping algorithm at any stress state. At each location, the model was subjected to 832 strain probes (increments) in all directions in principle strain space (ε_1-ε_2-ε_3) with an equal magnitude of 1×10^{-3} (1000 micron); i.e., at each location on the yield surface the return mapping algorithm was subjected to a strain sphere with radius of 1000 micron. The directions of the individual strain probes were obtained using the HEALPix software [52], which divided the surface of the sphere into equal area patches. The stress response to these strain probes (also known as Gudehus surfaces [53]) are shown in Figure 4.6a and Figure 4.6b for models with elastic moduli parameters of $\bar{K} = 150$ and $\bar{G} = 90$ ($\bar{K}/\bar{G} = 1.67$) and $\bar{K} = 60$ and $\bar{G} = 100$ ($\bar{K}/\bar{G} = 0.6$), respectively. The surfaces (clouds) are shaded according to the degree of dissipated work, calculated as

$$w^p = \boldsymbol{\sigma} : \dot{\boldsymbol{\varepsilon}}^p \tag{4.49}$$

where bright areas demonstrate where dissipation happened (i.e. the return mapping algorithm was activated) in accordance to the strain probes. Although both models were subjected to the same isotropic strain spheres, the stress responses (clouds) varied in size and shape. For strain probes that were toward the inside of the yield surface, the stresses were identical to the trial stresses (elastic predictor) and formed the part of the stress sphere (cloud) with greater radius (darker areas on the stress cloud). On the other hand, for strain probes directed outside of the yield surface, stress responses were determined via the elasto-plastic relation (using the stress return algorithm). For those strain probes where plastic work developed, the stress integration algorithm returned the stress back onto the yield surface (brighter areas on the stress cloud). Therefore, the stress was smaller than the trial stress and consequently formed the part of the stress cloud with smaller radius.

It was observed that the size of a stress response cloud varied with the hydrostatic pressure (p) corresponding to its location. This behaviour is attributed to the non-linear and pressure dependency of the constitutive elastic relations of the model. For strain increments probing at regions with low hydrostatic pressures (near the decompression apex), the corresponding stress clouds were smaller in size compared to stress clouds located near the compression apex of the yield surface with higher hydrostatic pressures.

The ratio of parameters corresponding to the elastic bulk and elastic shear moduli, $\bar{K}/\bar{G}$, governed the shape of the stress clouds. For the model using $\bar{K} > \bar{G}$, the stress clouds were elongated along the hydrostatic axis (Figure 4.6a), while for the model in which $\bar{G} > \bar{K}$, the stress clouds were flattened in the deviatoric plane. In conclusion, the non-linear elasticity employed for the model played an important role on the response of the model.

4
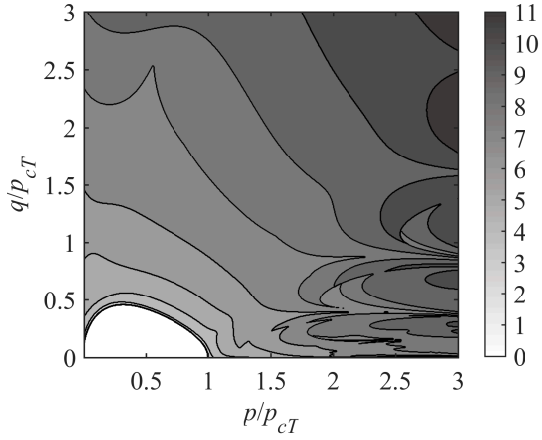
(a)
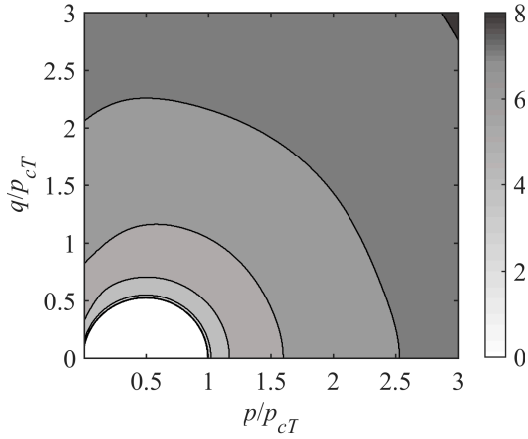
(b)
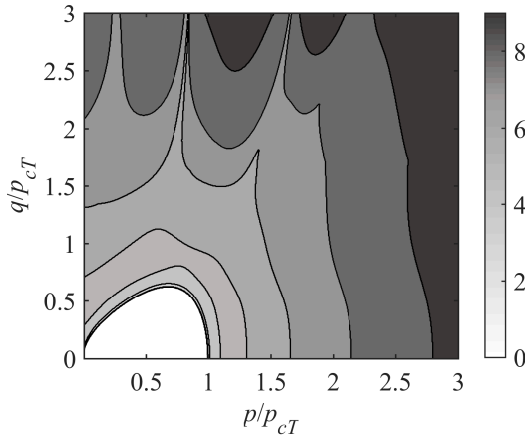
(c)

Figure 4.5: Number of iterations of the stress integration algorithm for various trial stress locations for yield surfaces with shape parameters (a) $\alpha = \gamma = -0.5$; (b) $\alpha = \gamma = 0$ (MCC); (c) $\alpha = \gamma = 0.5$
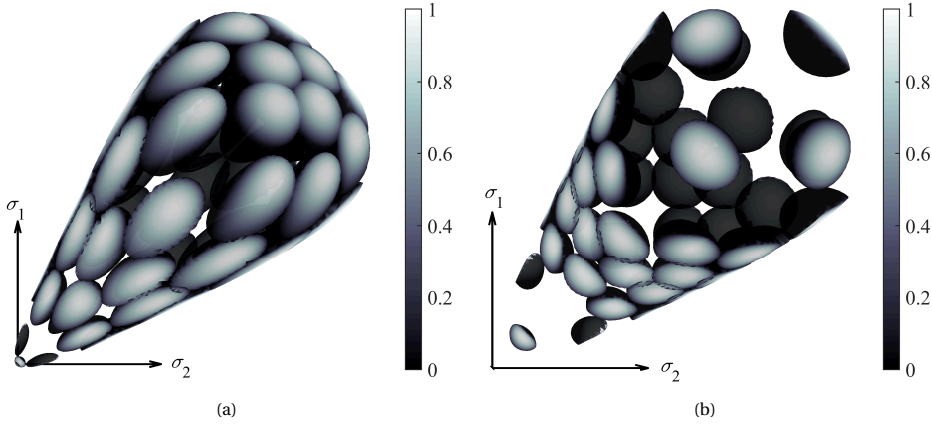
Figure 4.6: Stress response of the model in principle stress space (Gudehus plots) with elastic moduli
(a) $\bar{K}/\bar{G} = 1.67$; (b) $\bar{K}/\bar{G} = 0.6$. Stress responses are shaded according to the degree of dissipated work, where
dark areas correspond to elastic response and white areas represents elasto-plastic response

4.5.4. ISO-ERROR PLOTS

The accuracy of the stress integration algorithm on returning trial stresses back on to the
yield surface was investigated by studying the iso-error contours for yield surfaces with
different shapes. The parameters of the model were set to $\bar{K} = 250$, $\bar{G} = 400$, $n = 0.7$,
$\lambda = 0.45$, $\kappa = 0.05$, $M_{c0} = 0.7$, $\rho^* = 0.8$, and the yield surface was bounded at $p_{cT} = 200$
kPa. The trial stresses in the deviatoric plane were related to the deviatoric yield stress q_y
(calculated via Eq. (4.14)) at a specific hydrostatic pressure, so as to have a normalised
magnitude of $q^{trial}/q_y \in [1,7]$ and a direction corresponding to a Lode angle varying in
the range of $\theta \in [-\pi/6, \pi/6]$. Elastic deviatoric strains corresponding to trial deviatoric
stresses were calculated. Starting from an isotropic state at the desired normalised hy-
drostatic pressure ($p/p_{cT} = 0.2, 0.4, 0.6, 0.8$ and 0.95), the model was subjected to these
elastic deviatoric strains in a single step. The results (i.e. returned stresses σ_r) were then
compared with the returned stresses (σ_e), which were obtained by dividing each single
elastic daviatoric strain into 1000 sub-increments. The errors were then calculated using
the following equation:

$$\text{error} = \frac{\sqrt{\{\sigma_r - \sigma_e\} : \{\sigma_r - \sigma_e\}}}{\sqrt{\sigma_e : \sigma_e}} \tag{4.50}$$

where σ_r is the return stress when the model was subjected to the single elastic devia-
toric strain and σ_r is the (almost exact) returned stress obtained by splitting the single
elastic trial strain into 1000 sub-increments. The errors were measured in deviatoric
planes located at $p/p_{cT} = 0.95, 0.8, 0.6, 0.4$ and 0.2, and each is shown in Figure 4.7 in
one sixth of the deviatoric plane of the principle stress space, for three yield surfaces
with shape parameters $\alpha = \gamma = -0.5$ $\alpha = \gamma = 0$ and $\alpha = \gamma = 0.5$ (respectively, Figure 4.7a,
Figure 4.7b and Figure 4.7c). Respectively, in Figure 4.7d, Figure 4.7e and Figure 4.7f, the
corresponding numbers of iterations (NOI) required for converging the elastic deviatoric
strains when they are subjected in one step are presented. The errors and NOI to return

the trial stresses were observed, as expected, to increase when the stress integration algorithm was subjected to larger elastic deviatoric strains.

For all models, the smallest errors were measured at the deviatoric plane located at a normalised hydrostatic pressure of $p/p_{cT} = 0.95$ (region (I) near the compression apex), although it required the highest NOIs to pull-back the trial stress on to the yield surface. In addition, at the deviatoric plane near the decompression apex (region (V) for all models where $p/p_{cT} = 0.2$), the returned stresses had the largest deviation from the exact solution. These errors were higher for the yield surface with shape parameters $\alpha = \gamma = 0.5$, compared to the other two surfaces; up to 20% errors were measured for the elastic trial strains that were almost seven times larger than the deviatoric yield value ($q^{trial}/q_y \approx 7$).

All trial stresses on the deviatoric planes located at $p/p_{cT} \geq 0.6$ (regions (I), (II) and (III)) were returned back on to the yield surface with high accuracy (errors less than 4%). Errors started to build up as p/p_{cT} decreased. A maximum error of 10% was measured for trial stresses on the deviatoric planes located at $p/p_{cT} = 0.4$ and normalised magnitudes of $q^{trial}/q_y = 7$, which is a reasonable result for such large strain increments.

In conclusion, the proposed stress integration algorithm maps large elastic deviatoric strains at deviatoric planes located at $p/p_{cT} \geq 4$ on to the yield surface with high accuracy. For deviatoric planes located at low hydrostatic pressures (e.g. $p/p_{cT} < 0.4$), smaller elastic strains converged with a reasonable accuracy.
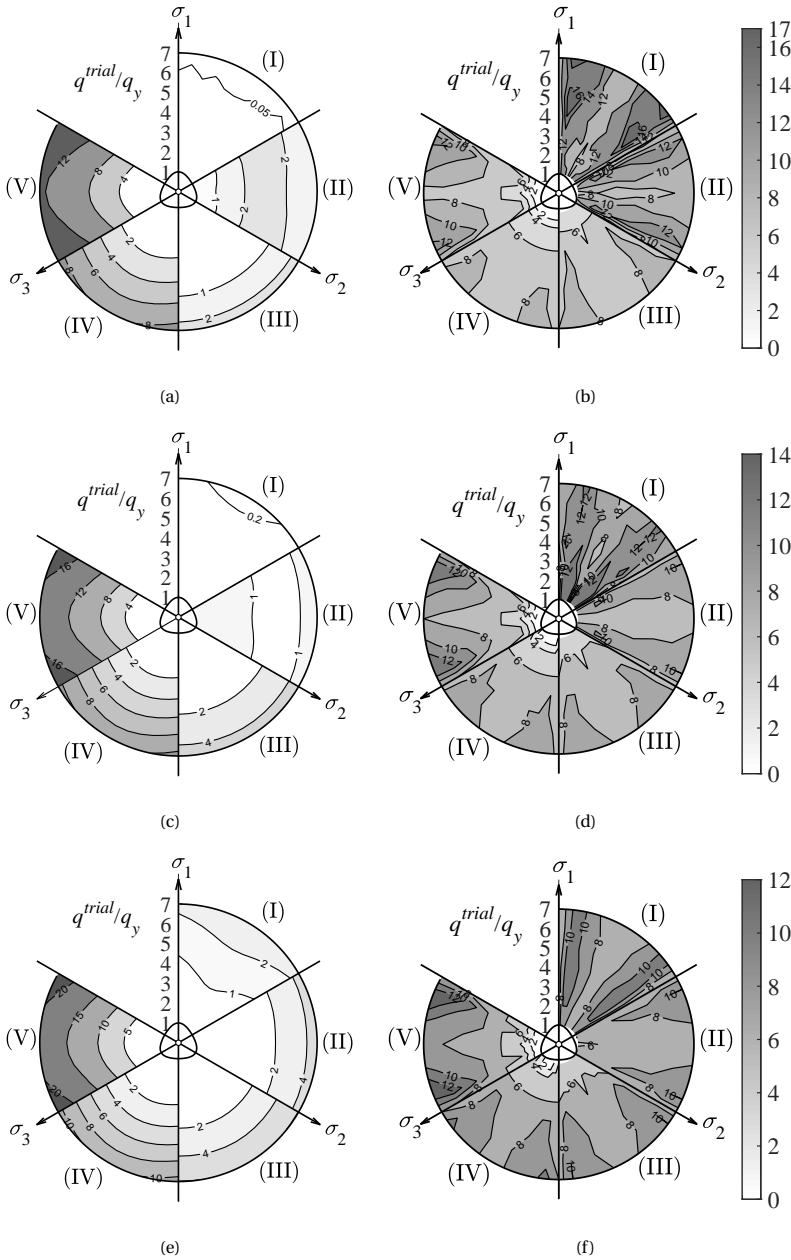
Figure 4.7: Maps of iso-error (left) and numbers of iterations (right) required for convergence corresponding to the single elastic trial strain on deviatoric planes located at (I) $p/p_{cT} = 0.95$, (II) $p/p_{cT} = 0.8$, (III) $p/p_{cT} = 0.6$, (IV) $p/p_{cT} = 0.4$, (V) $p/p_{cT} = 0.2$ (a) and (b) for the model with $\alpha = \gamma = -0.5$; (c) and (d) for the model with $\alpha = \gamma = 0$; (e) and (f) for the model with $\alpha = \gamma = 0.5$.

4.5.5. CONVERGENCE ANALYSIS AT THE MATERIAL POINT (GAUSSIAN POINT)

The effectiveness of the proposed return mapping algorithm was investigated by analysing the stress convergence at different locations on a stress path, at the material point (Gauss point) level. Material parameters were set to $\bar{K} = 50$, $\bar{G} = 150$, $n = 1$, $\lambda = 0.15$, $\kappa = 0.03$, $M_{c0} = 0.85$, $\rho^* = 0.8$ and $\alpha = \gamma = 0.5$, and the hydrostatic extent of the yield surface was initially set to $p_{cT} = p_a$. The material was subjected to drained isotropic compression starting from an isotropic stress state at the reference pressure, $(p, q) = (p_a, 0)$ to $(p, q) = (400\,\text{kPa}, 0)$. This was followed by shearing of the material under undrained conditions by subjecting the return mapping algorithm to strain increments of $\Delta \boldsymbol{\varepsilon} = 1 \times 10^{-4}$ [1 0 0; 0 -0.5 0; 0 0 -0.5]. The stress path in p-q stress space and the deviatoric stress versus deviatoric strain curve are shown, respectively, in Figure 4.8a and Figure 4.8b. Three points on the stress path, corresponding to loading steps of 5, 30 and 200 (demonstrated by open circles on the stress path and stress-strain curves in Figure 4.8a) were selected to investigate the convergence behaviour of the residuals ($|\mathbf{R}_1|$, R_2 and R_3) and residual stress. These loading steps were specifically selected to assess the convergence behaviour at the initial stage of shearing (step 5), Critical State conditions (step 200) and a location on the stress-strain curve with the highest change in gradients (step 30). The convergence of the residual stress, R_σ, was measured via

$$R_\sigma = \sqrt{\left(\boldsymbol{\sigma}^{est} - \boldsymbol{\sigma}^*\right) : \left(\boldsymbol{\sigma}^{est} - \boldsymbol{\sigma}^*\right)} \tag{4.51}$$

where $\boldsymbol{\sigma}^{est}$ is the estimated stress at each iteration and $\boldsymbol{\sigma}^*$ is the stress at the end of the iteration process.

The convergence of residuals, $|\mathbf{R}_1|$, R_2 and R_3, and their rate of convergence are, respectively, shown for each of the studied loading steps in Figure 4.8c and Figure 4.8d. In Figure 4.8e the residual stresses at each iteration, normalised with respect to the initial residual stress, are shown for each of the studied loading steps. It was observed that convergence of the residuals and stress residuals were obtained with 4 iterations for all loading steps with a quadratic pattern; i.e., the residuals and residual stresses reduced and converged quadratically. This is also demonstrated in Figure 4.8d and Figure 4.8f, where the residuals and residual stresses at each iteration are plotted against their corresponding previous step. The gradients of these lines indicated that the convergence rates for all the studied steps were equal or close to a value of two, which represented a quadratic convergence rate.
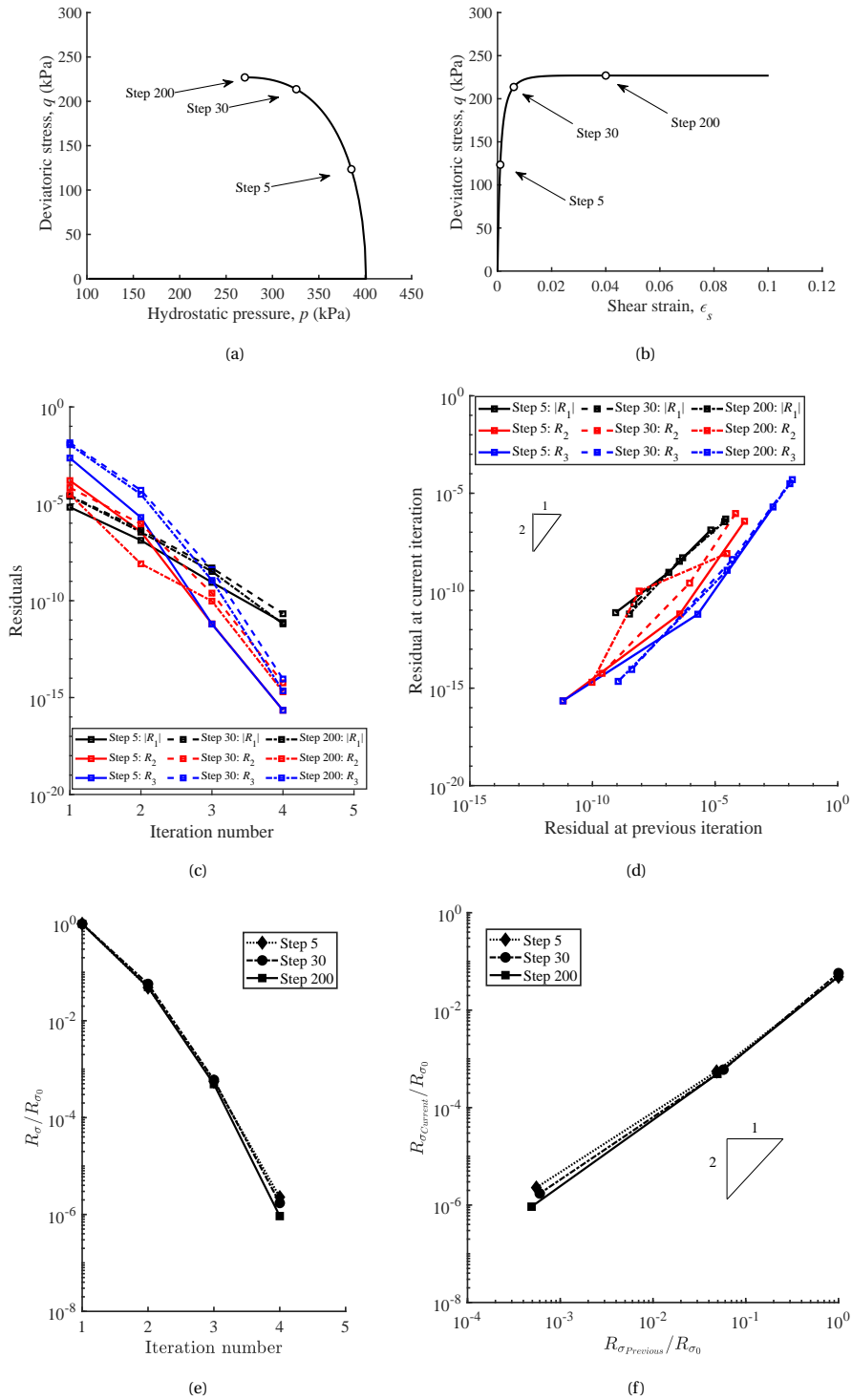
Figure 4.8: (a) Stress path in p-q stress space; (b) stress-strain curve; (c) residuals with respect to iteration number; (d) rate of convergence of residuals for the studied loading step; (e) normalised residual stress with respect to iteration number for the studied loading steps; (f) rate of convergence of residual stress for the studied loading step

4.6. NUMERICAL EXAMPLES

In Section 4.5 the performance of the return mapping algorithm was investigated locally on a Gaussian point. However, it is also essential to check the stability of the algorithm within the context of a finite element formulation when the algorithm is subjected to thermo-mechanical stress paths and when using different material parameters. Therefore, the implicit stress integration algorithm of the current thermomechanical model was implemented in the DIANA FEA finite element software via a user-defined subroutine. DIANA FEA supports the use of user-defined material models with hydro and thermal analyses in a fully coupled solution procedure. In this section, DIANA FEA is used to investigate the thermo-mechanical behaviour of fine-grained soils observed in triaxial and oedometer experimental soil mechanics tests subjected to various thermomechanical stress paths, along with a sensitivity analysis on the parameters of the material model.

4.6.1. TRIAXIAL TEST

A schematic view of the triaxial test is shown in Figure 4.9a. A cylindrical fine-grained soil specimen, with a height and diameter of 200 mm and 100 mm, respectively, is bounded between rigid plates on the top and the bottom. The specimen is subjected to a hydrostatic pressure σ_3 and an axial stress σ_1, which is the addition of σ_3 and σ_d (the deviatoric stress). Due to symmetry of the loading, boundary conditions and geometry, this test was modelled with a 2D axisymmetric formulation in FEM. The finite element model incorporating boundary conditions and FE mesh are shown in Figure 4.9b. The bottom rigid plate is modelled via vertical supports in which vertical displacements at bottom nodes were prevented. The top rigid plate applies uniformly distributed vertical displacements to the top of the soil specimen. This was modelled by relating the displacements of the top nodes of the soil specimen (slave nodes) to the displacement of the master node located at the top (along the axis of symmetry). The axial force is then applied on the master node. Therefore, any displacements, due to vertical force applied on this node, results in the same amount of displacement for all the nodes at the top of the soil specimen. Also, the hydrostatic pressure was modelled by applying a traction to the nodes on the right boundary of the soil specimen.

TRIAXIAL REFERENCE MODEL (TRM)

The soil specimen in the triaxial reference model is subjected to three thermomechanical stress path phases:

1. *Initial phase*: A normally consolidated soil with an apparent pre-consolidation pressure (p_{cT}) set to 50 kPa is subjected to an internal and external hydrostatic pressure of $\sigma_3 = 50$ kPa at ambient temperature ($T = 20°C$) (the material is initially in an isotropic stress state);

2. *Heating phase*: While the hydrostatic pressure was kept constant and the specimen was free to expand/shrink radially, the specimen was incrementally heated from the top, bottom and side boundaries to the target temperature $T = 40°C$. Sufficient time was allowed to reach a uniformly distributed temperature in all the elements.

3. *Mechanical phase*: After the completion of the heating phase, the axial load on the top boundary of the specimen was increased with displacement-controlled increments to reach a deviatoric strain (ε_s) level of 0.4 (40 %).

The above procedure represents a triaxial test subjected to compression and heating under drained conditions, where the material followed a stress path with $\Delta q/\Delta p = 3$ in the mechanical compression phase (Figure 4.10a).
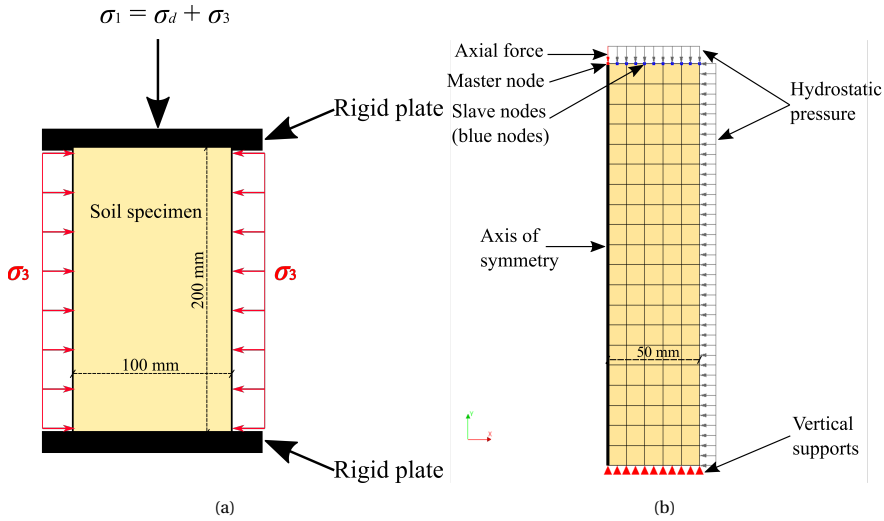

Figure 4.9: (a) Schematic view of triaxial test in the laboratory; (b) Finite element model of the triaxial test in DIANA FEA software
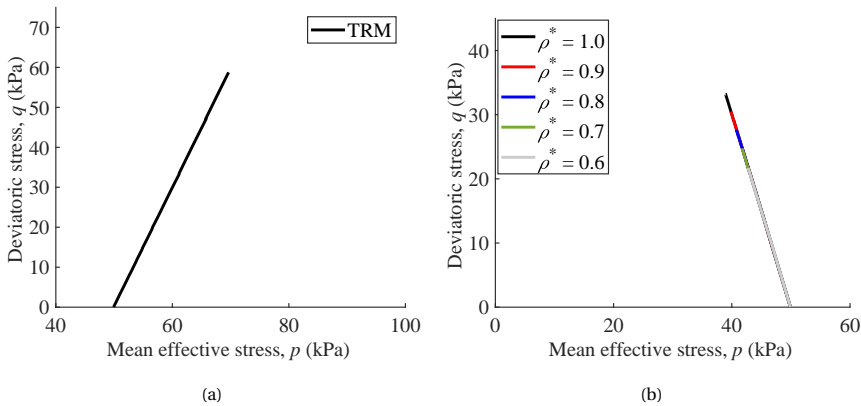

Figure 4.10: (a) Stress path of the reference model (triaxial compression test); (b) triaxial extension test stress paths
* TRM: Triaxial reference model

The parameters used in the reference model are presented in Table 4.2.

Table 4.2: Model parameters

α (-)	γ (-)	ρ^* (-)	M_{c0} (-)	π^* (1/K)	$\tilde{G}$ (-)	$\tilde{K}$ (-)	n (-)	λ (-)	κ (-)	μ_0 (1/K)	α^* (1/K)
0	0	1.0	0.85	0.000	900	350	0.5	0.2	0.09	0.005	$-3.04 * 10^{-5}$

In the following tests, the influence of the material parameters on the thermomechanical response of the specimen is studied.

In Figure 4.11 the thermomechanical response of FEM models, subjected to target temperatures of 20°C (not heated), 60°C and 80 °C in the heating phase, are compared to the response of the reference model (heated to 40°C). The material parameters of the reference model were used for all the simulations. It is observed that, as the temperature increased, the thermally induced volumetric strains (developed during the heating phase) increased (i.e., the material shrank more) (Figure 4.11a and Figure 4.11c), which is consistent with laboratory observations. Figure 4.11b shows the variation of deviatoric stress (q) versus deviatoric strain (ε_s) of all the models, which followed the same curve of the reference model. This response is due to the use of a temperature-independent Critical State parameter ($\pi^* = 0$). Therefore, all the models reached the same deviatoric stress when subjected to mechanical loads.

The effect of the thermal shrinkage parameter μ_0 on the thermomechanical response of the material is shown in Figure 4.12. Both simulations (i.e., the reference model using $\mu_0 = 0.005$ and $\mu_0 = 0.010$) were heated from the ambient temperature to 40°C in the heating phase. It is observed from Figure 4.12a and Figure 4.12c that, as μ_0 increased, a larger thermally-induced volumetric strain was produced during the heating phase.

Figure 4.13 presents the effect of temperature-dependency of the Critical State parameter (π^*) on the thermomechanical behaviour of the model. The thermomechanical responses of two simulations with $\pi^* = 0.002$ and $\pi^* = -0.002$ (while other parameters remained identical to those of the reference model) are compared to the response of the reference model ($\pi^* = 0$). The parameter did not affect the thermally-induced volumetric strain during heating. This behaviour is due to the freedom of the specimen to expand/shrink during heating (i.e., no vertical and radial constraints). However, as the material is subjected to mechanical loads, the models using $\pi^* = 0.002$ and $\pi^* = -0.002$ reached a higher and lower deviatoric stress (and therefore Critical State stress ratio), respectively, compared to the deviatoric stress of the reference model ($\pi^* = 0$) (Figure 4.13b). Due to the development of shear stresses and shear strains during mechanical loading, the mechanically-induced volumetric strains are influenced by the parameter which increased as π^* increased (Figure 4.13a and Figure 4.13c).

The effect of the shape parameters (α and γ) on the response of the material subjected to identical thermo-mechanical stress paths as the reference model ((α, γ) = (0,0); i.e., the MCC elliptical shape) are presented in Figure 4.14 for yield surfaces using (α, γ) = (0.5, 0.5) and (α, γ) = (−0.5, −0.5) (yield surfaces similar to Figure 4.1). It is evident that, in comparison with the reference model, a softer or stiffer response can be predicted by altering the shape parameters (while other parameters remain identical to the reference model). With the use of the yield surface with shape parameters (α, γ) = (0.5, 0.5) a stiffer deviatoric response and lower volumetric response was obtained, while a softer deviatoric behaviour accompanied with higher volumetric strain was observed when using the yield surface (α, γ) = (−0.5, −0.5).
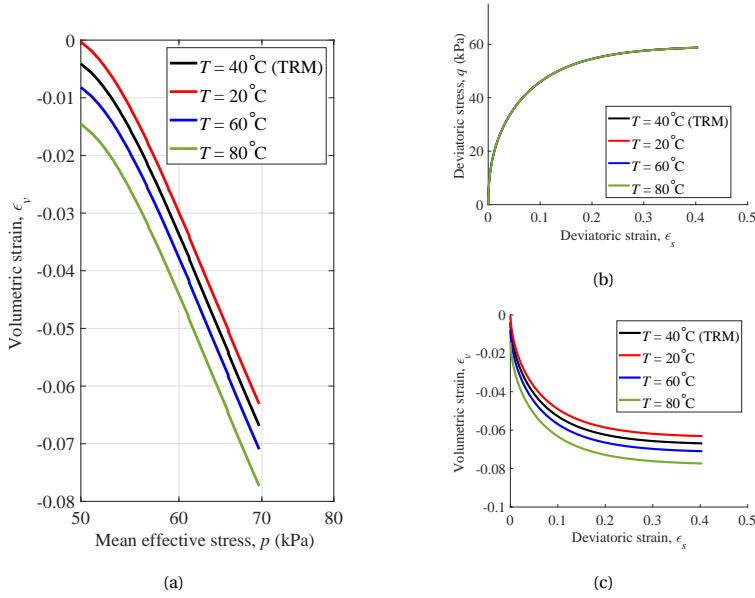
Figure 4.11: Effect of temperature on the material's thermomechanical response in triaxial test (a) ε_v vs. p; (b) q vs. ε_s; (c) ε_v vs. ε_s

* TRM: Triaxial reference model
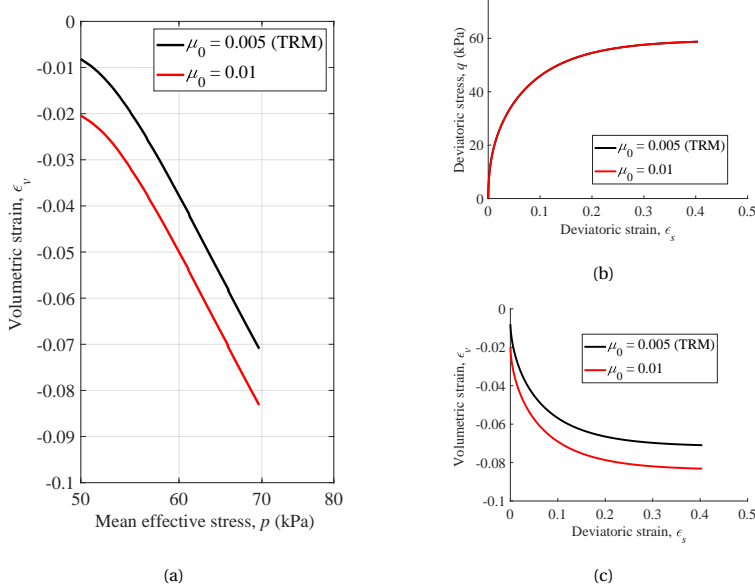
Figure 4.12: Effect of parameter μ_0 on the material's thermomechanical response in triaxial test (a) ε_v vs. p; (b) q vs. ε_s; (c) ε_v vs. ε_s

* TRM: Triaxial reference model

The effect of over-consolidation ratio (OCR = p/p_{cT}) is shown in Figure 4.15. In the *initial phase* step, the initial apparent pre-consolidation pressures (p_{cT}) were set to 50 (the reference model), 75, 150, 200, 250 and 300 kPa to form initial stress states at OCRs of 1.0, 1.5, 3.0, 4.0, 5.0 and 6.0, respectively. During the *heating phase* no thermally-induced plastic strains were produced for models with OCR > 1 and the material responded thermo-elastically (Figure 4.15a). During the mechanical loading phase, an elastic response was observed for models with OCR > 1 until the stress state of the material encountered the yield surface, after which an elasto-plastic response was obtained (Figure 4.15a). As the OCR increased, a larger dilation was observed (i.e., increase in volumetric strain) (Figure 4.15a and Figure 4.15c). In addition, higher peak deviatoric stresses were obtained for models with higher OCRs, followed by a softening in which all the models reached an identical deviatoric stress at large deviatoric strains, indicating that the Critical State conditions were reached (Figure 4.15b).

In the previous analyses all models were subjected to compression loading in the mechanical phase, where the deviatoric stress q increased with an increase in mean effective stress p, and the stress path shown in Figure 4.10a was followed. However, the Lode angle dependency of the material model is not observed with such a stress path. To investigate the role of LAD on the mechanical response, the *mechanical phase* step in the reference model was modified to extension loading. Extension loading was simulated by decreasing the axial force (in the mechanical phase step), where deviatoric stress q was developed as the mean effective stress p decreased following the stress path presented in Figure 4.10b. The thermomechanical responses of the material using $\rho^* = 1.0$, 0.9, 0.8, 0.7 and 0.6 are shown in Figure 4.16. As ρ^* decreased, the deviatoric stress (and stress ratio) at large deformations (representing the Critical State conditions) decreased (Figure 4.16b). In addition, slightly higher mechanically-induced volumetric strains were developed for models using higher ρ^*.
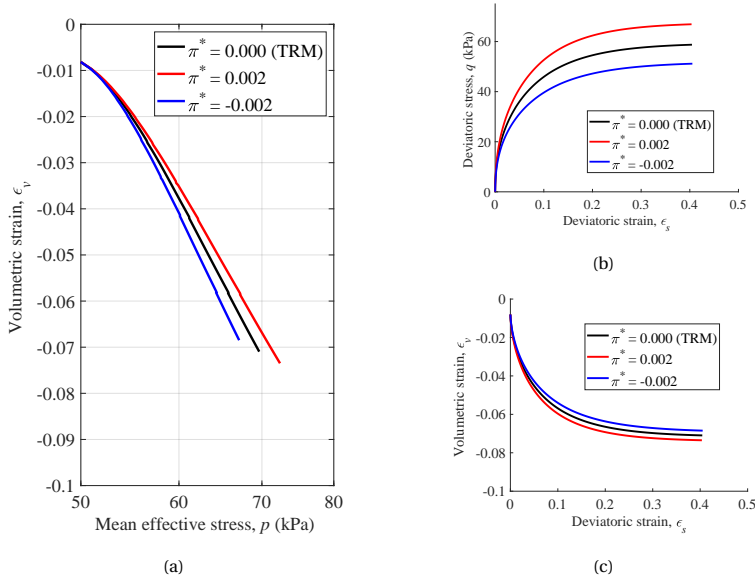
Figure 4.13: Effect of parameter π^* on the material's thermomechanical response in triaxial test (a) ε_v vs. p; (b) q vs. ε_s; (c) ε_v vs. ε_s
* TRM: Triaxial reference model
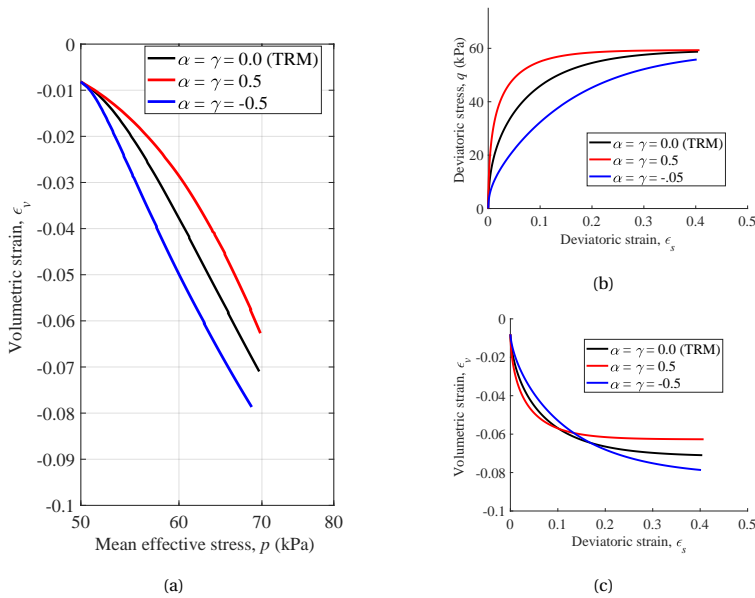
Figure 4.14: Effect of shape parameters (α and γ) on the material's thermomechanical response in triaxial test (a) ε_v vs. p; (b) q vs. ε_s; (c) ε_v vs. ε_s
* TRM: Triaxial reference model

(a)

(b)

(c)
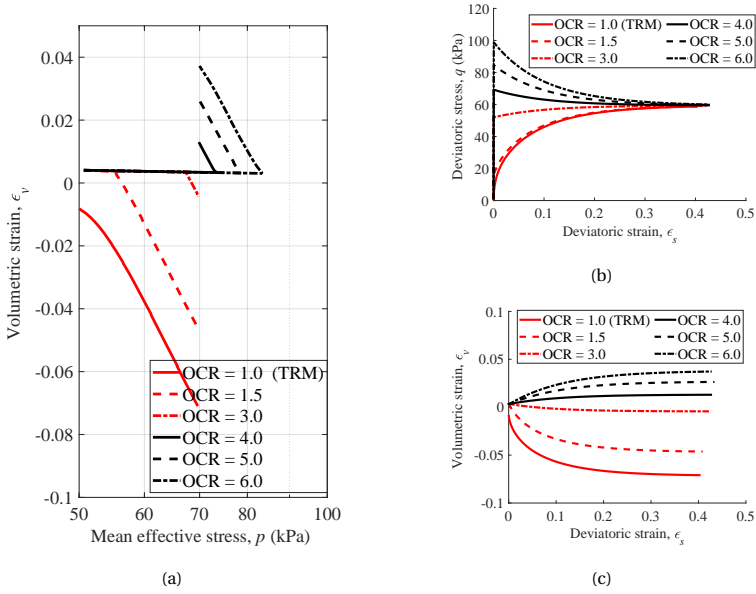
Figure 4.15: Effect of OCR on the material's thermomechanical response in triaxial test (a) ε_v vs.p; (b) q vs. ε_s; (c) ε_v vs. ε_s

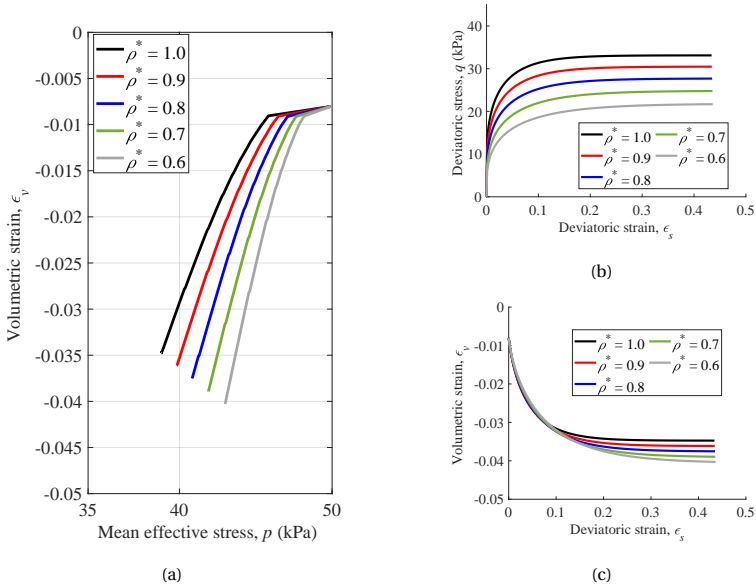* TRM: Triaxial reference model

(a)

(b)

(c)

Figure 4.16: Effect of Lode angle dependency on the material's thermomechanical response in triaxial test (a) ε_v vs.p; (b) q vs. ε_s; (c) ε_v vs. ε_s

4.6.2. OEDOMETER TEST

The schematic view of an oedometer test is shown in Figure 4.17a. A cylindrical fine-grained soil specimen with a height and diameter of 20 mm and 75 mm, respectively, is placed in a rigid mould and subjected to a vertical stress σ_v via a rigid load cap. Due to symmetry in the loading, boundary conditions and geometry, this test was modelled with a 2D axisymmetric formulation in FEM. The finite element model, including the boundary conditions and mesh, is shown in Figure 4.17b. The rigid mould is modelled using horizontal supports on the right boundary of the model, and vertical supports on the bottom boundary of the model, which prevents displacements in the horizontal and vertical directions, respectively. Considering a rigid load cap, the soil specimen is subjected to uniformly distributed vertical displacements at the top boundary. To model this loading condition, the vertical displacements of all the nodes of the soil specimen at the top boundary (slave nodes) are connected to the vertical displacement of the top node along the axis of symmetry (master node), and the vertical stress was applied on the top boundary. Consequently, all the top nodes follow the same amount of displacement as the master node due to the loading.

OEDOMETER REFERENCE MODEL (ORM)

The soil specimen in the reference model is subjected to four thermomechanical phases:

1. *Initial phase*: A normally consolidated soil with an apparent pre-consolidation pressure (p_{cT}) of 50 kPa is subjected to an external vertical force equal to a vertical stress of $\sigma_v = 50$ kPa and an internal pressure of 50 kPa at ambient temperature ($T = 20°C$) (the material is initially in an isotropic stress state);

2. *First compression loading phase*: At ambient temperature, the vertical load on the top boundary of the specimen was increased with stress-controlled increments from $\sigma_v = 50$ kPa to $\sigma_v = 100$ kPa;

3. *Thermal cycle phase*: While the vertical stress was kept constant, the specimen was incrementally heated from the top, bottom and side boundaries to the target temperature $T = 40°C$. This procedure was followed by a cooling phase to the ambient temperature. A sufficient amount of time was allowed for both thermal phases to reach a uniformly distributed temperature in all the elements.

4. *Second compression loading phase*: After the completion of the thermal cycle phase, the vertical load on the top boundary of the specimen was increased with stress-controlled increments to reach a vertical stress of 150 kPa (at ambient temperature).

Note that the parameters presented in Table 4.2 were used for the material in the reference model.
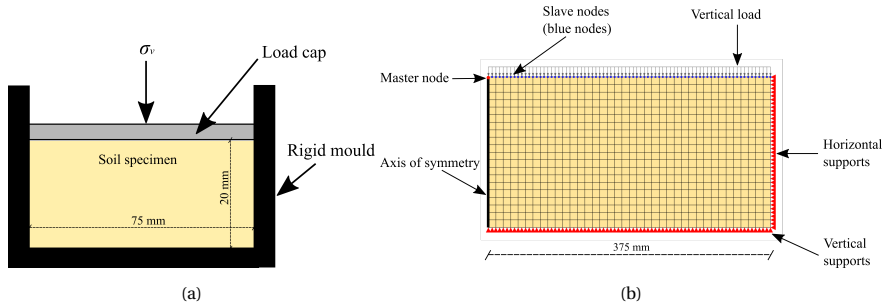
Figure 4.17: (a) Schematic view of oedometer test in the laboratory; (b) finite element model of the oedometer test

In Figure 4.18 the thermomechanical response of FEM models of the oedometer test, subjected to target temperatures of 20°C (unheated), 60°C and 80°C in the heating phase followed by cooling to the ambient temperature, are compared to the responses of the reference model (heated to 40°C). The material parameters of the reference model were used for all the simulations. The variation of volumetric strain with vertical stress (ε_v versus σ_v) and the variation of apparent pre-consolidation pressure versus temperature (T versus p_{cT}) are shown in Figure 4.18a and Figure 4.18b, respectively, for the entire thermomechanical stress path. All the models had an identical volume reduction versus vertical stress when following the *first compression loading phase*. As the temperature incrementally increased during the heating phase, p_{cT} tended to decrease due to thermal shrinkage and, at the same time, increased due to volumetric strain hardening (Eq. (4.20)), with an overall increase (Figure 4.18b). At the end of the *thermal cycle phase* p_{cT} was higher than the stress state of the material, inferring that the material was in an over-consolidated state. Thus, at the beginning of the *second compression loading phase* the material responded elastically until the stress state of the material encountered the yield surface, after which an elasto-plastic response was observed (a bilinear response in the *second compression loading phase* in Figure 4.18a). As the temperature increased, larger thermally-induced volumetric strains were produced (Figure 4.18a) and thus the material attained a higher p_{cT} (Figure 4.18b).

The effect of the thermal shrinkage parameter μ_0 on the thermomechanical response of the material in the oedometer test is shown in Figure 4.19. All simulations (models using $\mu_0 = 0.005$ (reference model), $\mu_0 = 0.001$ and $\mu_0 = 0.01$) were heated from the ambient temperature to 40°C in the heating phase and cooled back to the ambient temperature. It is observed in Figure 4.19a and Figure 4.19b that, as the μ_0 increased, larger thermally induced volumetric strains were produced during the heating phase and the material had a higher p_{cT} at the end of the thermal cycle. This led to a larger elastic response upon loading in the *second compression loading phase*.

In an oedometer test, due to the loading path and the constraints imposed by the rigid mould, the deviatoric stress q is developed as the specimen is subjected to a vertical force. Thus the temperature-dependency of the Critical State parameter (π^*) may affect the thermomechanical behaviour of the model, which is shown in Figure 4.20. The thermomechanical responses of two simulations using $\pi^* = 0.01$ and $\pi^* = -0.01$ (while

other parameters are identical to those of the reference model) are compared to the responses of the reference model ($\pi^* = 0$) when they are subjected to a thermal cycle of 20°C-40°C-20°C. It was observed that lower values of π^* (e.g. $\pi^* = -0.01$) lead to the larger development of thermally-induced volumetric strains and thus higher p_{cT} at the end of the thermal cycle. This infers that the material attains a higher over-consolidated state. Therefore, a larger elastic response was observed, initially after further compression (the *second compression loading phase*).

The influence of the initial over-consolidation ratio (OCR = p/p_{cT}) on the thermo-mechanical response of the model is presented in Figure 4.21. In the *initial phase* step, the initial (apparent) pre-consolidation pressures (p_{cT}) were set to 50 (the reference model), 75, 100 and 150 kPa to form OCRs of 1.0, 1.5, 2.0 and 3.0, respectively, and the parameters of the material model were set to be identical to the reference model. For FEM models with material stress states at OCR = 1.0 and 1.5, thermally-induced (plastic) volumetric strains were developed from the beginning of the heating phase (Figure 4.21a) and thus p_{cT} further increased (Figure 4.21b) with temperature increase. On the other hand, for the model with a material at OCR = 2.0, the initial response to heating was observed to be thermo-elastic and toward the end of heating phase the response became thermo-elasto-plastic. For the model with a material initial state at OCR= 3.0, the stress state of the material remained inside the yield surface and thus the entire response was thermo-elastic without significant changes in p_{cT}. The stress state of the material also remained inside the yield surface upon further compression and thus the material responded elastically.
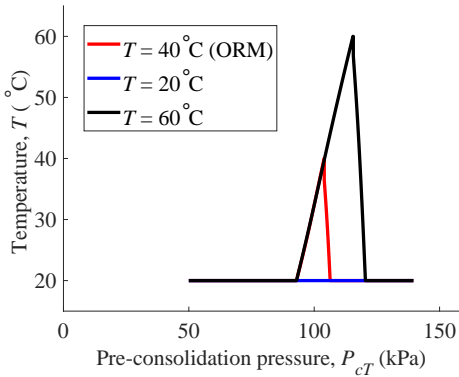
In conclusion, the return mapping algorithm was subjected to various thermo-mechanical paths, along with a wide range of material parameters. All simulations were stable, which indicates that the material tangent stiffness matrix was assembled within the global stiffness matrix (finite element) without difficulties.
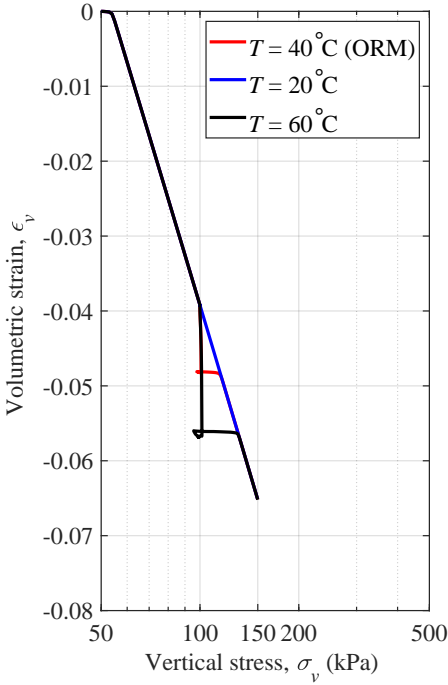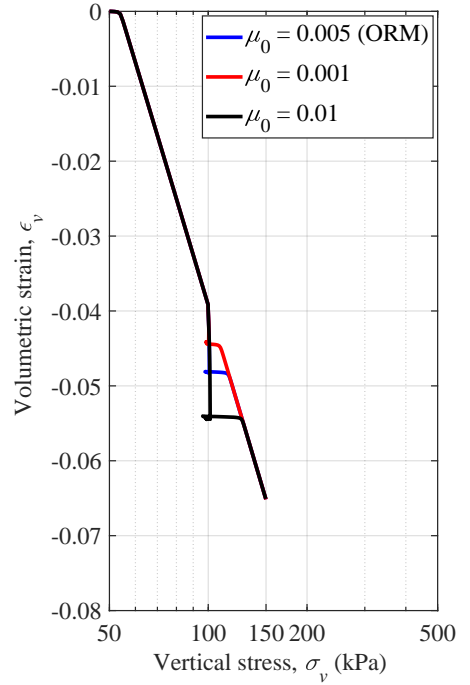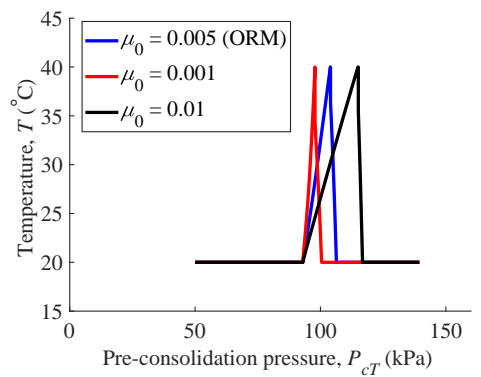
Figure 4.18: Effect of temperature on the material's thermomechanical response in oedometer test (a) ε_v vs. σ_v; (b) T vs. p_{cT}
* ORM: Oedometer reference model

Figure 4.19: Effect of parameter μ_0 on the material's thermomechanical response in oedometer test (a) ε_v vs. σ_v; (b) T vs. p_{cT}
* ORM: Oedometer reference model

(a)
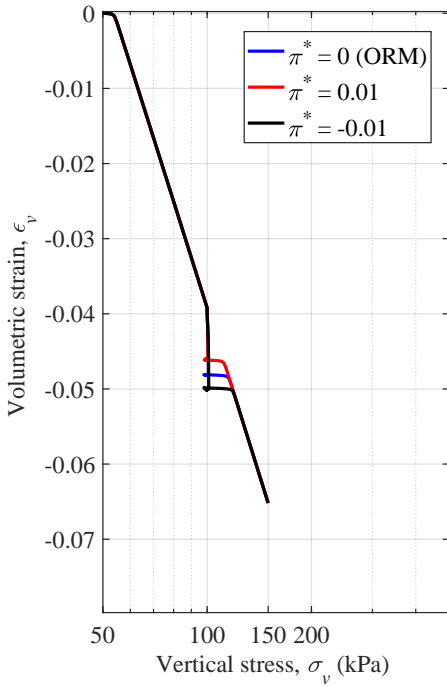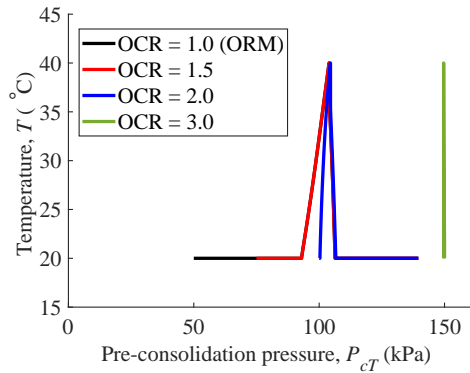
(b)

Figure 4.20: Effect of parameter π^* on the material's thermomechanical response in oedometer test (a) ε_v vs. σ_v; (b) T vs. p_{cT}
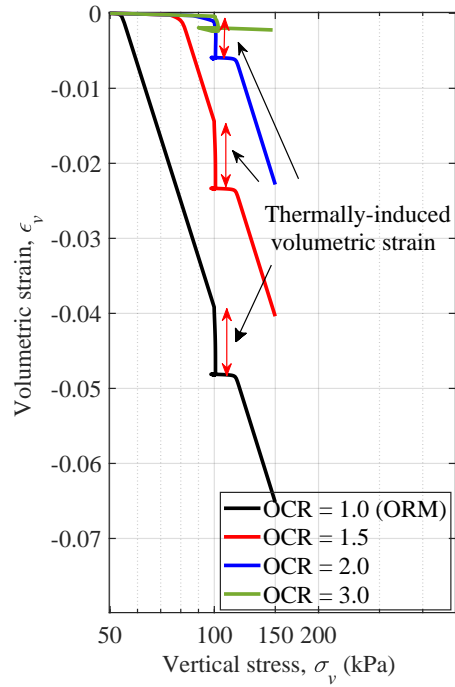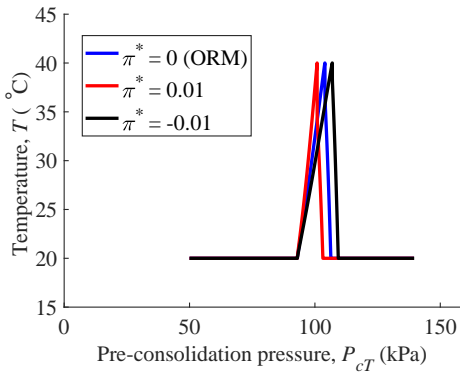* ORM: Oedometer reference model

(a)

(b)

Figure 4.21: Effect of OCR on the material's thermomechanical response in oedometer test (a) ε_v vs. σ_v; (b) T vs. p_{cT}
* ORM: Oedometer reference model

4

4.7. CONCLUSION

A new implicit stress integration technique for elasto-plastic models, with elasticity relationships derived from a Gibbs energy potential function, was proposed. The proposed stress integration technique was then employed to implement the thermomechanical model developed in Chapter 2 (with some modifications) in a finite element boundary-value solver via a user-defined material subroutine. The model was developed within the framework of hyperplasticity and many features of fine-grained soils, including non-linear elasticity, flexible yield surface, non-associated flow rule, Lode angle dependency, thermo-elastic expansion, thermal shrinkage of the yield surface and temperature-dependent Critical State stress ratio were embedded in the Gibbs energy potential and rate of dissipation potential functions. The accuracy, robustness and effectiveness of the stress integration algorithm of the thermomechanical constitutive model was thoroughly investigated via studying iso-error plots, iteration-stress maps and Gudehus plots, and the residuals and stress convergence were checked to be quadratic. Implementing the thermomechanical model within the DIANA FEA finite element software allowed a rigorous investigation of the stability performance of the algorithm and the constitutive model. An extensive number of finite element models subjected to various sophisticated mechanical and thermal cycle loading paths, similar to those encountered in thermomechanical drained triaxial and oedometer laboratory soil tests, were simulated and the role of the constitutive model parameters on the performance of the model and the algorithm was investigated. In all examples, the finite element model was stable. The analyses demonstrated in this chapter suggest that the thermo-mechanical constitutive model and the proposed stress integration approach show potential for simulating the thermo-mechanical behaviour of thermo-active geostructures, such as energy-piles using finite element software. It is important to note that the current study only explored triaxial conditions and one-dimensional conditions, and other load conditions prevalent in thermo-active piles were not comprehensively tested. Hence, further investigations are needed to fully validate this model and approach under more diverse and complex conditions.

REFERENCES

[1] Anandarajah, A. *Computational methods in elasticity and plasticity*. Springer, New York, 2010.

[2] Brandl, H. Energy foundations and other thermo-active ground structures. *Géotechnique*, (56):81–122, 2006.

[3] Abuel-Naga, H. M., Bergado, D. T., and Lim, B. F. Effect of temperature on shear strength and yielding behavior of soft Bangkok clay. *Soils and Foundations*, 47(3):423–436, 2007.

[4] Cui, Y. J., Sultan, N., and Delage, P. A thermomechanical model for saturated clays. *Canadian Geotechnical Journal*, 37(3):607–620, 2000.

[5] Hamidi, A., Tourchi, S., and Khazaei, C. Thermomechanical constitutive model for saturated clays based on critical state theory. *International Journal of Geomechanics*, 15(1):04014038, 2015.

[6] Kaliakin, V. N., Nieto-Leal, A., and Mashayekhi, M. Modeling the time- and temperature-dependent response of cohesive soils in a generalized bounding surface framework. *Transportation Infrastructure Geotechnology*, 5(3):250–286, 2018.

[7] Laloui, L., Cekerevac, C. and François, B. Constitutive modelling of the thermoplastic behaviour of soils. *Revue Européenne de Génie Civil*, 9(5-6):635–650, 2005.

[8] Laloui, L. and François, B. ACMEG-T: Soil thermoplasticity model. *Journal of Engineering Mechanics*, 135(9):932–944, 2009.

[9] Yao, Y. P. P. and Zhou, A. N. N. Non-isothermal unified hardening model: A thermoelasto-plastic model for clays. *Géotechnique*, 63(15):1328–1345, 2013.

[10] Zhou, C., Fong, K. Y. and Ng, C. W. W. A new bounding surface model for thermal cyclic behaviour. *International Journal for Numerical and Analytical Methods in Geomechanics*, 41(16):1656–1666, 2017.

[11] Zhou, C. and Ng, C. W. W. A thermomechanical model for saturated soil at small and large strains. *Canadian Geotechnical Journal*, 52(8):1101–1110, 2015.

[12] Houlsby, G. T. and Puzrin, A. M. *Principles of Hyperplasticity*. Springer London, London, 2007.

[13] Hardin, B. O. and Richart, F. E. Elastic wave velocities in granular soils. *Journal of the Soil Mechanics and Foundations Division*, 89(1):33–65, 1963.

[14] Koseki, J., Kawakami, S., Nagayama, H. and Sato, T. Change of small strain quasi-elastic deformation properties during undrained cyclic torsional shear and triaxial tests of Toyoura sand. *Soils and Foundations*, 40(3):101–110, 2000.

[15] Viggiani, G. and Atkinson, J. H. Stiffness of fine-grained soil at very small strains. *Géotechnique*, 45(2):249–265, 1995.

[16] Wichtmann, T. and Triantafyllidis, T. Influence of the grain-size distribution curve of quartz sand on the small strain shear modulus Gmax. *Journal of Geotechnical and Geoenvironmental Engineering*, 135(10):1404–1418, 2009.

[17] Collins, I. F. and Houlsby, G. T. Application of thermomechanical principles to the modelling of geotechnical materials. In *Proceedings: Mathematical, Physical and Engineering Sciences, JSTOR*, volume 453, pages 1975–2001. 1997.

[18] Borja, R. I., Tamagnini, C. and Alarcón, E. Elastoplastic consolidation at finite strain part 2: Finite element implementation and numerical examples. *Computer Methods in Applied Mechanics and Engineering*, 5:103–122, 1998.

[19] Golchin, A. and Lashkari, A. A critical state sand model with elastic–plastic coupling. *International Journal of Solids and Structures*, 51(15-16):2807–2825, 2014.

4

[20] Lashkari, A. and Golchin, A. On the influence of elastic–plastic coupling on sands response. *Computers and Geotechnics*, 55:352–364, 2014.

[21] Semnani, S. J., White, J. A. and Borja, R. I. Thermoplasticity and strain localization in transversely isotropic materials based on anisotropic critical state plasticity. *International Journal for Numerical and Analytical Methods in Geomechanics*, 40(18):2423–2449, 2016.

[22] Song, X., Wang, K. and Bate, B. A hierarchical thermo-hydro-plastic constitutive model for unsaturated soils and its numerical implementation. *International Journal for Numerical and Analytical Methods in Geomechanics*, 42(15):1785–1805, 2018.

[23] Borja, R. I. *Plasticity; Modeling & Computation.* Springer, Berlin, Heidelberg, 2013.

[24] Simo, J. C. and Hughes, T. J. R. *Computational inelasticity*, volume 7 of *Interdisciplinary Applied Mathematics.* Springer-Verlag, New York, 1998.

[25] Bennett, K. C. and Borja, R. I. Hyper-elastoplastic/damage modeling of rock with application to porous limestone. *International Journal of Solids and Structures*, 143:218–231, 2018.

[26] Borja, R. I., Lin, C. H. and Montáns, F. J. Cam-clay plasticity, Part IV: Implicit integration of anisotropic bounding suface model with nonlinear hyperelasticity and ellipsoidal loading function. *Computer Methods in Applied Mechanics and Engineering*, 190(26-27):3293–3323, 2001.

[27] Borja, R. I. and Andrade, J. E. Critical state plasticity. Part VI: Meso-scale finite element simulation of strain localization in discrete granular materials. *Computer Methods in Applied Mechanics and Engineering*, 195(37-40):5115–5140, 2006.

[28] Coombs, W. M. Continuously unique anisotropic critical state hyperplasticity. *International Journal for Numerical and Analytical Methods in Geomechanics*, 41(4):578–601, 2017.

[29] Coombs, W. M., Crouch, R. S. and Augarde, C. E. A unique Critical State two-surface hyperplasticity model for fine-grained particulate media. *Journal of the Mechanics and Physics of Solids*, 61(1):175–189, 2013.

[30] Coombs, W. M. and Crouch, R. S. Algorithmic issues for three-invariant hyperplastic Critical State models. *Computer Methods in Applied Mechanics and Engineering*, 200(25-28):2297–2318, 2011.

[31] Tamagnini, C., Castellanza, R. and Nova, R. A Generalized Backward Euler algorithm for the numerical integration of an isotropic hardening elastoplastic model for mechanical and chemical degradation of bonded geomaterials. *International Journal for Numerical and Analytical Methods in Geomechanics*, 26(10):963–1004, 2002.

[32] Scalet, G. and Auricchio, F. Computational methods for elastoplasticity: an overview of conventional and less-conventional approaches. *Archives of Computational Methods in Engineering*, 25(3):545–589, 2018.

[33] Chen, Y. N. and Yang, Z. X. A family of improved yield surfaces and their application in modeling of isotropically over-consolidated clays. *Computers and Geotechnics*, 90:133–143, 2017.

[34] Collins, I. F. and Hilder, T. A theoretical framework for constructing elastic/plastic constitutive models of triaxial tests. *International Journal for Numerical and Analytical Methods in Geomechanics*, 26(13):1313–1347, 2002.

[35] Mir, A., Nguyen, G. D. and Sheikh, A. A thermodynamics-based model for brittle to ductile behaviour and localised failure of porous rocks. *International Journal of Solids and Structures*, 152-153:161–184, 2018.

[36] Zhang, Z., Chen, Y. and Huang, Z. A novel constitutive model for geomaterials in hyperplasticity. *Computers and Geotechnics*, 98:102–113, 2018.

[37] Houlsby, G. T., Amorosi, A. and Rojas, E. Elastic moduli of soils dependent on pressure: A hyperelastic formulation. *Géotechnique*, 55(5):383–392, 2005.

[38] Ziegler, H. *An introduction to thermomechanics*, volume 21. North-Holland Series in Applied Mathematics and Mechanics, Amsterdam.

[39] Abuel-Naga, H. M., Bergado, D. T., Ramana, G. V., Grino, L., Rujivipat, P. and Thet, Y. Experimental evaluation of engineering behavior of soft Bangkok clay under elevated temperature. *Journal of Geotechnical and Geoenvironmental Engineering*, 132(7):902–910, 2006.

[40] Laloui, L. and Cekerevac, C. Thermo-plasticity of clays: An isotropic yield mechanism. *Computers and Geotechnics*, 30(8):649–660, 2003.

[41] Sultan, N., Delage, P. and Cui, Y. J. Temperature effects on the volume change behaviour of Boom clay. *Engineering Geology*, 64:135–145, 2002.

[42] Towhata, I., Kuntiwattanaku, P., Seko, I. and Ohishi, K. Volume change of clays induced by heating as observed in consolidation tests. *Soils and Foundations*, 33(4):170–183, 1993.

[43] Uchaipichat, A. and Khalili, N. Experimental investigation of thermo-hydro-mechanical behaviour of an unsaturated silt. *Géotechnique*, 59(4):339–353, 2009.

[44] Abuel-Naga, H. M., Bergado, D. T., Bouazza, A. and Ramana, G. V. Volume change behaviour of saturated clays under drained heating conditions: Experimental results and constitutive modeling. *Canadian Geotechnical Journal*, 44(8):942–956, 2007.

[45] Cekerevac, C. and Laloui, L. Experimental study of thermal effects on the mechanical behaviour of a clay. *International Journal for Numerical and Analytical Methods in Geomechanics*, 28(3):209–228, 2004.

4

[46] Ghahremannejad, B. *Thermo-mechanical behaviour of two reconstituted clays*. PhD thesis, University of Sydney, 2003.

[47] Tanaka, N., Graham, J. and Crilly, T. Stress-strain behaviour of reconstituted illitic clay at different temperatures. *Engineering Geology*, 47(4):339–350, 1997.

[48] Bigoni, D. and Piccolroaz, A. Yield criteria for quasibrittle and frictional materials. *International Journal of Solids and Structures*, 41(11-12):2855–2878, 2004.

[49] Gudehus, G. Comparison of some constitutive laws for soils under radially symmetric loading and unloading. In *Proceedings of the 3rd International Conference on Numerical Methods in Geomechanics*, pages 1309–1323, Aachen, 1979.

[50] Sheng, D., Sloan, S. W. and Yu, H. S. Aspects of finite element implementation of critical state models. *Computational Mechanics*, 26(2):185–196, 2000.

[51] Zienkiewicz, O. C. and Pande, G. N. Some useful forms of isotropic yield surfaces for soil and rock mechanics. In *Gudehus, G. (ed.) Finite Elements in Geomechanics*, pages 179–190, London, 1977. Wiley.

[52] Gorski, K. M., Hivon, E., Banday, A. J., Wandelt, B. D., Hansen, F. K., Reinecke, M. and Bartelmann, M. HEALPix: A framework for high-resolution discretization and fast analysis of data distributed on the sphere. *The Astrophysical Journal*, 622(2):759–771, 2005.

[53] Gudehus, G. Elastoplastische stoffgleichungen fur trockenen sand. *Ingenieur-Archiv*, 42(3):151–169, 1973.

[54] Golchin, A., Vardon, P. J. and Hicks, M. A. A thermo-mechanical constitutive model for fine-grained soils based on thermodynamics. *International Journal of Engineering Science*, 174:103579, 2022.

[55] Golchin, A., Vardon, P. J. and Hicks, M. A. A thermodynamically consistent two surface/bubble thermo-mechanical model considering thermal and mechanical cyclic behaviour of fine-grained soils. *International Journal of Solids and Structures*, page 111847, 2022.

[56] Golchin, A., Vardon, P. J., Coombs, W. M. and Hicks, M. A. A flexible and robust yield function for geomaterials. *Computer Methods in Applied Mechanics and Engineering*, 387:114162, 2021.

APPENDIX

4.A. APPENDIX A: RATES OF STRESS INVARIANTS AND THEIR DERIVATIVES WITH RESPECT TO STRESS TENSOR

Rate and derivative of the hydrostatic pressure, p:

$$\dot{p} = \frac{1}{3}\mathbf{1} : \dot{\boldsymbol{\sigma}} \tag{4.A.1a}$$

$$\frac{\partial p}{\partial \boldsymbol{\sigma}} = \frac{1}{3}\mathbf{1} \tag{4.A.1b}$$

Rate and derivative of the deviatoric stress tensor, $\mathbf{s}$:

$$\dot{\mathbf{s}} = \left(\mathbf{I} - \frac{1}{3}\mathbf{1} \otimes \mathbf{1}\right)\dot{\boldsymbol{\sigma}} \tag{4.A.2a}$$

$$\frac{\partial \mathbf{s}}{\partial \boldsymbol{\sigma}} = \mathbf{I} - \frac{1}{3}\mathbf{1} \otimes \mathbf{1} \tag{4.A.2b}$$

where $\mathbf{I}$ is the fourth-order identity tensor and $\mathbf{1}$ is the second-order identity tensor.

Rate and derivative of the deviatoric stress, q:

$$\dot{q} = \sqrt{\frac{3}{2}}\hat{\mathbf{n}} : \dot{\boldsymbol{\sigma}} \tag{4.A.3a}$$

$$\frac{\partial q}{\partial \boldsymbol{\sigma}} = \sqrt{\frac{3}{2}}\hat{\mathbf{n}} \tag{4.A.3b}$$

where $\hat{\mathbf{n}}$ is the direction (norm) of deviatoric stress tensor (or deviatoric strain tensor, since they are coaxial):

$$\hat{\mathbf{n}} = \frac{\mathbf{s}}{\|\mathbf{s}\|} = \frac{\mathbf{s}}{(\mathbf{s} : \mathbf{s})^{\frac{1}{2}}} = \sqrt{\frac{3}{2}}\frac{\mathbf{s}}{q} \tag{4.A.4}$$

Rate and derivative of the second stress invariant, J:

$$\dot{J} = \frac{\sqrt{3}}{2}\frac{\mathbf{s}}{q} : \dot{\boldsymbol{\sigma}} = \frac{\mathbf{s}}{2J} : \dot{\boldsymbol{\sigma}} \tag{4.A.5a}$$

$$\frac{\partial J}{\partial \boldsymbol{\sigma}} = \frac{\sqrt{3}}{2}\frac{\mathbf{s}}{q} = \frac{\mathbf{s}}{2J} \tag{4.A.5b}$$

Rate and derivative of the third stress invariant, S:

$$\dot{S} = \frac{1}{3S^2}\left(\tilde{\mathbf{s}} - \frac{2}{3}J^2\mathbf{1}\right):\dot{\boldsymbol{\sigma}} \tag{4.A.6a}$$

$$\frac{\partial S}{\partial \boldsymbol{\sigma}} = \frac{1}{3S^2}\left(\tilde{\mathbf{s}} - \frac{2}{3}J^2\mathbf{1}\right) \tag{4.A.6b}$$

where

$$\tilde{\mathbf{s}} = \tilde{s}_{ij} = s_{ir}s_{rj} = \begin{bmatrix} s_{1r}s_{r1} & s_{1r}s_{r2} & s_{1r}s_{r3} \\ s_{2r}s_{r1} & s_{2r}s_{r2} & s_{2r}s_{r3} \\ s_{3r}s_{r1} & s_{3r}s_{r2} & s_{3r}s_{r3} \end{bmatrix} \tag{4.A.7}$$

Rate and derivative of the Lode angle, θ:

$$\dot{\theta} = \frac{\sqrt{3}}{2J\cos3\theta}\left(\frac{\tilde{s}}{J^2} - \frac{2}{3}\mathbf{1} - \frac{3\sqrt{2}}{2}\left(\frac{S}{J}\right)^3\hat{\mathbf{n}}\right):\dot{\boldsymbol{\sigma}} \tag{4.A.8a}$$

$$\frac{\partial S}{\partial \boldsymbol{\sigma}} = \frac{\sqrt{3}}{2J\cos3\theta}\left(\frac{\tilde{s}}{J^2} - \frac{2}{3}\mathbf{1} - \frac{3\sqrt{2}}{2}\left(\frac{S}{J}\right)^3\hat{\mathbf{n}}\right) \tag{4.A.8b}$$

4.B. APPENDIX B: COEFFICIENTS OF DERIVATIVES

Coefficient $\mathbf{A}$:

$$\mathbf{A} = \frac{\partial \mathbf{R}_1}{\partial \boldsymbol{\sigma}_{n+1}} = -\frac{\partial^2 g_1}{\partial \boldsymbol{\sigma}_{n+1}\partial \boldsymbol{\sigma}_{n+1}} + \Delta\Lambda\frac{\partial \mathbf{r}}{\partial \boldsymbol{\sigma}_{n+1}} \tag{4.B.1}$$

where $-\frac{\partial^2 g_1}{\partial \boldsymbol{\sigma}_{n+1}\partial \boldsymbol{\sigma}_{n+1}} = \mathbf{c}$ and $\frac{\partial \mathbf{r}}{\partial \boldsymbol{\sigma}_{n+1}}$ are computed respectively, via Eqs. (4.E.11) and (4.D.5).

Coefficient $\mathbf{B}$:

$$\mathbf{B} = \frac{\partial \mathbf{R}_1}{\partial p_{cT}^{n+1}} = \Delta\Lambda\frac{\partial \mathbf{r}}{\partial p_{cT}^{n+1}} \tag{4.B.2}$$

where $\frac{\partial \mathbf{r}}{\partial p_{cT}^{n+1}}$ is computed via Eq. (4.D.14).

Coefficient $\mathbf{F}$:

$$\mathbf{F} = \frac{\partial \mathbf{R}_1}{\partial \Delta\Lambda} = \mathbf{r} \tag{4.B.3}$$

where $\mathbf{r}$ is calculated via Eq. (4.D.1).

Coefficient $\mathbf{H}^{\mathrm{T}}$:

$$\mathbf{H}^{\mathrm{T}} = \frac{\partial R_2}{\partial \boldsymbol{\sigma}_{n+1}} = \frac{\partial R_2}{\partial \Delta\varepsilon_{kk}^p}\frac{\partial \Delta\varepsilon_{kk}^p}{\partial \boldsymbol{\sigma}_{n+1}} = -\Delta\Lambda\frac{1+e_0}{\lambda-\kappa}\frac{\partial r_p}{\partial \boldsymbol{\sigma}_{n+1}}e^{\frac{1+e_0}{\lambda-\kappa}-\mu_0\Delta T} \tag{4.B.4}$$

where $\frac{\partial r_p}{\partial \boldsymbol{\sigma}_{n+1}}$ is computed via Eq. (4.D.3).

Coefficient ω:

$$\omega = \frac{\partial R_2}{\partial p_{cT}^{n+1}} = \frac{1}{p_{cT}^n} - \Delta\Lambda \frac{1+e_0}{\lambda-\kappa} \frac{\partial r_p}{p_{cT}^{n+1}} e^{\frac{1+e_0}{\lambda-\kappa} - \mu_0\Delta T} \tag{4.B.5}$$

where $\frac{\partial r_p}{p_{cT}^{n+1}}$ is computed via Eq. (4.D.15).

Coefficient ρ:

$$\rho = \frac{\partial R_2}{\partial \Delta\Lambda} = \frac{\partial R_2}{\partial \Delta\varepsilon_{kk}^p} \frac{\partial \Delta\varepsilon_{kk}^p}{\partial \Delta\Lambda} = -r_p \frac{1+e_0}{\lambda-\kappa} e^{\frac{1+e_0}{\lambda-\kappa} - \mu_0\Delta T} \tag{4.B.6}$$

Coefficient $\mathbf{E}^T$:

$$\mathbf{E}^T = \frac{\partial R_3}{\partial \boldsymbol{\sigma}_{n+1}} = \frac{\partial y}{\partial \boldsymbol{\sigma}_{n+1}} \tag{4.B.7}$$

where $\frac{\partial y}{\partial \boldsymbol{\sigma}_{n+1}}$ is calculated via Eq. (4.C.1).

Coefficient ϖ:

$$\varpi = \frac{\partial R_3}{\partial p_{cT}^{n+1}} = \frac{\partial y}{\partial p_{cT}} \tag{4.B.8}$$

where $\frac{\partial y}{\partial p_{cT}}$ is computed via Eq. (4.C.11).

Coefficient ϑ:

$$\vartheta = \frac{\partial R_3}{\partial \Delta\Lambda} = \frac{\partial y}{\partial \Delta\Lambda} = 0 \tag{4.B.9}$$

4.C. Appendix C: Derivatives of the yield surface

Derivative of the yield surface, y, with respect to stress tensor $\boldsymbol{\sigma}$:
The derivative of a yield surface, defined by stress invariants p, q and θ ($y = y(p, q, \theta)$), with respect to the stress tensor, is

$$\frac{\partial y}{\partial \boldsymbol{\sigma}} = \mathbf{n} = \frac{\partial y}{\partial p} \frac{\partial p}{\partial \boldsymbol{\sigma}} = \frac{\partial y}{\partial q} \frac{\partial q}{\partial \boldsymbol{\sigma}} = \frac{\partial y}{\partial \theta} \frac{\partial \theta}{\partial \boldsymbol{\sigma}} \tag{4.C.1}$$

where $\frac{\partial p}{\partial \boldsymbol{\sigma}}$, $\frac{\partial q}{\partial \boldsymbol{\sigma}}$ and $\frac{\partial \theta}{\partial \boldsymbol{\sigma}}$ are determined, respectively, in Eqs. (4.A.1), (4.A.3) and (4.A.8). For the current yield function (Eq. (4.E.14)), the derivatives with respect to stress invariants are

$$\frac{\partial y}{\partial p} = r_p + \frac{\partial y}{\partial A} \frac{\partial A}{\partial p} + \frac{\partial y}{\partial B} \frac{\partial B}{\partial p} \tag{4.C.2}$$

$$\frac{\partial y}{\partial q} = r_q \tag{4.C.3}$$

$$\frac{\partial y}{\partial \theta} = \frac{\partial y}{\partial B}\frac{\partial B}{\partial \theta} \tag{4.C.4}$$

and

$$\frac{\partial y}{\partial A} = -2\frac{(p-C)^2}{A^3} \tag{4.C.5}$$

$$\frac{\partial y}{\partial B} = -2\frac{q^2}{B^3} \tag{4.C.6}$$

$$\frac{\partial y}{\partial C} = -2\frac{(p-C)}{A^2} \tag{4.C.7}$$

and

$$\frac{\partial A}{\partial p} = -\frac{\gamma}{\pi}\left(1+\gamma^2\left(\frac{1}{2}\frac{p}{p_{cT}}\right)^2\right)^{-1} \tag{4.C.8}$$

$$\frac{\partial B}{\partial p} = \alpha\frac{B}{p_{cT}} \tag{4.C.9}$$

$$\frac{\partial B}{\partial \theta} = \frac{\partial B}{\partial \bar{M}}\frac{\partial \bar{M}}{\partial \theta} = \frac{3}{4}\frac{B\left(1-(\rho^*)^4\right)cos3\theta}{1+(\rho^*)^4-\left(1-(\rho^*)^4\right)sin3\theta} \tag{4.C.10}$$

Derivative of the yield surface, y, with respect to p_{cT}:

$$\frac{\partial y}{\partial p_{cT}} = \frac{\partial y}{\partial A}\frac{\partial A}{\partial p_{cT}} + \frac{\partial y}{\partial B}\frac{\partial B}{\partial p_{cT}} + \frac{\partial y}{\partial C}\frac{\partial C}{\partial p_{cT}} \tag{4.C.11}$$

where

$$\frac{\partial A}{\partial p_{cT}} = \frac{A}{p_{cT}} + \left(\frac{\gamma p}{\pi p_{cT}}\right)\left(1+\gamma\left(\frac{1}{2}-\frac{p}{p_{cT}}\right)^2\right)^{-1} \tag{4.C.12}$$

$$\frac{\partial B}{\partial p_{cT}} = -\alpha B\frac{(p-C)}{(p_{cT})^2} + \frac{\partial B}{\partial C}\frac{\partial C}{\partial p_{cT}} \tag{4.C.13}$$

$$\frac{\partial C}{\partial p_{cT}} = \frac{C}{p_{cT}} \tag{4.C.14}$$

$$\frac{\partial B}{\partial C} = B\left(\frac{1}{C} - \frac{\alpha}{p_{cT}}\right) \tag{4.C.15}$$

4.D. Appendix D: Plastic flow tensor and its deriva-tives

Plastic flow tensor is determined using its invariants r_p and r_q as

$$\mathbf{r} = r_p \frac{\partial p}{\partial \boldsymbol{\sigma}} + r_q \frac{\partial q}{\partial \boldsymbol{\sigma}} = \frac{1}{3} r_p \mathbf{1} + \sqrt{\frac{3}{2}} \hat{\mathbf{n}} \qquad (4.D.1)$$

The derivative of plastic flow with respect to stress tensor, $\boldsymbol{\sigma}$, is

$$\frac{\partial \mathbf{r}}{\partial \boldsymbol{\sigma}} = \frac{1}{3} \frac{\partial r_p}{\partial \boldsymbol{\sigma}} \mathbf{1} + \sqrt{\frac{3}{2}} \frac{\partial r_q}{\partial \boldsymbol{\sigma}} \hat{\mathbf{n}} + \sqrt{\frac{3}{2}} r_q \frac{\partial \hat{\mathbf{n}}}{\partial \boldsymbol{\sigma}} \qquad (4.D.2)$$

r_p and r_q may be dependent on the stress invariants (p, q and θ). Thus, their derivative with respect to the stress tensor results in

$$\frac{\partial r_p}{\partial \boldsymbol{\sigma}} = \frac{\partial r_p}{\partial p} \frac{\partial p}{\partial \boldsymbol{\sigma}} + \frac{\partial r_p}{\partial q} \frac{\partial q}{\partial \boldsymbol{\sigma}} + \frac{\partial r_p}{\partial \theta} \frac{\partial \theta}{\partial \boldsymbol{\sigma}} =$$
$$\frac{1}{3} \frac{\partial r_p}{\partial p} \mathbf{1} + \sqrt{\frac{3}{2}} \frac{\partial r_p}{\partial q} \hat{\mathbf{n}} + \frac{\sqrt{3}}{2 J cos 3\theta} \frac{\partial r_p}{\partial \theta} \left(\frac{\tilde{\mathbf{s}}}{J^2} - \frac{2}{3} \mathbf{1} - \frac{3\sqrt{2}}{2} \left(\frac{S}{J} \right)^3 \hat{\mathbf{n}} \right) \qquad (4.D.3)$$

$$\frac{\partial r_q}{\partial \boldsymbol{\sigma}} = \frac{\partial r_q}{\partial p} \frac{\partial p}{\partial \boldsymbol{\sigma}} + \frac{\partial r_q}{\partial q} \frac{\partial q}{\partial \boldsymbol{\sigma}} + \frac{\partial r_q}{\partial \theta} \frac{\partial \theta}{\partial \boldsymbol{\sigma}} =$$
$$\frac{1}{3} \frac{\partial r_q}{\partial p} \mathbf{1} + \sqrt{\frac{3}{2}} \frac{\partial r_q}{\partial q} \hat{\mathbf{n}} + \frac{\sqrt{3}}{2 J cos 3\theta} \frac{\partial r_q}{\partial \theta} \left(\frac{\tilde{\mathbf{s}}}{J^2} - \frac{2}{3} \mathbf{1} - \frac{3\sqrt{2}}{2} \left(\frac{S}{J} \right)^3 \hat{\mathbf{n}} \right) \qquad (4.D.4)$$

Further substituting Eqs. (4.D.3) and (4.D.4) in Eq. (4.D.2) results in the following fourth-order tensor:

$$\frac{\partial \mathbf{r}}{\partial \boldsymbol{\sigma}} = \left(\frac{\partial \mathbf{r}}{\partial \boldsymbol{\sigma}} \right)_1 + \left(\frac{\partial \mathbf{r}}{\partial \boldsymbol{\sigma}} \right)_2 + \left(\frac{\partial \mathbf{r}}{\partial \boldsymbol{\sigma}} \right)_3 + \left(\frac{\partial \mathbf{r}}{\partial \boldsymbol{\sigma}} \right)_4 + \left(\frac{\partial \mathbf{r}}{\partial \boldsymbol{\sigma}} \right)_5 + \left(\frac{\partial \mathbf{r}}{\partial \boldsymbol{\sigma}} \right)_6 + \left(\frac{\partial \mathbf{r}}{\partial \boldsymbol{\sigma}} \right)_7 \qquad (4.D.5a)$$

$$\left(\frac{\partial \mathbf{r}}{\partial \boldsymbol{\sigma}} \right)_1 = \frac{3}{2} \frac{r_q}{q} \mathbf{I} \qquad (4.D.5b)$$

$$\left(\frac{\partial \mathbf{r}}{\partial \boldsymbol{\sigma}} \right)_2 = \frac{1}{9} \left(\frac{\partial r_p}{\partial p} - \frac{\sqrt{3}}{J cos 3\theta} \frac{\partial r_p}{\partial \theta} - \frac{9}{2} \frac{r_q}{1} \right) (\mathbf{1} \otimes \mathbf{1}) \qquad (4.D.5c)$$

$$\left(\frac{\partial \mathbf{r}}{\partial \boldsymbol{\sigma}} \right)_3 = \sqrt{\frac{1}{6}} \left(\frac{\partial r_p}{\partial p} - \frac{\sqrt{3}}{J cos 3\theta} \frac{\partial r_p}{\partial \theta} \right) (\hat{\mathbf{n}} \otimes \mathbf{1}) \qquad (4.D.5d)$$

$$\left(\frac{\partial \mathbf{r}}{\partial \boldsymbol{\sigma}} \right)_4 = \sqrt{\frac{1}{6}} \left(\frac{\partial r_q}{\partial p} - \frac{\sqrt{3}}{J cos 3\theta} \frac{\partial r_q}{\partial \theta} \right) (\mathbf{1} \otimes \hat{\mathbf{n}}) \qquad (4.D.5e)$$

$$\left(\frac{\partial \mathbf{r}}{\partial \boldsymbol{\sigma}}\right)_5 = \frac{3}{2}\left(\frac{\partial r_q}{\partial q} - \frac{1}{Jcos3\theta}\left(\frac{S}{J}\right)^3\frac{\partial r_q}{\partial \theta} - \frac{r_q}{q}\right)(\hat{\mathbf{n}} \otimes \hat{\mathbf{n}}) \qquad (4.D.5f)$$

$$\left(\frac{\partial \mathbf{r}}{\partial \boldsymbol{\sigma}}\right)_6 = \frac{1}{2\sqrt{3}J^3 cos3\theta}\frac{\partial r_p}{\partial \theta}(\tilde{\mathbf{s}} \otimes \mathbf{1}) \qquad (4.D.5g)$$

$$\left(\frac{\partial \mathbf{r}}{\partial \boldsymbol{\sigma}}\right)_7 = \frac{3}{2\sqrt{2}j^3 cos3\theta}\frac{\partial r_q}{\partial \theta}(\tilde{\mathbf{s}} \otimes \hat{\mathbf{n}}) \qquad (4.D.5h)$$

and

$$\frac{\partial r_p}{\partial p} = \frac{2}{A^2} + \frac{\partial r_p}{\partial A}\frac{\partial A}{\partial p} \qquad (4.D.6)$$

$$\frac{\partial r_p}{\partial q} = 0 \qquad (4.D.7)$$

$$\frac{\partial r_p}{\partial \theta} = 0 \qquad (4.D.8)$$

$$\frac{\partial r_q}{\partial p} = \frac{\partial r_q}{\partial B}\frac{\partial B}{\partial p} \qquad (4.D.9)$$

$$\frac{\partial r_q}{\partial q} = \frac{2}{B^2} \qquad (4.D.10)$$

$$\frac{\partial r_q}{\partial \theta} = \frac{\partial r_q}{\partial B}\frac{\partial B}{\partial \theta} \qquad (4.D.11)$$

where

$$\frac{\partial r_p}{\partial A} = -4\frac{(p-C)}{A^3} \qquad (4.D.12)$$

$$\frac{\partial r_q}{\partial B} = -4\frac{q}{B^3} \qquad (4.D.13)$$

The derivative of plastic flow tensor with respect to p_{cT} is

$$\frac{\partial \mathbf{r}}{\partial p_{cT}} = \frac{1}{3}\frac{\partial r_p}{\partial p_{cT}}\mathbf{1} + \sqrt{\frac{3}{2}}\frac{\partial r_q}{\partial p_{cT}}\hat{\mathbf{n}} \qquad (4.D.14)$$

where

$$\frac{\partial r_p}{\partial p_{cT}} = \frac{\partial r_p}{\partial A}\frac{\partial A}{\partial p_{cT}} + \frac{\partial r_p}{\partial C}\frac{\partial C}{\partial p_{cT}} \qquad (4.D.15)$$

$$\frac{\partial r_q}{\partial p_{cT}} = \frac{\partial r_p}{\partial B}\frac{\partial B}{\partial p_{cT}} \qquad (4.D.16)$$

4.E. Appendix E: First and second derivatives of the Gibbs (complementary) energy potential at isothermal conditions

The Gibbs energy potential at isothermal conditions (Eq. (4.6)) is a function of p and q. By using the chain rule, the elastic strain tensor is derived:

$$\varepsilon^e = -\frac{\partial g_1(p,q)}{\partial \boldsymbol{\sigma}} = -\left(\frac{\partial g_1}{\partial p}\frac{\partial p}{\partial \boldsymbol{\sigma}} + \frac{\partial g_1}{\partial q}\frac{\partial q}{\partial \boldsymbol{\sigma}}\right) \tag{4.E.1}$$

In addition, $\frac{\partial g_1}{\partial p} = \varepsilon_v^e$ and $\frac{\partial g_1}{\partial p} = \varepsilon_s^e$ (according to hyperplasticity theory), and by substituting Eqs. (4.A.1) and (4.A.3) in Eq. (4.E.1), the elastic strain tensor is determined:

$$\varepsilon^e = \frac{\partial g_1}{\partial \boldsymbol{\sigma}} = \frac{1}{3}\varepsilon_v^e \mathbf{1} + \sqrt{\frac{3}{2}}\varepsilon_s^e \hat{\mathbf{n}} \tag{4.E.2}$$

The rate of elastic strain tensor is

$$\dot{\varepsilon}^e = \frac{1}{3}\dot{\varepsilon}_v^e \mathbf{1} + \sqrt{\frac{3}{2}}\dot{\varepsilon}_s^e \hat{\mathbf{n}} + \sqrt{\frac{3}{2}}\dot{\hat{\mathbf{n}}} \tag{4.E.3}$$

For the above equation, $\dot{\varepsilon}_v^e$, $\dot{\varepsilon}_s^e$ and $\dot{\hat{\mathbf{n}}}$ need to be determined.

With two times differentiating the Gibbs (complementary) energy potential, g_1, with respect to p and q, the elastic constitutive relationship is derived:

$$\begin{Bmatrix} \dot{\varepsilon}_v^e \\ \dot{\varepsilon}_s^e \end{Bmatrix} = \begin{bmatrix} c_{11}^e & c_{12}^e \\ c_{21}^e & c_{22}^e \end{bmatrix} \begin{Bmatrix} \dot{p} \\ \dot{q} \end{Bmatrix} = -\begin{bmatrix} \frac{\partial^2 g_1}{\partial p \partial p} & \frac{\partial^2 g_1}{\partial q \partial p} \\ \frac{\partial^2 g_1}{\partial p \partial q} & \frac{\partial^2 g_1}{\partial q \partial q} \end{bmatrix} \begin{Bmatrix} \dot{p} \\ \dot{q} \end{Bmatrix} \tag{4.E.4}$$

where $C_{21}^e = C_{12}^e$. Substituting Eqs. (4.A.1) and (4.A.3), respectively, for $\dot{p}$ and $\dot{q}$ results in

$$\dot{\varepsilon}_v^e = \left(\frac{1}{3}C_{11}^e \mathbf{1} + \sqrt{\frac{3}{2}}C_{12}^e \hat{\mathbf{n}}\right) : \dot{\boldsymbol{\sigma}} \tag{4.E.5}$$

$$\dot{\varepsilon}_s^e = \left(\frac{1}{3}C_{21}^e \mathbf{1} + \sqrt{\frac{3}{2}}C_{22}^e \hat{\mathbf{n}}\right) : \dot{\boldsymbol{\sigma}} \tag{4.E.6}$$

The derivative of $\hat{\mathbf{n}}$ with respect to stress tensor, $\boldsymbol{\sigma}$, is

$$\frac{\partial \hat{\mathbf{n}}}{\partial \boldsymbol{\sigma}} = \frac{1}{\|\mathbf{s}\|}\left(\frac{\partial \mathbf{s}}{\partial \boldsymbol{\sigma}} - \frac{\mathbf{s}}{\|\mathbf{s}\|}\frac{\partial \|\mathbf{s}\|}{\partial \boldsymbol{\sigma}}\right) = \frac{1}{\|\mathbf{s}\|}\left(\frac{\partial \mathbf{s}}{\partial \boldsymbol{\sigma}} - \hat{\mathbf{n}}\frac{\partial \|\mathbf{s}\|}{\partial \boldsymbol{\sigma}}\right) \tag{4.E.7}$$

where

$$\frac{\partial \|\mathbf{s}\|}{\partial \boldsymbol{\sigma}} \tag{4.E.8}$$

Further substituting Eqs. (4.A.2) and (4.E.8) in Eq. (4.E.7), lead to

$$\frac{\partial \hat{\mathbf{n}}}{\partial \boldsymbol{\sigma}} = \sqrt{\frac{3}{2}} \frac{1}{q} \left(\mathbf{I} - \frac{1}{3} \mathbf{1} \otimes \mathbf{1} - \hat{\mathbf{n}} \otimes \hat{\mathbf{n}} \right) \tag{4.E.9a}$$

$$\dot{\hat{\mathbf{n}}} = \sqrt{\frac{3}{2}} \frac{1}{q} \left(\mathbf{I} - \frac{1}{3} \mathbf{1} \otimes \mathbf{1} - \hat{\mathbf{n}} \otimes \hat{\mathbf{n}} \right) : \dot{\boldsymbol{\sigma}} \tag{4.E.9b}$$

Substituting Eqs. (4.E.5), (4.E.6) and (4.E.9) in Eq. (4.E.3), the incremental elastic strain tensor is derived:

$$\dot{\boldsymbol{\varepsilon}}^e = \mathbf{c} : \dot{\boldsymbol{\sigma}} \tag{4.E.10}$$

where **c** is the fourth-order elastic compliance tensor:

$$\mathbf{c} = \frac{3}{2} \frac{\varepsilon_s^e}{1} \mathbf{I} + \left(\frac{1}{9} C_{11}^e - \frac{1}{2} \frac{\varepsilon_s^e}{q} \right) (\mathbf{1} \otimes \mathbf{1}) + \sqrt{\frac{1}{6}} C_{12}^e (\hat{\mathbf{n}} \otimes \mathbf{1} + \mathbf{1} \otimes \hat{\mathbf{n}}) + \frac{3}{2} \left(C_{22}^e - \frac{\varepsilon_s^e}{q} \right) (\hat{\mathbf{n}} \otimes \hat{\mathbf{n}}) \tag{4.E.11}$$

The above equation also serves as the second derivative of Gibbs energy potential with respect to the stress tensor, $\boldsymbol{\sigma}$:

$$\mathbf{c} = -\frac{\partial^2 g_1}{\partial \boldsymbol{\sigma} \partial \boldsymbol{\sigma}} \tag{4.E.12}$$

For the Gibbs energy potential defined for $n \neq 1$ (Eq. (4.E.7)), it follows that

$$C_{11}^e = \frac{1}{\bar{K} (1-n) p_a^{1-n} p_o^n} \left(1 - \frac{np^2}{p_o^2} \right) \tag{4.E.13a}$$

$$C_{22}^e = \frac{1}{3\bar{G} p_a^{1-n} p_o^n} \left(1 - \frac{n\bar{K}(1-n)q^2}{3\bar{G}p_o^2} \right) \tag{4.E.13b}$$

$$C_{21}^e = C_{12}^e = -\frac{n}{3\bar{G}} \frac{pq}{p_a^{1-n} P_o^{n+2}} \tag{4.E.13c}$$

$$\varepsilon_s^e = -\frac{\partial g_1 (p,q)}{\partial q} = \frac{q}{3\bar{G} p_a^{1-n} p_o^n} \tag{4.E.13d}$$

For the Gibbs energy potential with $n = 1$ (Eq. (4.E.7)), it follows that

$$C_{11}^e = \frac{1}{\bar{K}_p} \left(1 + \frac{\bar{K}}{3\bar{G}} \frac{q^2}{p^2} \right) \tag{4.E.14a}$$

$$C_{22}^e = \frac{1}{3\bar{G}p} \tag{4.E.14b}$$

$$C_{21}^e = C_{12}^e = -\frac{1}{3\bar{G}}\frac{q}{p^2} \tag{4.E.14c}$$

$$\varepsilon_s^e = -\frac{\partial g_1(p,q)}{\partial q} = \frac{q}{3\bar{G}p} \tag{4.E.14d}$$

Note that, for the case of $n = 1$, $\frac{\varepsilon_s^e}{q} = C_{22}^e$, so that the elastic compliance tensor reduces to

$$\mathbf{c} = \frac{3}{2}C_{22}^e\mathbf{I} + \left(\frac{1}{9}C_{11}^e - \frac{1}{2}C_{22}^e\right)(\mathbf{1}\otimes\mathbf{1}) + \sqrt{\frac{1}{6}}C_{12}^e(\hat{\mathbf{n}}\otimes\mathbf{1}+\mathbf{1}\otimes\hat{\mathbf{n}}) \tag{4.E.15}$$

4.F. APPENDIX F: TRIAL STRESS TENSOR

The elastic volumetric strain and the elastic deviatoric strain (ε_v^e and ε_s^e) are calculated, respectively, as the derivative of Gibbs energy potential under isothermal conditions with respect to p and q. For the Gibbs energy potential defined for $n \neq 1$ (Eq.4.E.7), these variables are

$$\varepsilon_v^e = -\frac{\partial g_1(p,q)}{\partial p} = \frac{1}{\bar{K}(1-n)}\left(\frac{p}{p_a^{1-n}p_o^n} - 1\right) \tag{4.F.1a}$$

$$\varepsilon_v^e = -\frac{\partial g_1(p,q)}{\partial q} = \frac{q}{3\bar{G}p_a^{1-n}p_o^n} \tag{4.F.1b}$$

For the Gibbs energy potential with $n = 1$ (Eq. (4.E.7)), these variables are

$$\varepsilon_v^e = -\frac{\partial g_1(p,q)}{\partial p} = \frac{1}{\bar{K}}ln\left(\frac{p}{p_a}\right) - \frac{q^2}{6\bar{G}p^2} \tag{4.F.2a}$$

$$\varepsilon_s^e = -\frac{\partial g_1(p,q)}{\partial q} = \frac{q}{3\bar{G}p} \tag{4.F.2b}$$

By combining the elastic deviatoric strain with the elastic volumetric strain, it is possible to obtain (trial stress invariants) p and q which are defined by elastic strain increments. For Gibbs energy potential with $n \neq 1$, they are

$$p = p_a\left(\bar{K}(1-n)\varepsilon_v^e+1\right)^{\frac{1}{1-n}}\left(1+\frac{3\bar{G}\bar{K}(1-n)\left(\varepsilon_s^e\right)^2}{\left(\bar{K}(1-n)\varepsilon_v^e+1\right)^2}\right)^{\frac{n}{2-2n}} \tag{4.F.3a}$$

$$q = \left(\frac{3\bar{G}\varepsilon_s^e}{\bar{K}(1-n)\varepsilon_v^e+1}\right)p \tag{4.F.3b}$$

and for the Gibbs energy potential with $n = 1$, these variables are

$$p = p_a exp\left(\bar{K}\varepsilon_v^e + \frac{3\bar{G}\bar{K}}{2}\left(\varepsilon_s^e\right)^2\right) \tag{4.F.4a}$$

$$q = 3\bar{G}\varepsilon_s^e p \tag{4.F.4b}$$

5

A THERMO-MECHANICAL TWO SURFACE/BUBBLE MODEL FOR FINE-GRAINED SOILS

The formulation of a two surface/bubble thermo-mechanical constitutive model consistent with the principles of thermodynamics is presented. This allows plastic deformations inside the outer yield surface, resulting in a smooth stress-strain prediction and progressive cyclic deformations. This is achieved by the translation of the inner yield surface (also known as the bubble surface) with the stress state of the soil, inside the outer yield surface, by using a kinematic rule. The constitutive equations, including the hardening rules, are derived by specifying a Gibbs-type energy potential and a rate of dissipation potential function, ensuring thermodynamic consistency. The kinematic rule is divided into isothermal and non-isothermal parts. With the isothermal component, the model is capable of capturing the hysteresis behaviour of soils during cyclic mechanical loading. With the non-isothermal part, the model is able to predict the shakedown behaviour of soils observed when they are subjected to heating-cooling cycles. The performance of the model is compared with various experimental data for isothermal and non-isothermal conditions, and is shown to be in good agreement.

LIST OF SYMBOLS

Roman

1	Second order identity tensor
$\langle\rangle$	Macaulay bracket
A_i	Stress-like function for the inner yield surface
A_o	Stress-like function for the outer yield surface
B_i	Stress-like function for the inner yield surface
B_o	Stress-like function for the outer yield surface
b	Parameter controlling the accumulated thermo-plastic strains
C_i	Stress-like function for the inner yield surface
C_o	Stress-like function for the outer yield surface
C_χ	Parameter controlling the plastic strains
CS	Critical State
$\mathbf{C}^e$	Elastic compliance matrix
c_1	Thermodynamical constraint function
c_2	Thermodynamical constraint function
$(c_I)_p$	Thermodynamical constraint function under isothermal conditions along the p-axis
$(c_H)_p$	Thermodynamical constraint function under heating phase along the p-axis
$(c_I)_q$	Thermodynamical constraint function under isothermal conditions along the q-axis
$(c_H)_q$	Thermodynamical constraint function under heating phase along the q-axis
$\mathbf{D}^e$	Elastic stiffness matrix

Greek

α	Parameter related to the shape of the yield surface
α^*	Coefficient of linear thermal expansion
γ	Parameter related to the shape of the yield surface
ε	Strain tensor
ε^p	Plastic strain tensor
$\boldsymbol{\varepsilon}^e$	Elastic strain vector in triaxial space
$\boldsymbol{\varepsilon}^{Therm}$	Thermo-elastic strain vector in triaxial space
$\boldsymbol{\varepsilon}^p$	Plastic strain vector in triaxial space
$\boldsymbol{\varepsilon}^p_i$	Plastic strain vector related to d_i
$\boldsymbol{\varepsilon}^p_o$	Plastic strain vector related to d_o
$\dot{\boldsymbol{\varepsilon}}$	Rate of strain vector
$\dot{\boldsymbol{\varepsilon}}^p_i$	Rate of plastic strain vector related to inner yield surface
ε_v	Total volumetric strain
ε_s	Total deviatoric strain
ε^e_v	Elastic volumetric strain
ε^e_s	Elastic deviatoric strain
$\dot{\varepsilon}^e_v$	Elastic volumetric strain increment
$\dot{\varepsilon}^e_s$	Elastic deviatoric strain increment
ε^p_v	Plastic volumetric strain

d	Rate of dissipation potential function	ε_s^p	Plastic deviatoric strain
d_i	Sub-rate of dissipation function related to inner yield surface	$\dot{\varepsilon}_v^p$	Plastic volumetric strain increment
d_o	Sub-rate of dissipation function related to outer yield surface	$\dot{\varepsilon}_s^p$	Plastic deviatoric strain increment
e	Void ratio	$\varepsilon_{v,i}^p$	Plastic volumetric strain related to the inner yield surface
e_0	Initial void ratio	$\varepsilon_{v,o}^p$	Plastic volumetric strain related to the outer yield surface
$\mathbf{e}^p$	Plastic deviatoric strain tensor	$\varepsilon_{s,i}^p$	Plastic deviatoric strain related to the inner yield surface
g	Gibbs free energy potential	$\varepsilon_{s,o}^p$	Plastic deviatoric strain related to the outer yield surface
g_1	Isothermal Gibbs free energy potential	$\dot{\varepsilon}_{v,i}^p$	Plastic volumetric strain increment related to the inner yield surface
$\bar{G}$	Maximum elastic shear modulus	$\dot{\varepsilon}_{v,o}^p$	Plastic volumetric strain increment related to the outer yield surface
H	Function	$\dot{\varepsilon}_{s,i}^p$	Plastic deviatoric strain increment related to the inner yield surface
$\bar{K}$	Maximum elastic bulk modulus	$\dot{\varepsilon}_{s,o}^p$	Plastic deviatoric strain increment related to the outer yield surface
M	Critical State stress ratio	κ	Elastic compression index
M_0	Critical State stress ratio at ambient temperature	λ	Elasto-plastic compression index
n	Power of p for shear modulus	Λ_1	Lagrangian multiplier
OCR	Over consolidation ratio	Λ_2	Lagrangian multiplier
p	Hydrostatic pressure	$\dot{\Lambda}$	Plastic multiplier
p_{cT}	Apparent pre-consolidation pressure	μ	Coefficient of thermal softening of the inner yield surface
p_{c0}	Initial pre-consolidation pressure	μ_0	Coefficient of thermal softening of the outer yield surface
$\dot{p}_{cT}$	Rate of the apparent pre-consolidation pressure	υ	Specific volume
p_{iT}	Compression apex of the inner yield surface	π^*	Coefficient of Critical State stress ratio variation with temperature

5

$\dot{p}_{iT}$	Rate of change of the compression axis of the inner yield surface	$\boldsymbol{\rho}$	Coordinates of the decompression apex of the inner yield surface
$\tilde{p}_{iT}$	Size of the major-axis of the inner yield surface	$\dot{\boldsymbol{\rho}}$	Kinematic rule
$\tilde{p}_{i0}$	Initial size of the major-axis of the inner yield surface	$\dot{\boldsymbol{\rho}}_I$	Kinematic rule under isothermal conditions
$\dot{\tilde{p}}_{iT}$	Rate of change of the major-axis of the inner yield surface	$\dot{\boldsymbol{\rho}}_H$	Kinematic rule during heating phase
$\hat{p}$	Hydrostatic coordinate of projection centre	ρ_p	Hydrostatic coordinate of decompression apex of the inner yield surface
$\bar{p}$	Hydrostatic coordinate of image stress	ρ_q	Deviatoric coordinate of decompression apex of the inner yield surface
p_a	Atmospheric hydrostatic pressure	$\dot{\rho}_p$	Kinematic rule along the p-axis
q	Deviatoric stress	$(\dot{\rho}_I)_p$	Kinematic rule along the p-axis under isothermal conditions
$\hat{q}$	Deviatoric coordinate of projection centre	$(\dot{\rho}_H)_p$	Kinematic rule along the p-axis under heating phase
$\bar{q}$	Deviatoric coordinate of image stress	$\dot{\rho}_p$	Kinematic rule along the q-axis
r_p^i	Plastic flow along the p-axis	$(\dot{\rho}_I)_q$	Kinematic rule along the q-axis under isothermal conditions
r_q^i	Plastic flow along the q-axis	$\boldsymbol{\sigma}$	Stress tensor
$\mathbf{r}^i$	Plastic flow tensor	$\boldsymbol{\sigma}$	Stress vector
$\boldsymbol{r}^i$	Plastic flow vector in triaxial space	$\dot{\boldsymbol{\sigma}}$	Stress increment tensor
R_{ini}	Ratio between the inner and outer yield surfaces	$\hat{\boldsymbol{\sigma}}$	Stress coordinates of the projection centre
$\mathbf{s}$	Deviatoric stress tensor	$\dot{\hat{\boldsymbol{\sigma}}}$	Incremental changes of the projection centre
T	Absolute temperature	$\bar{\boldsymbol{\sigma}}$	Coordinates of the image stress in triaxial space
T_0	Initial absolute temperature	χ_i	Dissipative stress related to d_i
$\dot{T}$	Temperature increment	χ_o	Dissipative stress related to d_o
u_p	Pore water pressure	χ_ρ	Dissipative stress related to kinematic variable $\boldsymbol{\rho}$
$\dot{W}^p$	Total plastic work increment	χ_p^i	Hydrostatic dissipative stress related to d_i

y_i	Inner yield surface in true stress space	χ_p^o	Hydrostatic dissipative stress related to d_o
y_o	Outer yield surface in true stress space	χ_q^i	Deviatoric dissipative stress related to d_i
y_i^d	Inner yield surface in dissipative stress space	χ_q^o	Deviatoric dissipative stress related to d_o
y_o^d	Outer yield surface in dissipative stress space	$\bar{\chi}_i$	Generalised stress related to ε_i^p
$\dot{y}_i$	Rate of change of inner yield surface	$\bar{\chi}_o$	Generalised stress related to ε_o^p
		$\bar{\chi}_p^i$	Hydrostatic generalised stress related to ε_i^p
		$\bar{\chi}_p^o$	Hydrostatic generalised stress related to ε_o^p
		$\bar{\chi}_q^i$	Deviatoric generalised stress related to ε_i^p
		$\bar{\chi}_q^o$	Deviatoric generalised stress related to ε_o^p

5

5.1. INTRODUCTION

To account for plastic strains in over-consolidated states and to capture the cyclic mechanical behaviour of soils, several theories and models in plasticity of soils have been developed, of which multi-surface models and bounding surface models are examples. Multi-surface models (also known as nested surface models), which were proposed originally for metals, were developed independently by Mróz [1] and Iwan [2]. In these models, it is assumed that several yield surfaces exist, each with an associated hardening modulus, that can kinematically translate with the stress state of the material. In bounding surface models, which were first proposed by Dafalias & Popov [3] and Krieg [4] for metals, and later extended for soils by Dafalias [5] and Dafalias & Herrmann [6], mainly two surfaces were employed; a "*bounding surface*" which encloses all the admissible stress states and a "*yield surface*" which translates within the bounding surface. The stress state, when located on the yield surface, is mapped (with different approaches) onto the bounding surface (using the so-called image stress) and the distance between these stresses indicates how far the stress state is from the bounding surface, which controls the magnitude of plastic strain increments through the plastic modulus formulation. The further the distance, the smaller the plastic strain increment. These concepts have been employed by many researchers (e.g. [7–23]), and have been successful in capturing the main behaviour of soils.

The concept of bounding surface plasticity has been also extended to account for the effects of temperature on the behaviour of soils and for capturing the thermal cyclic shakedown behaviour of soils [24–27]. As previously discussed, these types of constitutive model may not always satisfy the laws of thermodynamics; i.e., by employing a certain range of parameters or following a certain stress path these models may not conserve energy (first law of thermodynamics) or result in negative dissipation (second law of thermodynamics) for deformations associated with plastic behaviour and, therefore, they are not unconditionally thermodynamically consistent. For example [24] showed that the response of their thermo-mechanical model is stress path independent when it is subjected to stress paths under isotropic conditions (where the deviatoric stress $q = 0$). However, for stress paths including non-isotropic stress states (where $q \neq 0$) their model fails to satisfy thermodynamics criteria.

As also previousy outlined, constitutive equations may also be obtained by using the principles of thermodynamics and several frameworks have been proposed (see [28; 29], for example). Hyperplasticity, firstly developed by Collins & Houlsby [30], is one of those approaches, which has been initially described in Chapter 2. There, a single surface thermo-mechanical constitutive model within this framework was developed which successfully captured the monotonic response under isothermal conditions, the temperature effects on volumetric behaviour and shear behaviour, and the cyclic response of normally and slightly consolidated fine-grained soils when subjected to a single heating-cooling cycle. These results were consistent with the majority of thermo-mechanical models, but has the advantage of being unconditionally thermodynamically consistent.

Similar also to the majority of (non-hyperplastic) models found in literature (e.g., [31–34]), the model presented in Chapter 2 also failed to capture a number of key features for advanced stress paths. This included not capturing a smooth stress-strain response for highly over-consolidated states, due to the use of a single yield surface which

resulted in an abrupt change in response when the mechanical behaviour changed from an elastic to an elasto-plastic response. Moreover, when simulating the mechanical cyclic behaviour of soils (loading-unloading) for over-consolidated states, since the state of the material is inside the yield surface, a portion of the response (depending on the OCR) was predicted to be purely elastic. This issue was also attributed to the use of a single yield surface in the model. In addition, the model could not predict the accumulated plastic strains when soils were subjected to several heating-cooling cycles. After the first heating-cooling cycle (for normally and slightly over-consolidated soils), the model predicted the subsequent behaviour as a thermo-elastic response. Therefore, to some extent, the model was incapable of predicting the thermo-plastic behaviour of slightly over-consolidated soils during heating-cooling cycles. One approach to resolve the aforementioned shortcomings is to utilise an inner yield surface, similar to bounding surface plasticity models, which can translate (move) in the stress space within the outer (bounding) surface. Thus, a certain amount of plasticity within the outer yield surface is developed.

In this chapter, the single surface thermo-mechanical constitutive model developed in in Chapter 2 is upgraded to a two surface (bubble-type) constitutive model. The model is developed using the framework of hyperplasticity with a newly defined rate of dissipation potential function (resulting in the yield surface formulation proposed in Chapter 3 and a newly proposed temperature-dependent kinematic hardening rule. Consequently, the model is capable of capturing the mechanical cyclic behaviour and thermal (heating-cooling) cyclic shakedown behaviour of fine-grained soils, as well as their monotonic thermo-mechanical behaviour, and the formulation is ensured to be consistent with the principles of thermodynamics.

Note that the formulations presented here are in accordance with geotechnical conventions, where compressive stresses and contractive strains are considered to be positive and all stresses are effective stresses. In line with this context, the thermal expansion coefficient utilised in this chapter are presented with negative values.

5.2. THERMO-MECHANICAL BEHAVIOUR OF FINE-GRAINED SOILS

The thermo-mechanical behaviour of fine-grained soils is reviewed in depth in Section 2.2, a summary is provided here, highlighting the features referenced in this chapter.

At elevated temperatures, fine-grained soils exhibit a reduction in pre-consolidation pressure in comparison with the pre-consolidation pressure at ambient temperature [35–38]. The observed variation of normalised pre-consolidation pressure (p_{cT}/p_{cT_0}, where p_{cT_0} is the pre-consolidation pressure at ambient temperature $T = T_0$) with temperature (T) for several soils is shown in Figure 5.1a.

Depending on the mineralogy and constituents of the soil, the influence of temperature on the shear behaviour of soils does not show a unique pattern. Figure 5.1b shows the variation of Critical State stress ratio (M) against temperature for a wide range of soils. It is observed that M may increase, decrease or remain unchanged at elevated temperatures [36–40].

When a fine-grained soil is subjected to heating at normally and slightly over-

consolidated states, the soil undergoes permanent (plastic) volumetric contraction [25; 41]. As the soil attains higher over-consolidated states (higher OCRs), the severity of permanent volumetric strains due to heating reduces [42] and the thermo-elastic behaviour, caused by the volumetric expansion of soil particles, dominates the deformation of the soil. This is demonstrated in Figure 5.1d, where the soil samples were subjected to a single heating-cooling cycle between 20°C and 95°C at different OCRs.
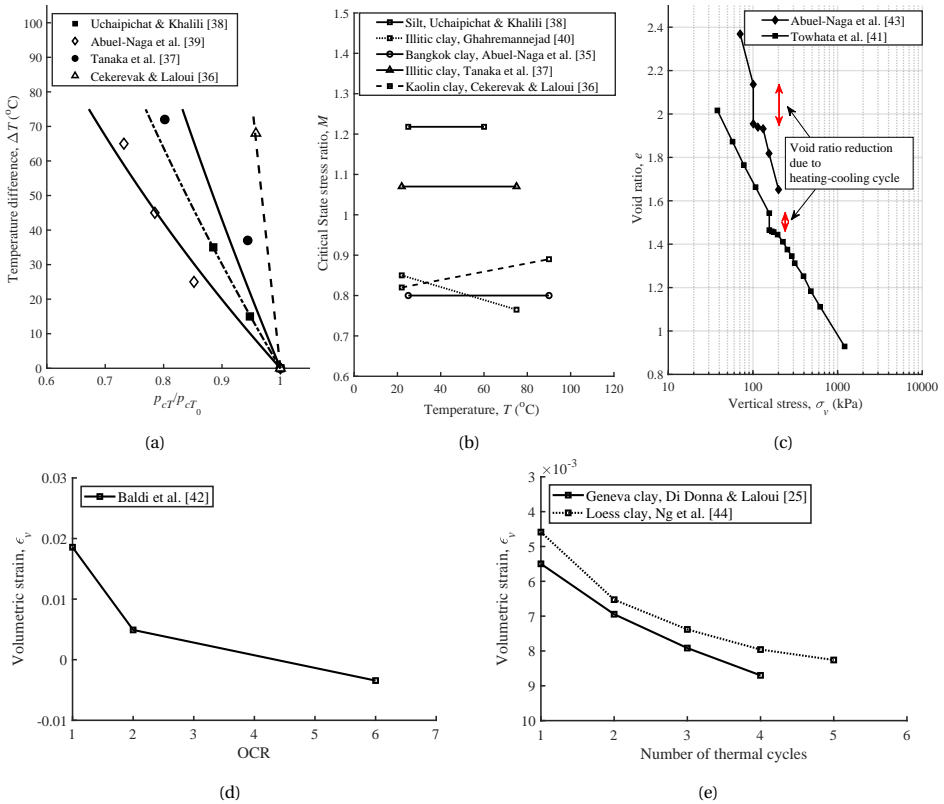
Figure 5.1: Thermo-mechanical behaviour of fine-grained soils: (a) normalised pre-consolidation pressure variation with temperature; (b) variation of Critical State stress ratio with temperature; (c) oedometer test results of void ratio reduction due to heating-cooling cycle; (d) thermo-plastic behaviour of soils subjected to heating at various OCRs; (e) shakedown behaviour of soils when subjected to several heating-cooling cycles

Fine-grained soils also exhibit hardening behaviour when they are subjected to heating-cooling cycles; i.e., after being subjected to thermal cycles, the soil attains a denser state due to the reduction of its volume. The oedometer results for the void ratio reduction of two different clays [41; 43] subjected to one heating-cooling cycle is presented in Figure 5.1a. Moreover, permanent volumetric strains are accumulated when the soil is subjected to several thermal cycles [25; 44]. However, the amount of permanent strains reduces as the number of thermal cycles increase, and this continues until the behaviour becomes thermo-elastic (Figure 5.1e). This is known as cyclic thermal

shakedown behaviour and is shown in Figure 5.1e for Geneva clay subjected to thermal cycles between 5°C and 60°C [25] and Loess clay subjected to heating-cooling cycles between 70°C and 15°C [44].

5.3. CONCEPTUAL FRAMEWORK

The proposed constitutive model utilises the formulation of an adapted Modified Cam-Clay type surface which is able to have non-elliptical shapes, proposed in Chapter 3, for both the outer yield surface and the inner yield surface. The outer yield surface is extended into the temperature domain, in a manner consistent with [31], so that the observed reduction in pre-consolidation pressure is captured. However, this constitutive model uses the existing formulation in Chapter 2 as a starting point, as this approach is thermodyamically consistent. In order to capture a smooth stress-strain response and the observed thermo-mechanical cyclic behaviour, a second surface (the inner yield or bubble surface) is included, as is shown schematically in Figure 5.2a.
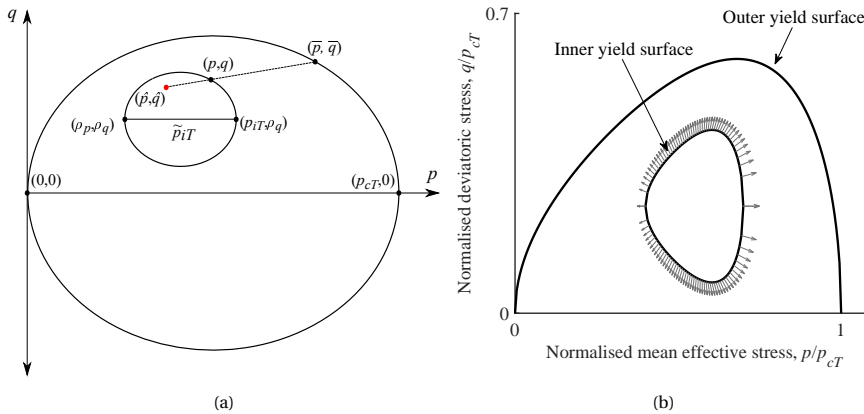

Figure 5.2: (a) The inner and outer yield surfaces ($\alpha = \gamma = 0$) in meridian plane; (b) non-associated flow rule of the inner yield surface ($\alpha = \gamma = 0.5$)

The two surfaces are geometrically similar in shape, with the possibility of having elliptical (Figure 5.2a) and non-elliptical shapes (Figure 5.2b) in the meridian (p-q) plane. The outer yield surface is pinned to the origin of the stress space $(p, q) = (0, 0)$ and is bounded at the apparent pre-consolidation pressure at the current temperature $(p, q) = (p_{cT}, 0)$ (Figure 2(a)). This surface is regarded as the surface encapsulating the loading history that the soil has experienced (i.e., the bounding surface) and can expand/shrink with temperature without hardening/softening (temperature dependent yield surface) (Figure 5.3) and with hardening/softening for plastic (volumetric) strains, consistent with the observed behaviour of fine-grained soils. The inner yield surface indicates the elastic domain and is bounded on the p-axis between ρ_p, as the de-compression apex, and p_{iT}, as the compression apex, with a major-axis size (hydrostatic extent) of $\tilde{p}_{iT}$ ($\tilde{p}_{iT} = p_{iT} - \rho_p$) (Figure 5.2a). When the state of the soil is inside the inner yield surface, the mechanical behaviour is (thermo) elastic, and stress states ly-

ing on the inner yield surface indicate an elasto-plastic response. The magnitude of the plastic strains is controlled by the proximity of the inner yield surface to the outer yield surface (i.e., controlled by the distance between the stress state (p, q) lying on the inner yield surface, and the geometrically similar position on the outer yield surface $(\bar{p}, \bar{q})$ (also called the image stress)). The inner surface can move (translate) with the state of the soil inside the outer yield surface; i.e., the domain in which the inner yield surface can move is limited by the enclosed area of the outer yield surface in temperature and stress space.

The translation of the inner yield surface is triggered when plastic strain increments are developed and is governed by a kinematic rule, which is controlled by the distance between the stress (on the inner yield surface) and the image stress (on the outer yield surface) and the growth of the inner and outer yield surfaces.

The inner yield surface, similar to the outer yield surface, shrinks in size in response to an increase in temperature (heating phase) (Figure 5.3a). To capture the progress of plasticity during consecutive heating-cooling cycles, the hydrostatic extent of this surface reacts neutrally to a decrease in temperature, i.e., the size of the major-axis of the surface remains unchanged during cooling (Figure 5.3b). This feature enables the state of the material to encounter the inner yield surface during the heating phase and is in contrast to the outer yield surface which expands as temperature decreases. With these features, the model is able to predict a smooth stress-strain response at any state, simulate the mechanical cyclic response, and predict the shakedown behaviour and accumulated plastic strains observed when soils are subjected to several heating-cooling cycles.
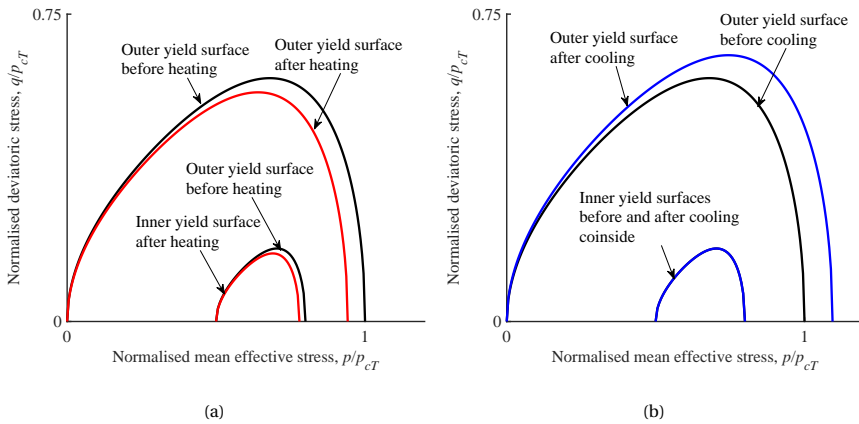

Figure 5.3: (a) The inner and outer yield surfaces under heating phase in meridian (p-q) space ($\alpha = \gamma = 0.5$); (b) the inner and outer yield surfaces under cooling phase

The elasticity formulation used for the model is non-linear and the plastic flow is non-associated, i.e., not necessarily perpendicular to the inner yield surface (Figure 5.2b), without the necessity of defining a separate plastic potential as is the case for conventional plasticity models. This feature is obtained by following the thermodynamically consistent hyperplastic approach [28; 30]. The temperature effects on the shear

behaviour are accounted for by defining a temperature-dependent Critical State stress ratio (*M*). The effect of temperature on volumetric behaviour is encapsulated in the temperature-dependency of the outer yield surface, and in the temperature-dependent isotropic hardening rule of the inner yield surface (Figure 5.3). In addition, the thermal-dependency of the inner yield surface is proposed to be dependent on the state of the soil, to capture the thermo-mechanical behaviour of the soil at highly over-consolidated states, as well as slightly over and normally consolidated states. Note that all the aforementioned mechanisms are embedded in the formulation of a newly proposed rate of dissipation potential.

5.4. FORMULATION

The constitutive equations presented here are defined in triaxial stress space and are developed within the framework of hyperplasticity theory [28; 30], where the formulations are derived by specifying an energy potential and a rate of dissipation function (for rate independent materials). A detailed description of the thermodynamics equations relating to the thermo-mechanical aspects can be found in Chapter 2. A Gibbs-type energy potential, defined by the independent variables, is selected for the energy potential. The independent variables are the true stress invariants in triaxial stress space (hydrostatic pressure or mean effective stress, $p = tr(\boldsymbol{\sigma})/3$ (kPa) and deviatoric stress, $q = (3/2\ \mathbf{s}{:}\mathbf{s})^{1/2}$ (kPa), where $\boldsymbol{\sigma}$ and $\mathbf{s} = \boldsymbol{\sigma} - tr(\boldsymbol{\sigma})/3 : \mathbf{1}$ are, respectively, the stress and deviatoric stress tensors), internal variables (which here are the plastic strain invariants, i.e., the plastic volumetric strain, $\varepsilon_v^p = tr(\boldsymbol{\varepsilon}^p)$, and the plastic deviatoric strain, $\varepsilon_s^p = (2/3\ \mathbf{e}^p : \mathbf{e}^p)^{1/2}$; $\mathbf{e}^p = \boldsymbol{\varepsilon}^p - tr(\boldsymbol{\varepsilon}^p)/3 : \mathbf{1}$, where $\boldsymbol{\varepsilon}^p$, $\mathbf{e}^p$ and $\mathbf{1}$ are the plastic strain, plastic deviatoric strain, and identity tensors, respectively), and the absolute temperature T(K). The energy potential is defined as

$$g = g_1\left(p, q\right) - \left(p\varepsilon_{v,o}^p + q\varepsilon_{s,o}^p\right) - \left(p\varepsilon_{v,i}^p + q\varepsilon_{s,i}^p\right) - 3\alpha^* p\left(T - T_0\right) \tag{5.1}$$

where "*i*" and "*o*", respectively, correspond to the variables of the inner and outer yield surfaces, α^* is the linear thermal expansion coefficient of the soil skeleton and $g_1(p, q)$ represents the Gibbs energy potential at isothermal conditions, where the elastic component of the model is derived from Appendix 5.A. The form of the energy potential considered here (Eq. (5.1)) results in a "*decoupled*" material behaviour [30] through the decoupling terms $p\varepsilon_v^p$ and $q\varepsilon_s^p$, in which the elastic and plastic behaviours became independent of each other. The choice for a decoupled formulation is made in order to obtain a less complex formulation and ease of implementing the constitutive equations into boundary-value solvers such as FEM and MPM. Energy potentials incorporating elastic-plastic coupling can be found in the works of [11; 14; 45]. Note that some researchers may argue that plastic strains should not be considered as internal variables (see for example [46; 47] and assume that by nature the behaviour of the material is the sum of elastic and plastic strains. For such an assumption, the decoupling terms drop out of the energy potential function.

To derive the rate-independent plasticity formulation, the definition of an appropriate rate of dissipation potential function (*d*) is necessary and this is required to be a first order homogenous function of plastic strain rates [30], and unlike [48; 49], the rate of

dissipation function (Eq. (5.2)) is defined in such a way that the use of a shift stress to transfer stresses from dissipative stress space to true stress space is eliminated [28; 50]. As a result, the derived formulations become simpler. The total rate of dissipation potential consists of two sub-rate of dissipation potentials (d_o and d_i) relating to the rate of dissipation of the outer yield surface and the inner yield (bubble) surface. The constitutive model is enriched by a kinematic rule assigned to the internal variable $\boldsymbol{\rho}$. The approach proposed by [50; 51] is followed here to ensure that the proposed kinematic rule is formulated in a consistent manner with thermodynamics. This operation is performed via the addition of thermodynamic complementary constraint functions (c_1 and c_2) using the standard method of Lagrangian multipliers. The rate of dissipation function is defined as

$$d = d_o + d_i + \Lambda_1 c_1 + \Lambda_2 c_2 \tag{5.2a}$$

$$d_o = C_o \dot{\varepsilon}_{v,o}^p + \sqrt{A_o^2 \left(\dot{\varepsilon}_{v,o}^p\right)^2 + B_o^2 \left(\dot{\varepsilon}_{s,o}^p\right)^2} \tag{5.2b}$$

$$d_i = \left(C_i + \rho_p\right) \dot{\varepsilon}_{v,i}^p + \rho_q \dot{\varepsilon}_{s,i}^p + \sqrt{A_i^2 \left(\dot{\varepsilon}_{v,i}^p\right)^2 + B_i^2 \left(\dot{\varepsilon}_{s,i}^p\right)^2} \tag{5.2c}$$

$$c_1 \left(\dot{\varepsilon}_{v,i}^p, \dot{\rho}_p, p, \rho_p, p_{cT}, \tilde{p}_{iT}\right) = 0 \tag{5.2d}$$

$$c_2 \left(\dot{\varepsilon}_{s,i}^p, \dot{\rho}_q, q, \rho_q, p_{cT}, \tilde{p}_{iT}\right) = 0 \tag{5.2e}$$

where d_o and d_i are, respectively, the rate of dissipation potentials that the outer and inner yield surfaces are derived from; $\dot{\varepsilon}_{v,k}^p$ and $\dot{\varepsilon}_{s,k}^p$ ($k = i, o$) are plastic volumetric and deviatoric strain increments corresponding to the inner and outer yield surfaces; A_k, B_k and C_k are stress-like functions of the inner and outer yield surfaces; ρ_p and ρ_q are, respectively, the hydrostatic and deviatoric components of the kinematic variable $\boldsymbol{\rho}$ which represent the coordinates (location) of the de-compression apex of the inner yield surface in meridian stress space; and, $\dot{\rho}_p$ and $\dot{\rho}_q$ are the incremental translations of the inner yield surface along the p-axis and q-axis, respectively. Note that the sub-rate of dissipation potentials considered in Eq. (5.2a) have the general formulation of the rate of dissipation function in the existing formulation of Chapter 2 without considering the rotation/shearing of the surface with respect to the p-axis.

The thermodynamic constraint functions, c_1 and c_2, are augmented by Lagrangian multipliers (Λ_1 and Λ_2) in the rate of dissipation potential d (Eq. (5.2a)) [50; 51]. Note that c_1 and c_2 are numerically zero (Eq. (5.2d) and Eq. (5.2e)), which implies that

$$d = d_o + d_i \tag{5.2f}$$

This means that the terms $\Lambda_1 c_1$ and $\Lambda_2 c_2$ in Eq. (5.2a) do not produce any work and they represent constraints to optimise the maximum rate of dissipation, d (Eq. (5.2a)) [52]; i.e., the addition of constraints restricts the solutions for maximising d to a subset where

the conditions $c_1 = 0$ and $c_2 = 0$ are valid. The specific formulations of c_1 and c_2 are considered later in this section.

According to the principles of thermodynamics, it is assumed that dissipative materials (e.g. geomaterials) prefer to follow a state path which produces the maximum rate of dissipation (to ensure the second law of thermodynamics is satisfied). When the rate of dissipation is maximised, i.e., when Ziegler's postulation is valid, it follows that $\Lambda_1 = \Lambda_2 = 0$ (see Appendix 5.A). This means that constitutive equations may be obtained from the Gibbs energy potential (Eq. (5.1)) along with the rate of dissipation potential function Eq. (5.2f), with extra conditions that satisfy the constraint functions (c_1 and c_2). These additional conditions form the kinematic rule. In short, the addition of the constraint functions ensures that only the possible state paths (i.e., when the kinematic rule is valid) are considered. This approach has been used by other researchers to add several constraints to constitutive equations [50–53].

The outer yield surface and the inner yield surface are derived from the sub-rate of dissipation potentials and are defined by dissipative stresses which are obtained by differentiating the rate of dissipation potential with respect to the internal variables. The flow rule is derived by considering associated conditions to the inner yield surface in dissipative stresses (i.e., the flow rule is perpendicular to the inner yield surface defined in dissipative stress space). The derivation of the outer yield surface, the inner yield surface, and the plastic flow in true (triaxial) stress space (p, q) are provided in Appendix 5.A and are summarised, respectively, as

$$\text{Outer yield surface}: \quad y_o = B_o^2 \left(p - C_o \right)^2 + A_o^2 q^2 - A_o^2 B_o^2 = 0 \tag{5.3}$$

$$\text{Inner yield surface}: \quad y_i = B_i^2 \left(\tilde{p} - C_i \right)^2 + A_i^2 \tilde{q}^2 - A_i^2 B_i^2 = 0 \tag{5.4}$$

$$\text{flow}: \quad \left\{ \boldsymbol{r}^i \right\} = \left\{ \begin{array}{c} r_p^i \\ r_q^i \end{array} \right\} = 2 \left\{ \begin{array}{c} B_i^2 \left(\tilde{p} - C_i \right) \\ A_i^2 \tilde{q} \end{array} \right\} \tag{5.5}$$

where $\tilde{p} = p - \rho_p$ and $\tilde{q} = q - \rho_q$; $\boldsymbol{r}^i$, r_p^i, and r_q^i are, respectively, the plastic flow vector (in triaxial stress space), the plastic flow along the p-axis and the plastic flow along the q-axis. Note that, although the plastic flow in dissipative stress space (Eq. (5.A.15)) is associated with respect to the inner yield surface in dissipative stress space (Eq. (5.A.14)), the plastic flow in true stress space (Eq. (5.5)) may become non-associated with respect to the inner yield surface defined in true stress space (Eq. (5.4)) (see Figure 5.2b). This observation is due to the stress dependency of the rate of dissipation potential function via stress-like functions (see Chapter 2 for more details).

The stress-like functions (A_k, B_k and C_k; $k = i, o$) define the shape and the size of the surfaces in true stress space and are generally expressed by terms consisting of the true stresses, isotropic hardening variables and shape parameters. In Chapter 3 a new set of these functions was proposed, which provides flexibility for the yield surface to attain various non-elliptical shapes and improves the robustness when using implicit stress integration schemes for numerically implementing in boundary-value solvers. This was

achieved by eliminating the potential for false elastic nuclei and divergent zones. The stress-like functions for the outer yield surface are

$$A_o\left(p, p_{cT}\right) = \frac{p_{cT}}{2\pi}\left(2\arctan\left(\gamma\left(\frac{1}{2} - \frac{p}{p_{cT}}\right)\right) + \pi\right) \tag{5.6a}$$

$$B_o\left(p, p_{cT}\right) = MC_o\exp\left(\frac{\alpha\left(p - C_o\right)}{p_{cT}}\right) \tag{5.6b}$$

$$C_o\left(p_{cT}\right) = \frac{p_{cT}}{2\pi}\left(2\arctan\left(\frac{\gamma}{2}\right) + \pi\right) \tag{5.6c}$$

where α and γ are shape parameters that affect the shape of the surface to form a wide range of non-elliptical shapes (e.g. tear and bullet shapes) observed for fine-grained soils and have values in the range $-2 \le \alpha, \gamma \le 2$ (see Appendix 5.F). The effect of these parameters on the shape of the outer and the inner yield surfaces in meridian stress space (p, q) for $(\alpha, \gamma) = (0, -1)$, $(0, 0)$ and $(0, 1.5)$ is shown in Figure 5.4. Note that for $(\alpha, \gamma) = (0, 0)$ the elliptical shape of the MCC model is obtained.
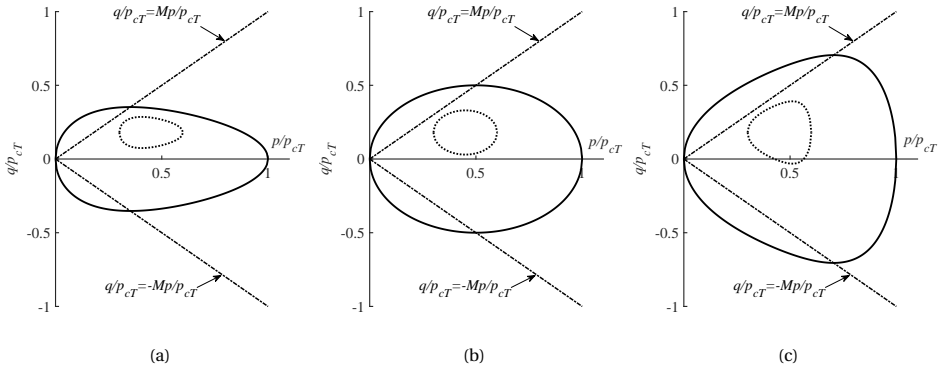
Figure 5.4: The inner and outer yield surfaces in meridian $(p\text{-}q)$ space: (a) $(\alpha, \gamma) = (0, -1)$; (b) $(\alpha, \gamma) = (0, 0)$; (c) $(\alpha, \gamma) = (0, 1.5)$

p_{cT} is the apparent pre-consolidation pressure defined as

$$p_{cT} = p_{c0}\exp\left(\frac{1 + e_0}{\lambda - \kappa}\varepsilon_v^p\right)\exp\left(-\mu_0\left(T - T_0\right)\right) \tag{5.7}$$

where p_{c0} is the initial pre-consolidation pressure, λ and κ are the bi-logarithmic elasto-plastic and elastic compressibility indices, respectively, e_0 is the initial void ratio, and μ_0 is the coefficient of thermal shrinkage of the outer yield surface, first presented by [31], to capture the observed pre-consolidation pressure reduction due to temperature increase (Figure 5.1a). M is the stress ratio at Critical State conditions and is defined as

$$M = M_0 + \pi^*\left(T - T_0\right) \tag{5.8}$$

where π^* is the gradient of the variation of M with temperature T, and M_0 is the Critical State stress ratio at ambient temperature $T = T_0$, which is compatible with the observed behaviour in Figure 5.1b.

The corresponding stress-like functions for the inner yield surface are similar to those for the outer yield surface, where p and p_{cT} are respectively replaced by $\tilde{p}$ and $\tilde{p}_{iT}$:

$$A_i\left(\tilde{p}, \tilde{p}_{iT}\right) = \frac{\tilde{p}_{iT}}{2\pi} \left(2\arctan\left(\gamma\left(\frac{1}{2} - \frac{\tilde{p}}{\tilde{p}_{iT}}\right)\right) + \pi\right) \tag{5.9a}$$

$$B_i\left(\tilde{p}, \tilde{p}_{iT}\right) = MC_i \exp\left(\frac{\alpha\left(\tilde{p} - C_i\right)}{\tilde{p}_{iT}}\right) \tag{5.9b}$$

$$C_i\left(\tilde{p}_{iT}\right) = \frac{\tilde{p}_{iT}}{2\pi} \left(2\arctan\left(\frac{\gamma}{2}\right) + \pi\right) \tag{5.9c}$$

where $\tilde{p}_{iT}$ is the isotropic hardening variable representing the size of the major-axis of the inner yield surface, and is defined as

$$\tilde{p}_{iT} = \tilde{p}_{i0} \exp\left(\frac{1 + e_0}{\lambda - \kappa} \varepsilon_v^p\right) \exp\left(-\mu \langle T - T_0 \rangle\right) \tag{5.10}$$

where $\tilde{p}_{i0}$ is the initial value of $\tilde{p}_{iT}$, $\langle \rangle$ is the Macaulay bracket which operates as $\langle x \rangle = (x + |x|)/2$, and

$$\mu = \mu_0 \left(\frac{p_{iT}}{p_{cT}}\right)^b \tag{5.11}$$

where $p_{iT}(= \rho_p + \tilde{p}_{iT})$ indicates the coordinates of the compression apex of the inner yield surface (Figure 5.2a) along the p-axis. The coefficient of thermal shrinkage of the inner yield surface, μ, varies with the ratio of the hydrostatic coordinate of the compression apex of the inner yield surface with respect to the hydrostatic coordinate of the compression apex of the outer yield surface, p_{iT}/p_{cT}, in order to capture the thermomechanical behaviour of soils at various over-consolidated stress states. For normally-consolidated states, $p_{iT}/p_{cT} = 1$, and thus $\mu = \mu_0$. For over-consolidated states, however, $p_{iT}/p_{cT} < 1$ which results in $\mu < \mu_0$. As a result, the coefficient of thermal shrinkage (and consequently, thermally induced plastic strain increments) reduces as the state of the soil becomes over-consolidated, which is compatible with experimental observations (Figure 5.1d). The parameter b in Eq. (5.11) controls the amount of accumulated plastic strains when the soil is subjected to heating-cooling cycles.

Plastic strain increments in triaxial space are calculated as

$$\left\{\dot{\boldsymbol{\varepsilon}}^p\right\} = \dot{\Lambda}\left\{\boldsymbol{r}^i\right\} = \dot{\Lambda}\left\{\begin{array}{c} r_p^i \\ r_q^i \end{array}\right\} \tag{5.12}$$

where $\dot{\Lambda}$ is the plastic multiplier representing the magnitude of the plastic strain increments and is defined, for strain controlled conditions (see Appendix 5.C), as

$$\dot{\Lambda} = \frac{\left\{\frac{\partial y_i}{\partial \tilde{\boldsymbol{\sigma}}}\right\}^{\mathrm{T}} [\mathbf{D}^e]\left\{\dot{\boldsymbol{\varepsilon}} - \dot{\boldsymbol{\varepsilon}}^{Therm}\right\} + \frac{\partial y_i}{\partial \tilde{p}_{iT}} U_{\tilde{p}_{iT}} + \frac{\partial y_i}{\partial M}\dot{M}}{\left\{\frac{\partial y_i}{\partial \tilde{\boldsymbol{\sigma}}}\right\}^{\mathrm{T}} [\mathbf{D}^e]\left\{\boldsymbol{r}^i\right\} + \left\{\frac{\partial y_i}{\partial \tilde{\boldsymbol{\sigma}}}\right\}^{\mathrm{T}}\left\{\boldsymbol{M}_I + \boldsymbol{M}_H\right\} - \frac{\partial y_i}{\partial \tilde{p}_{iT}} M_{\tilde{p}_{iT}}} \tag{5.13}$$

where $\mathbf{D}^e$ is the elastic stiffness matrix; $\dot{\boldsymbol{\varepsilon}}$ and $\dot{\boldsymbol{\varepsilon}}^{Therm}$ are, respectively, the vectors of total strain and thermal strain increments in triaxial space; $\partial y_i/\partial\tilde{\boldsymbol{\sigma}}$, $\partial y_i/\partial\tilde{p}_{iT}$ and $\partial y_i/\partial M$ are the derivatives of the inner yield surface with respect to $\tilde{\boldsymbol{\sigma}}$, $\tilde{p}_{iT}$ and M (see Appendix 5.D); and $U_{\tilde{p}_{iT}}$, M_I, M_H and $M_{\tilde{p}_{iT}}$ are defined in Appendix 5.C.

5.4.1. ISOTROPIC HARDENING RULES

The model has two isotropic hardening rules assigned to the isotropic hardening variables of the outer and inner yield surfaces (p_{cT} and $\tilde{p}_{iT}$, respectively). Two mechanisms control the size of the outer yield surface, in which one, similar to the MCC model, is due to the development of plastic strains and the other is influenced by temperature changes. The isotropic hardening rule of the outer yield surface is determined from the rate of Eq. (5.7)

$$\dot{p}_{cT} = p_{cT}\left(\frac{1+e_0}{\lambda-\kappa}\dot{\varepsilon}_v^p - \mu_0\dot{T}\right) \tag{5.14}$$

The rate of Eq. (5.10) defines the isotropic hardening rule for the inner yield surface:

$$\dot{\tilde{p}}_{iT} = \tilde{p}_{iT}\left(\frac{1+e_0}{\lambda-\kappa}\dot{\varepsilon}_v^p - \left(\mu\langle\dot{T}\rangle + \dot{\mu}\langle T - T_0\rangle\right)\right) \tag{5.15}$$

The outer yield surface and the inner yield surface harden (grow) incrementally with plastic volumetric strain increments, via the respective terms $p_{cT}\left((1+e_0)/(\lambda-\kappa)\right)\dot{\varepsilon}_v^p$ and $\tilde{p}_{iT}\left((1+e_0)/(\lambda-\kappa)\right)\dot{\varepsilon}_v^p$.

The hydrostatic extent of the outer yield surface changes for any variation of temperature (heating and cooling). The surface shrinks or expands due to an increase or decrease of temperature, respectively, via the term $\dot{p}_{cT} = -\mu_0 p_{cT}\dot{T}$. However, due to the presence of Macaulay brackets in Eq. (5.15), the hydrostatic extent of the inner yield surface only shrinks as the temperature increases (heating phase) and remains unchanged when the temperature decreases (cooling phase) (see Figure 5.3). This behaviour is controlled via the term $\dot{\tilde{p}}_{iT} = -\tilde{p}_{iT}\left(\mu\langle\dot{T}\rangle + \dot{\mu}\langle T - T_0\rangle\right)$.

Note that the constitutive assumption of independent behaviour of the inner yield surface on the cooling phase is consistent with experimental observations. For example, Ng et al. [44] observed that when Loess clay samples were subjected to thermal cycles (and the vertical stress was kept constant), the gradients of the strain-temperature curves during cooling were almost always the same. In addition, these gradients were the same as the recoverable gradient after many thermal cycles. Therefore, it can be inferred that the response of the soil during cooling is recoverable (thermo-elastic) and that the inner surface is independent on cooling.

5.4.2. KINEMATIC RULE

The purpose of introducing the inner yield surface is to capture the plastic strains that have been observed for stress states inside the outer yield surface. This requires the inner yield surface to move (translate), in accordance with the state of the soil, within the domain enclosed by the outer yield surface. Therefore, a so-called kinematic rule is needed. The kinematic rule can be assigned to any specific point of the inner yield surface. For example, in a number of models the kinematic rule is assigned to the centre of the inner yield surface [17–19; 21; 49; 54]. For the model proposed here, the kinematic rule is assigned to the internal variable $\boldsymbol{\rho} = (\rho_p, \rho_q)$, which represents the coordinates of the decompression apex of the inner surface. This reduces the geometrical complexity of the kinematic rule, specifically when the two surfaces have non-elliptical shapes.

The thermodynamic constraint functions in Eq. (5.2) are defined as

$$c_1 = \dot{\rho}_p - (c_I)_p - (c_H)_p = 0 \tag{5.16a}$$

$$c_2 = \dot{\rho}_q - (c_I)_q - (c_H)_q = 0 \tag{5.16b}$$

where $(c_I)_p$ and $(c_H)_p$ are the hydrostatic kinematic constraint functions under isothermal and heating conditions respectively, and $(c_I)_q$ and $(c_H)_q$ are the respective deviatoric kinematic constraint functions under isothermal and heating conditions, which, all together, form the kinematic rule of the inner yield surface. Note that these constraint functions should be first order homogenous functions with respect to their internal variables (a thermodynamic requirement), similar to the definition of the rate of dissipation function d. As explained before, when the rate of dissipation is maximised, Eq. (5.2d) and Eq. (5.2e) are valid ($c_1 = c_2 = 0$) (see Appendix 5.A). Therefore, from c_1 and c_2 (Eq. (5.16b)), the kinematic rule along the hydrostatic and deviatoric axes are determined:

$$\{\dot{\boldsymbol{\rho}}\} = \left\{ \begin{array}{c} \dot{\rho}_p \\ \dot{\rho}_q \end{array} \right\} = \left\{ \begin{array}{c} (c_I)_p \\ (c_I)_q \end{array} \right\} + \left\{ \begin{array}{c} (c_H)_p \\ (c_H)_q \end{array} \right\} = \{\dot{\boldsymbol{\rho}}_I\} + \{\dot{\boldsymbol{\rho}}_H\} \tag{5.17}$$

The kinematic rule has been decomposed into components due to isothermal $\dot{\rho}_I$ and heating $\dot{\rho}_H$, which are explained in the following subsections.

INTERACTION BETWEEN THE INNER YIELD SURFACE AND THE OUTER YIELD SURFACE UNDER ISOTHERMAL CONDITIONS

The derivation of the kinematic rule under isothermal conditions, by modifying the approach of Coombs et al. [49], is explained in detail in Appendix 5.B. With this kinematic rule, the inner yield surface and the outer yield surface interact with each other, such that a stress point on the inner yield surface (with an elasto-plastic response) moves toward the image stress projected on the outer yield surface. The kinematic rule under isothermal conditions is defined as

$$\{\dot{\boldsymbol{\rho}}_I\} = \left\{ \begin{array}{c} (c_I)_p \\ (c_I)_q \end{array} \right\} = \left(\frac{1}{W_r} \left(\frac{\dot{p}_c}{p_{cT}} - \frac{\dot{p}_i}{p_{cT}} \right) - C_\chi \left\| \dot{\varepsilon}^p \right\| \right) \{\boldsymbol{\rho}\} + C_\chi \left\| \dot{\varepsilon}^p \right\| W_r \{\boldsymbol{\sigma}\} \tag{5.18}$$

where $\| \dot{\varepsilon}^p \|$ is the magnitude of the plastic strain increment; C_χ is a parameter which controls the pace of the inner yield surface approaching the outer yield surface; and W_r,

p_c, $\dot{p}_c$ and $\dot{p}_i$ are defined in Appendix 5.B. This kinematic rule is activated when plastic strain increments are produced, i.e., when the response is elastic it is zero. In addition, it can be shown that the proposed formulation is a first order homogenous function of its rate variables (a thermodynamic requirement).

KINEMATIC RULE UNDER NON-ISOTHERMAL CONDITIONS

The kinematic rule under isothermal conditions (Eq. (5.18)) is extended in order to capture the accumulated plastic strains and shakedown behaviour observed, when soils are subjected to consecutive heating-cooling cycles. This kinematic rule allows the simulation of progressive strains due to thermal cycles. The kinematic rule under non-isothermal conditions is defined as

$$\{\dot{\boldsymbol{\rho}}_H\} = \left\{ \begin{array}{c} (\dot{\rho}_H)_p \\ (\dot{\rho}_H)_q \end{array} \right\} = \left\{ \begin{array}{c} (c_H)_p \\ (c_H)_q \end{array} \right\} = -H(\dot{T}) \left\{ \begin{array}{c} (\dot{\rho}_I)_p \\ 0 \end{array} \right\} \tag{5.19}$$

where $H(\dot{T})$ is a function similar to the Heaviside function, defined as

$$H(\dot{T}) = \begin{cases} 0 & \text{when } \dot{T} \leq 0 \text{ (under isothermal and cooling phase)} \\ 1 & \text{when } \dot{T} > 0 \text{ (heating phase)} \end{cases} \tag{5.20}$$

Due to the presence of $H(\dot{T})$, the model activates the kinematic rule $\dot{\boldsymbol{\rho}}_H$ only during the heating phase. For isothermal conditions and during cooling, $\dot{T} \leq 0$ which results in $H = 0$. On the other hand, during heating $\dot{T} > 0$ which results in $H = 1$ and activates the kinematic rule $\dot{\boldsymbol{\rho}}_H$. An example of a soil element that is subjected to thermal cycles is provided to explain the role of the kinematic rule $\dot{\boldsymbol{\rho}}_H$ on capturing the shakedown behaviour and the progressive development of plastic strains due to thermal cycles.

Assume a soil in an isotropic state ($q = 0$) and at an ambient temperature ($T = T_0$) has a hydrostatic pressure of p_1 and has experienced a maximum hydrostatic pressure of p_{cT} (pre consolidation pressure) where $p_{cT} > p_1$. The state of the soil is $(p, q, T) = (p_1, 0, T_0)$ and is inside the inner yield surface. While the hydrostatic pressure is held constant ($p = p_1$), the soil is subjected to heating from $T = T_0$ to $T = T_1$ (as shown in Figure 5.5a in p-T space). Due to heating and considering that the state of the soil is inside the yield surface (thermo-elastic response), the isotropic hardening rules for the outer and inner yield surfaces (Eqs. (5.14) and (5.15), respectively) reduce to $\dot{p}_{cT} = -\mu_0 p_{cT} \dot{T}$ and $\dot{p}_{iT} = -\tilde{p}_{iT}(\mu\langle\dot{T}\rangle + \dot{\mu}\langle T - T_0\rangle)$. Therefore, the outer and inner yield surfaces shrink in accordance with their respective isotropic rule. While the state of the material is inside the inner yield surface, the behaviour is thermo-elastic and the kinematic rule $\dot{\boldsymbol{\rho}}_I$ is deactivated. The shrinkage of the inner surface continues (as the temperature increases) until the state of the soil encounters it at $T = T^*$ (position $p_{iT}^* = p_1$). Due to the consistency condition, which requires that the stress state remains on the yield surface, and, since p is kept constant, $\dot{p}_{iT} = 0$. Hence, plastic volumetric strain increments are then produced to compensate the thermal shrinkage and are determined from Eq. (5.15) as $\dot{\varepsilon}_v^p = \left(\frac{1+e_0}{\lambda-\kappa}\right)^{-1}(\mu\langle\dot{T}\rangle + \dot{\mu}\langle T - T_0\rangle)$. As plastic volumetric strain increments are produced, the kinematic rule $\dot{\boldsymbol{\rho}}_I$ activates and drags the inner yield surface to the right. By using the heating kinematic rule $\dot{\boldsymbol{\rho}}_H$ (Eq. (5.19)), the inner yield surface is moved by

the same magnitude of $\dot{\boldsymbol{\rho}}_I$ in the opposite direction (position $\rho_p{}^{**}$). Therefore, during the heating phase, plastic volumetric strains are produced progressively while the state of the soil (p, q, T) remains on the compression apex of the inner yield surface (position $p_{iT}{}^{**}$) and the size of the inner surface and the coordinates of the decompression apex remain unchanged (Figure 5.5). This observation is mathematically expressed as $\dot{p}_{iT} \left(= \dot{\tilde{p}}_{iT} + \dot{\rho}_p\right) = \dot{\tilde{p}}_{iT} = \dot{\rho}_p = 0$.

For a cooling phase following the heating phase (from $T = T_1$ to $T = T_0$ in Figure 5.5b), due to Macaulay bracket in Eq. (5.15) the isotropic rule for the inner yield surface is deactivated ($\dot{\tilde{p}}_{iT} = 0$). In addition, during cooling the state of the soil does not go outside the inner yield surface, and thus the response of the soil becomes thermo-elastic and no plastic strains are developed. This implies that the kinematic rule (Eq. (5.17)) is not activated ($\dot{\rho} = 0$). Thus, the size and position of the inner yield surface does not change (i.e. $\rho_p{}^{***} = \rho_p{}^{**}$ and $p_{iT}{}^{***} = p_{iT}{}^{**}$). Therefore, at the end of the cooling phase (at $T = T_0$) the state of the soil remains at the compression apex of the inner yield surface ($p_{iT}{}^{***} = p_1$). Upon subsequent heating, plastic strains are produced from the beginning of heating. Moreover, during the cooling phase the isotropic rule for the outer yield surface is activated (Eq. (5.14)) and is $\dot{p}_{cT} = -\mu_0 p_{cT} \dot{T}$ (where $\dot{T} < 0$). Consequently, at the end of cooling the size of the out surface is larger than before being subjected to heating-cooling ($p_{cT}{}^{***} > p_{cT}$).

The aforementioned strategy allows the inner yield surface to capture the plastic strains in successive thermal cycles and the shakedown behaviour. The magnitude of plastic strains developed during the heating phase is related to the coefficient of thermal shrinkage μ (Eq. (5.11)). After each heating-cooling cycle, the size of the outer yield surface, p_{cT}, increases, while the coordinate of p_{iT} remains unchanged (e.g. $p_{cT}{}^{***} > p_{cT}$ and $p_{iT}{}^{***} = p_{iT}{}^{**} = p_1$ in Figure 5.5b). According to Eq. (5.11), the coefficient of thermal shrinkage (μ) decreases, i.e., $\mu^{***} = \mu_0 \left(p_{iT}{}^{***} / p_{cT}{}^{***}\right)^b < \mu = \mu_0 \left(p_{iT} / p_{cT}\right)^b$. This implies that the magnitude of plastic strains produced during the subsequent heating phase decreases. Therefore, the generated plastic strains in subsequent thermal cycles decrease progressively, until at a sufficiently high number of thermal cycles the produced plastic strains become negligible, resulting in shakedown behaviour.

5.5. CALIBRATION AND THE ROLE OF PARAMETERS

The model is defined by 13 parameters and, except for the new parameters of C_χ and b defined in this model, the others are the same as those defined in the model developed in Chapter 2 and are calibrated in accordance with Chapter 2. Therefore, the original parameters are briefly explained, and then the new parameters are investigated comprehensively.

λ, κ and M_0 are defined similarly to the ones in the MCC model. Hence, λ and κ are the bi-logarithmic elasto-plastic and elastic compressibility indices, respectively, and can be determined from oedometer and isotropic triaxial tests. M_0 is the Critical State stress ratio at ambient temperature ($T = T_0$) and is determined as the gradient between the stress ratio (q/p) at Critical State and the origin $(p, q) = (0, 0)$ in the stress space of drained and undrained triaxial tests.

$\bar{G}$ and $\bar{K}$ are the coefficients representing the maximum shear and bulk moduli
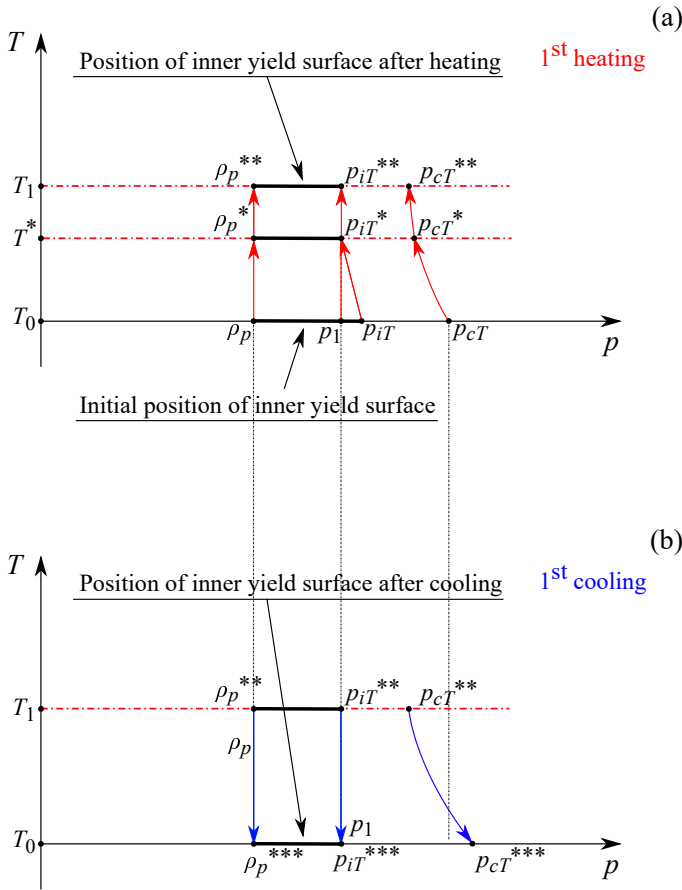
Figure 5.5: Performance of the model: (a) during heating phase; (b) during cooling

(which are related to the initial small strains), respectively, and can be determined from resonant column tests, bender element tests or approximately from the tangential values of the q-ε_s and p-ε_v curves of the drained and undrained triaxial tests at low strain levels. The pressure-dependency (p) of the shear and bulk moduli are linked through the parameter n which usually has a value less than one.

The flexibility of the inner and outer yield surfaces, i.e., adapting them with experimentally determined loci of the yield stresses of geomaterials, is via parameters α and γ. Typically, at least three triaxial tests, consisting of one isotropic compression test at a normally consolidated state, and two triaxial shear tests at lightly over-consolidated and highly over-consolidated states, are needed to adjust the parameters α and γ via regression analysis to provide the best fit to the yield stresses.

$3\alpha^*$ is the volumetric thermal expansion coefficient. As shown in Figure 5.1e, when fine-grained soils at isotropic stress states ($q = 0$) are subjected to several heating-cooling cycles, thermal (plastic) volumetric strains are accumulated at each thermal cycle and,

when the soil is subjected to a sufficiently high number of thermal cycles, the accumulated strains level-off. This means that, in subsequent thermal cycles, the response of the soil becomes thermo-elastic and the volumetric behaviour of the soil is mostly dominated by the volumetric thermal expansion of the grains. $3\alpha^*$ can then be determined as $3\alpha^* = \Delta\varepsilon_v/\Delta T$, where $\Delta\varepsilon_v$ is the volumetric change due to heating ΔT. In addition, the gradient of the ΔT-ε_v curve during cooling may also be used to determine $3\alpha^*$, because it is assumed that soils behave thermo-elastically during cooling.

π^* is the gradient of M with respect to temperature changes ΔT (Figure 5.1b) and is determined as $\pi^* = (M_T - M_{T0})/(T - T_0)$ (Eq. (5.8)), where M_T and M_{T0} are, respectively, the Critical State stress ratio at the current temperature and the ambient temperature.

μ_0 represents the variation of the apparent pre-consolidation pressure, p_{cT}, as the temperature changes (Figure 5.1a). μ_0 is calculated from Eq. (5.7) as $\mu_0 = -\ln(p_{cT}/p_{cT0})/(T - T_0)$, where p_{cT} and p_{cT0} are the pre-consolidation pressures at the current temperature and the ambient temperature, respectively. This equation indicates that at least two triaxial tests with the same pre-consolidation pressure at two different temperatures are needed to determine μ_0.

C_χ controls the pace with which the inner yield surface approaches the outer yield surface, i.e., it controls the magnitude of the generated plastic strains when the inner yield surface is inside the outer yield surface. Figure 5.6 shows the deviatoric stress versus axial strain (q-ε_a) and volumetric strain versus axial strain (ε_v-ε_a) curves of the soil response for C_χ values of 100, 1000 and 10000 at different stress states (OCRs of 1, 2, 6 and 12), when subjected to drained triaxial shearing under isothermal conditions. By comparing the q-ε_a curves, it can be seen that, at a specific deviatoric stress (e.g. $q = 150$ kPa), lower (plastic) axial strains are produced at larger values of C_χ, which implies that a stiffer response is obtained when a higher C_χ is used. Moreover, although all responses are smooth, a sharper response is observed at higher C_χ when the inner yield surface approaches the outer yield surface. In addition, by comparing Figure 5.6b with Figure 5.6f, it is seen that the amount of dilation of the soil specimens at high OCRs (e.g. 6 and 12) is smaller at higher C_χ.

The stiffening effect of C_χ is more pronounced on the hysteresis behaviour of the soil. Figure 5.7 presents the response of a soil subjected to several isotropic loading-unloading-reloading cycles at ambient temperature, for various C_χ values. For lower C_χ (e.g. $C_\chi = 100$ in Figure 5.7a), more plastic strains are produced upon reloading, which results in bigger hysteresis loops. At higher values of C_χ the hysteresis loops become flatter, which indicates a stiffer response of the soil where less plastic strains are produced during reloading. In the aforementioned analysis, C_χ can be determined by matching the best fit to the size of the hysteresis response (loop) in cyclic loading tests, including conventional isotropic loading-unloading-reloading compression tests. Note that R_{ini} in Figure 5.7 is the initial ratio between the size of the inner yield surface and the outer yield surface ($R_{ini} = \tilde{p}_{iT}/p_{cT}$).

The coefficient of thermal shrinkage of the inner yield surface, Eq. (5.11), varies between 0 and μ_0 as a function of the coordinates of the compression apex of the inner yield surface with respect to the outer yield surface, through the value of the term p_{iT}/p_{cT} which is controlled by the parameter b. This mechanism is designed to capture the thermo-plastic behaviour observed at over-consolidated states and the accumulated

thermo-plastic strains during cyclic thermal loadings. The variation of the normalised thermal shrinkage coefficient, μ/μ_0, with p_{iT}/p_{cT} for various values of b are shown in Figure 5.8. For low values of b (e.g. $b = 0.01$), μ is almost the same as μ_0 for most stress states inside the outer yield surface, while for higher values (e.g. $b = 100$) μ becomes nearly zero at stress states slightly less than the normally-consolidated states.

The effect of parameter b on the response of the soil is best observed when the soil is subjected to several heating-cooling cycles (Figure 5.9). Figure 5.9a-5.9c show the volumetric strains developed with $b = 0.01$, 1 and 100, when the soil is subjected to five thermal cycles at a normally consolidated state ($p_{iT}/p_{cT} = 1$ and $q = 0$). In the first heating phase of all the simulations, $p_{iT}/p_{cT} = 1$ (the inner and outer yield surfaces coincide on p_{cT}); thus, $\mu = \mu_0$ and the magnitudes of thermally-induced volumetric strains are identical. Simultaneously, the outer yield surface becomes bigger (see Eq. (5.14)). Upon cooling, the response of the soil is thermo-elastic and the compression apex of the inner yield surface (p_{iT}) remains unchanged. Therefore, after the first heating-cooling cycle, $p/p_{iT} = 1$ and $p_{iT}/p_{cT} < 1$, which represents an over-consolidated state. For the second heating phase when using lower b values (e.g. $b = 0.01$ in Figure 5.9a), $\mu \approx \mu_0$, and hence the amount of plastic volumetric strains produced during subsequent heating-cooling cycles remains almost the same as for the first heating phase. As the parameter b increases (e.g. $b = 100$), μ becomes smaller during the subsequent heating phase, and so the amount of plastic strains in each thermal cycle becomes smaller. The accumulated volumetric strains after each thermal cycle for different values for b are plotted in Figure 5.9d. It can be seen that, for lower values of b (e.g. $b = 0.01$), the accumulated strains due to the heating-cooling cycles have not levelled-off after five thermal cycles, whereas when using higher values (e.g. $b = 100$) the accumulated volumetric stains remain almost steady after three cycles, thereby representing how the model can successfully capture the shakedown behaviour of fine-grained soils when they are subjected to several thermal cycles. From the knowledge of accumulated volumetric strains and number of cycles (e.g. Figure 5.1e), the parameter b can be calibrated.
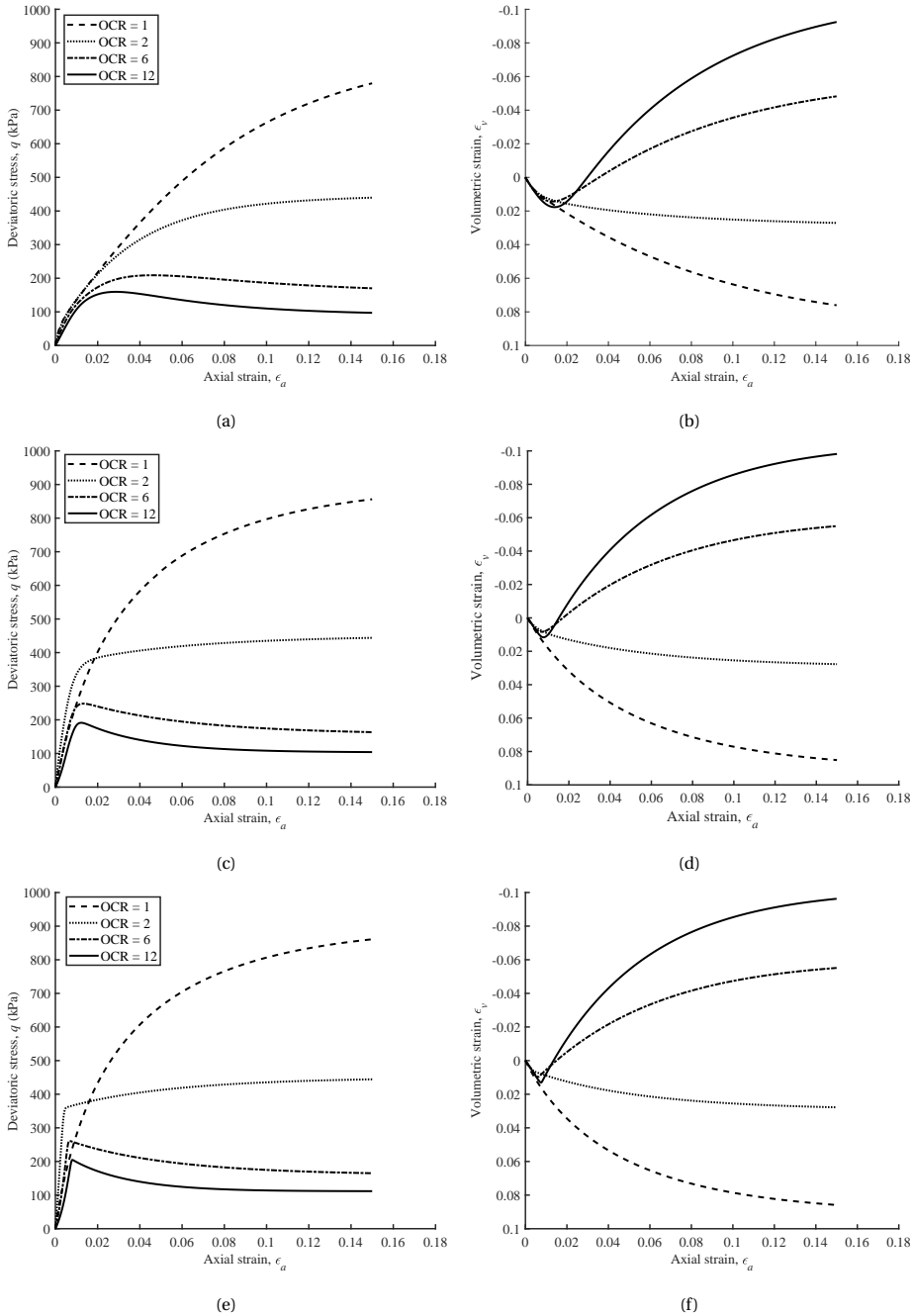
Figure 5.6: Effect of parameter C_χ on drained behaviour response: (a) q-ε_a response with $C_\chi = 100$; (b) ε_v-ε_a response with $C_\chi = 100$; (c) q-ε_a response with $C_\chi = 1000$; (d) ε_v-ε_a response with $C_\chi = 1000$; (e) q-ε_a response with $C_\chi = 10000$; (f) ε_v-ε_a response with $C_\chi = 10000$
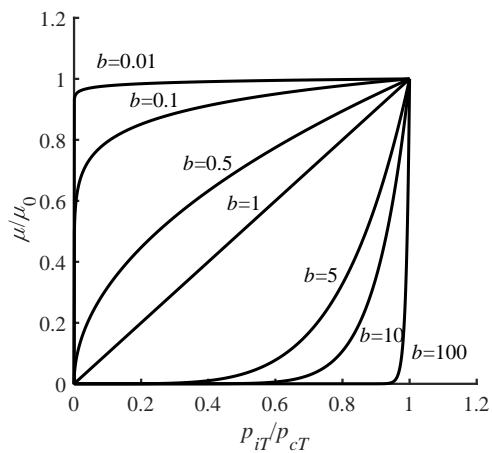
Figure 5.8: Effect of parameter b on the variation of normalised μ/μ_0 with normalised p_{iT}/p_{cT}
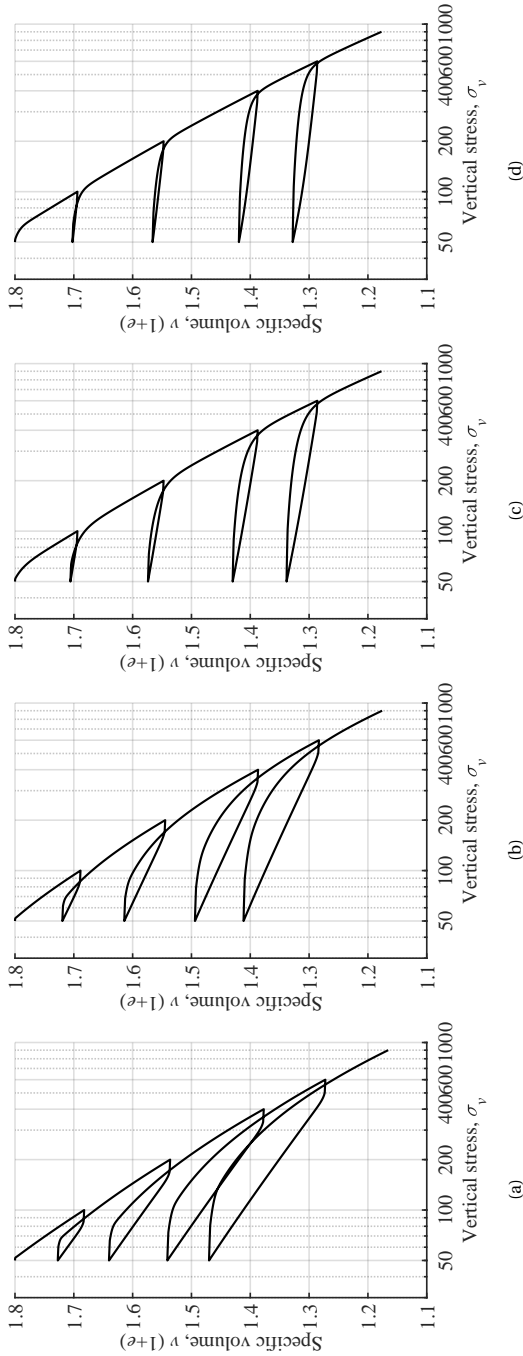
Figure 5.7: Effect of C_χ on hysteresis behaviour of isotropic compression loading-unloading-reloading with $R_{ini} = 0.2$: (a) $C_\chi = 50$; (b) $C_\chi = 100$; (c) $C_\chi = 500$; (d) $C_\chi = 1000$.
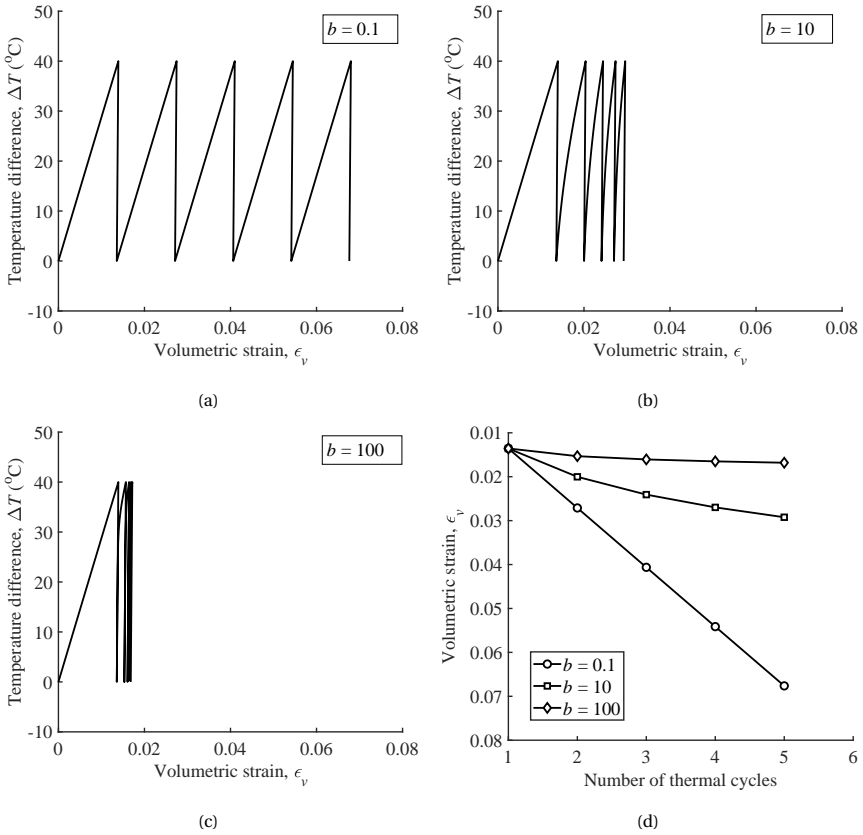
Figure 5.9: Effect of parameter b on the volumetric strain vs. temperature difference response for: (a) $b = 0.1$; (b) $b = 10$; (c) $b = 100$; (d) effect of parameter b on the accumulated volumetric strain with thermal cycles

5.6. PERFORMANCE OF THE MODEL

The performance of the model has been validated by comparing simulations with a variety of experimental data, including oedometer and triaxial tests subjected to thermal cycles and tests under drained and undrained conditions on different soil types. The tests cover a wide range of stress paths and loading histories. The calibrated parameters used for the simulations are reported in Table 5.1.

Table 5.1: Summary of model parameters

Parameters	Ng et al. [44]	Di Donna & Laloui [25]	Baldi et al. [42]	Abuel-Naga et al. [43]	Uchaipichat & Khalili [38]	Ghahremannejad [40]	Suddeepong et al. [55]	Nakai & Hinokio ([56])
α (-)	0.0	0.0	0.0	0.0	0.2	-0.4	-0.05	0.5
γ (-)	0.0	0.0	0.0	-2.0	0.3	-0.2	0.0	0.5
λ (-)	0.095	0.062	0.180	0.450	0.090	0.150	0.155	0.098
κ (-)	0.060	0.017	0.020	0.090	0.006	0.030	0.012	0.005
M_0 (-)	-	-	-	0.80	1.20	0.85	1.00	1.04
$\bar{K}$ (-)	$1/\kappa$	$1/\kappa$	$1/\kappa$	18.5	45.0	$1/\kappa$	$1/\kappa$	700.0
$\bar{G}$ (-)	-	-	-	15	120	270	200	550
n (-)	1.00	1.00	1.00	1.00	0.70	1.00	1.00	1.00
α^* (1/K)	-3.1×10^{-6}	-3.50×10^{-6}	-1.75×10^{-5}	-3.10×10^{-6}	-3.40×10^{-5}	-3.00×10^{-5}	-	-
μ_0 (1/K)	2.01×10^{-3}	5.15×10^{-3}	3.42×10^{-3}	7.70×10^{-3}	3.40×10^{-3}	9.09×10^{-4}	-	-
π^* (1/K)	-	-	-	0	0	-1.6×10^{-3}	-	-
b (-)	30.70	21.50	0.75	-	-	-	-	-
C_χ (-)	-	-	-	2000	2000	5000	3300	11500
R_{ini} (-)	0.25	0.25	0.25	0.6	0.2	0.2	0.05	0.01

NG ET AL. [44] TEST

Ng et al. [44] investigated the thermo-mechanical behaviour of a reconstituted Loess clay, subjected to several heating-cooling cycles, by using a temperature-controlled oedometer apparatus. The soil specimen was first consolidated to a vertical stress of 50 kPa and then subjected to five heating-cooling cycles between 70°C and 15°C, starting from an ambient temperature of 25°C. The performance of the model is compared with experimental data in T-ε_v space and the accumulated volumetric strain versus number of thermal cycles in Figure 5.10a and Figure 5.10b, respectively. The experimental data show a shakedown response with respect to thermal cycles, in which, after five thermal cycles, the response of the soil becomes almost thermo-elastic. It is observed that the model can capture the amplitude of thermally-induced volumetric strains at each thermal cycle accurately, and the accumulated strains with respect to the number of cycles matches well with the experimental data.
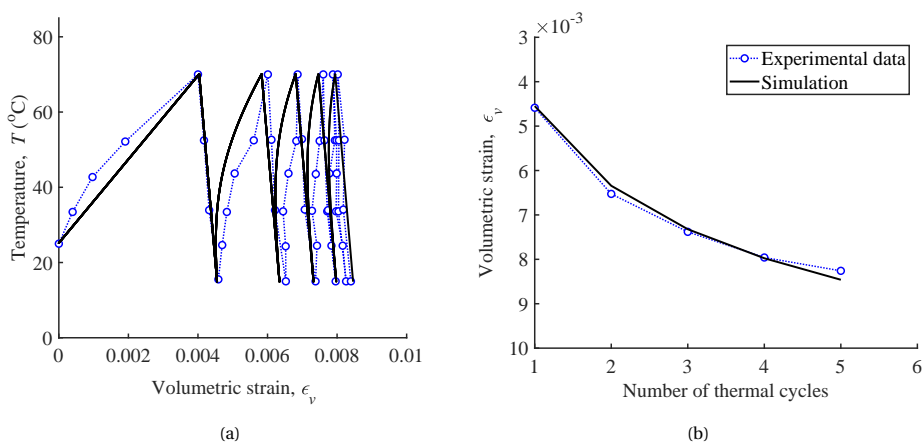
Figure 5.10: Comparison of model predictions with experimental data of Ng et al. [44]: (a) temperature vs. volumetric strain; (b) accumulated volumetric strain vs. the number of thermal cycles

DI DONNA & LALOUI [25] TEST

The cyclic response of Geneva clay, subjected to several heating-cooling cycles, was investigated by Di Donna & Laloui [25] by using a temperature-controlled oedometer apparatus. The soil specimen was compressed under a vertical stress of 250 kPa and then subjected to four thermal cycles between 60°C and 5°C, starting from an ambient temperature of 20°C. The predictions of the model are compared with experimental data in Figure 5.11. The soil, similar to Loess clay (Figure 5.10), shows a shakedown behaviour which is well captured by the model.

BALDI ET AL. [42] TESTS

Baldi et al. [42] studied the thermo-mechanical behaviour of Boom clay by performing a single thermal cycle at different stress states. Soil specimens with an initial preconsolidation pressure of 6 MPa where subjected to heating and cooling between 20°C and 95°C at hydrostatic pressures of 1 MPa, 2 MPa and 6 MPa, giving OCRs of 6, 3 and

1, respectively. The predictions of the model (with calibrated parameters) and experimental data are shown in Figure 5.12 (variation of volumetric strain with temperature at different stress states). The model accurately predicts the volume changes of the soil at OCRs of 1 and 3 and slightly over-predicts the thermo-mechanical compressive strain behaviour of the highly over-consolidated specimen (OCR = 6).
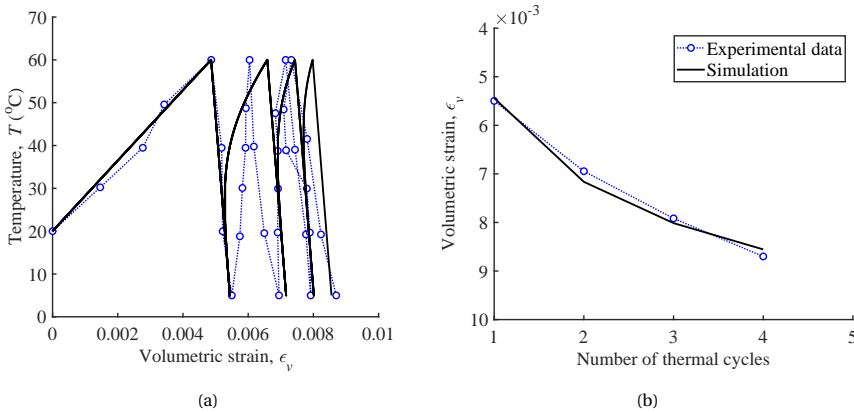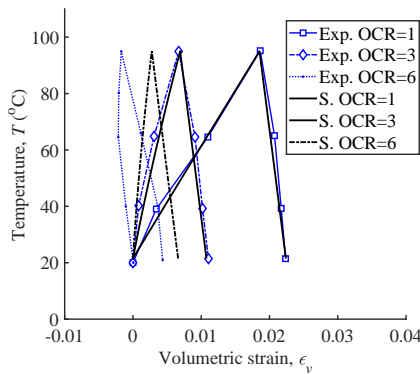

(a)   (b)

Figure 5.11: Comparison of model predictions with experimental data of Di Donna & Laloui [25]: (a) temperature vs. volumetric strain; (b) accumulated volumetric strain vs. the number of thermal cycles

Figure 5.12: Comparison of the model predictions with experimental data of Baldi et al. [42]: temperature vs. volumetric strain

ABUEL-NAGA ET AL. [43] TESTS

The thermo-mechanical behaviour of Bangkok clay, using a temperature-controlled oedometer and triaxial apparatus, is shown in Figure 5.13.

The void ratio (e) variation versus the vertical stress of a soil specimen in the temperature-controlled oedometer is shown in Figure 5.13a. At an ambient temperature of 22°C, the soil specimen was compressed to 100 kPa. Next, with the vertical stress being held constant, the specimen was subjected to a single heating-cooling cycle between

95°C and 22°C. As a result, the soil experienced a reduction in void ratio, i.e., it attained a denser state. The test was ended by further compression with the vertical stress increasing to 200 kPa at room temperature. Due to the heating-cooling cycle, the soil exhibited an initial stiffer response upon the second compression phase, i.e., the soil behaved as an over-consolidated soil. This behaviour is attributed to the denser state that the soil had attained after the thermal cycle. This behaviour, as well as the void ratio reduction during the thermal cycle, is well captured by the model.

Figure 5.13b presents the volumetric behaviour of the same soil in an isotropic compression test using a triaxial apparatus, at three different temperatures of 25, 70 and 90°C. Samples were first compressed to 300 kPa at an ambient temperature ($T = 25°C$) and then unloaded to 25 kPa to attain an OCR of 12. This was followed by a heating phase to reach the desired temperature. Finally, the specimens were isotropically loaded with the hydrostatic pressure increasing beyond 300 kPa. The predictions of the model are also depicted in Figure 5.13b and show satisfactory results. It should be noted that the stress-strain curves predicted by the model are smooth, in contrast to the model developed in Chapter 2 which exhibited a bilinear response.

(a)

(b)
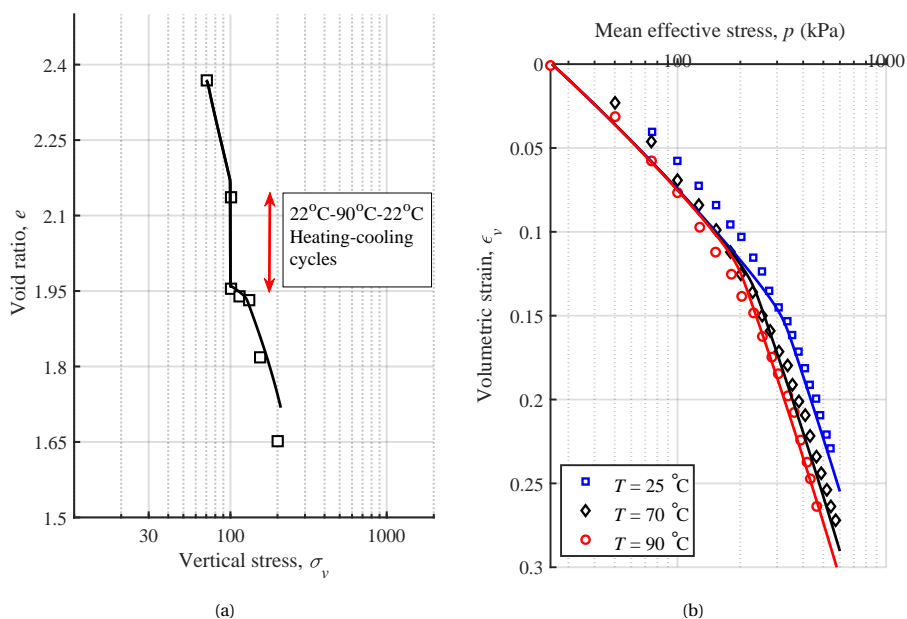
Figure 5.13: Comparison of model predictions with experimental data of Abuel-Naga et al. [43]: (a) void ratio vs. vertical stress in oedometer test; (b) volumetric strain vs. mean effective stress during isotropic triaxial compression at different temperatures

UCHAIPICHAT & KHALILI [38] TESTS

The drained behaviours of a saturated silty soil at various stress states and three temperatures of 25, 40 and 60°C were investigated by Uchaipichat & Khalili [38] by using a temperature-controlled triaxial apparatus. At a room temperature of 25°C, all the samples were first isotropically compressed under a hydrostatic pressure of 200 kPa, and

then unloaded by the hydrostatic pressure decreasing to 50 kPa, 100 kPa and 150 kPa, resulting in respective stress states with OCR = 4, OCR = 2 and OCR = 4/3. The temperatures of the samples for each over-consolidated state were then elevated to the targeted temperatures and this was followed by shearing under drained conditions. Experimental data of deviatoric stress versus deviatoric strain (q-ε_s) and volumetric strain versus deviatoric strains (ε_v-ε_s), as well as the corresponding model predictions, are presented in Figure 5.14. The predictions of the model, similar to those in Chapter 2, are in good agreement with experimental data, except for the early stage of ε_v-ε_s curves for over-consolidated states (OCR = 4). Note that Uchaipichat & Khalili [38] reported that the Critical State stress ratio (M) of the studied soil was temperature independent. Therefore, the simulations were conducted using $\pi = 0$.

(a)

(b)
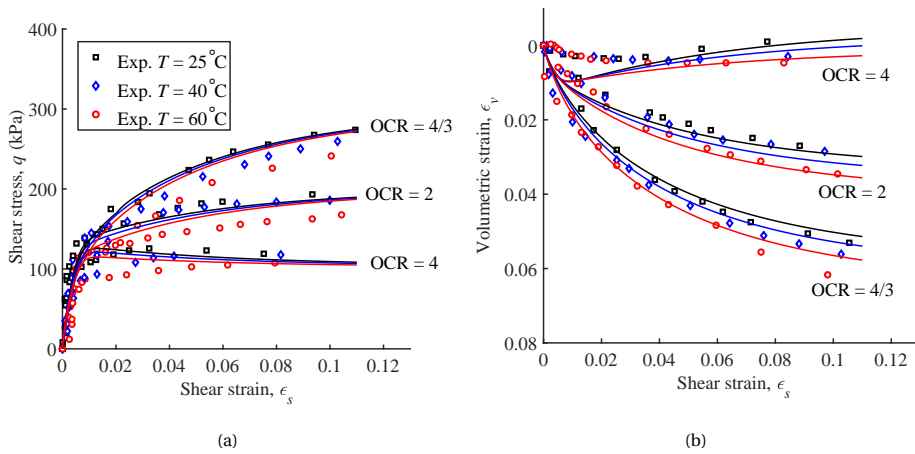
Figure 5.14: Comparison of model predictions with experimental data of Uchaipichat & Khalili [38]: (a) deviatoric stress vs. deviatoric strain at different OCRs and temperatures; (b) volumetric strain vs. deviatoric strain at different OCRs and temperatures

GHAHREMANNEJAD [40] TESTS

In the study of Ghahremannejad [40], illitic clay samples were first heated to reach the target temperatures of 22°C (room temperature) and 75°C. With the temperature held constant, specimens were subjected to drained isotropic compression with the hydrostatic pressure increasing to 400 kPa, resulting in a normally-consolidated stress state. Then, the specimens were sheared under undrained conditions. The stress path in p-q stress space, and the corresponding deviatoric stress and pore pressure (u_p) versus deviatoric strain experimental data, along with model predictions are shown, respectively, in Figure 5.15a, Figure 5.15b and Figure 5.15c. Comparison of the simulations with experimental data indicates that the current model successfully captures the undrained behaviour of fine-grained soils at various temperatures.
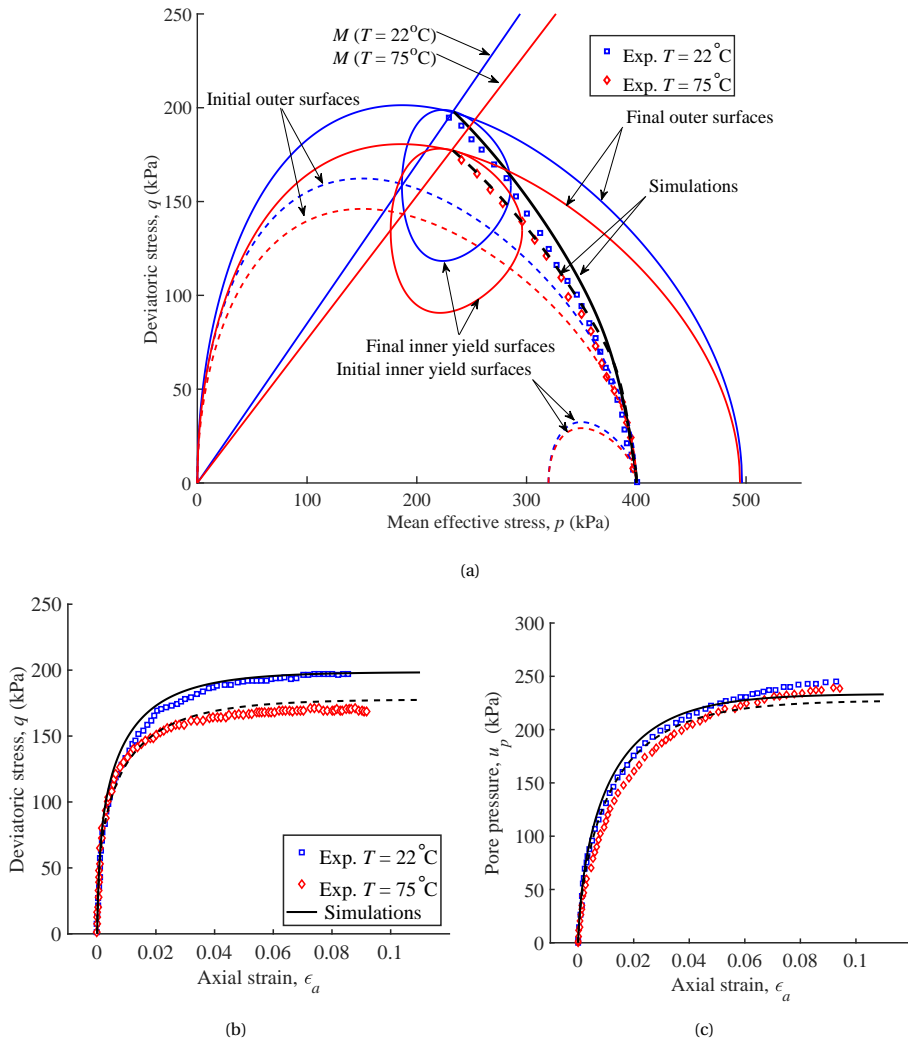
Figure 5.15: Comparison of model predictions with undrained experimental data of Ghahremannejad [40] at different temperatures: (a) stress path; (b) deviatoric stress vs. axial strain; (c) pore pressure vs. axial strain

For clarification on how the model performs, the initial and final configurations of the inner (bubble) and outer yield surfaces are also plotted in p-q stress space in Figure 5.15a. The initial states of the surfaces are shown by dashed lines and the final configurations of the surfaces are depicted by solid lines. The stress path, Critical State stress ratio (M) and yield surfaces in blue correspond to test results and model predictions at $T = 22°C$, while those in red correspond to model predictions and tests results at $T = 75°C$. The soil exhibits a temperature-dependent Critical State stress ratio (M) where its value is reduced at elevated temperatures. This observation is well captured by the model through the parameter π^*. As a result, the sizes of the initial and final inner

and outer yield surfaces are smaller at $T = 75°C$, compared to the corresponding surfaces at $T = 22°C$. Therefore, the inner yield surface corresponding to $T = 75°C$ follows a shorter stress path to reach the outer yield surface during undrained shearing.

OTHER SIMULATIONS

While the main focus of this section is to validate the proposed model with thermomechanical test results, the capability of the model in capturing the hysteresis behaviour of soils is investigated here.

Figure 5.16 shows the specific volume ($v = 1 + e$) versus logarithm of vertical stress from an oedometer test on undisturbed Ariake clay (Suddeepong et al. [55]), along with the model prediction. The specimen, under isothermal conditions, was subjected to two loading-unloading-reloading paths and hysteresis loops were therby formed. The model well captures the hysteresis loops through the parameter C_χ.
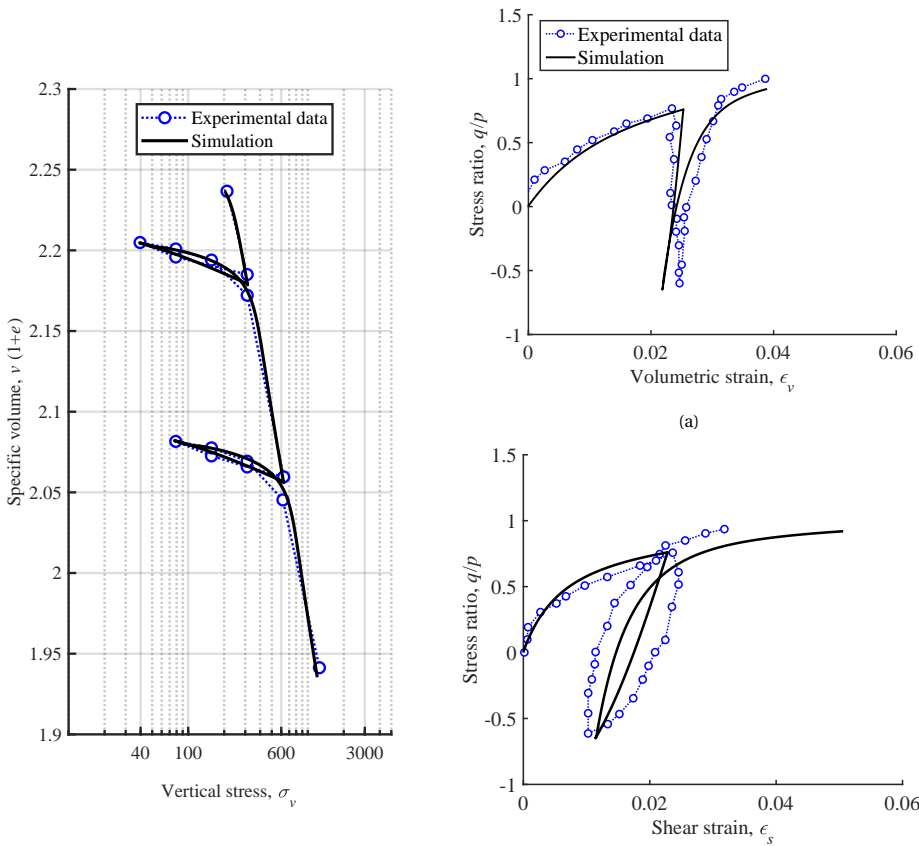
Figure 5.16: Comparison of the model predictions with oedometer experimental data of Suddeepong et al. [55]

(a)

(b)

Figure 5.17: Comparison of the model predictions with drained cyclic triaxial experimental data of Nakai & Hinokio [56]

Nakai & Hinokio [56] performed drained cyclic tests with different stress paths on Fujinomori clay by using a triaxial apparatus under isothermal conditions. Figure 5.17 shows the results of a normally-consolidated clay which was subjected to one cyclic drained shearing at a hydrostatic pressure of 196 kPa. The model predictions (q/p-ε_v and q/p-ε_s curves) are compared with experimental data in Figure 5.17a and Figure 5.17b, respectively. It can be seen that the model can successfully predict the narrow hysteresis loop of the experimental q/p-ε_v curve and the wider hysteresis loop in the experimental q/p-ε_s curve.

5.7. CONCLUSION

A thermodynamically consistent two surface/bubble model has been developed which successfully simulates the hysteresis behaviour of soils during cyclic mechanical loadings and shakedown behaviour when they are subjected to heating-cooling cycles. These behaviours have been captured by assigning a kinematic rule for the heating phase along with an isothermal kinematic rule. As a result, the model predicts plastic strains at highly over-consolidated states and during the heating phase of cyclic thermal loads. The magnitude of thermally-induced plastic strains reduces as the state of the soil becomes over-consolidated and the model has a control on the accumulated plastic strains due to thermal loads.

REFERENCES

[1] Mróz, Z. On the description of anisotropic work hardening. *Journal of the Mechanics and Physics of Solids*, 15(3):163–175, 1967.

[2] Iwan, W. D. On a class of models for the yielding behavior of continuous and composite systems. *Journal of Applied Mechanics*, 34(3):612–617, 1967.

[3] Dafalias, Y. F. and Popov, E. P. A model of nonlinearly hardening materials for complex loading. *Acta Mechanica*, 21(3):173–192, 1975.

[4] Krieg, R. D. A practical two surface plasticity theory. *Journal of Applied Mechanics*, 42(3):641–646, 1975.

[5] Dafalias, Y. F. Bounding surface plasticity. I: Mathematical foundation and hypoplasticity. *Journal of Engineering Mechanics*, 112(9):966–987, 1986.

[6] Dafalias, Y. F. and Herrmann, L. R. Bounding surface plasticity. II: Application to isotropic cohesive soils. *Journal of Engineering Mechanics*, 112(12):1263–1291, 1986.

[7] Corti, R., Diambra, A., Wood, M. D., Escribano, D. E. and Nash, D. F. Memory surface hardening model for granular soils under repeated loading conditions. *Journal of Engineering Mechanics*, 142(12):04016102, 2016.

[8] Dafalias, Y. F. and Manzari, M. T. Simple plasticity sand model accounting for fabric change effects. *Journal of Engineering Mechanics*, 130(6):622–634, 2004.

[9] Elia, G. and Rouainia, M. Investigating the cyclic behaviour of clays using a kinematic hardening soil model. *Soil Dynamics and Earthquake Engineering*, 88:399–411, 2016.

[10] Gajo, A. and Wood, D. M. A new approach to anisotropic, bounding surface plasticity: General formulation and simulations of natural and reconstituted clay behaviour. *International Journal for Numerical and Analytical Methods in Geomechanics*, 25(3):207–241, 2001.

[11] Golchin, A. and Lashkari, A. A critical state sand model with elastic-plastic coupling. *International Journal of Solids and Structures*, 51(15-16):2807–2825, 2014.

[12] Kavvadas, M. and Amorosi, A. A constitutive model for structured soils. *Géotechnique*, 50(3):263–273, 2000.

[13] Khalili, N., Habte, M. A. and Valliappan, S. A bounding surface plasticity model for cyclic loading of granular soils. *International Journal for Numerical Methods in Engineering*, 63(14):1939–1960, 2005.

[14] Lashkari, A. and Golchin, A. On the influence of elastic-plastic coupling on sands response. *Computers and Geotechnics*, 55:352–364, 2014.

[15] Li, T. and Meissner, H. Two-surface plasticity model for cyclic undrained behavior of clays. *Journal of Geotechnical and Geoenvironmental Engineering*, 128(7):613–626, 2002.

[16] Manzari, M. T. and Dafalias, Y. F. A critical state two-surface plasticity model for sands. *Géotechnique*, 47(2):255–272, 1997.

[17] Mróz, Z., Norris, V. A. and Zienkiewicz, O. C. An anisotropic hardening model for soils and its application to cyclic loading. *International Journal for Numerical and Analytical Methods in Geomechanics*, 2:203–221, 1978.

[18] Mróz, Z., Norris, V. A. and Zienkiewicz, O. C. Application of an anisotropic hardening model in the analysis of elasto-plastic deformation of soils. *Géotechnique*, 29(1):1–34, 1979.

[19] Puzrin, A. M. and Kirschenboim, E. Kinematic hardening model for overconsolidated clays. *Computers and Geotechnics*, 28(1):1–36, 2001.

[20] Rezania, M. and Dejaloud, H. BS-CLAY1: Anisotropic bounding surface constitutive model for natural clays. *Computers and Geotechnics*, 135:104099, 2021.

[21] Stallebrass, S. E. and Taylor, R. N. The development and evaluation of a constitutive model for the prediction of ground movements in overconsolidated clay. *Géotechnique*, 47(2):235–253, 1997.

[22] Sun, Y., Wichtmann, T., Sumelka, W. and Kan, M. E. Karlsruhe fine sand under monotonic and cyclic loads: Modelling and validation. *Soil Dynamics and Earthquake Engineering*, 133:106119, 2020.

5

[23] Al-Tabbaa, A. and Wood , D. M. An experimentally based bubble model for clay. In *Proceedings of the 3rd international symposium on numerical models in geomechanics, NUMOG III*, pages 91–99. 1989.

[24] Cheng, W., Chen, R., Hong, P., Cui, Y. and Pereira, J. M. A two-surface thermomechanical plasticity model considering thermal cyclic behavior. *Acta Geotechnica*, 15(10):2741–2755, 2020.

[25] Di Donna, A. and Laloui, L. Response of soil subjected to thermal cyclic loading: Experimental and constitutive study. *Engineering Geology*, 190:65–76, 2015.

[26] Zhou, C., Fong, K. Y. and Ng, C. W. W. A new bounding surface model for thermal cyclic behaviour. *International Journal for Numerical and Analytical Methods in Geomechanics*, 41(16):1656–1666, 2017.

[27] Zhou, C. and Ng, C. W. W. A new thermo-mechanical model for structured soil. *Géotechnique*, 68(12):1109–1115, 2018.

[28] Houlsby, G. T. and Puzrin, A. M. *Principles of Hyperplasticity*. Springer London, London, 2007.

[29] Rajagopal, K. R. and Srinivasa, A. R. Some remarks and clarifications concerning the restrictions placed on thermodynamic processes. *International Journal of Engineering Science*, 140:26–34, 2019.

[30] Collins, I. F. and Houlsby, G. T. Application of thermomechanical principles to the modelling of geotechnical materials. In *Proceedings: Mathematical, Physical and Engineering Sciences, JSTOR*, volume 453, pages 1975–2001. 1997.

[31] Cui, Y. J., Sultan, N. and Delage, P. A thermomechanical model for saturated clays. *Canadian Geotechnical Journal*, 37(3):607–620, 2000.

[32] Graham, J., Tanaka, N., Crilly, T. and Alfaro, M. Modified Cam-Clay modelling of temperature effects in clays. *Canadian Geotechnical Journal*, 38(3):608–621, 2001.

[33] Hueckel, T. and Baldi, G. Thermoplasticity of saturated clays: Experimental constitutive study. *Journal of Geotechnical Engineering*, 116:1778–1796, 1991.

[34] Zhou, C. and Ng, C. W. W. A thermomechanical model for saturated soil at small and large strains. *Canadian Geotechnical Journal*, 52(8):1101–1110, 2015.

[35] Abuel-Naga, H. M., Bergado, D. T. and Lim, B. F. Effect of temperature on shear strength and yielding behavior of soft Bangkok clay. *Soils and Foundations*, 47(3):423–436, 2007.

[36] Cekerevac, C. and Laloui, L. Experimental study of thermal effects on the mechanical behaviour of a clay. *International Journal for Numerical and Analytical Methods in Geomechanics*, 28(3):209–228, 2004.

[37] Tanaka, N., Graham, J. and Crilly, T. Stress-strain behaviour of reconstituted illitic clay at different temperatures. *Engineering Geology*, 47(4):339–350, 1997.

[38] Uchaipichat, A. and Khalili, N. Experimental investigation of thermo-hydro-mechanical behaviour of an unsaturated silt. *Géotechnique*, 59(4):339–353, 2009.

[39] Abuel-Naga, H. M., Bergado, D. T., Bouazza, A. and Ramana, G. V. Volume change behaviour of saturated clays under drained heating conditions: Experimental results and constitutive modeling. *Canadian Geotechnical Journal*, 44(8):942–956, 2007.

[40] Ghahremannejad, B. *Thermo-mechanical behaviour of two reconstituted clays*. PhD thesis, University of Sydney, 2003.

[41] Towhata, I., Kuntiwattanaku, P., Seko, I. and Ohishi, K. Volume change of clays induced by heating as observed in consolidation tests. *Soils and Foundations*, 33(4):170–183, 1993.

[42] Baldi, G., Hueckel, T., Peano, A. and Pellegrini, R. Development in modelling of thermo-hydro-geomechanical behaviour of Boom clay and clay-based buffer materials. Technical report, Luxembourg, 1991.

[43] Abuel-Naga, H. M., Bergado, D. T., Ramana, G. V., Grino, L., Rujivipat, P. and Thet, Y. Experimental evaluation of engineering behavior of soft Bangkok clay under elevated temperature. *Journal of Geotechnical and Geoenvironmental Engineering*, 132(7):902–910, 2006.

[44] Ng, C. W. W., Mu, Q. Y. and Zhou, C. Effects of specimen preparation method on the volume change of clay under cyclic thermal loads. *Géotechnique*, 69(2):146–150, 2019.

[45] Collins, I. F. Associated and non-associated aspects of the constitutive laws for coupled elastic/plastic materials. *International Journal of Geomechanics*, 2(2):259–267, 2002.

[46] Maugin, G. A. The saga of internal variables of state in continuum thermo-mechanics (1893–2013). *Mechanics Research Communications*, 69:79–86, 2015.

[47] Rubin, M. B. Physical reasons for abandoning plastic deformation measures in plasticity and viscoplasticity theory. *Archives of Mechanics*, 53(4-5):519–539, 2001.

[48] Collins, I. F. and Hilder, T. A theoretical framework for constructing elastic/plastic constitutive models of triaxial tests. *International Journal for Numerical and Analytical Methods in Geomechanics*, 26(13):1313–1347, 2002.

[49] Coombs, W. M., Crouch, R. S. and Augarde, C. E. A unique Critical State two-surface hyperplasticity model for fine-grained particulate media. *Journal of the Mechanics and Physics of Solids*, 61(1):175–189, 2013.

[50] Rollo, F. and Amorosi, A. SANICLAY-T: Simple thermodynamic-based anisotropic plasticity model for clays. *Computers and Geotechnics*, 127:103770, 2020.

5

[51] Rollo, F. *Elastic anisotropy and elastoplastic coupling of soils: A thermodynamic approach.* PhD thesis, Sapienza Universita di Roma, 2018.

[52] Karrech, A., Regenauer-Lieb, K. and Poulet, T. A damaged visco-plasticity model for pressure and temperature sensitive geomaterials. *International Journal of Engineering Science*, 49(10):1141–1150, 2011.

[53] Houlsby, G. T., Abadie, C. N., Beuckelaers, W. J. A. P. and Byrne, B. W. A model for nonlinear hysteretic and ratcheting behaviour. *International Journal of Solids and Structures*, 120:67–80, 2017.

[54] Maranha, J. R., Pereira, C. and Vieira, A. A viscoplastic subloading soil model for rate-dependent cyclic anisotropic structured behaviour. *International Journal for Numerical and Analytical Methods in Geomechanics*, 40(11):1531–1555, 2016.

[55] Suddeepong, A., Chai, J., Shen, S. and Carter, J. Deformation behaviour of clay under repeated one-dimensional unloading-reloading. *Canadian Geotechnical Journal*, 52(8):1035–1044, 2015.

[56] Nakai, T. and Hinokio, M. A simple elastoplastic model for normally and over consolidated soils with unified material parameters. *Soils and Foundations*, 44(2):53–70, 2004.

[57] Brandl, H. Energy foundations and other thermo-active ground structures. *Géotechnique*, (56):81–122, 2006.

[58] Golchin, A., Vardon, P. J., Coombs, W. M. and Hicks, M. A. A flexible and robust yield function for geomaterials. *Computer Methods in Applied Mechanics and Engineering*, 387:114162, 2021.

[59] Golchin, A., Vardon, P. J. and Hicks, M. A. A thermo-mechanical constitutive model for fine-grained soils based on thermodynamics. *International Journal of Engineering Science*, 174:103579, 2022.

[60] Hamidi, A., Tourchi, S. and Kardooni, F. A critical state based thermo-elasto-plastic constitutive model for structured clays. *Journal of Rock Mechanics and Geotechnical Engineering*, 9(6):1094–1103, 2017.

[61] Houlsby, G. T., Amorosi, A. and Rojas, E. Elastic moduli of soils dependent on pressure: A hyperelastic formulation. *Géotechnique*, 55(5):383–392, 2005.

[62] Laloui, L. and François, B. ACMEG-T: Soil thermoplasticity model. *Journal of Engineering Mechanics*, 135(9):932–944, 2009.

[63] Likitlersuang, S. and Houlsby, G. T. Development of hyperplasticity models for soil mechanics. *International Journal for Numerical and Analytical Methods in Geomechanics*, 30(3):229–254, 2006.

[64] Maranha, J. R., Pereira, C. and Vieira, A. Improved subloading thermo-viscoplastic model for soil under strictly isotropic conditions. *Geomechanics for Energy and the Environment*, 14:38–47, 2018.

[65] Thomas, H. R., Vardon, P. J. and Cleall, P. J. Three-dimensional behaviour of a proto-type radioactive waste repository in fractured granitic rock. *Canadian Geotechnical Journal*, 51(3):246–259, 2014.

[66] Aung, Y., Khabbaz, H. and Fatahi, B. Mixed hardening hyper-viscoplasticity model for soils incorporating non-linear creep rate–H-creep model. *International Journal of Plasticity*, 120:88–114, 2019.

[67] Collins, I. F. and Kelly, P. A. A thermomechanical analysis of a family of soil models. *Geotechnique*, 52(7):507–518, 2002.

[68] Coombs, W. M. Continuously unique anisotropic critical state hyperplasticity. *International Journal for Numerical and Analytical Methods in Geomechanics*, 41(4):578–601, 2017.

[69] Lai, Y., Xu, X., Yu, W. and Qi, J. An experimental investigation of the mechanical behavior and a hyperplastic constitutive model of frozen loess. *International Journal of Engineering Science*, 84:29–53, 2014.

[70] Zhang, Z., Chen, Y. and Huang, Z. A novel constitutive model for geomaterials in hyperplasticity. *Computers and Geotechnics*, 98:102–113, 2018.

5

APPENDIX

5.A. APPENDIX A: ENERGY POTENTIAL, YIELD SURFACE AND PLASTIC FLOW

The Gibbs energy potential proposed by Houlsby et al. [61] is used as the energy potential for isothermal conditions

$$g_1(p,q) = -\frac{p_o^{2-n}}{\bar{K}(2-n)(1-n)p_a^{1-n}} - \frac{p}{\bar{K}(1-n)} \tag{5.A.1a}$$

where

$$p_o^2 = p^2 + \frac{\bar{K}(1-n)}{3\bar{G}}q^2 \tag{5.A.1b}$$

and p_a (kPa) is the atmospheric pressure (101 kPa); $\bar{K}$ and $\bar{G}$ are material constants, respectively related to the elastic bulk modulus and shear modulus; and n ($0 < n < 1$) is the constant representing the power dependence of the bulk and shear moduli on the hydrostatic pressure p. For the case when the elastic bulk and shear moduli are linearly proportional to p (for cases in which $n = 1$), the free energy is natural-log dependent on p

$$g_1(p,q) = -\frac{1}{\bar{K}}p\left(\ln\left(\frac{p}{p_a}\right) - 1\right) - \frac{q^2}{6\bar{G}p} \tag{5.A.1c}$$

The total strain and generalised stresses (in triaxial space) are derived, respectively, by differentiating the energy potential (Eq. (5.1)) with respect to the true triaxial stresses ($\boldsymbol{\sigma} = \{p,q\}^{\mathrm{T}}$) and the internal variables ($\boldsymbol{\varepsilon}_i^p = \{\varepsilon_{v,i}^p, \varepsilon_{s,i}^p\}^{\mathrm{T}}$, $\boldsymbol{\varepsilon}_o^p = \{\varepsilon_{v,o}^p, \varepsilon_{s,o}^p\}^{\mathrm{T}}$ and $\boldsymbol{\rho} = \{\rho_p, \rho_q\}^{\mathrm{T}}$)

$$\{\boldsymbol{\varepsilon}\} = -\left\{\frac{\partial g}{\partial \boldsymbol{\sigma}}\right\} = \{\boldsymbol{\varepsilon}^e\} + \{\boldsymbol{\varepsilon}_i^p\} + \{\boldsymbol{\varepsilon}_o^p\} + \{\boldsymbol{\varepsilon}^{Therm}\}$$

$$= -\left\{\begin{array}{c} \frac{\partial g_1}{\partial p} \\ \frac{\partial g_1}{\partial q} \end{array}\right\} + \left\{\begin{array}{c} \varepsilon_{v,i}^p \\ \varepsilon_{s,i}^p \end{array}\right\} + \left\{\begin{array}{c} \varepsilon_{v,o}^p \\ \varepsilon_{s,o}^p \end{array}\right\} + 3\alpha^*(T - T_0)\left\{\begin{array}{c} 1 \\ 0 \end{array}\right\} \tag{5.A.2}$$

$$\{\bar{\boldsymbol{\chi}}_i\} = -\left\{\frac{\partial g}{\partial \boldsymbol{\varepsilon}_i^p}\right\} = \{\boldsymbol{\sigma}\} = \left\{\begin{array}{c} p \\ q \end{array}\right\} \tag{5.A.3}$$

$$\{\bar{\boldsymbol{\chi}}_o\} = -\left\{\frac{\partial g}{\partial \boldsymbol{\varepsilon}_o^p}\right\} = \{\boldsymbol{\sigma}\} = \left\{\begin{array}{c} p \\ q \end{array}\right\} \tag{5.A.4}$$

213

$$\{\bar{\boldsymbol{\chi}}_\rho\} = -\left\{\frac{\partial g}{\partial \boldsymbol{\rho}}\right\} = -\left\{\begin{array}{c} \frac{\partial g}{\partial \rho_p} \\ \frac{\partial g}{\partial \rho_q} \end{array}\right\} = \left\{\begin{array}{c} 0 \\ 0 \end{array}\right\} \tag{5.A.5}$$

where $\boldsymbol{\varepsilon}$ is the total strain (in triaxial space), and $\bar{\boldsymbol{\chi}}_i$, $\bar{\boldsymbol{\chi}}_o$ and $\bar{\boldsymbol{\chi}}_\rho$, respectively, are the generalised stresses related to the inner yield surface, outer yield surface and kinematic variable. It should be noted that $\boldsymbol{\rho}$ is an internal variable that is introduced in the definition of the rate of dissipation potential function (Eq.(5.2)) (and not in the definition of the energy potential, Eq. (5.1)).

Dissipative stresses are derived by differentiating the total rate of dissipation potential (Eq. (5.2a)) with respect to the rates of the internal variables ($\boldsymbol{\varepsilon}_i^p = \{\varepsilon_{v,i}^p, \varepsilon_{s,i}^p\}^T$, $\boldsymbol{\varepsilon}_o^p = \{\varepsilon_{v,o}^p, \varepsilon_{s,o}^p\}^T$ and $\boldsymbol{\rho} = \{\rho_p, \rho_q\}^T$)

$$\{\boldsymbol{\chi}_i\} = \left\{\frac{\partial d}{\partial \dot{\boldsymbol{\varepsilon}}_i^p}\right\} = \left\{\begin{array}{c} \frac{\partial d}{\partial \dot{\varepsilon}_{v,i}^p} \\ \frac{\partial d}{\partial \dot{\varepsilon}_{s,i}^p} \end{array}\right\} = \left\{\begin{array}{c} (C_i + \rho_p) + \dfrac{A_i^2 \dot{\varepsilon}_{v,i}^p}{\sqrt{A_i^2\left(\dot{\varepsilon}_{v,i}^p\right)^2 + B_i^2\left(\dot{\varepsilon}_{s,i}^p\right)^2}} \\[4ex] \rho_q + \dfrac{B_i^2 \dot{\varepsilon}_{s,i}^p}{\sqrt{A_i^2\left(\dot{\varepsilon}_{v,i}^p\right)^2 + B_i^2\left(\dot{\varepsilon}_{s,i}^p\right)^2}} \end{array}\right\} + \left\{\begin{array}{c} \Lambda_1 \dfrac{\partial c_1}{\partial \dot{\varepsilon}_{v,i}^p} \\[2ex] \Lambda_2 \dfrac{\partial c_2}{\partial \dot{\varepsilon}_{s,i}^p} \end{array}\right\} \tag{5.A.6}$$

$$\{\boldsymbol{\chi}_o\} = \left\{\frac{\partial d}{\partial \dot{\boldsymbol{\varepsilon}}_o^p}\right\} = \left\{\begin{array}{c} \frac{\partial d}{\partial \dot{\varepsilon}_{v,o}^p} \\ \frac{\partial d}{\partial \dot{\varepsilon}_{s,o}^p} \end{array}\right\} = \left\{\begin{array}{c} C_o + \dfrac{A_o^2 \dot{\varepsilon}_{v,o}^p}{\sqrt{A_o^2\left(\dot{\varepsilon}_{v,o}^p\right)^2 + B_o^2\left(\dot{\varepsilon}_{s,o}^p\right)^2}} \\[4ex] \dfrac{B_o^2 \dot{\varepsilon}_{s,o}^p}{\sqrt{A_o^2\left(\dot{\varepsilon}_{v,o}^p\right)^2 + B_o^2\left(\dot{\varepsilon}_{s,o}^p\right)^2}} \end{array}\right\} \tag{5.A.7}$$

$$\{\boldsymbol{\chi}_\rho\} = \left\{\frac{\partial d}{\partial \dot{\boldsymbol{\rho}}}\right\} = \left\{\begin{array}{c} \frac{\partial d}{\partial \dot{\rho}_p} \\ \frac{\partial d}{\partial \dot{\rho}_p} \end{array}\right\} = \left\{\begin{array}{c} \Lambda_1 \dfrac{\partial c_1}{\partial \dot{\rho}_p} \\[2ex] \Lambda_2 \dfrac{\partial c_2}{\partial \dot{\rho}_p} \end{array}\right\} \tag{5.A.8}$$

where $\boldsymbol{\chi}_o$ and $\boldsymbol{\chi}_i$ are the dissipative stresses related to d_o and d_i, respectively, and $\boldsymbol{\chi}_\rho$ is the dissipative stress related to the kinematic variable $\boldsymbol{\rho}$. Note that $\partial c_1/\partial \dot{\varepsilon}_{v,i}^p$, $\partial c_2/\partial \dot{\varepsilon}_{s,i}^p$, $\partial c_1/\partial \dot{\rho}_p$, and $\partial c_2/\partial \dot{\rho}_q$ are non-zero terms.

By maximising the rate of dissipation, i.e., using Ziegler's postulate [30] (where $\boldsymbol{\chi} = \bar{\boldsymbol{\chi}}$), $\boldsymbol{\chi}_i = \bar{\boldsymbol{\chi}}_i$ (equating Eq. (5.A.3) with Eq. (5.A.6)), $\boldsymbol{\chi}_o = \bar{\boldsymbol{\chi}}_o$ (equating Eq. (5.A.4) with Eq. (5.A.7)) and $\boldsymbol{\chi}_\rho = \bar{\boldsymbol{\chi}}_\rho$ (equating Eq. (5.A.5) with Eq. (5.A.8)), it is determined that

$$\{\boldsymbol{\chi}_i\} = \{\boldsymbol{\sigma}\} = \left\{\begin{array}{c} p \\ q \end{array}\right\} \tag{5.A.9}$$

$$\Lambda = 0 \tag{5.A.10}$$

By substituting Eq. (5.A.10) in Eqs. (5.A.6) and (5.A.8), the dissipative stresses related to

the inner yield surface and kinematic variable are simplified to

$$\{\boldsymbol{\chi}_i\} = \left\{ \frac{\partial d}{\partial \dot{\boldsymbol{\varepsilon}}_i^p} \right\} = \left\{ \begin{array}{c} \frac{\partial d}{\partial \dot{\varepsilon}_{v,i}^p} \\ \frac{\partial d}{\partial \dot{\varepsilon}_{s,i}^p} \end{array} \right\} = \left\{ \begin{array}{c} \left(C_i + \rho_p\right) + \frac{A_i^2 \dot{\varepsilon}_{v,i}^p}{\sqrt{A_i^2 \left(\dot{\varepsilon}_{v,i}^p\right)^2 + B_i^2 \left(\dot{\varepsilon}_{s,i}^p\right)^2}} \\ \rho_q + \frac{B_i^2 \dot{\varepsilon}_{s,i}^p}{\sqrt{A_i^2 \left(\dot{\varepsilon}_{v,i}^p\right)^2 + B_i^2 \left(\dot{\varepsilon}_{s,i}^p\right)^2}} \end{array} \right\} \qquad (5.A.11)$$

$$\{\boldsymbol{\chi}_\rho\} = \left\{ \frac{\partial d}{\partial \dot{\boldsymbol{\rho}}} \right\} = \left\{ \begin{array}{c} 0 \\ 0 \end{array} \right\} \qquad (5.A.12)$$

The general approach of deriving the inner and outer yield surfaces for rate-independent materials, with the rate of dissipation potential being a first order homogenous function of plastic strain increments, is by invoking the Legendre-Fenchel transform on the rate of dissipation potential. This procedure can also be done in a simpler way by eliminating the sub-rate of dissipation functions d_o and d_i in Eq. (5.A.7) and Eq. (5.A.11), respectively. Eventually, the surfaces in the dissipative stress space (χ_p-χ_q) are determined as

$$\text{Outer yield surface:} \quad y_o^d = B_o^2 \left(\chi_{p,o} - C_0\right)^2 + A_o^2 \left(\chi_{q,o}\right)^2 - A_o^2 B_o^2 = 0 \qquad (5.A.13)$$

$$\text{Inner yield surface:} \quad y_i^d = B_i^2 \left(\chi_{p,i} - \rho_p - C_i\right)^2 + A_i^2 \left(\chi_{q,i} - \rho_q\right)^2 - A_i^2 B_i^2 = 0 \qquad (5.A.14)$$

which form ellipses in χ_p-χ_q space (dissipative stress space).

The flow rule (direction of plastic strain increments) is always normal to the inner yield surface in dissipative stress space (y_i^d), i.e., it is along the derivatives of the inner yield surface with respect to dissipative stresses corresponding to the inner yield surface ($\chi_{p,i}$ and $\chi_{q,i}$)

$$\{\boldsymbol{r}_d^i\} = \left\{ \begin{array}{c} r_p^i \\ r_q^i \end{array} \right\} = 2 \left\{ \begin{array}{c} B_i^2 \left(\chi_{p,i} - \rho_p - C_i\right) \\ A_i^2 \left(\chi_{q,i} - \rho_q\right) \end{array} \right\} \qquad (5.A.15)$$

Substituting Eq. (5.A.9) in Eqs. (5.A.13)-(5.A.15), the inner yield surface, the outer yield surface and the plastic flow in true stress space (p-q) are derived as those in Eqs. (5.3)-(5.5), respectively.

The incremental formulations for strain controlled conditions and stress controlled conditions (as the input) are presented in Appendix 5.C.

5.B. APPENDIX B: ISOTHERMAL KINEMATIC RULE

The projection or similarity centre is the point about which the inner yield surface and the outer yield surface are geometrically similar, such that a ray extending from the projection centre passes through points on the inner yield surface and the outer yield surface with a common normal. The projection point can be determined by considering the intersection of two lines. Each line connects two points, one on the inner yield surface and the other on the outer yield surface, that have an identical normal on

each surface. Here, these two lines are selected to connect the compression and de-compression apexes of both surfaces (Figure 5.18a). The decompression apexes of the inner and the outer yield surfaces, respectively, have coordinates $(p, q) = (\rho_p, \rho_q)$ and $(p, q) = (0, 0)$, and the compression apexes for corresponding surfaces have coordinates $(p, q) = (p_{iT}, \rho_q)$ and $(p, q) = (p_{cT}, 0)$, where p_{iT} is geometrically defined as

$$p_{iT} = \rho_p + \tilde{p}_{iT} \tag{5.B.1}$$

By determining these two lines, the projection centre is their point of intersection $(\hat{p}, \hat{q})$ and is determined as

$$\left.\begin{array}{l} \hat{p} = \rho_p / W_r \\ \hat{q} = \rho_q / W_r \end{array}\right\} \rightarrow \left\{\begin{array}{l} \hat{p} \\ \hat{q} \end{array}\right\} = \frac{1}{W_r}\left\{\begin{array}{l} \rho_p \\ \rho_q \end{array}\right\} \tag{5.B.2a}$$

or

$$\hat{\boldsymbol{\sigma}} = \frac{\boldsymbol{\rho}}{W_r} \tag{5.B.2b}$$

where W_r is defined as

$$W_r = 1 - \frac{\tilde{p}_{iT}}{p_{cT}} \tag{5.B.3}$$

where $\tilde{p}_{iT}$ and p_{cT} are the size of the major-axis of the inner and outer yield surfaces, respectively. The coordinates of the projection centre are controlled by W_r and the coordinates of the decompression apex of the inner yield surface, $\boldsymbol{\rho}$ (Eq. (5.B.2b)). Vice versa, the decompression apex of the inner yield surface is linked to the projection centre

$$\boldsymbol{\rho} = W_r \hat{\boldsymbol{\sigma}} \tag{5.B.4}$$
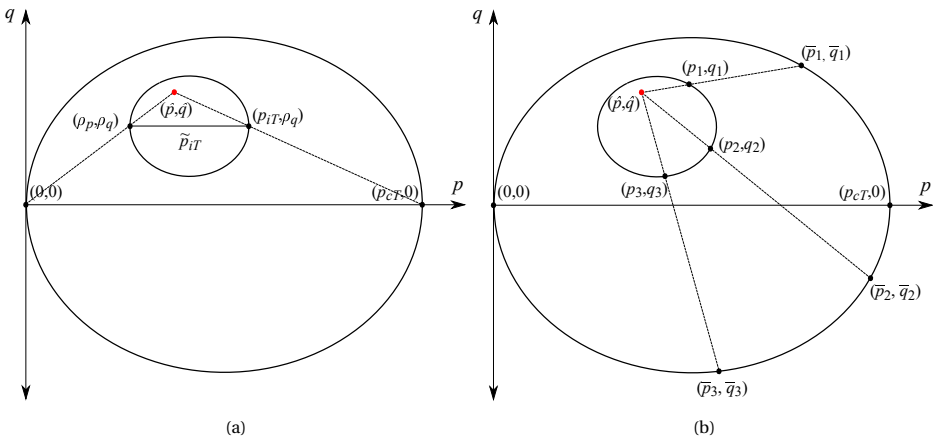
Figure 5.18: (a) Definition of projection centre; (b) definition of image stress

The corresponding image stress on the outer yield surface can be obtained from any stress on the inner yield surface (Figure 5.18b). The image stress, $(\bar{p}, \bar{q})$, on the outer yield surface is determined from the properties of similar triangles (Figure 5.18a)

$$\left.\begin{array}{l} \bar{p} = p + \left(\frac{W_r}{1-W_r}\right)(p - \hat{p}) \\ \bar{q} = q + \left(\frac{W_r}{1-W_r}\right)(q - \hat{q}) \end{array}\right\} \rightarrow \left\{\begin{array}{c} \bar{p} \\ \bar{q} \end{array}\right\} = \left\{\begin{array}{c} p \\ q \end{array}\right\} + \left(\frac{W_r}{1-W_r}\right)\left(\left\{\begin{array}{c} p \\ q \end{array}\right\} - \left\{\begin{array}{c} \hat{p} \\ \hat{q} \end{array}\right\}\right) \tag{5.B.5a}$$

or, equivalently,

$$\{\bar{\boldsymbol{\sigma}}\} = \{\boldsymbol{\sigma}\} + \left(\frac{W_r}{1-W_r}\right)(\{\boldsymbol{\sigma}\} - \{\hat{\boldsymbol{\sigma}}\}) \tag{5.B.5b}$$

The kinematic rule is the rate of Eq. (5.B.4):

$$\{\dot{\boldsymbol{\rho}}\} = \dot{W}_r \{\hat{\boldsymbol{\sigma}}\} + W_r \{\dot{\hat{\boldsymbol{\sigma}}}\} \tag{5.B.6}$$

where

$$\dot{W}_r = (1 - W_r)\frac{\dot{p}_{cT}}{p_{cT}} - \frac{\dot{\hat{p}}_{iT}}{p_{cT}} \tag{5.B.7}$$

Under isothermal conditions, the temperature dependency terms of $\dot{\hat{p}}_{iT}$ (Eq. (5.14)) and $\dot{p}_{cT}$ (Eq. (5.15)) are dropped; thereby, they are respectively defined by $\dot{\hat{p}}_i$ and $\dot{p}_c$:

$$\dot{\hat{p}}_i = \tilde{p}_{iT}\frac{1+e_0}{\lambda - \kappa}\dot{\varepsilon}_v^p \tag{5.B.8}$$

$$\dot{p}_c = p_{cT}\frac{1+e_0}{\lambda - \kappa}\dot{\varepsilon}_v^p \tag{5.B.9}$$

The isothermal kinematic rule, assigned to the decompression apex ($\dot{\boldsymbol{\rho}}$), is complete once the evolution rule of the projection centre ($\dot{\hat{\boldsymbol{\sigma}}}$) is designed. Two mechanisms form the evolution rule of the projection centre, $\hat{\boldsymbol{\sigma}} = (\hat{p}, \hat{q})$:

- When the inner yield surface translates with the stress state along the hydrostatic pressure axis (p-axis) under isothermal conditions (no temperature change), incremental plastic volumetric strains are produced and, simultaneously, the outer yield surface hardens isotropically with the plastic volumetric strain increments (see Eq. (5.A.9))). The hydrostatic translation (along the p-axis) of the inner yield surface is restricted by the isotropic growth of the outer yield surface, which implies that the projection centre translates proportionally to the hydrostatic incremental growth of the outer yield surface (isotropic hardening). Mathematically, this means that

$$\{\dot{\hat{\boldsymbol{\sigma}}}_1\} = \frac{\dot{p}_c}{p_{cT}}\{\hat{\boldsymbol{\sigma}}\} \tag{5.B.10}$$

- When plastic strains are developed, the inner yield surface translates toward the image stress, projected on the outer yield surface, which is mathematically expressed as

$$\{\dot{\hat{\boldsymbol{\sigma}}}_2\} = C_\chi \left\| \dot{\boldsymbol{\varepsilon}}^p \right\| (\{\boldsymbol{\sigma}\} - \{\hat{\boldsymbol{\sigma}}\}) \tag{5.B.11}$$

where $\left\| \dot{\boldsymbol{\varepsilon}}^p \right\|$ is the magnitude of the plastic strain increment and C_χ is a parameter which controls the pace of the inner yield surface approaching the outer yield surface.

The evolution rule of the projection centre is the sum of $\{\dot{\hat{\boldsymbol{\sigma}}}_1\}$ and $\{\dot{\hat{\boldsymbol{\sigma}}}_2\}$,

$$\{\dot{\hat{\boldsymbol{\sigma}}}\} = C_\chi \left\| \dot{\boldsymbol{\varepsilon}}^p \right\| (\{\boldsymbol{\sigma}\} - \{\hat{\boldsymbol{\sigma}}\}) + \frac{\dot{p}_c}{p_{cT}} \{\hat{\boldsymbol{\sigma}}\} \tag{5.B.12}$$

and consequently, by using Eq. (5.B.6), the kinematic rule assigned to the decompression apex for isothermal conditions is determined as

$$\{\dot{\boldsymbol{\rho}}_I\} = \left(\frac{\dot{p}_c}{p_{cT}} - \frac{\dot{\tilde{p}}_i}{p_{cT}} \right) \{\hat{\boldsymbol{\sigma}}\} + C_\chi \left\| \dot{\boldsymbol{\varepsilon}}^p \right\| W_r (\{\boldsymbol{\sigma}\} - \{\hat{\boldsymbol{\sigma}}\}) \tag{5.B.13}$$

By further substituting Eq. (5.B.2b) in Eq. (5.B.13) and eliminating $\{\hat{\boldsymbol{\sigma}}\}$, the kinematic rule (Eq. (5.18)) is derived.

5.C. APPENDIX C: RATE-FORM FORMULATION

STRAIN-CONTROLLED INCREMENTAL FORMULATION

In order to determine the strain-controlled rate-form formulation, all the incremental formulations, including the isotropic and kinematic rules, need to be re-written. Here, the rate equations are split into plastic multiplier ($\dot{\Lambda}$) dependent and independent terms, which are respectively denoted by M_i and U_i, where subscript i represents the variable.

The isotropic hardening rule for the outer yield surface (Eq. (5.14)) is rewritten as

$$\dot{p}_{cT} = \dot{\Lambda} M_{p_{cT}} + U_{p_{cT}} \tag{5.C.1a}$$

where

$$M_{p_{cT}} = p_{cT} \frac{1 + e_0}{\lambda - \kappa} r_p^i \tag{5.C.1b}$$

$$U_{p_{cT}} = -\mu_0 p_{cT} \dot{T} \tag{5.C.1c}$$

where r_p^i is the flow rule along the p-axis and $\dot{\varepsilon}_v^p = \dot{\Lambda} r_p^i$. The isotropic hardening of the inner yield surface (Eq. (5.15)) is rewritten as

$$\dot{\tilde{p}}_{iT} = \dot{\Lambda} M_{\tilde{p}_{iT}} + U_{\tilde{p}_{iT}} \tag{5.C.2a}$$

where

$$M_{\tilde{p}_{iT}} = \tilde{p}_{iT} \left(\frac{1 + e_0}{\lambda - \kappa} r_p^i - M_\mu \langle T - T_0 \rangle \right) \tag{5.C.2b}$$

$$U_{\tilde{p}_{iT}} = -\left(\mu\langle\dot{T}\rangle + U_\mu\langle T - T_0\rangle\right)\tilde{p}_{iT} \tag{5.C.2c}$$

The kinematic rule under isothermal conditions (Eq. (5.18)) is rewritten as

$$\{\dot{\boldsymbol{\rho}}_I\} = \dot{\Lambda}\{\boldsymbol{M}_I\} \tag{5.C.3a}$$

where

$$\{\boldsymbol{M}_I\} = \left\{ \begin{array}{c} (M_I)_p \\ (M_I)_q \end{array} \right\} = \left(\frac{1}{W_r}\left(\frac{M_{p_c}}{p_{cT}} - \frac{M_{\tilde{p}_i}}{p_{cT}}\right) - C_\chi\left\|\mathbf{r}^i\right\|\right)\left\{ \begin{array}{c} \rho_p \\ \rho_q \end{array} \right\} + C_\chi\left\|\mathbf{r}^i\right\|W_r\left\{ \begin{array}{c} p \\ q \end{array} \right\} \tag{5.C.3b}$$

and

$$M_{\tilde{p}_i} = \tilde{p}_{iT}\frac{1+e_0}{\lambda-\kappa}r_p^i \tag{5.C.3c}$$

$$M_{p_c} = p_{cT}\frac{1+e_0}{\lambda-\kappa}r_p^i \tag{5.C.3d}$$

The kinematic rule under non-isothermal conditions (Eq. (5.18)) is rewritten as

$$\{\dot{\boldsymbol{\rho}}_H\} = \dot{\Lambda}\{\boldsymbol{M}_H\} \tag{5.C.4a}$$

where

$$\{\boldsymbol{M}_H\} = \left\{ \begin{array}{c} (M_H)_p \\ (M_H)_q \end{array} \right\} = -H\left(\dot{T}\right)\left\{ \begin{array}{c} (M_I)_p \\ 0 \end{array} \right\} \tag{5.C.4b}$$

The kinematic rule is therefore, the sum of Eq. (5.C.3a) and Eq. (5.C.4a)

$$\{\dot{\boldsymbol{\rho}}\} = \{\dot{\boldsymbol{\rho}}_I\} + \{\dot{\boldsymbol{\rho}}_H\} \tag{5.C.5}$$

$\dot{\mu}$ is the rate of μ (Eq. (5.11))

$$\dot{\mu} = \mu b\left(\frac{\dot{p}_{iT}}{p_{iT}} - \frac{\dot{p}_{cT}}{p_{cT}}\right) \tag{5.C.6}$$

which can be rewritten as

$$\dot{\mu} = \dot{\Lambda}\left(K_p\right)_\mu + H_\mu \tag{5.C.7a}$$

where

$$M_\mu = \left(\frac{1}{\mu b} + \frac{\tilde{p}_{iT}}{p_{iT}}\langle T - T_0\rangle\right)^{-1}\left(\frac{(M_I)_p + (M_H)_p}{p_{iT}} - \frac{M_{p_{cT}}}{p_{cT}} + \frac{1+e_0}{\lambda-\kappa}\frac{\tilde{p}_{iT}}{p_{iT}}r_p^i\right) \tag{5.C.7b}$$

$$U_\mu = -\left(\frac{1}{\mu b} + \frac{\tilde{p}_{iT}}{p_{iT}}\langle T - T_0\rangle\right)^{-1}\left(\mu\frac{\tilde{p}_{iT}}{p_{iT}}\langle\dot{T}\rangle + \frac{U_{p_{cT}}}{p_{cT}}\right) \tag{5.C.7c}$$

The total strain increment can be determined by differentiating Eq. (5.A.2)

$$\{\dot{\boldsymbol{\varepsilon}}\} = \{\dot{\boldsymbol{\varepsilon}}^e\} + \{\dot{\boldsymbol{\varepsilon}}_i^p\} + \{\dot{\boldsymbol{\varepsilon}}_o^p\} + \left\{\dot{\boldsymbol{\varepsilon}}^{Therm}\right\} \tag{5.C.8}$$

where the elastic strain increments are

$$\{\dot{\boldsymbol{\varepsilon}}^e\} = \left\{ \begin{array}{c} \dot{\varepsilon}_v^e \\ \dot{\varepsilon}_s^e \end{array} \right\} = [\mathbf{C}^e]\{\dot{\boldsymbol{\sigma}}\} = - \left[\begin{array}{cc} \frac{\partial^2 g_1}{\partial p^2} & \frac{\partial^2 g_1}{\partial p \partial q} \\ \frac{\partial^2 g_1}{\partial q \partial p} & \frac{\partial^2 g_1}{\partial q^2} \end{array} \right] \left\{ \begin{array}{c} \dot{p} \\ \dot{q} \end{array} \right\} \tag{5.C.9}$$

where $[\mathbf{C}^e]$ is the elastic compliance (or flexibility) matrix. With respect to Eq. (5.A.1a) or Eq. (5.A.1c), the components of the elastic compliance matrix can be derived, respectively, as

$$[\mathbf{C}^e] = \frac{1}{3\bar{G}p_a^{1-n}p_o^n} \left[\begin{array}{cc} \frac{3\bar{G}}{\bar{K}(1-n)}\left(1 - \frac{np^2}{p_o^2}\right) & -\frac{npq}{p_o^2} \\ -\frac{npq}{p_o^2} & 1 - \frac{n(1-n)\bar{K}}{3\bar{G}}\frac{q^2}{p_o^2} \end{array} \right] \tag{5.C.10a}$$

$$[\mathbf{C}^e] = \frac{1}{3\bar{G}p} \left[\begin{array}{cc} \frac{3\bar{G}}{\bar{K}}\left(1 + \frac{\bar{K}}{3\bar{G}}\frac{q^2}{p^2}\right) & -\frac{q}{p} \\ -\frac{q}{p} & 1 \end{array} \right] \tag{5.C.10b}$$

The thermo-elastic strain increments are

$$\left\{\dot{\boldsymbol{\varepsilon}}^{Therm}\right\} = \left\{ \begin{array}{c} \dot{\varepsilon}_v^{Therm} \\ \dot{\varepsilon}_s^{Therm} \end{array} \right\} = 3\alpha^* \dot{T} \left\{ \begin{array}{c} 1 \\ 0 \end{array} \right\} \tag{5.C.11}$$

By using Eqs. (5.12) and (5.C.8), the stress increments are determined:

$$\{\dot{\boldsymbol{\sigma}}\} = [\mathbf{D}^e]\left(\{\dot{\boldsymbol{\varepsilon}}\} - \left\{\dot{\boldsymbol{\varepsilon}}^{Therm}\right\} - \dot{\Lambda}\left\{\boldsymbol{r}^i\right\}\right) \tag{5.C.12}$$

where $[\mathbf{D}^e]$ is the elastic stiffness matrix, which is the inverse of elastic flexibility matrix $[\mathbf{C}^e]$.

The consistency condition of the inner yield surface ($\dot{y}_i = 0$) is

$$\dot{y}_i = \left\{\frac{\partial y_i}{\partial \tilde{\boldsymbol{\sigma}}}\right\}^T \{\dot{\boldsymbol{\sigma}}\} + \frac{\partial y_i}{\partial \tilde{p}_{iT}}\dot{\tilde{p}}_{iT} + \frac{\partial y_i}{\partial M}\dot{M} \tag{5.C.13}$$

where $\left\{\frac{\partial y_i}{\partial \tilde{\boldsymbol{\sigma}}}\right\} = \left\{ \begin{array}{c} \partial y_i/\partial \tilde{p} \\ \partial y_i/\partial \tilde{q} \end{array} \right\}$, $\{\dot{\boldsymbol{\sigma}}\} = \left\{ \begin{array}{c} \dot{p} \\ \dot{q} \end{array} \right\}$ and $\dot{M} = \pi^* \dot{T}$.

By further substituting Eq. (5.C.2), Eq. (5.C.5) and Eq. (5.C.12) in Eq. (5.C.13), the plastic multiplier for strain-controlled loading conditions is derived

$$\dot{\Lambda} = \frac{\left\{\frac{\partial y_i}{\partial \tilde{\boldsymbol{\sigma}}}\right\}^T [\mathbf{D}^e]\{\dot{\boldsymbol{\varepsilon}} - \dot{\boldsymbol{\varepsilon}}^{Therm}\} + \frac{\partial y_i}{\partial \tilde{p}_{iT}}U_{\tilde{p}_{iT}} + \frac{\partial y_i}{\partial M}\dot{M}}{\left\{\frac{\partial y_i}{\partial \tilde{\boldsymbol{\sigma}}}\right\}^T [\mathbf{D}^e]\{\boldsymbol{r}^i\} + \left\{\frac{\partial y_i}{\partial \tilde{\boldsymbol{\sigma}}}\right\}^T \{\boldsymbol{M}_I + \boldsymbol{M}_H\} - \frac{\partial y_i}{\partial \tilde{p}_{iT}}M_{\tilde{p}_{iT}}} \tag{5.C.14}$$

The derivatives of the yield surface with respect to its variables $(\partial y_i/\partial \tilde{\boldsymbol{\sigma}}, \partial y_i/\partial \tilde{p}_{iT}, \partial y_i/\partial M)$ are presented in Appendix 5.D.

For stress-controlled conditions, the stress increment $\{\dot{\boldsymbol{\sigma}}\}$ is the input and the corresponding strain increment is calculated. To derive the stress-controlled incremental formulations, the plastic multiplier (Eq. (5.C.14)) needs to be revised. By using Eq. (5.C.8) and substituting for the term $\{\dot{\boldsymbol{\varepsilon}} - \dot{\boldsymbol{\varepsilon}}^{Therm}\}$ in Eq. (5.C.14), and using Eq. (5.C.10), the plastic multiplier is revised as

$$\dot{\Lambda} = \frac{\left\{\frac{\partial y_i}{\partial \tilde{\boldsymbol{\sigma}}}\right\}^{\mathrm{T}} \{\dot{\boldsymbol{\sigma}}\} + \frac{\partial y_i}{\partial \tilde{p}_{iT}} U_{\tilde{p}_{iT}} + \frac{\partial y_i}{\partial M} \dot{M}}{\left\{\frac{\partial y_i}{\partial \tilde{\boldsymbol{\sigma}}}\right\}^{\mathrm{T}} \{\boldsymbol{M}_I + \boldsymbol{M}_H\} - \frac{\partial y_i}{\partial \tilde{p}_{iT}} M_{\tilde{p}_{iT}}} \tag{5.C.15}$$

5.D. APPENDIX D: DERIVATIVE OF THE YIELD SURFACE WITH RESPECT TO ITS VARIABLES

The derivatives of the yield surface with respect to its variables are presented here:

$$\left\{\frac{\partial y_i}{\partial \tilde{\boldsymbol{\sigma}}}\right\} = \left\{\begin{array}{c} \frac{\partial y_i}{\partial \tilde{p}} \\ \frac{\partial y_i}{\partial \tilde{q}} \end{array}\right\} = \left\{\begin{array}{c} r_p^i + \frac{\partial y_i}{\partial A_i}\frac{\partial A_i}{\partial \tilde{p}} + \frac{\partial y_i}{\partial B_i}\frac{\partial B_i}{\partial \tilde{p}} \\ r_q^i \end{array}\right\} \tag{5.D.1}$$

$$\frac{\partial y_i}{\partial \tilde{p}_{iT}} = \frac{\partial y_i}{\partial A_i}\frac{\partial A_i}{\partial \tilde{p}_{iT}} + \frac{\partial y_i}{\partial B_i}\frac{\partial B_i}{\partial \tilde{p}_{iT}} + \frac{\partial y_i}{\partial C_i}\frac{\partial C_i}{\partial \tilde{p}_{iT}} \tag{5.D.2}$$

$$\frac{\partial y_i}{\partial M} = \frac{\partial y_i}{\partial B_i}\frac{\partial B_i}{\partial M} \tag{5.D.3}$$

where

$$\frac{\partial y_i}{\partial A_i} = 2A_i\left(\tilde{q}^2 - B_i^2\right) \tag{5.D.4}$$

$$\frac{\partial y_i}{\partial B_i} = 2B_i\left(\left(\tilde{p} - C_i\right)^2 - A_i^2\right) \tag{5.D.5}$$

$$\frac{\partial y_i}{\partial C_i} = -2B_i^2\left(\tilde{p} - C_i\right) + \frac{\partial y_i}{\partial B_i}\frac{\partial B_i}{\partial C_i} \tag{5.D.6}$$

$$\frac{\partial B_i}{\partial C_i} = B_i\left(\frac{1}{C_i} - \frac{\alpha}{\tilde{p}_{iT}}\right) \tag{5.D.7}$$

$$\frac{\partial A_i}{\partial \tilde{p}} = -\frac{\gamma}{\pi}\left(1 + \left(\frac{\gamma}{2} - \frac{\gamma\tilde{p}}{\tilde{p}_{iT}}\right)^2\right)^{-1} \tag{5.D.8}$$

$$\frac{\partial A_i}{\partial \tilde{p}_{iT}} = \frac{A_i}{\tilde{p}_{iT}} + \left(\frac{\gamma \tilde{p}}{\pi \tilde{p}_{iT}}\right)\left(1 + \left(\frac{\gamma}{2} - \frac{\gamma \tilde{p}}{\tilde{p}_{iT}}\right)^2\right)^{-1} \tag{5.D.9}$$

$$\frac{\partial B_i}{\partial \tilde{p}} = \frac{\alpha B_i}{\tilde{p}_{iT}} \tag{5.D.10}$$

$$\frac{\partial B_i}{\partial p_{iT}} = -\frac{\alpha\left(\tilde{p} - C_i\right)B_i}{\tilde{p}_{iT}^2} \tag{5.D.11}$$

$$\frac{\partial B_i}{\partial M} = \frac{B_i}{M} \tag{5.D.12}$$

$$\frac{\partial C_i}{\partial p_{cT}} = \frac{C_i}{\tilde{p}_{iT}} \tag{5.D.13}$$

$$\dot{M} = \pi^* \dot{T} \tag{5.D.14}$$

5.E. APPENDIX E: THE MAGNITUDE OF PLASTIC STRAIN INCREMENTS IN TRIAXIAL SPACE

The magnitude of the plastic strain increment produced by activation of the inner yield surface, $\left\|\dot{\varepsilon}^p\right\|$, is calculated here. The plastic volumetric strain increment and plastic deviatoric strain increment are defined respectively as

$$\dot{\varepsilon}_v^p = tr\left(\dot{\varepsilon}^p\right) \tag{5.E.1}$$

$$\dot{\varepsilon}_s^p = \left(2/3\,\dot{\mathbf{e}}^p : \dot{\mathbf{e}}^p\right)^{1/2} \tag{5.E.2}$$

where ":" is the double contract operator, and $\dot{\varepsilon}^p$ and $\dot{\mathbf{e}}^p$ are, respectively, the plastic strain increment tensor and the plastic deviatoric strain increment tensor defined as

$$\dot{\mathbf{e}}^p = \dot{\varepsilon}^p - \left(\dot{\varepsilon}_v^p/3\right) : \mathbf{1} \tag{5.E.3}$$

where $\mathbf{1}$ is the second order identity tensor.
The magnitude of the plastic strain increment is

$$\left\|\dot{\varepsilon}^p\right\| = \left(\dot{\varepsilon}^p : \dot{\varepsilon}^p\right)^{1/2} \tag{5.E.4}$$

Substituting Eq. (5.E.3) in Eq. (5.E.4) results in

$$\left\|\dot{\varepsilon}^p\right\| = \left(\underbrace{\dot{\mathbf{e}}^p : \dot{\mathbf{e}}^p}_{=3/2\left(\dot{\varepsilon}_s^p\right)^2} + \left(2\dot{\varepsilon}_v^p/3\right)\underbrace{\mathbf{1} : \dot{\mathbf{e}}^p}_{=0} + \left(\dot{\varepsilon}_v^p/3\right)^2 \underbrace{\mathbf{1} : \mathbf{1}}_{=3}\right)^{1/2} \tag{5.E.5}$$

which simplifies to

$$\left\| \dot{\boldsymbol{\varepsilon}}^p \right\| = \left(\frac{3}{2} \left(\dot{\varepsilon}_s^p \right)^2 + \frac{1}{3} \left(\dot{\varepsilon}_v^p \right)^2 \right)^{1/2}$$

(5.E.6)

It can also be rewritten in terms of the plastic multiplier and flow rule as

$$\left\| \dot{\boldsymbol{\varepsilon}}^p \right\| = \dot{\Lambda} \left\| \boldsymbol{r}^i \right\| = \dot{\Lambda} \left(\frac{3}{2} \left(r_q^i \right)^2 + \frac{1}{3} \left(r_p^i \right)^2 \right)^{1/2}$$

(5.E.7)

5.F. APPENDIX F: RANGE OF SHAPE PARAMETERS α AND γ

The range of shape parameters α and γ are investigated from two perspectives:

CONVEXITY AND RANGE OF SHAPE PARAMETERS α AND γ

From constitutive modelling and numerical perspectives, yield surfaces should be convex to avoid numerical difficulties. In Chapter 3, with the use of convexity analysis, it was demonstrated that the yield surface presented by Eq. (5.3) and stress-like functions defined in Eq. (5.6) are always convex when $-2 \le \alpha, \gamma \le 2$. The proposed yield surface was shown to successfully represent the yield stress points of a wide range of geomaterials.

THERMODYNAMICS AND RANGE OF SHAPE PARAMETERS α AND γ

From a thermodynamics perspective, the rate of dissipation is required to be non-negative. Therefore, shape parameters defining the rate of dissipation and the yield surfaces may need to be limited within a range that satisfies this thermodynamical requirement.

The total plastic work increment $\dot{W}^p$ associated with a continuum element is the product of the effective stress $\boldsymbol{\sigma}$ and plastic strain increment $\dot{\boldsymbol{\varepsilon}}^p$ and is equal to the rate of dissipation d (since there is no shift stress) [48]:

$$\dot{W}^p = \boldsymbol{\sigma} \dot{\boldsymbol{\varepsilon}}^p = d$$

(5.F.1a)

where, in triaxial stress space, it is rewritten as:

$$\dot{W}^p = p \dot{\varepsilon}_v^p + q \dot{\varepsilon}_s^p = d; \text{ where } d \ge 0$$

(5.F.1b)

Using Eq. (5.F.2) and considering that plastic deformations are associated with the inner yield surface, Eq. (5.F.1b) reduces to

$$\dot{W}^p = \left(\tilde{p} + \rho_p \right) \dot{\varepsilon}_v^p + \left(\tilde{q} + \rho_q \right) \dot{\varepsilon}_s^p = d_i$$

(5.F.1c)

where $\tilde{p} = p - \rho_p$ and $\tilde{q} = q - \rho_q$. Substituting Eq. (5.C.2) in Eq. (5.F.1c) results in

$$\left(\tilde{p} - C_i \right) \dot{\varepsilon}_v^p + \tilde{q} \dot{\varepsilon}_s^p = \sqrt{ A_i^2 \left(\dot{\varepsilon}_{v,i}^p \right)^2 + B_i^2 \left(\dot{\varepsilon}_{s,i}^p \right)^2 }$$

(5.F.2)

The right-hand side of Eq. (5.F.2) is non-negative. Therefore, the ranges of the shape parameters α and γ are restricted to values resulting in non-negative values of the term

on the left-hand side of Eq. (5.F.2). The range of values of the term $\left(\tilde{p} - C_i\right)\dot{\varepsilon}_v^p + \tilde{q}\dot{\varepsilon}_s^p$ (left-hand side of Eq. (5.F.2)) was investigated for $-2 \leq \alpha, \gamma \leq 2$ (obtained from convexity analysis) and $0 \leq \tilde{p}/p_{iT} \leq 1$ (the range of $\tilde{p}$ varying inside the inner yield surface) which where non-negative, similar to the right-hand side of Eq. (5.F.2). Therefore, it was concluded that the accepted range of the shape parameters α and γ is $-2 \leq \alpha, \gamma \leq 2$.

5

6

EXPERIMENTAL INVESTIGATION OF SOIL–STRUCTURE INTERFACE BEHAVIOUR UNDER MONOTONIC AND CYCLIC THERMAL LOADING

The effect of temperature on the monotonic and cyclic shearing response of a soil–structure interface is of critical importance for the application of thermal-active geo-structures. To investigate this, soils and soil-concrete interfaces were comprehensively tested with a temperature-controlled direct shear device under both fixed temperatures and thermal/mechanical cycles within the range of 2–38°C. Monotonic and cyclic shearing with various boundary conditions, including constant normal load (CNL), constant normal stiffness (CNS) and constant volume (CV) were conducted to resemble the conditions that thermal-active-geo-structures may experience. The strength properties of the sand, clay, and sand–concrete and clay–concrete interfaces were partially influenced by heating and cooling under all boundary conditions. However, several effects were observed which could affect the performance of thermo-active structures. Heating cycles caused the clay–concrete interface to be overconsolidated, implying a lower excess pore pressure would be generated during shearing. The cyclic CNS tests suggested that the interface strength could degrade due to (thermally induced) cyclic shear displacements, with this effect strongly related to the state of the soil rather than the temperature directly. In these tests, the medium dense sand–concrete interface degraded to almost zero shear strength after 5 cycles, whereas the clay–concrete interface asymptotically degraded to around 60% of its strength after 10 cycles.

6.1. INTRODUCTION

The soils adjacent to thermo-active geo-structures are typically subjected to annual and daily cyclic temperature variation, depending on the operation mode of the ground source heat pump (GSHP) system. The mechanical behaviour of the soil–structure interaction may change due to these thermal effects and thereby influence the bearing capacity or settlement of the structure. At the same time, the thermally-induced deformation of the structure imposes cyclic shearing along the interface [1; 2], which may also impact the bearing capacity or settlements. While the thermo-mechanical behaviour of soils has been investigated thoroughly under triaxial boundary conditions [3–11], investigations on thermo-mechanical response at the interface level are limited. Therefore, a more comprehensive investigation into the thermo-mechanical behaviour of interfaces subjected to monotonic and cyclic thermal loadings, as well as on thermal effects on the cyclic shearing induced by energy-structures, is required.

The isothermal behaviour of a soil–structure interface element depends on several factors, such as the material type (wood, steel or concrete) of the structure [12], the surface roughness [13–16], soil crushability [17], particle angularity [18–20], particle size [21], the rate of shearing [22], and soil anisotropy [23]. Amongst these, the soil mean particle size and the roughness of the surface of the structure play a crucial role, for which the normalised roughness R_n was proposed [14; 24]:

$$R_n = \frac{R_{max}(L = D_{50})}{D_{50}} \tag{6.1}$$

where R_{max} is the distance between the highest peak and lowest valley within a gauged length of $L = D_{50}$ (where D_{50} is the mean particle size). R_n is suitable for describing granular material interfaces because it considers the microscopic angle between asperities and the particles, while parameter R_{max} is more often used to characterise clay interfaces, due to the difference in failure mechanism along the interface (i.e., sliding of a thin layer of oriented clay) [25; 26]. The roughness was shown to be linearly correlated with the soil interface friction coefficient before prior to a threshold value, after which the friction coefficient approached that of the soil indicating a failure inside the soil rather than along the soil–structure interface [17; 22; 27].

Another aspect influencing the mechanical response of the soil-interface is the boundary conditions. The volumetric response of the shear zone (a thin layer around structures where large shear strains are localised) during shearing can alter the normal stress applied to the interface (depending on the normal boundary conditions) which could lead to a different shear resistance. Three scenarios are often used for the boundary conditions in direct shear tests and these may be quantified by the normal stiffness (K) acting on the interface layer, which is the ratio of normal stress and normal displacement rates (i.e., $K = \Delta\sigma_n/\Delta\delta$ where $\Delta\sigma_n$ is the normal stress variation and $\Delta\delta$ is the normal displacement variation on the interface). The boundary conditions may be mimicked as springs with a stiffness of K [28] attached to the soil (Figure 6.1). Assuming a zero stiffness for the springs (i.e. $K = 0$), conventional direct shear tests known as constant normal load (CNL) may be performed (Figure 6.1a), which is the simplest way to determine the shear strength parameters [24]. By keeping the stiffness constant during shearing, it is possible to perform a constant normal stiffness (CNS) test via a di-

rect shear apparatus (Figure 6.1b). This may be most representative of field conditions, in which deformations in the shear zone are confined by the surrounding soil, which leads to changes in the normal stress [29]. This was verified by comparing centrifuge, in-situ pile experiments and laboratory CNS tests [30–32]. Cyclic degradation of the pile-interface was successfully replicated by cyclic CNS tests [33; 34]. In some direct shear tests the height of the specimen during shearing may be fixed (also known as constant volume, i.e., CV). For these tests the normal stiffness tends to infinity ($K = \infty$, Figure 6.1c) and represent an equivalent undrained shear condition [25; 35; 36]. The vertical stress change in CV shearing is equal to the pore pressure developed during undrained direct shear tests [37].
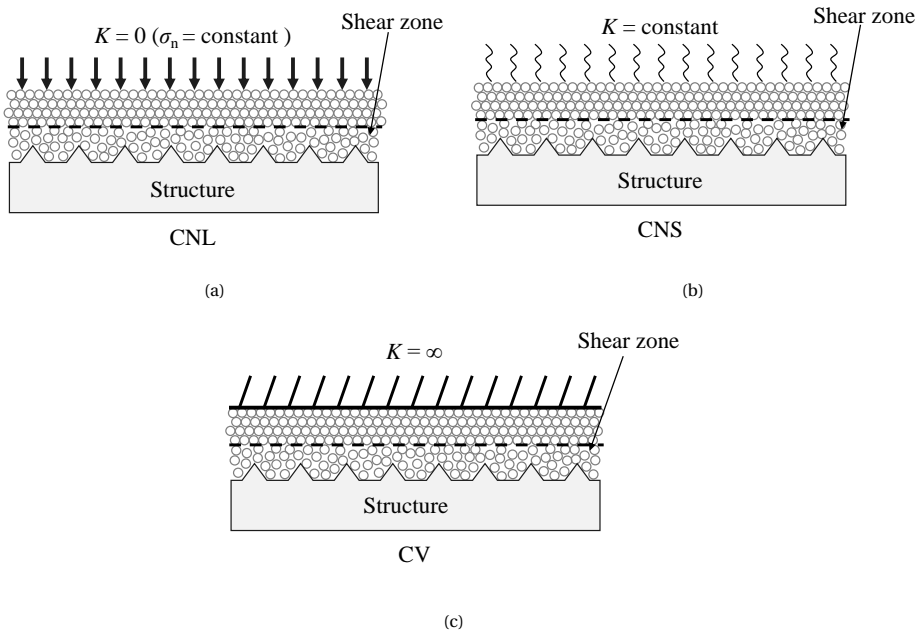
Figure 6.1: Schematic of boundary conditions normal to the soil-interface: (a) constant normal load; (b) constant normal stiffness; (c) constant volume

During energy pile system operations, these boundary conditions may be encountered along the soil–structure interface in different circumstances. For GSHP systems operating continuously, the temperature at the interface is expected to change monotonically until a quasi-static heat transfer is reached. Since the temperature is almost unchanged or varies at a relatively low rate, the normal stress on the structure is expected to be relatively constant (e.g. thermal expansion of structure, volume change of the interface induced by soil–structure displacement is negligible) resembling the CNL condition. For intermittent operation, where the energy pile provides both heating and cooling at different periods during the year and/or only operates for given hours within a day, the thermal impulse could cause significant short-term temperature fluctuations.

The cyclic shearing imposed by thermal deformation of the pile is more likely to be confined elastically by the surrounding soil, resembling the CNS condition. For energy piles bearing a variable load (e.g. in a de-icing system for a bridge deck [38]) or for short term thermal loads, the loading would impose a "*fast shearing*" along the soil–structure interface, which can be undrained and can be investigated under CV conditions. Therefore, it is of interest to evaluate the thermal effects under suitable boundary conditions. CNL and CV conditions can be reasonably considered fundamental soil behaviour and used in the calibration of constitutive models, whereas the CNS condition represents a soil element in a certain problem dependent condition.

At present, there has only been a limited amount of work investigating the impact of temperature on soil-interfaces and the results exhibit some inconsistencies/variabilities, especially for clay–concrete interfaces. Direct shear tests on quartz sand [39; 40] and Fontainebleau sand [41; 42] subjected to CNL boundary conditions have suggested that sand–concrete interface behaviour is not affected in the temperature range of 5 – 60°C. However, temperature effects on clay–concrete interfaces are less consistent. The friction angle (at the interface level) was found to be unchanged [42–45] or to decrease [39] with temperature. A more evident thermal influence was the increase of adhesion after heating, as observed with interfaces of illite [39], kaolin [42; 46] and red clay [40], while the overconsolidated (OC) kaolin [43] and red clay [44] interfaces exhibited temperature independent adhesion. Yazdani et al. [47] observed that the shear strength of a kaolin interface subjected to heating was unchanged under a normal stress of 150 kPa, whereas the shear strength increased under normal stresses of 225 and 300 kPa. They concluded that the thermal strengthening was related to normal stress level, and not due to temperature effects.

Temperature has also been shown to affect the volumetric response of clay-interfaces during shearing. It was observed from monotonic CNL and cyclic CNS shearing tests [39; 42] that the contraction of normally consolidated clay-interfaces during shearing was reduced due to thermal consolidation, while this was not obvious in other experiments [44; 45].

Previous studies have mostly focused on the monotonic temperature influence, especially heating, on the monotonic shearing behaviour of the soil interface, although the results show somewhat inconsistent trends. Moreover, limited data are available relating to thermal influences on cyclic shearing and undrained shearing behaviour of the soil–structure interface. Regarding these aspects, a comprehensive series of tests were performed using a well calibrated temperature controlled direct shear system, to investigate the shear response of interfaces within the temperature range of 2–38°C (compatible with minimum and maximum temperatures that an energy-pile may experience) under CNL, CNS and CV conditions. The void ratios of all samples were recorded and the thermal influences on the volume change during shearing carefully examined considering the creep effect. The objective is to provide a comprehensive data set, which covers a large range of conditions to which energy geo-structures are subjected, and to draw conclusions on the overall shear behaviour of interfaces under various thermal and mechanical stress paths relevant for energy geo-structures.

6.2. EXPERIMENTAL SETUP AND CALIBRATION

A modified direct-shear apparatus manufactured by Wille Geotechnik was used in this study (Figure 6.2a). The shear box was $10 \times 10 \times 3.2$ cm and installed inside a thermally insulated carriage. As shearing proceeds, the extent of the shearing surface reduces continuously, and therefore the effective surface area is used for calculating stresses. The load cap has a porous contact with the sample allowing water outflow (Figure 6.2b). The lower part of the shear box was 1 cm in depth, with a porous stone at the bottom. A concrete block was embedded inside for the soil–concrete tests. The shearing platform was levelled via a bubble level and the levelness was monitored throughout the tests. Vertical and horizontal displacements were measured by two linear variable differential transformers (LVDTs), with an accuracy of 0.001 mm. In this work, positive normal displacements signify contraction and negative signify dilation.

The thermal load was provided by a heat pump connected with two pairs of heat exchangers embedded in the load cap and the base of carriage (Figure 6.2b). The temperature at the interface level was monitored by a PT100 sensor (TP1, accuracy 0.1°C) in the shear box, which was also used to control the heat pump. The load cap and the carriage were thermally insulated. Similarly, insulation lids were installed surrounding the shear box to prevent thermal loss and water evaporation, and thus the temperature of the soil–concrete system was relatively uniform. The maximum temperature difference between the top insulation board and TP1 was found less than 0.5°C after thermal equilibrium. The whole system was kept in a climate room maintaining a constant temperature of 20 ± 2°C. Considering that the magnitude of thermal influences on the volume change and the shear strength of a sample could be relatively small, the LVDTs and shear force measurements were carefully calibrated by imposing thermo-mechanical paths analogous to that in the subsequent experiments, using a dummy iron sample or the empty shear box. Details of the calibration process are presented in the Appendix 6.B.

6.3. MATERIAL PROPERTIES AND SAMPLE PREPARATION

6.3.1. SAND

Geba sand, a commercial fine uniform silica sand, was used in this study. Its physical properties are given in Table 6.1. The size of particles ranged from 0.05 to 0.46 mm, and the grain size distribution [48] is shown in Figure 6.3. To prepare the sample, the thermocouple (Figure 6.2b) was first placed inside the shear box. Then, dry sand was poured uniformly and levelled with a 10×10 cm square tamper. A 20 mm thick medium dense ($D_r = 50$%) sand sample, with a targeted dry density of 1.43 g/cm^3, was reached by compaction.

6.3.2. CLAY

Speswhite clay was used to investigate the thermo-mechanical behaviour of fine-grained soils. This clay consists of kaolinite with a small fraction of illite [49]. The Atterberg limits (Table 6.1) were measured in accordance with BS1377-2 [50], and its particle-size distribution (Figure 6.3) was obtained via the laser diffraction method.

The samples were prepared by mixing kaolin powder with sufficient water to form a homogenous slurry with a water content of 1.5 liquid limit (LL). Then, the slurry was
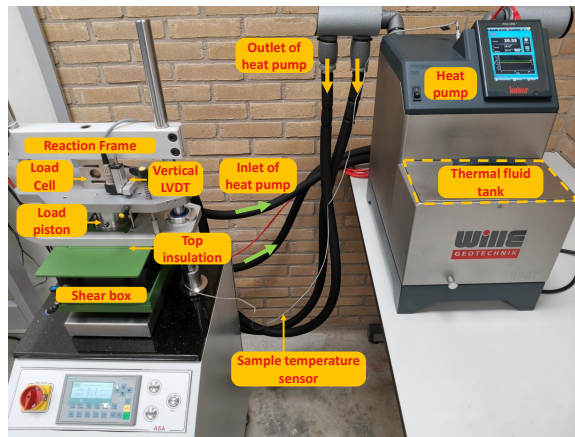
(a)
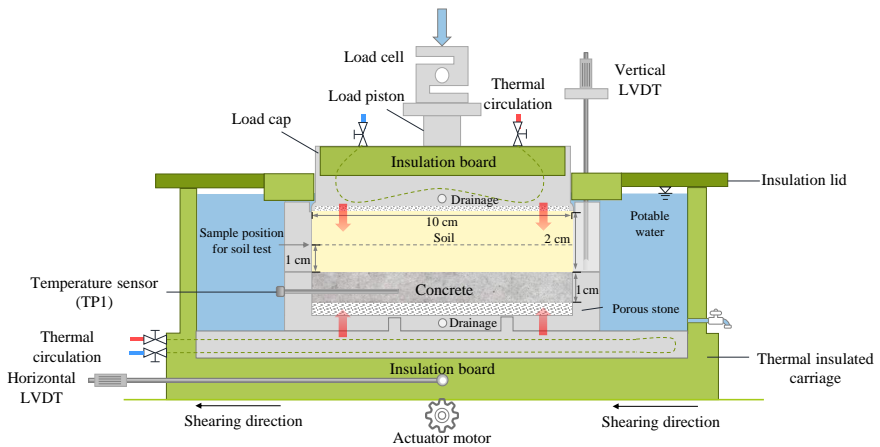
(b)

Figure 6.2: (a) Layout of temperature direct shear system; (b) Schematic view of the temperature-controlled direct shear box

consolidated under 47.5 kPa in a large oedometer cell (diameter of 19 cm). After consolidation, samples of 10 ×10× 2 cm were trimmed from the clay cake via a cutting ring. The water contents of samples varied between 47.6% and 48.5%. After lowering the sample into the shear box, the thermocouple was inserted into the sample.
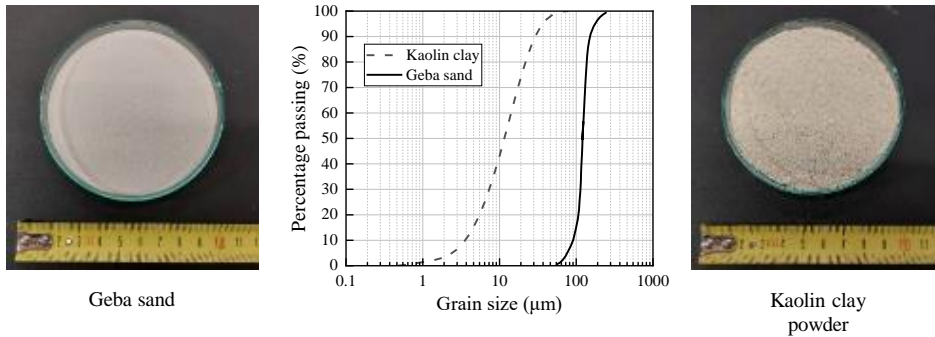
Figure 6.3: Grain-size distribution of Geba sand and kaolin clay

Table 6.1: Summary of physical properties of Geba sand [48] and kaolin clay

Geba sand	$c_u = D_{60}/D_{10}$	Minimum void ratio	Maximum void ratio	D_{50} (mm)	Specific gravity (G_s)
	1.38	0.64	1.07	0.11	2.68
kaolin clay	LL(%)	PL(%)	I_p(%)	Hydraulic conductivity (m/s)	Specific gravity (G_s)
	49.3	27.4	21.9	$10^{-8} \sim 10^{-9}$	2.65

6.3.3. SOIL–CONCRETE INTERFACE

For the interface tests, a 10 ×10 ×1 cm concrete block was first positioned in the lower shear box (Figure 6.2b) followed by a similar procedure for preparing the soil samples. The thermocouple was inserted through a pre-drilled hole inside the concrete block to record and control the temperature at the interface.

The surface of the concrete block was profiled via an optical stereo microscope along 5 lines in the shearing direction as illustrated in Figure 6.4a. For each line, the average R_n over two measurements of 13 mm was calculated (Figure 6.4b). Paikowsky et al. [18] suggested that values of R_n between 0.02 and 0.5 are categorised as "*intermediate*" roughness, which implies that a portion of the shear strength of the soil mobilises at the interface level.

6.4. EXPERIMENTAL PROGRAMME

6.4.1. TEST PARAMETERS FOR SOIL AND SOIL-INTERFACE

After preparation, samples were consolidated in the shear box at room temperature (20°C). Initially, a normal contact force of 5 kPa was applied on the samples, and then samples were submerged by distilled water [51] and left for 1–2 hours. Then, the target normal stress was reached following the loading sequence of 25, 50, 100 and 150 kPa (stopping where required) prior to temperature variation. Each intermediate load step
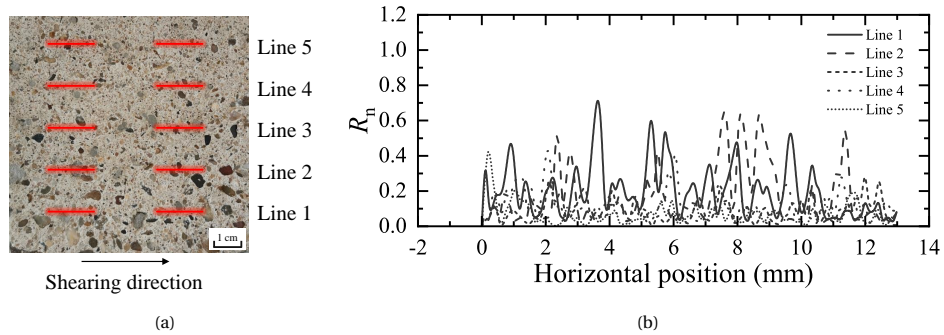
Figure 6.4: (a) Surface of the concrete block; (b) normalized roughness at different lines

was maintained for 2 hours. It should be noted that creep would proceed simultaneously during the temperature variation. Thus, the last consolidation step for iso-thermal tests was prolonged for the same duration used to achieve the target temperature in the parallel experiments. Any thermal or shearing load was imposed on the sample under a normally consolidated (NC) state.

The thermo-mechanical behaviour was investigated at ambient temperature (20°C), 2 and 38°C. Sand and sand interface samples were subjected to temperature variation and shearing at rates of 9°C/h and 0.25 mm/min, respectively. For clay and clay interface tests, 3°C/h for the monotonic thermal loading were chosen and 5°C/h for thermal cycles to reduce the test duration. Insignificant excess pore pressure would be induced by such rates [39; 42; 43]. Based on the one-dimensional consolidation tests results of the clay samples subjected to normal stresses between 50–150 kPa, a shear rate of 0.26 mm/min was recommended [51]. Here, monotonic shear tests were conducted at 0.012 mm/min to ensure no excess pore pressure was generated. A shearing rate of 0.12 mm/min was selected for cyclic shearing after a comparison between the results of the two rates showing negligible differences.

6.4.2. Thermo-mechanical loading paths
The performed tests are categorised in four series:

Series I: Temperature effect on the mechanical behaviour of soils and soil-concrete interface
The loading paths of these tests are depicted in Figure 6.5a. Samples were first consolidated (path $O - A$, where normal stresses, σ_n = 50, 100, and 150 kPa were selected), heated/cooled to 38 or 2°C from the ambient temperature (20°C) (path $A - A_1/A_2$), followed by monotonic shearing with the normal stress kept constant (CNL).

Series II: Effect of thermal cycles on the mechanical behaviour of soil–concrete interface
Samples were first consolidated to normal stresses of 50 or 150 kPa (path $O - A$). Then, samples were subjected to 5 heating or cooling cycles (path $A - A_1/A_2$) varying respectively between 20 to 38°C, or 20 to 2°C. After the thermal cycles, the sand-concrete sam-
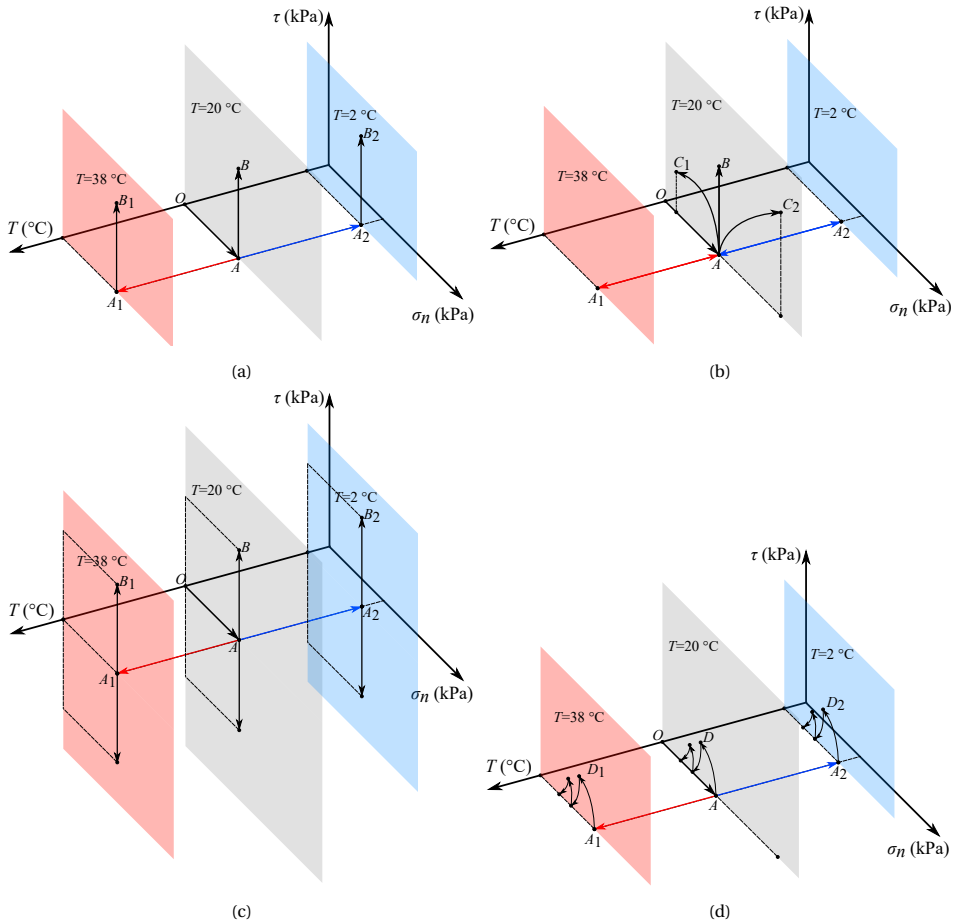
Figure 6.5: Schematic diagram of thermo-mechanical load paths: (a) Series I; (b) Series II; (c) Series III; (d) Series IV

Loading path description: $O - A$: Consolidation; $A - B$: CNL (monotonic shearing); $A - C$: CV (1: contraction, 2: dilation); $A - D$: CNS (cyclic shearing); $A - A_1/A_2$: Temperature variation (drained condition)

ples were monotonically sheared under drained conditions at 20°C while the normal stress was kept constant (CNL) (path $A - B$). On the other hand, clay–concrete samples were sheared while the total volume of the sample was kept constant (CV) (path $A - C_1/C_2$), to investigate the thermal cycle effect under undrained shearing conditions [35; 52]. The possible loading paths are shown in Figure 6.5b.

SERIES III: TEMPERATURE EFFECT ON THE CYCLIC SHEAR RESPONSE OF SOIL–CONCRETE INTERFACE

The soil-interface of an energy pile may experience cyclic mechanical shearing, due to the thermal elongation/shortening of the pile caused by the thermal loading. The distribution of shear displacement is highly dependent on the constraints from surrounding

soils and the superstructure. Therefore, it is possible to identify a location along the length of the pile (also known as the null point) at which the magnitude of soil–structure displacement would be zero. Then the magnitude of the soil–structure displacement increases from the null point toward the two ends of the pile in the opposite direction. In a idealised case where the null point is situated near the pile head (e.g. in a floating pile, with a uniform soil profile where the pile head is almost completely restrained at the surface) the pile tip would experience the largest displacement [53].

To identify a maximum realistic magnitude of the shearing displacement, the unrestrained expansion of a 20m long concrete pile, with a 20°C temperature increase and a thermal expansion of 10^{-5}/°C is calculated. This results in a 4 mm expansion. In longer piles this could be higher, but is likely to be lower due to soil restraints.

To investigate the thermal effects under such a loading condition, samples were first consolidated to 150 kPa, then heated/cooled to 38°C or 2°C from 20°C, followed by a series of two-way cyclic shearing tests with a displacement amplitude of ±4 mm. CNL conditions were selected to represent (i) the fundamental soil shear strength in relation to different stress levels (which is most useful to describe the behaviour numerically), and (ii) long duration shear processes (e.g. a half year) for which due to creep processes the normal force on the pile could be reasonably constant. The loading paths of these tests are demonstrated in Figure 6.5c.
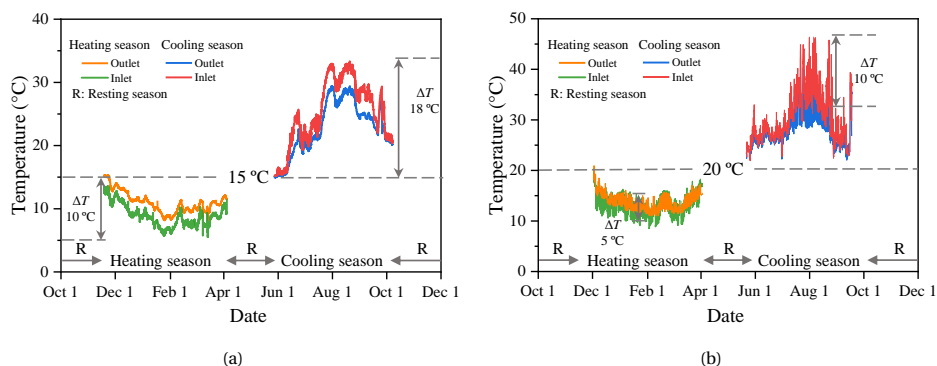
Figure 6.6: Field monitoring data of inlet and outlet temperature of GSHP systems in Jiangsu Province, China.
(a) Continuous operation system; (b) Intermittent operation system

SERIES IV: TEMPERATURE EFFECT ON CYCLIC SHEAR RESPONSE OF SOIL–CONCRETE INTERFACE WITH CNS BOUNDARY CONDITIONS

For an intermittent operation GSHP system, the daily thermal load is applied to the pile at a much higher rate. The temperature of the pile could change from the ground temperature to a maximum value of approximately 10°C higher in a few hours as observed from another field monitoring record (Figure 6.6b). In this case, a more rapid cyclic shearing would likely be imposed along the soil-interface. Considering such loading condition, samples were consolidated to 150 kPa and then one-way cyclic interface shear tests with a maximum displacement of 2 mm were conducted at temperatures 2, 20 and 38°C. Due to the relatively short duration of the shearing process (note, this is still

much slower than for cyclic loading typically observed in offshore foundations), the surrounding soil is assumed to react elastically (and drained) to the volume changes at the interface, and thus a CNS condition was chosen for this test series. Based on the elastic expanding cylinder theory [30], a range of K would be reasonable, e.g., 100 to 1200 kPa/mm [39], and therefore a medium level stiffness of $K = 500$ kPa/mm was selected for the current qualitative investigation. Where creep is low, longer duration thermal cycles can also be well represented by these conditions. The loading paths are presented in Figure 6.5d.

6.5. EXPERIMENTAL RESULTS

To ensure the reliability of the test results, repeatability tests were conducted at 20°C on Geba sand and kaolin clay specimens consolidated to 50 kPa, and the results are shown in Figure 6.7. Although the parallel tests results were not perfectly overlapping, the maximum difference was 1.5 kPa for Geba sand and 1.8 kPa for kaolin clay which are considered acceptable. This could be regarded as a reference for an overall accuracy of the experiment and only the variation beyond this accuracy could be considered as the consequence of thermal influences.
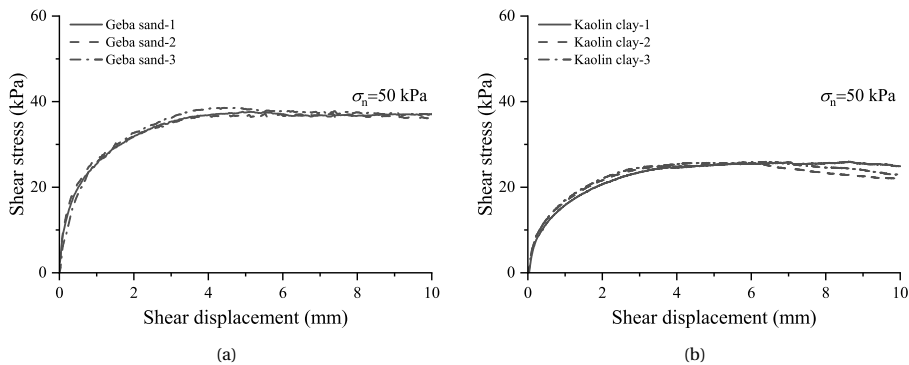
Figure 6.7: atability tests: (a) Geba sand and (b) kaolin clay

6.5.1. SERIES I-A: TEMPERATURE EFFECT ON THE SOILS

The test results for sand–sand and clay–clay shearing are presented in Figure 6.8. The shear stress versus shear displacement responses (Figure 6.8a and Figure 6.8d) demonstrate that temperature has a negligible effect on the drained shearing behaviour in terms of ultimate shear strength. The ultimate shear stresses and the corresponding normal stresses were linearly correlated and are shown in Figure 6.8b and Figure 6.8e. The average peak friction angle obtained from the best-fitted line for the sand and clay were 33.90° and 20.87° respectively. The average apparent cohesion for clay was 4.79 kPa. The difference between the friction angles at three levels of temperature are less than 1° for the two soils, which suggests a negligible influence of the temperature variation on the shear behaviour. Normal displacement versus shear displacement curves of soil–soil interface shearing are presented in Figure 6.8c and Figure 6.8f. The thermal effects on the
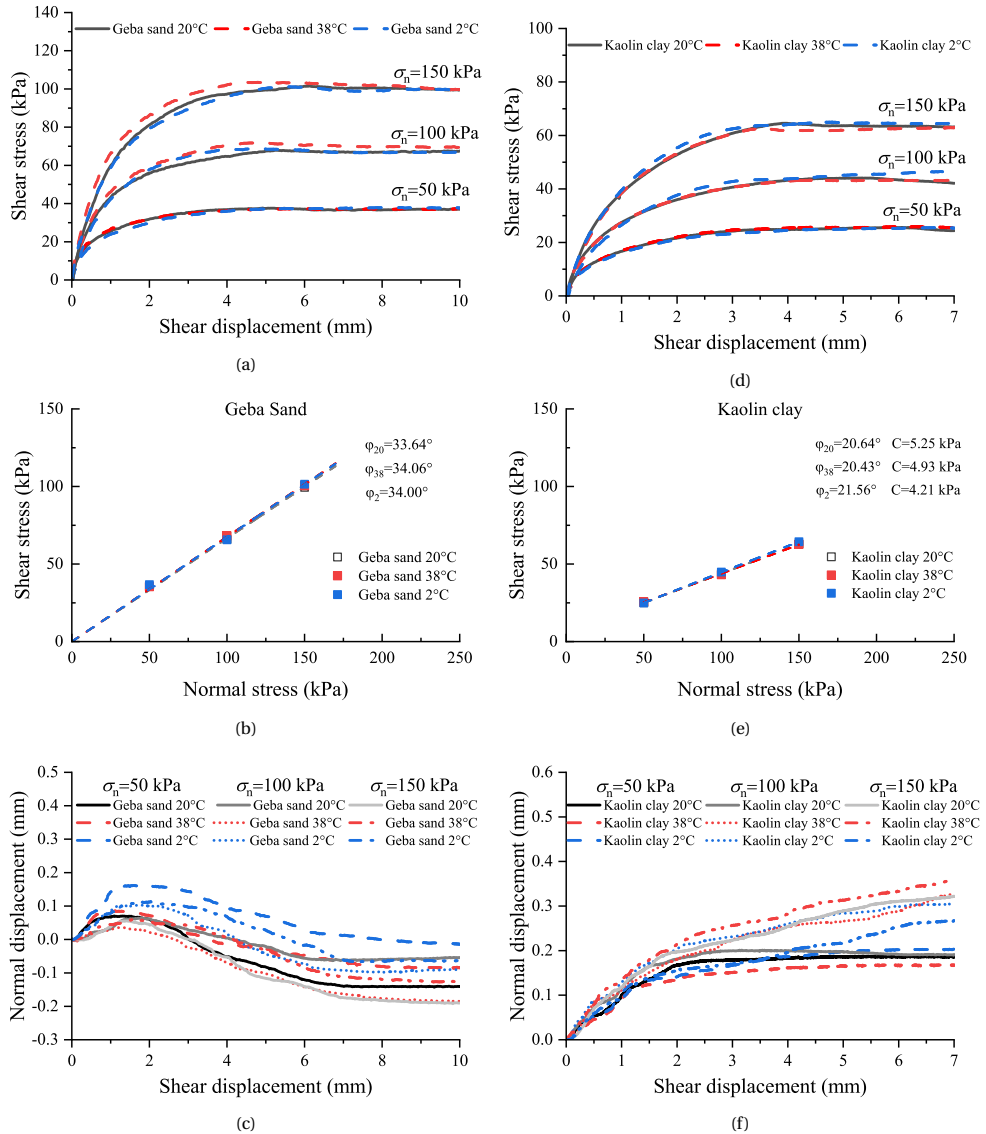
Figure 6.8: CNL results for soil samples at $T = 2, 20, 38°C$. Geba sand: (a) shear stress vs. shear displacement; (b) failure envelopes; (c) normal displacement vs. shear displacement; kaolin clay: (d) shear stress vs. shear displacement; (e) failure envelopes; (f) normal displacement vs. shear displacement

normal displacements versus shear displacements for sand and clay at different temperatures are not obvious. The reason is hypothesised to be that the thermally-induced volume change is relatively insignificant compared to the pre-shear void ratio differences (due to sample preparation). The volume changes of each sample during temperature variation differed depending on the material (sand or clay), normal stress level, creep,

and thermal load direction (i.e. heating or cooling), with hypotheses for the underlying cause discussed in more detail in Section 6.5.3. For brevity, the evolutions of volume change in the heating/cooling process for each sample were not presented, as they were almost identical as the first half cycle from the cyclic results presented in Figure 6.10 and Figure 6.13. Overall, for sand specimens, the maximum thermally-induced volume strain was less than 0.1%, equal to a void ratio change (Δe) around 0.002. For clay specimens, the maximum volume strain developed during heating, and was about 0.08% corresponding to $\Delta e \approx 0.001$ (comparable to experiments in the literature [3; 8; 54]). These volume changes are less than the variation of initial void ratio (e_0) after sample preparation (see Table 6.2 in Appendix 6.A). The specimens with a higher void ratio contracted slightly more during shearing, and therefore the differences of initial state (even when small) become significant and make the thermal influence, if any, harder to identify.

6.5.2. Series I-B: Temperature effect on the soil–concrete interfaces

The corresponding tests results for a soil–concrete interface are presented in Figure 6.9. The sand–concrete interface exhibited a hardening behaviour and mobilised 80±3% of the ultimate shear strength of the sand tests. The volumetric response (Figure 6.9c) of the sand–concrete interface is dominantly contractive, compared to the sand–sand shearing behaviour (Figure 6.8c), indicating that more sliding of the soil grains occurred along the interface [55]. For the results at 2°C, the mobilised shear stresses matched very well with that at 20°C, and represents an friction angle 26.3°. For shearing tests at 38°C, although a slight increase on the mobilised shear stress was observed (Figure 6.9a and Figure 6.9b), similar to the observations from Vasilescu et al. [56], the differences were within the accuracy of the direct shear apparatus and were too small to be considered as the consequence of temperature. It can be concluded that the effect of temperature on the sand–concrete interfaces, in the studied range, can be neglected for practical purposes.

In Figures 6.9d–6.9f, the test results related to clay–concrete interface shearing are presented. A strain hardening mechanism was observed at the clay–concrete interface until a peak shear stress was mobilised at shear displacements of 1.5–2.5 mm, after which a strain softening mechanism was followed. This behaviour indicates that failure occurs at the interface level and can be attributed to the sliding of clay particles along the interface [57]. The average peak and ultimate shear stresses were about 82% and 68% of those mobilised at the clay–clay interface, respectively. Figure 6.9d and Figure 6.9e show a negligible effect of temperature on the peak shear stresses and the ultimate shear stresses.

The limited clay–concrete interface studies [42; 43; 47; 58] also indicate a small variation of the friction angle with temperature, in agreement with this study. However, the temperature effects on adhesion differ between studies. The change of the liquid film thickness could explain such a difference [44]. The viscous impulse (I_v) for two circular interfaces bridged by a fluid film may be given by [59]

$$I_v = \frac{16\eta R^3}{3ht_s} \tag{6.2}$$

where η is the dynamic viscosity of the thin liquid film along the interface, h is the thick-

6
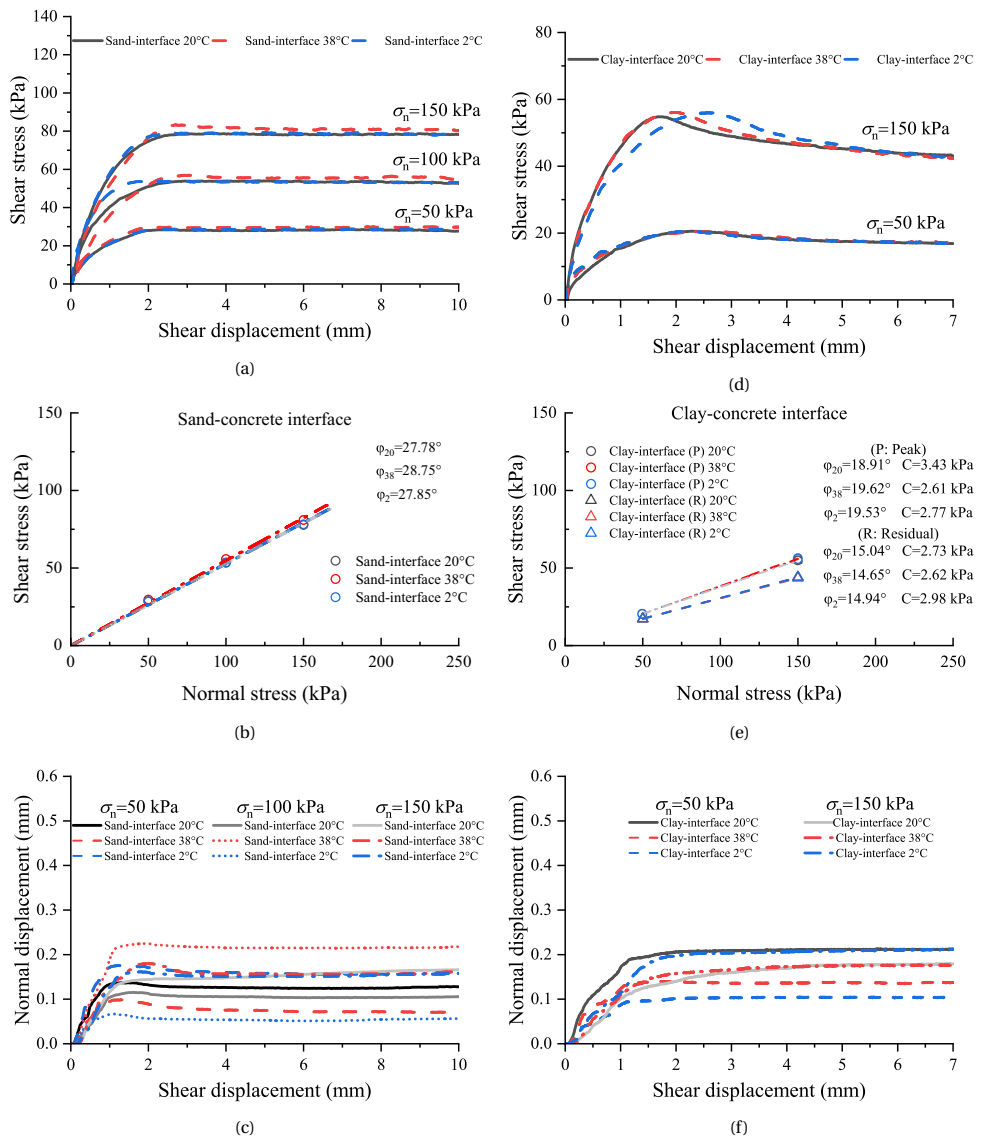

Figure 6.9: CNL results for soil-interface samples at $T = 2$, 20, 38°C. Geba sand–concrete interface: (a) shear stress vs. shear displacement; (b) failure envelopes; (c) normal displacement vs. shear displacement; kaolin clay–concrete interface: (d) shear stress vs. shear displacement; (e) failure envelopes; (f) normal displacement vs. shear displacement

ness of the liquid film, t_s is the shearing time, and R is the circular meniscus radius. This indicates that adhesion is related to the change of η and h. The temperature variations in previous studies were similar ($\Delta T = 20$–30°C) yielding a comparable change of water viscosity. The different adhesions could have resulted from Δh, which strongly depends

on how clay fabric rearranges during temperature variation. The thermal response of the clay fabric is known to be stress history dependent. For NC clay [39; 44], the collapse of clay fabric during thermal consolidation would reduce the h and increase the adhesion. For an OC soil during heating [43] or a NC soil during a cooling process [42], the arrangement of clay fabric is considered to be dispersed or unchanged, and thus the cohesion is found to slightly drop or to be unchanged after heating. Meanwhile, the physicochemical mechanisms proposed by [60] suggested that soils with higher plasticity would undergo greater volume change during heating because of their higher chemical reactivity. Due to the low-medium plasticity clay used in this study, it experienced a relatively low volume change during temperature change (details addressed in the next section) and thus exhibited a small variation of adhesion due to temperature change.

The temperature effects on the normal displacement response during shearing are again almost indistinguishable (Figure 6.9c and Figure 6.9f), which is suggested to be for the same reason as for the soil tests.

6.5.3. SERIES II: EFFECT OF THERMAL CYCLES ON THE SOIL–CONCRETE INTERFACE

Figure 6.10 shows the volume change and temperature variation (recorded by TP1) in sand–concrete interfaces subjected to heating/cooling cycles at normal stresses of 50 and 150 kPa. Thermo-elastic behaviour was assumed for the concrete block ($\alpha = 1.2 \times 10^{-5}/°C$), and its thermal vertical deformation was removed during data processing. Due to a relatively low rate of temperature change, it was essential to consider creep effects [61] in the interpretation of data to reveal the net influence of thermal cycles. The secondary compression index ($C_{\alpha e}$) is defined as [62]

$$C_{\alpha e} = -de/d\left(\log t\right) \tag{6.3}$$

where t is the elapsed time of the secondary compression. Accordingly, the volumetric strain during thermal cycles caused by creep (dashed line in Figure 6.10) was estimated by extending the logarithmic fitting of the deformation after the completion of the primary consolidation assuming a temperature independent $C_{\alpha e}$. Examples of the consolidation process are provided in Appendix 6.C.

Under the lower normal stress (50 kPa), both heating and cooling cycle induced plastic strains in addition to creep (Figure 6.10a and Figure 6.10b), mainly observed within the initial 1–2 thermal cycles. A thermo-elastic response is also seen via the strain fluctuating with temperature. Under the higher normal stress (150 kPa), the observed deformations (Figure 6.10c and Figure 6.10d) are virtually identical with the estimated creep throughout the test, with the thermo-elastic fluctuation still observed. The thermo-plastic strains at the end of each cycle are presented in Figure 6.11a, after the subtraction of the estimated creep from the total deformation. It can be inferred that the thermally-induced plastic strain was dependent on vertical stress and becomes less significant under higher normal stress (150 kPa). This behaviour is different from the established theory for clay [63–65], which assumes thermo-plastic strain is dependent on the thermal loading direction. The observed phenomenon can be explained from a micro-mechanism that may occur in sand. The external load is mainly carried by the "*strong force network*" of particles with larger inter-particle forces, while the rest (up to
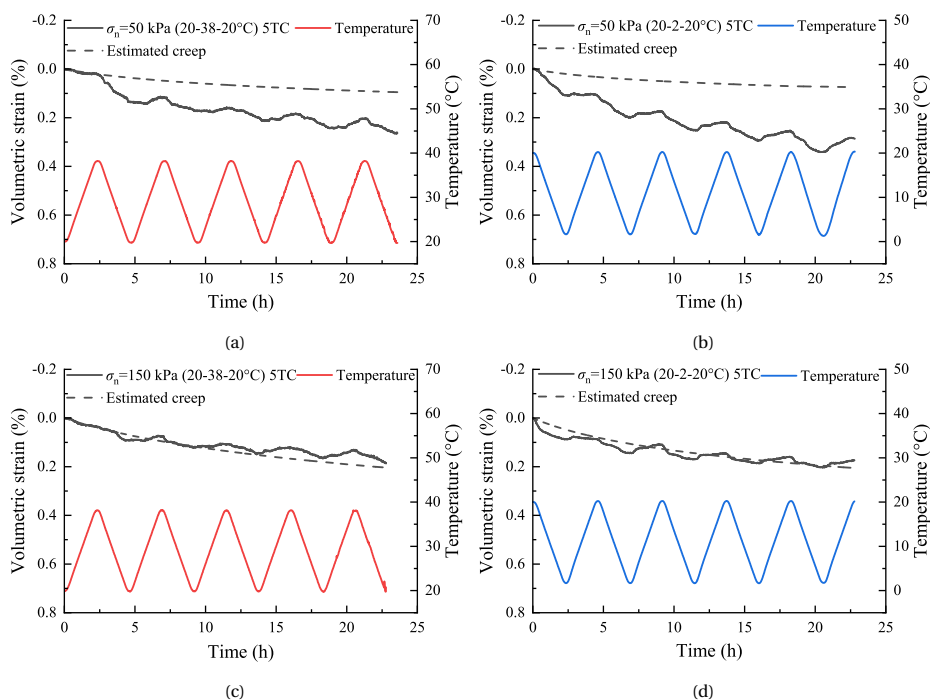
Figure 6.10: Volume change of sand–concrete interface during thermal cycles: (a) Heating cycles at 50 kPa; (b) Cooling cycles at 50 kPa; (c) Heating cycles at 150 kPa; (d) Cooling cycles at 150 kPa

60% [66]) carries small load constituting the "*weak cluster*" [62]. Under lower normal stress, the contact between grains could be relatively lose with some unstable voids [67]. When temperature changes, the thermal-elastic deformation of grains could be sufficient to trigger the rearrangement of the soil skeleton, resulting in a macro-scale deformation. However, under higher confinement, sand particles forming strong chain-forces are more stable and less influenced by thermal agitation.

After the thermal cycles, the sand–concrete interface samples were sheared to 10 mm and compared with the isothermal tests. Figure 6.12a shows that the effects of heating/cooling cycles, prior to shearing, are negligible on the mobilised shear stress at the interface level. Some unexpected abrasion happened on the concrete surface during the sample preparation for the cooling cycle test and it led to a small strength increase. The test was thus repeated under 20°C (dashed grey line) to verify such an increase was not caused by the thermal cycles.

The volumetric strains of the clay–concrete interface samples subjected to heating/cooling cycles are shown in Figure 6.13. The creep effect was estimated in the same way as for the sand-interface programme. During the cooling cycles, the volume change followed the trend of secondary consolidation and showed a nearly thermo-elastic response (Figure 6.13b and Figure 6.13d). For the heating cycle tests, irreversible contraction was mainly induced during the first 2–3 cycles, after which it kept increasing at a
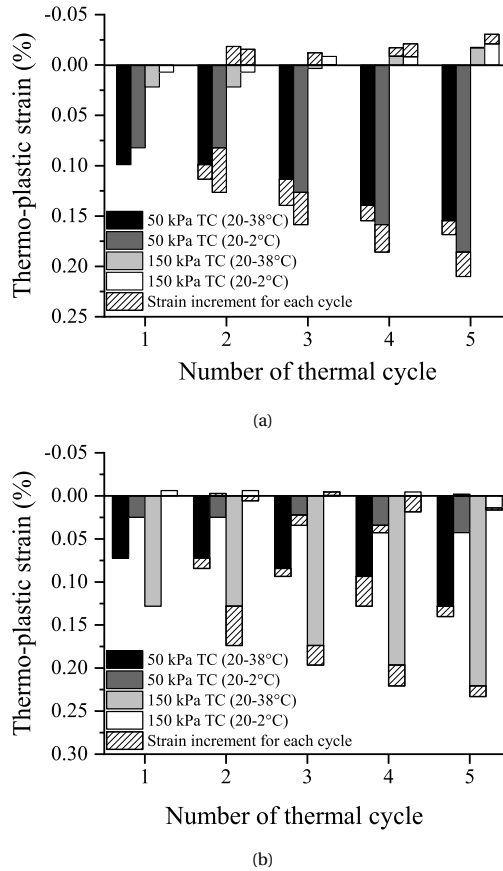
Figure 6.11: Accumulated thermo-plastic strain after the completion of each thermal cycle: (a) Sand–interface; (b) Clay–interface

lower rate. The thermo-plastic deformation for each cycle is plotted in Figure 6.11b. The thermo-elastic deformation became more visible in the 4–5 cycles (Figure 6.13a and Figure 6.13c) because of the lower plastic strains generated. As opposed to the thermal cycle effects observed in the sand-concrete interface samples, in clay-concrete interface samples, the higher vertical stress resulted in larger thermo-plastic strains.

After the heating/cooling cycles, the clay–concrete samples were sheared under CV conditions (resembling undrained conditions). The variation of shear stress against normal stress is shown in Figure 6.14a. To ensure the only variable between the parallel CV shearing tests was the thermal history, two isothermal specimens were consolidated under 150 kPa for 35h (equal to the duration of the thermal cycles) and 2h respectively. During shearing, the former behaved stiffer (the black line labelled with "20°C, 35h" in Figure 6.14b), indicating that the creep process does influence the subsequent shearing, and therefore was selected as the reference. Figure 6.14a shows that heating/cooling cycles have a significant effect on the clay–concrete interface and this effect is more pro-

(a)   (b)
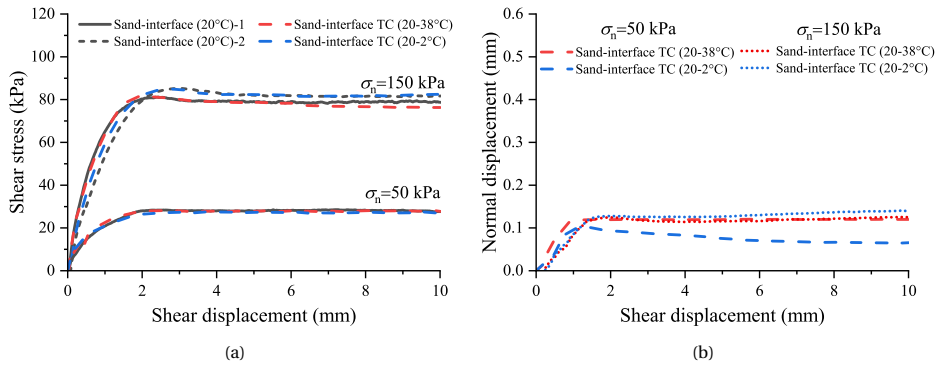
Figure 6.12: CNL results for sand–concrete interface after heating/cooling cycles: (a) shear stress vs. shear displacement; (b) normal displacement vs. shear displacement

(a)   (b)

(c)   (d)
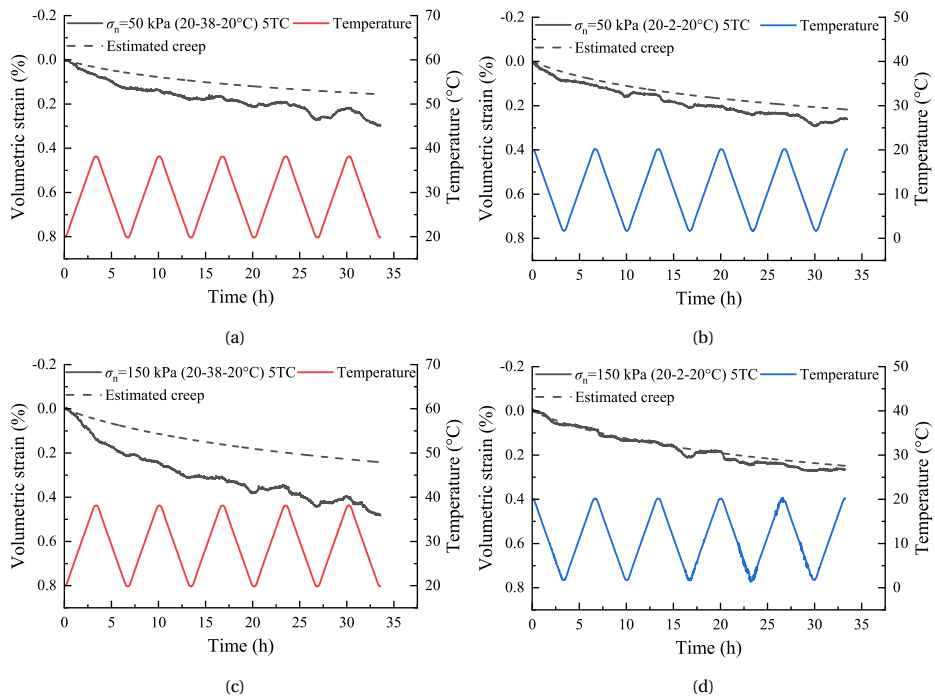
Figure 6.13: Volume change of clay–concrete interface during thermal cycles: **a** Heating cycles at 50 kPa; **b** Cooling cycles at 50 kPa; **c** Heating cycles at 150 kPa; **d** Cooling cycles at 150 kPa

nounced at higher stresses. All samples experienced a normal stress reduction during shearing, where the maximum change was in the isothermal sample and the minimum change was in the sample after heating cycles. The reduction of normal stress in the CV conditions imply contraction and therefore the generation of positive pore water pressures. Therefore, the shear stress versus (effective) normal stress curves of the interface

experiments resemble the stress path (deviatoric stress versus mean effective stress) of undrained triaxial experiments on clays samples [4; 9; 68–70]. The peak and residual failure envelopes obtained from isothermal tests (Figure 6.9e) are considered to fit well with the CV shear results. Therefore, the strength parameters of the clay–concrete interface are considered to be independent of the temperature history.

(a)

(b)
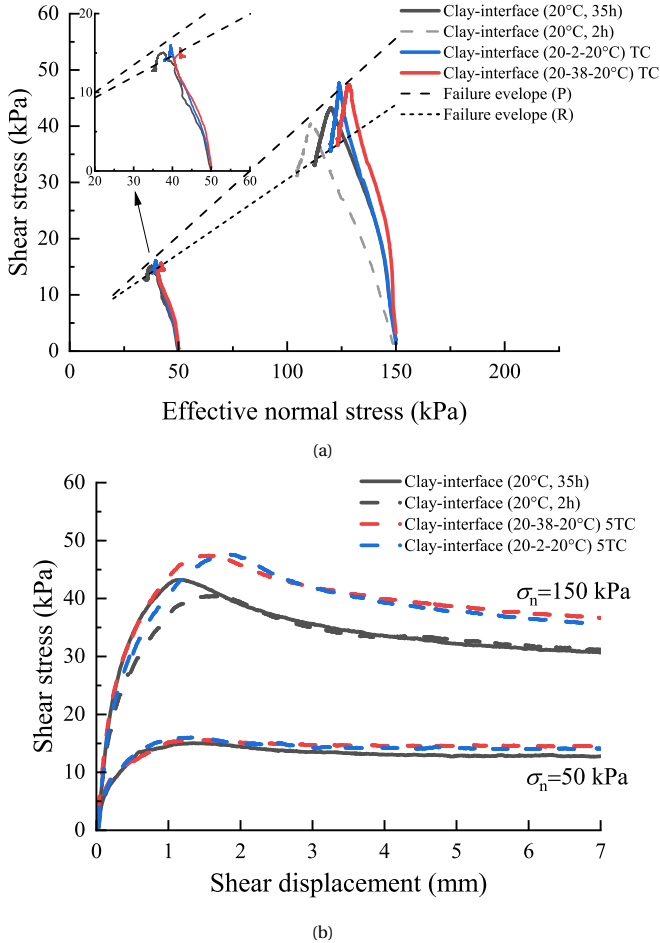
Figure 6.14: Constant-volume shearing results for clay–concrete interface tests after thermal cycles. (a) shear stress vs. effective normal stress; (b) shear stress vs. shear displacement. The labels "20ºC, 35h" and "20ºC, 2h" indicate the consolidation duration for the iso-thermal samples.

For the sample consolidated at a normal stress of 150 kPa and subjected to heating cycles (shown by red solid line), the stress path started to evolve vertically at the beginning of shearing before inclining towards the peak failure envelope. Based on Critical State soil mechanics, such a stress path implies a typical OC soil response, suggesting an expanded yield surface after heating cycles, and would imply lower pore pressure generation in field conditions. In contrast, the path after cooling cycles mostly overlapped

with the isothermal one, and the vertical stress decreased immediately after the shearing started. Such a trajectory, without the "*vertical*" segment, implies the stress state remains NC. It is assumed in many constitutive models (see [64; 71; 72] and Chapters 2 and 4 for example) that the yield surface will expand during drained heating, and therefore be larger when the soil returns to the ambient temperature, while cooling cycles would not alter the size of the yield surface. Therefore, it appears that the thermo-mechanical response of a clay–concrete interface may also be characterised in the framework of Critical State soil mechanics with a temperature-dependent yield surface.

6.5.4. Series III: Temperature effect on the cyclic shear response of soil–concrete interface layer

The sand–concrete interfaces were subjected to 30 two-way shearing cycles at three temperatures (2, 20 and 38°C). For clarity, only the results of cycle numbers 1, 5, 29 and 30 are presented in Figure 6.15a and Figure 6.15c. In the first cycle, for all temperatures, the maximum shear stress reached 88 kPa, which is similar to the value observed for the monotonic shearing tests. For the rest of the cycles, the shear stress decreased and then stabilised at 85 kPa. The shear responses at different temperatures were very similar indicating a negligible thermal effect of the shear strength and stiffness under cyclic CNL shearing.

The normal displacement against shear displacement forms a hysteresis loop (Figure 6.15c) and the sample volume continued to reduce as the cyclic shearing proceeded (Figure 6.15d). The net contraction at each shearing cycle decreased with increasing cycles and almost 60% of the contraction was accumulated in the first 5 cycles. Comparing the volume changes at different temperatures, the sand–concrete interface samples at 2 and 20°C, respectively, experienced the highest and the least accumulated volume reduction (Figure 6.15d). This may be for two reasons: temperature effects, and the slight differences in pre-shear void ratios, which were 0.821, 0.847 and 0.831, respectively, for the interface elements sheared at 20, 38 and 2°C. The sample sheared at 20°C had the smallest pre-shear void ratio and thus exhibited less contraction due to shearing. The interface sample sheared at 2°C, while having a lower pre-shear void ratio compared to the interface sample sheared at 38°C, experienced a higher volume change during cyclic shearing. This behaviour may reflect the effect of temperature on the volumetric behaviour.

The same test programme was performed on clay–concrete interface samples for 10 cycles and the results are shown in Figure 6.16. For all three interface specimens, sheared at 2, 20 and 38°C, the shear stresses peaked at 57 kPa and then decreased to 48 kPa at +4 mm within the first cycle (Figure 6.16a). As the shearing cycle continued, the peak shear stresses decreased to 46 kPa, with the residual shear stress stabilised at ± 37 kPa after the 3rd cycle (Figure 6.16b). Although the peak shear stresses were reached at different shear displacements in the first cycle (Figure 6.16a), the difference was eliminated in subsequent cycles (i.e., second, fifth and tenth cycles). Thus, the temperature influences on the cyclic peak shear and residual shear strengths are again observed to be insignificant.

The accumulated volume changes during the cycles are depicted in Figure 6.16c and Figure 6.16d. The volume change was significant at the beginning and then kept increasing with a lower rate as the shearing proceeded. Up to 60% of the total deformation was
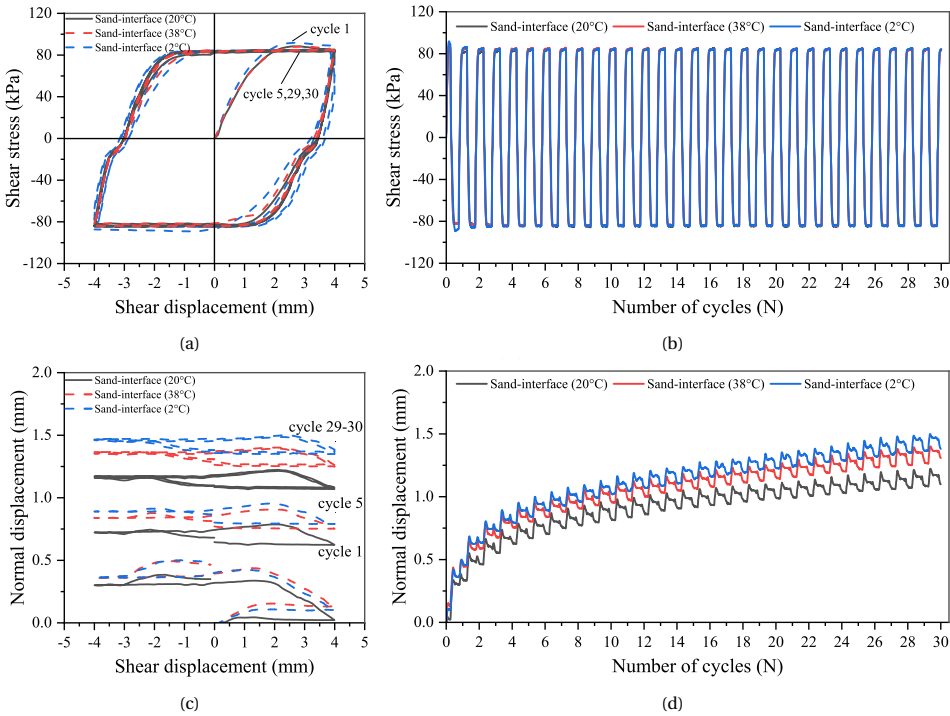
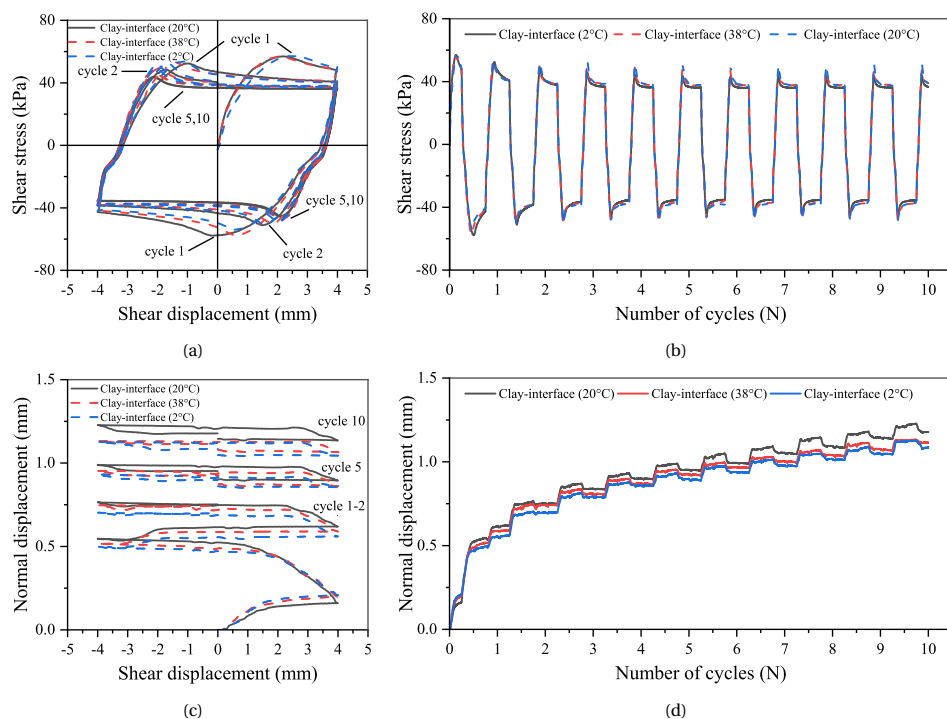Figure 6.15: Two-way cyclic shearing tests of sand–concrete interface at $T = 2, 20, 38°C$ under CNL (150 kPa) condition: (a) shear stress vs. displacement; (b) shear stress vs. cycle number; (c) normal displacement vs. shear displacement; (d) normal displacement vs. cycle number

accumulated within the first 1.5 cycles (Figure 6.16d). The specimen sheared at 20°C experienced the largest net contraction within most of the cycles. This result reflects that the temperature change could (partially) mitigate the contraction during cyclic shearing, while this was not observed in monotonic shearing (the first 1/4 cycle in Figure 6.16c). Note that the pre-shear void ratio for clay–concrete interface samples sheared at 20, 38 and 2°C were 0.959, 0.964 and 0.961 respectively, which would not explain this behaviour. This observation requires further confirmation before firm conclusions can be made.

6.5.5. Series IV: Temperature effect on cyclic shear response of soil–concrete interfaces with CNS boundary conditions

The test results of the sand–concrete interface for Series IV are summarised in Figure 6.17. Due to the relative contractive characteristic of medium-dense sand during shearing, the normal stress and mobilised shear strengths reduced significantly within the first 1–2 cycles (Figure 6.17a and Figure 6.17b) where most of the normal displacement occurred (Figure 6.17c). Similar stress paths were observed for tests at 2, 20 and 38°C. These stress paths varied inside a failure envelope (Figure 6.17a) and with a slope determined to be 0.56, which is identical to the stress ratio (τ/σ_n) derived from the cyclic CNL tests. Thus, the temperature is seen to have negligible influence on the cyclic friction angle
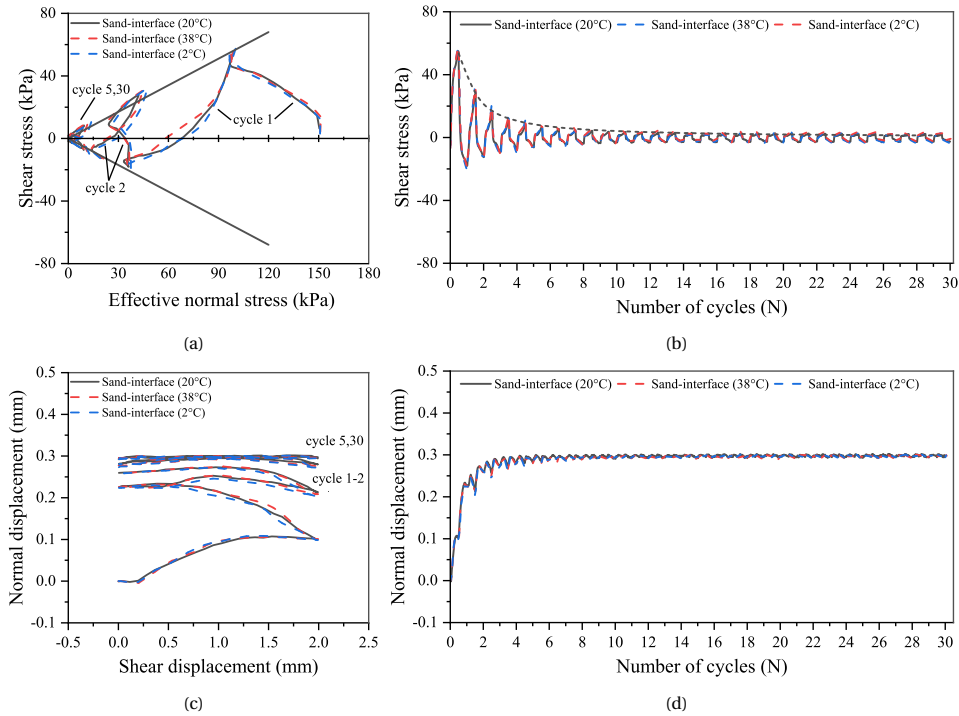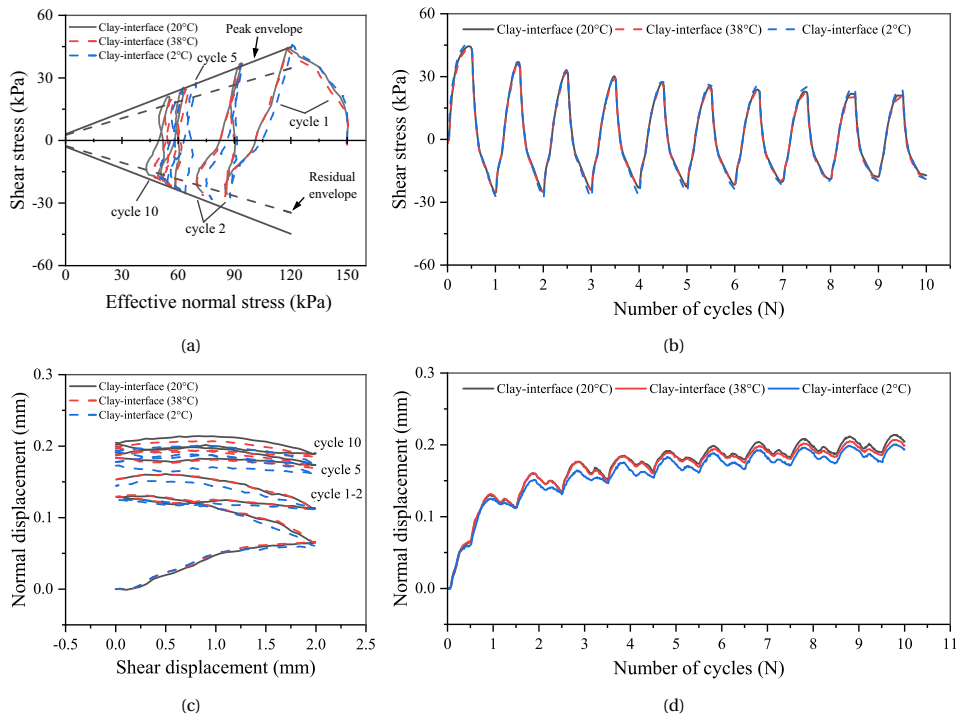
Figure 6.16: Two-way cyclic shearing tests of clay–concrete interface at $T = 2, 20, 38°C$ under CNL (150 kPa) condition: (a) shear stress vs. displacement; (b) shear stress vs. cycle number; (c) normal displacement vs. shear displacement; (d) normal displacement vs. cycle number

of the sand–concrete interface, regardless of the boundary conditions. The temperature effect on the volumetric response (Figure 6.17d) was not distinguishable because sand-interfaces tend to approach the e_{min} state of sand during cyclic CNS shearing [73]. Thus, for thermo-active geo-structures, the possible strength degradation/reduction of the sand–structure interface due to thermal effects may be neglected.

The shearing responses for the clay–concrete interface are shown in Figure 6.18. The normal stresses and shear stresses decreased gradually under CNS shearing (Figure 6.18a and Figure 6.18b). The stress paths under three levels of temperature were bounded at the peak shear stress envelope rather than the residual strength envelope (Figure 6.18a) derived from the monotonic tests (Figure 6.9e), indicating temperature-independent strength parameters in cyclic CNS shearing. The rate of degradation (Figure 6.18b) is far less than that of the sand-interface (Figure 6.17b), as the normal stress and shear stress of the sample sheared at 20°C remained at 56 kPa and 21 kPa, respectively, after 10 shearing cycles. Moreover, the degradation tended to stabilise in the last few cycles.

The stress paths of the samples sheared at 38 and 2°C (Figure 6.18a) converged with the stress path of the sample sheared at 20°C in the first 1–2 cycles, but progressively shifted towards the right side with increasing cycles suggesting a lower reduction in the normal stress, consistent with the observations made in Section 6.5.4. As the friction

Figure 6.17: One-way cyclic shearing tests of sand–concrete interface at $T = 2, 20, 38°C$ under CNS (500 kPa/mm) condition: (a) shear stress vs. displacement; (b) shear stress vs. cycle number; (c) normal displacement vs. shear displacement; (d) normal displacement vs. cycle number

angle remained unchanged, the shear stress degradation is closely associated with the volumetric behaviour at different temperatures (Figure 6.18c and Figure 6.18d). The pre-sheared void ratio cannot be overlooked to draw a rigorous statement on the temperature effect. Note that the void ratios before shearing were 0.964, 0.963, 0.948 for specimens sheared at 20, 38 and 2°C. The differences of the initial state between 20 and 38°C specimens can be safely ignored, and thus heating process can be again seen to partially mitigate the contraction during cyclic CNS shearing.

Figure 6.18: One-way cyclic shearing tests of clay–concrete interface at $T = 2, 20, 38°C$ under CNS (500 kPa/mm) condition: (a) shear stress vs. displacement; (b) shear stress vs. cycle number; (c) normal displacement vs. shear displacement; (d) normal displacement vs. cycle number

6.6. Conclusions

The shearing behaviour of soil-interfaces was investigated via a series of temperature-controlled direct shear tests. These were conducted within a temperature range of 2–38°C and a normal stress range of 50-150 kPa, thereby covering the most common operating conditions of GSHP applications. Based on this study, the following conclusions can be drawn:

1. The strength parameters of the sand and clay interface may reasonably be considered as constant within the relatively mild temperature range typical of energy-structure applications under various boundary conditions (e.g., CNL, CNS and CV) (e.g. see Figure 6.9).

2. Thermal cycles could introduce volume reduction to the interface layer, depending on the soil type, stress level, and thermal load direction. For sand–concrete interfaces, both heating and cooling cycles introduced plastic deformation under lower normal stress, but elastic deformation under higher normal stress (see Figure 6.10). For clay–concrete interfaces, heating cycles caused plastic deformation while cooling cycles did not, regardless of normal stress level, which is consistent

with the observed thermal behaviour of clays in oedometer and triaxial tests (see Figure 6.13).

3. The volumetric strains caused by temperature variation have minimal influence on the volumetric response of sandy specimens during monotonic shearing due to the insignificant strain magnitude; maximum 0.1% in monotonic thermal loading (see Figure 6.8) and maximum 0.23% in cyclic thermal loading) (see Figure 6.12).

4. After heating cycles, the stress paths from CV shearing of clay-interfaces exhibited a typical OC clay response during undrained shearing (see Figure 6.14a), and therefore indicated that a lower excess pore pressure would be generated, and implying a potential to be characterized in constitutive models with a temperature-dependent yield surface.

5. The cyclic movements between the structure and surrounding soil, induced by annual or daily temperature variations (corresponding to two-way cyclic CNL shearing and one-way cyclic CNS shearing, respectively) are shown to likely cause more significant effects at the interface compared with the direct temperature effects (see Figure 6.15 and Figure 6.16 for two-way cyclic shearing under CNL conditions and Figure 6.17 and Figure 6.18 for one-way cyclic shearing under CNS conditions). Such effects are more significant for one-way CNS tests, where a medium dense sand-concrete interface shear strength reached negligible values after 5 cycles, whereas a clay-concrete interface maintained 60% of its strength after 10 cycles.

6. The mechanical cyclic shearing tests indicated the possible progressive reduction of shaft friction, especially for sand–concrete interfaces (see Figure 6.17), and the consequences should be addressed in energy pile applications. For piles founded in sand, which are generally considered end-bearing, this impact may not significantly reduce the bearing capacity, but it may result in changes in stress redistribution over cycles and additional settlements. In floating piles, which rely on clay–concrete interface strength for both ultimate bearing capacity and settlements, this reduction in shear strength can be significant (see Figure 6.18). However, for long term loads (annual cycles), creep may increase the confining stresses and have a strengthening impact. The degree of such mechanical impacts will vary along the pile depending on the relatively distance to the null point and magnitude of the temperature change.

References

[1] Fang, J., Kong, G. and Yang, Q. Group performance of energy piles under cyclic and variable thermal loading. *Journal of Geotechnical and Geoenvironmental Engineering*, 148(8):04022060, 2022.

[2] Li, R., Kong, G., Chen, Y. and Yang, Q. Thermomechanical behaviour of an energy pile–raft foundation under intermittent cooling operation. *Journal of Geomechanics for Energy and the Environment*, 28:100240, 2021.

[3] Hueckel, T. and Baldi, G. Thermoplasticity of saturated clays: Experimental constitutive study. *Journal of Geotechnical Engineering*, 116(12):1778–1796, 1990.

[4] Kuntiwattanakul, P., Towhata, I., Ohishi, K. and Seko, I. Temperature effects on undrained shear characteristics of clay. *Soils and Foundations*, 35(1):147–162, 1995.

[5] Tanaka, N., Graham, J. and Crilly, T. Stress-strain behaviour of reconstituted illitic clay at different temperatures. *Engineering Geology*, 47(4):339–350, 1997.

[6] Burghignoli, A., Desideri, A. and Miliziano, S. A laboratory study on the thermomechanical behaviour of clayey soils. *Canadian Geotechnical Journal*, 37(4):764–780, 2000.

[7] Marques, M. E. S., Leroueil, S. and Soares de Almeida, M. S. Viscous behaviour of St-Roch-de-l'Achigan clay, Quebec. *Canadian Geotechnical Journal*, 41(1):25–38, 2004.

[8] Cekerevac, C. and Laloui, L. Experimental study of thermal effects on the mechanical behaviour of a clay. *International Journal for Numerical and Analytical Methods in Geomechanics*, 28(3):209–228, 2004.

[9] Abuel-Naga, H. M., Bergado, D. T. and Lim, B. F. Effect of temperature on shear strength and yielding behavior of soft Bangkok clay. *Soils and Foundations*, 47(3):423–436, 2007.

[10] Alsherif, N. A. and McCartney, J. S. Yielding of silt at high temperature and suction magnitudes. *Geotechnical and Geological Engineering*, 34(2):501–514, 2016.

[11] Yazdani, S., Helwany, S. and Olgun, G. Experimental evaluation of shear strength of Kaolin clay under cyclic and noncyclic thermal loading. *Geotechnical Testing Journal*, 42(6):1518–1548, 2018.

[12] Potyondy, J. G. Skin friction between various soils and construction materials. *Géotechnique*, 11(4):339–353, 1961.

[13] Yoshimi, Y. and Kishida, T. A ring torsion apparatus for evaluating friction between soil and metal surfaces. *Geotechnical Testing Journal*, 4(4):145–152, 1981.

[14] Uesugi, M. and Kishida, H. Frictional resistance at yield between dry sand and mild steel. *Soils and foundations*, 26(4):139–149, 1986.

[15] Tehrani, F. S., Han, F., Salgado, R., Prezzi, M., Tovar, R. D. and Castro, A. G. Effect of surface roughness on the shaft resistance of non-displacement piles embedded in sand. *Géotechnique*, 66(5):386–400, 2016.

[16] Martinez, A. and Frost, J. D. The influence of surface roughness form on the strength of sand–structure interfaces. *Géotechnique Letters*, 7(1):104–111, 2017.

[17] Uesugi, M., Kishida, H. and Uchikawa, Y. Friction between dry sand and concrete under monotonic and repeated loading. *Soils and Foundations*, 30(1):115–128, 1990.

6

[18] Paikowsky, S. G., Player, C. M. and Connors, P. J. A dual interface apparatus for testing unrestricted friction of soil along solid surfaces. *Geotechnical Testing Journal*, 18(2):168–193, 1995.

[19] Martinez, A., Frost, J. D. and Hebeler, G. L. Experimental study of shear zones formed at sand/steel interfaces in axial and torsional axisymmetric tests. *Geotechnical Testing Journal*, 38(4):1–18, 2015.

[20] Afzali-Nejad, A., Lashkari, A. and Shourijeh, P. T. Influence of particle shape on the shear strength and dilation of sand-woven geotextile interfaces. *Geotextiles and Geomembranes*, 45(1):54–66, 2017.

[21] Han, F., Ganju, E., Salgado, R. and Prezzi, M. Effects of interface roughness, particle geometry, and gradation on the sand–steel interface friction angle. *Journal of Geotechnical and Geoenvironmental Engineering*, 144(12):04018096, 2018.

[22] Lemos, L. J. L. and Vaughan, P. R. Clay–interface shear resistance. *Géotechnique*, 50(1):55–64, 2000.

[23] Farhadi, B. and Lashkari, A. Influence of soil inherent anisotropy on behavior of crushed sand-steel interfaces. *Soils and Foundations*, 57(1):111–125, 2017.

[24] Kishida, H. and Uesugi, M. Tests of the interface between sand and steel in the simple shear apparatus. *Géotechnique*, 37(1):45–52, 1987.

[25] Tsubakihara, Y. and Kishida, H. Frictional behaviour between normally consolidated clay and steel by two direct shear type apparatuses. *Soils and Foundations*, 33(2):1–13, 1993.

[26] Taha, A. and Fall, M. Shear behavior of sensitive marine clay-concrete interfaces. *Journal of Geotechnical and Geoenvironmental Engineering*, 139(4):644–650, 2013.

[27] DeJong, J. T. and Westgate, Z. J. Role of initial state, material properties, and confinement condition on local and global soil-structure interface behavior. *Journal of Geotechnical and Geoenvironmental Engineering*, 135(11):1646–1660, 2009.

[28] Fakharian, K. and Evgin, E. Cyclic simple-shear behavior of sand-steel interfaces under constant normal stiffness condition. *Journal of Geotechnical and Geoenvironmental Engineering*, 123(12):1096–1105, 1997.

[29] Porcino, D., Fioravante, V., Ghionna, V. N. and Pedroni, S. Interface behavior of sands from constant normal stiffness direct shear tests. *Geotechnical Testing Journal*, 26(3):289–301, 2003.

[30] Johnston, I. W., Lam, T. S. K. and Williams, A. F. Constant normal stiffness direct shear testing for socketed pile design in weak rock. *Géotechnique*, 37(1):83–89, 1987.

[31] Fioravante, V., Ghionna, V. N., Pedroni, S. and Porcino, D. A constant normal stiffness direct shear box for soil-solid surface interface tests. *Rivista Italiana di geotecnica*, 3:7–22, 1999.

6

[32] Fioravante, V. On the shaft friction modelling of non-displacement piles in sand. *Soils and Foundations*, 42(2):23–33, 2002.

[33] Airey, D. W., Al-Douri, R. H. and Poulos, H. G. Estimation of pile friction degradation from shearbox tests. *Geotechnical Testing Journal*, 15:388–388, 1992.

[34] Tabucanon, J. T., Airey, D. W. and Poulos, H. G. Pile skin friction in sands from constant normal stiffness tests. *Geotechnical Testing Journal*, 18(3):350–364, 1995.

[35] Takada, N. Mikasa's direct shear apparatus, test procedures and results. *Geotechnical Testing Journal*, 16(3):314–322, 1993.

[36] Sadrekarimi, A. and Olson, S. M. Shear band formation observed in ring shear tests on sandy soils. *Journal of Geotechnical and Geoenvironmental Engineering*, 136(2):366–375, 2010.

[37] Dyvik, R., Berre, T., Lacasse, S. and Raadim, B. Comparison of truly undrained and constant volume direct simple shear tests. *Géotechnique*, 37(1):3–10, 1987.

[38] Kong, G., Wu, D., Liu, H., Laloui, L., Cheng, X. and Zhu, X. Performance of a geothermal energy deicing system for bridge deck using a pile heat exchanger. *International Journal of Energy Research*, 43(1):596–603, 2019.

[39] Di Donna, A., Ferrari, A. and Laloui, L. Experimental investigations of the soil–concrete interface: Physical mechanisms, cyclic mobilization, and behaviour at different temperatures. *Canadian Geotechnical Journal*, 53(4):659–672, 2016.

[40] Wang, D., Lu, L. and Cui, P. Simulation of thermo-mechanical performance of pile geothermal heat exchanger (PGHE) considering temperature-depend interface behavior. *Applied Thermal Engineering*, 139:356–366, 2018.

[41] Vasilescu, A. R., Fauchille, A. L., Dano, C., Kotronis, P., Manirakiza, R. and Gotteland, P. Impact of temperature cycles at soil–concrete interface for energy piles. In *International Symposium on Energy Geotechnics*, pages 35–42. Springer, 2018.

[42] Maghsoodi, S., Cuisinier, O. and Masrouri, F. Thermal effects on mechanical behaviour of soil–structure interface. *Canadian Geotechnical Journal*, 57(1):32–47, 2020.

[43] Yavari, N., Tang, A. M., Pereira, J. M. and Hassen, G. Effect of temperature on the shear strength of soils and the soil–structure interface. *Canadian Geotechnical Journal*, 53(7):1186–1194, 2016.

[44] Li, C., Kong, G., Liu, H. and Abuel-Naga, H. Effect of temperature on behaviour of red clay–structure interface. *Canadian Geotechnical Journal*, 56(1):126–134, 2019.

[45] Ravera, E., Sutman, M. and Laloui, L. Cyclic thermomechanical response of fine-grained soil–concrete interface for energy piles applications. *Canadian Geotechnical Journal*, 58(8):1216–1230, 2021.

[46] Hashemi, A., Sutman, M. and Abuel-Naga, H. Thermomechanical response of kaolin clay–concrete interface in the context of energy geostructures. *Canadian Geotechnical Journal*, 60(3):380–396, 2023.

[47] Yazdani, S., Helwany, S. and Olgun, G. Influence of temperature on soil–pile interface shear strength. *Geomechanics for Energy and the Environment*, 18:69–78, 2019.

[48] Maghsoudloo, A., Askarinejad, A., De Jager, R. R., Molenkamp, F. and Hicks, M. A. Experimental investigation of pore pressure and acceleration development in static liquefaction induced failures in submerged slopes. In *Physical Modelling in Geotechnics*, pages 987–992. CRC Press, 2018.

[49] Zimnik, A. R., Van Baalen, L. R., Verhoef, P. N. W. and Ngan-Tillard, D. J. M. The adherence of clay to steel surfaces. In *ISRM International Symposium*, 2000.

[50] BS1377-2:1990. Methods of test for soils for civil engineering purposes: Classification tests. Standard, British Standards Institution, 1990.

[51] D3080/D3080M. Standard test method for direct shear test of soils under consolidated drained conditions. Standard, American Society for Testing and Materials, 2011.

[52] Hanzawa, H., Nutt, N., Lunne, T., Tang, Y. X. and Long, M. A comparative study between the NGI direct simple shear apparatus and the Mikasa direct shear apparatus. *Soils and Foundations*, 47(1):47–58, 2007.

[53] Knellwolf, C., Peron, H. and Laloui, L. Geotechnical analysis of heat exchanger piles. *Journal of Geotechnical and Geoenvironmental Engineering*, 137(10):890–902, 2011.

[54] Ng, C. W. W., Wang, S. H. and Zhou, C. Volume change behaviour of saturated sand under thermal cycles. *Géotechnique Letters*, 6(2):124–131, 2016.

[55] Uesugi, M., Kishida, H. and Tsubakihara, Y. Behavior of sand particles in sand–steel friction. *Soils and Foundations*, 28(1):107–118, 1988.

[56] Vasilescu, R., Yin, K., Fauchille, A. L., Kotronis, P., Dano, C., Manirakiza, R. and Gotteland, P. Influence of thermal cycles on the deformation of soil–pile interface in energy piles. In *E3S Web of Conferences*, volume 92, page 13004. EDP Sciences, 2019.

[57] Tsubakihara, Y., Kishida, H. and Nishiyama, T. Friction between cohesive soils and steel. *Soils and Foundations*, 33(2):145–156, 1993.

[58] Parchment, J. and Shepley, P. The influence of temperature on shear strength at a soil-structure interface. In *Physical Modelling in Geotechnics*, pages 149–154. CRC Press, 2018.

[59] Bhushan, B. Adhesion and stiction: Mechanisms, measurement techniques, and methods for reduction. *Journal of Vacuum Science & Technology B: Microelectronics and Nanometer Structures Processing, Measurement, and Phenomena*, 21(6):2262–2296, 2003.

6

[60] Golchin, A., Vardon, P. J. and Hicks, M. A. A thermo-mechanical constitutive model for fine-grained soils based on thermodynamics. *International Journal of Engineering Science*, 174:103579, 2022.

[61] Lade, P. V. and Liu, C. T. Experimental study of drained creep behavior of sand. *Journal of Engineering Mechanics*, 124(8):912–920, 1998.

[62] Mitchell, J. K. and Soga, K. *Fundamentals of soil behavior*, volume 3. John Wiley & Sons New York, 2005.

[63] Wu, Z. X., Yang, L., Wang, Z., Zhuang, Y. C. and Tu, D. M. A simple discrete-element model for numerical studying the dynamic thermal response of granular materials. *Materials Research Express*, 8(11):115502, 2021.

[64] Cui, Y. J., Sultan, N. and Delage, P. A thermomechanical model for saturated clays. *Canadian Geotechnical Journal*, 37(3):607–620, 2000.

[65] Zhou, C. and Ng, C. W. W. A thermomechanical model for saturated soil at small and large strains. *Canadian Geotechnical Journal*, 52(8):1101–1110, 2015.

[66] Radjai, F., Jean, M., Moreau, J. J. and Roux, S. Force distributions in dense two-dimensional granular systems. *Physical Review Letters*, 77(2):274, 1996.

[67] Sitharam, T. Discrete element modelling of cyclic behaviour of granular materials. *Geotechnical & Geological Engineering*, 21(4):297–329, 2003.

[68] Graham, J., Tanaka, N., Crilly, T. and Alfaro, M. Modified Cam-Clay modelling of temperature effects in clays. *Canadian Geotechnical Journal*, 38(3):608–621, 2001.

[69] Perkins, S. W. and Sjursen, M. Effect of cold temperatures on properties of unfrozen Troll clay. *Canadian Geotechnical Journal*, 46(12):1473–1481, 2009.

[70] Trani, L., Bergado, D. and Abuel-Naga, H. Thermo-mechanical behavior of normally consolidated soft Bangkok clay. *International Journal of Geotechnical Engineering*, 4(1):31–44, 2010.

[71] Hueckel, T. and Pellegrini, R. Effective stress and water pressure in saturated clays during heating–cooling cycles. *Canadian Geotechnical Journal*, 29(6):1095–1102, 1992.

[72] Laloui, L. and Cekerevac, C. Thermo-plasticity of clays: An isotropic yield mechanism. *Computers and Geotechnics*, 30(8):649–660, 2003.

[73] DeJong, J. T., White, D. J. and Randolph, M. F. Microscale observation and modeling of soil-structure interface behavior using particle image velocimetry. *Soils and Foundations*, 46(1):15–28, 2006.

APPENDIX

6.A. APPENDIX A: PRE-SHEARED VOID RATIO AND VOLUME CHANGE AFTER SHEARING FOR SERIES I

Table 6.2: Summary of pre-sheared void ratio and volume change after shearing for Series I, where e_o = void ratio before temperature variation, ΔV_s = volume change after shearing (+ for contraction, - for dilation)

Test	Material	Normal stress σ_n (kPa)	Thermal path	e_0	ΔV_s (mm)
1		50	20°C	0.836	-0.141
2		50	20-38°C	0.844	-0.084
3		50	20-2°C	0.857	-0.015
4		100	20°C	0.835	-0.054
5	Sand	100	20-38°C	0.850	-0.184
6		100	20-2°C	0.823	-0.089
7		150	20°C	0.811	-0.190
8		150	20-38°C	0.823	-0.126
9		150	20-2°C	0.813	-0.064
10		50	20°C	0.839	0.128
11		50	20-38°C	0.821	0.071
12		50	20-2°C	0.839	0.156
13		100	20°C	0.823	0.105
14	Sand–interface	100	20-38°C	0.837	0.218
15		100	20-2°C	0.821	0.056
16		150	20°C	0.824	0.166
17		150	20-38°C	0.826	0.162
18		150	20-2°C	0.826	0.158
19		50	20°C	1.015	0.129
20		50	20-38°C	1.055	0.166
21		50	20-2°C	1.058	0.186
22		100	20°C	0.979	0.192
23	Clay	100	20-38°C	1.037	0.345
24		100	20-2°C	1.017	0.307
25		150	20°C	0.984	0.361
26		150	20-38°C	0.977	0.395
27		150	20-2°C	0.979	0.291
28	Clay–concrete	50	20°C	1.063	0.212
29		50	20-38°C	1.047	0.137
30		50	20-2°C	1.022	0.103
31		150	20°C	0.967	0.179
32		150	20-38°C	0.962	0.177
33		150	20-2°C	0.945	0.212

6.B. APPENDIX B: CALIBRATION OF THE TEMPERATURE CONTROLLED DIRECT-SHEAR APPARATUS

The calibration of a modified direct-shear apparatus manufactured by Wille Geotechnik in response to temperature change is presented here.

The shear box was kept in a climate room fixed at constant room temperature and was carefully insulated to minimise thermal exchanges with the surroundings, although temperature changes are induced during the testing which had the potential to affect the sensor readings. In addition, consequential thermal expansion/contraction of the system may occur. Therefore, the system was calibrated for changes of temperature.

CALIBRATION OF THE LVDT

The vertical displacements of samples subjected to mechanical and thermal loads, are recorded via a vertical LVDT. An iron dummy sample (with known coefficient of thermal expansion) of 32 mm height was installed in the shear box and a 50 kPa vertical stress was applied to ensure a full contact between the sample and the load cell. Subsequently, the sample was subjected to thermal cycles between 2°C and 38°C (covering the temperature range studied in this work) with a relatively slow rate of 5°C/h, and displacements were recorded. The readings of the LVDT with the thermo-elastic deformations of the dummy sample subtracted, along with temperature variation, are shown in Figure 6.19a. The recorded vertical displacement variation accounted for the thermal deformation from the components of the apparatus plus any temperature shift of the readings. The variation was seen to have an almost linear relationship with the temperature change and resulted in no apparent accumulation after thermal cycles. Therefore, all records from the vertical LVDT in this study were calibrated by a linear temperature calibration factor. For the horizontal LVDT, it changed by less than 0.002 mm during these thermal cycles and thus no calibration was necessary.
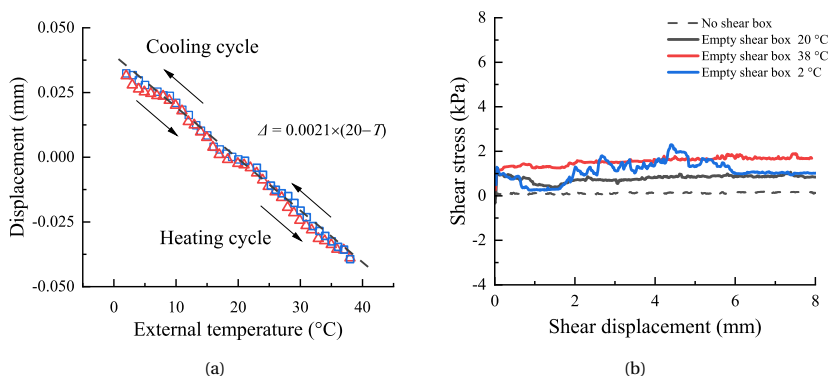
Figure 6.19: Calibration of the apparatus: (a) vertical LVDT under thermal cycle; (b) shear stress under test temperature

Two shear tests were conducted at ambient temperature (20°C), with and without using the (empty) shear box, followed by two shear tests using the empty shear box at 2°C and 38°C. For the test without shear box, the shear box was disassembled then shear test was conducted. The recorded shear stress accounted for the friction on the actuator motor. For the tests using the empty shear box, the load cap was lowered inside the shear box, filled with water, and insulated to minimise thermal losses. Then, after reaching the desired temperatures (with a thermal rate of 5°C/h), shearing continued to 10 mm. The measured shear stresses against shear displacements are presented in Figure 6.19b. It is demonstrated that for the shear test without using the shear box (dashed line in Figure 6.19b), the measured shear stress is negligible and remains almost constant (less than 0.05 kPa fluctuation) during the test. The test result with an empty shear box at ambient conditions yielded a mean shear stress of 0.90 kPa, which should be subtracted from the readings of the shear stress to extract the actual stress carried by the soil sample. For the shear tests with the empty shear box at 2°C and 38°C, it can be seen that the shear stress readings deviate by about 0.95 kPa and 1.73 kPa, respectively, from the test without the shear box. These values are subtracted from the measured shear stresses during data processing.

6.C. APPENDIX C: EXAMPLES OF THE PRIMARY CONSOLIDA-TION
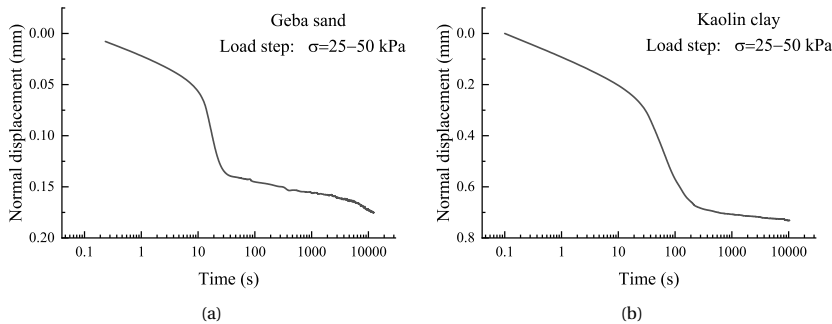
Figure 6.20: Examples of the primary consolidation process for the two soils: (a) Geba sand; (b) Kaolin clay

7

SHEAR CREEP BEHAVIOUR OF SOIL-STRUCTURE INTERFACES UNDER THERMAL CYCLIC LOADING

The coupling effect of initial shear stress and thermal cycles on the thermomechanical behaviour of clay- and sand-concrete interfaces was studied. A set of drained monotonic direct shear tests was conducted at the soil-concrete interface level. Samples were initially sheared to half of the material's shear strength and then they were subjected to 5 heating/cooling cycles before being sheared to failure. The test results showed that the effect of thermal cycles on the shear strength of the materials was negligible, yet shear displacement occurred during application of thermal cycles without an increase in shear stress, confirming the coupling between the initial shear stresses and temperature. In addition, a slight increase of stiffness due to the coupling was observed which diminished on further shearing.

7.1. INTRODUCTION

Several investigations have been carried out to study the effect of thermal cycles on the behaviour of soil-structure interfaces (see [1–8] and Chapter 6 for example). In general, thermal cycles were found to have a limited effect on the soil-interface strength and deformation. However, previous studies mostly considered the effect of thermal cycles without initial shear stresses being applied. In energy geo-structures, due to the structural loads, interfaces are likely to be subjected to mechanical (shear) loads prior to application of the thermal loads. In this chapter, the coupling effects of thermal cycles with constant shear stresses on the behaviour of soil-structure interfaces are investigated, which is one of the first studies investigating this phenomenon.

Direct shear element tests have been used here as they resemble the mechanism of shear strength mobilisation at the interface layer between soil and structures [9] and may mimic many boundary conditions (BCs) that are applied on interface layers, affecting the mechanical behaviour of the interface layer. In this work, as the most significant temperature cycles in thermo-active geo-structures are annual and the aim is to illustrate fundamental material behaviour, rather than a problem specific behaviour, CNL conditions are selected.

7.2. EXPERIMENTAL SETUP AND MATERIALS

The experimental setup, calibration of the thermomechanical apparatus, material used for the thermomechanical tests, and specimen preparation method are similar to those explained in Chapter 6 and are described in detail in Sections 6.2 and 6.3.

7.3. EXPERIMENTAL PROGRAMME

A set of tests was designed to resemble the thermomechanical loading paths of thermo-active geo-structures already subjected to shear stresses, as indicated by the loading paths presented in Figure 7.1. Samples at ambient temperature (20°C) were firstly consolidated to the desired normal stresses (50 kPa and 150 kPa, corresponding to paths O–A_1 and O–A_2, respectively). With the normal stresses held constant, the samples were then sheared using stress-controlled loading to half of the shear strength (τ_f) on the soil-concrete interface; i.e., the ratio of mobilised shear stress (τ) to shear strength (τ/τ_f) reached 0.5 (paths A_1–B_1 and A_2–B_2, respectively, for tests at σ_n =50 kPa and σ_n = 150 kPa). The shear strength values had been obtained by monotonic shearing (at the desired normal stress). Clay- and sand-concrete interfaces were sheared at rates of 0.12mm/min and 0.25mm/min, respectively. Samples were then left for 3 hours (on average) to allow creep behaviour to evolve. Then, starting from room temperature (20°C), with the shear stress kept constant, samples were subjected to 5 heating cycles (20–38–20°C) or 5 cooling cycles (20–2–20°C). Clay- and sand-concrete interfaces were subjected to temperature changes at 3°C/h and 9°C/h, respectively. Finally, at ambient (room) temperature, the samples were sheared to failure under constant normal stress loading (CNL) conditions (paths B_1–C_1 and B_2–C_2).
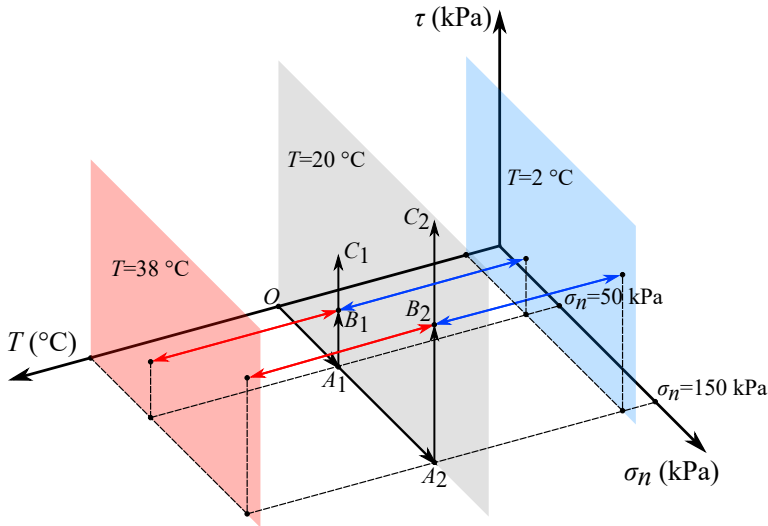
Figure 7.1: Thermomechanical stress path of the experimental programme; heating cycles and cooling cycles are shown, respectively, by red and blue arrows

7.4. RESULTS AND DISCUSSION

The evolution of total shear displacements recorded for the clay- and sand-concrete interfaces when subjected to thermal cycles (with an initially applied shear stress which is kept constant) are shown in Figure 7.2 and Figure 7.3, respectively. It is observed that, for both types of soil, the displacement increased with time. Before being subjected to thermal cycles, the temperature of the samples was kept at 20°C for approximately two hours. The solid vertical line (shown in green) in Figure 7.2 and Figure 7.3 indicates when the thermal cycles began. Before starting the thermal cycles, the measured displacement of all samples exhibited an almost logarithmic correlation with time (i.e., the measured displacement between Time = 0 and the solid line). The shear displacement induced by creep (i.e., with respect to time) was then extrapolated by extending the logarithmic curve fitted to the initial phase of the shear displacement versus time curve.

The sample void ratios prior to applying the shear stress, after applying the shear stress and immediately before applying the thermal cycles, and after applying the thermal cycles are presented in Table 7.1. Table 7.2 presents the measured shear displacements at different stages of the thermomechanical loading paths, including at $\tau/\tau_f = 0.5$ (i.e. under the initial shear stress), and at the beginning and end of the thermal cycles. Note that shear displacements due to creep are also included in Table 7.2. The percentage ratio (R_a) of the measured shear displacement during the thermal cycles (ΔL_{TC}) over the measured shear displacement at $\tau/\tau_f = 0.5$ (L_S) for the clay- and sand-concrete interfaces were higher at $\sigma_n = 50$ kPa compared to $\sigma_n = 150$ kPa. For clay-concrete interfaces, R_a varied approximately between 30% and 33% at $\sigma_n = 50$ kPa, and between 21% and 25% at $\sigma_n = 150$ kPa. For sand-concrete interfaces, the corresponding values were lower, with Ra varying approximately between 17% and 19% at $\sigma_n = 50$ kPa, and between

13% and 16% at $\sigma_n = 150$ kPa.

The net shear displacement evolution due to thermal effects was then calculated as the difference between the recorded shear displacement and the estimated shear displacement due to creep. Figure 7.4 shows the percentage ratio (R_{na}) of the net accumulated temperature induced shear displacement over the corresponding L_S with respect to the number of thermal cycles. The results show that additional shear displacement (approximately between 13% and 22% of the shear displacement at the initial shear stress of $\tau/\tau_f = 0.5$ for clay-concrete interfaces and approximately between 6% and 11% of the shear displacement at the initial shear stress of $\tau/\tau_f = 0.5$ for sand-concrete interfaces) took place at both the clay- and sand-concrete interfaces as a consequence of temperature variation occurring with a constant shear stress, with most additional shear displacement occurring within the first two thermal cycles. Note that, for most samples, the net shear displacement due to temperature variation increased during heating, whereas it became steadier (or slightly reduced) when the temperature decreased.

After the thermal cycles were completed, the specimens were further sheared until failure. The shear stress versus shear displacement curves for the entire process (paths $A_1–C_1$ and $A_2–C_2$) for clay- and sand-concrete interfaces, respectively, are presented in Figure 7.5 and Figure 7.6, and are compared with monotonic soil-interface shearing results at ambient temperature in order to identify the changes of ultimate shear strength due to thermal cycles. It is observed that the effect of coupling between thermal cycles and initial shear stress on the peak and Critical State shear strengths, for both types of soil interfaces, was negligible.

The specimens after thermal cycles initially behaved more stiffly (zones A and B in Figure 7.5 and Figure 7.6), with the tangent to the shear stress versus shear displacement curves being higher after thermal cycles compared to the corresponding slope before thermal cycles. Such reinforcement was destroyed after a further slight shearing (shear displacements less than 0.1 mm for both types of soil interface) and the stiffnesses returned to a similar level to those of specimens monotonically sheared at ambient temperature.

Table 7.1: Void ratio at different stages of thermomechanical loading paths

	Normal stress, σ_n (kPa)	Thermal cycles	e_{con}	e_{S_ini}	e_{TC_ini}	e_{TC_end}
	50	Heating	1.248	1.056	1.046	1.041
Clay-concrete	50	Cooling	1.270	1.051	1.047	1.040
interface	150	Heating	1.262	0.945	0.935	0.925
	150	Cooling	1.263	0.991	0.981	0.977
	50	Heating	0.837	0.782	0.769	0.766
Sand-concrete	50	Cooling	0.835	0.780	0.761	0.759
interface	150	Heating	0.820	0.728	0.706	0.699
	150	Cooling	0.825	0.733	0.721	0.717
e_{con}: Initial void ratio (i.e. void ratio before consolidation)						
e_{S_ini}: Void ratio before applying shear stress to $\tau/\tau_f = 0.5$						
e_{TC_ini}: Void ratio before applying thermal cycles						
e_{TC_end}: Void ratio after applying thermal cycles						

Table 7.2: Shear displacement at different stages of thermomechanical loading paths

	Normal stress, σ_n (kPa)	Thermal cycles	L_S (mm)	L_{TC_ini} (mm)	L_{TC_end} (mm)	ΔL_{TC} (mm)	R_a (%)
Clay-concrete interface	50	Heating	0.40	0.42	0.55	0.13	32.5
	50	Cooling	0.20	0.24	0.30	0.06	30
	150	Heating	0.58	0.64	0.76	0.12	20.7
	150	Cooling	0.44	0.48	0.59	0.11	25
Sand-concrete interface	50	Heating	0.37	0.38	0.45	0.07	19
	50	Cooling	0.41	0.46	0.53	0.07	17
	150	Heating	0.63	0.64	0.72	0.08	12.7
	150	Cooling	0.50	0.51	0.59	0.08	16

L_S: Shear displacement at $\tau/\tau_f = 0.5$
L_{TC_ini}: Shear displacement at the beginning of thermal cycles
L_{TC_end}: Shear displacement at the end of thermal cycles
ΔL_{TC}: Shear displacement during thermal cycles (= L_{TC_end} - L_{TC_ini})
R_a: Percentage of the measured shear displacement during thermal cycles with respect to the measured shear displacement at τ/τ_f=0.5 (= $\Delta L_{TC}/L_S \times 100$)

(a)

(b)

(c)

(d)
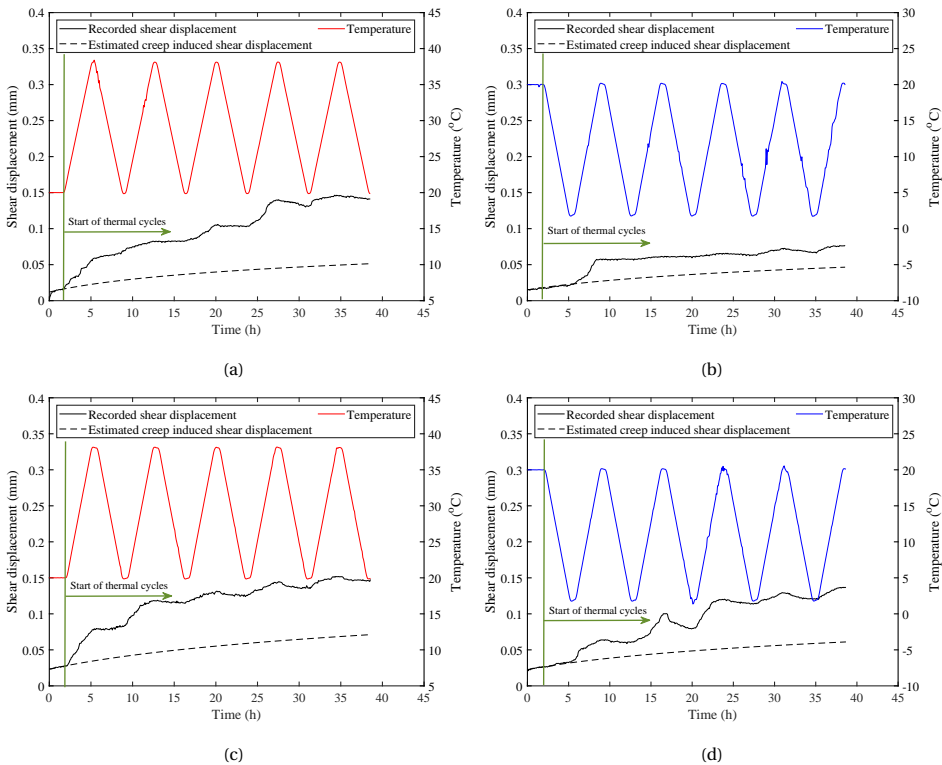
Figure 7.2: Evolution of shear displacement of clay-concrete interface during thermal cycles: (a) heating cycles at σ_n = 50 kPa; (b) cooling cycles at σ_n = 50 kPa; (c) heating cycles at σ_n = 150 kPa; (d) cooling cycles at σ_n = 150 kPa

Figure 7.3: Evolution of shear displacement of sand-concrete interface during thermal cycles: : (a) heating cycles at $\sigma_n = 50$ kPa; (b) cooling cycles at $\sigma_n = 50$ kPa; (c) heating cycles at $\sigma_n = 150$ kPa; (d) cooling cycles at $\sigma_n = 150$ kPa

For the first time, the phenomenon of shear displacements of soil-concrete interfaces under thermal cycles, where the interface is subjected to a constant shear stress, has been observed. The process is complex and may be explained by utilising and combining several aspects of existing knowledge on the thermomechanical mechanism of sands and clays, the micro- and macro-mechanical interaction between soil grains, and energy generation and dissipation (energy level changes) at the interface level (thermodynamics perspective).

The "*interface layer*" between soils and structures (in this study, a soil-concrete interface) is a thin layer of the soil that is in contact with the structure. Therefore, the thermomechanical behaviour of soils may (partially) govern the thermomechanical behaviour of the interface layer.

The thermomechanical behaviour of saturated sandy soils is mostly dominated by the difference in the volumetric thermal expansion coefficients between the soil particles and water, as well as the change in the viscosity of water due to temperature variation [10; 11].

On the other hand, the thermomechanical behaviour of saturated fine-grained soils, especially clayey soils, is dominated by physicochemical internal forces which

result in changes in the thickness of the hydration layers of soil particles, and the development of "*disjoining pressures*" (see 2 for more details). In addition, Houhou et al. [12] demonstrated that thermal loads affect the microstructure of clayey soils which are formed by clay particles and pores between them (pores varying in size; i.e., micro- and macro-size, and density). Due to thermal loads, macro-size pores may collapse which consequently may reduce in size and/or may experience a change in their density, resulting to volume change, while micro-size pores are less affected or remain intact [12]. In both of these cases (sands and clays), the cyclic thermal loads impact the force chains on a micro-scale allowing additional shear deformation to occur under constant shear stresses when subjected to thermal cycles.

In addition, the micro- and macro-mechanics at the interface level significantly affect the mechanical response of the interface layer. The initial shear loading induces shear forces/stresses between the soil particles. The normalised roughness between the soil and the structure also influences the level of mobilised forces/stresses; larger values of normalised roughness result in higher mobilised forces/stresses at the interface layer and potentially failure through the soil, not at the interface. In this work, an intermediate roughness of the interface is found , which implies that failure at the interface and in the soil at the same time is likely to occur (see Chapter 6). In such a case, the representative volume element (RVE) of the material in contact with the structure (at the interface level) may be considered to be comprised of two fractions associated with strong and weak force chains [13], where the majority of the shear deformations (plastic deformations) occur in the fraction of the RVE corresponding to weak force chains as a result of inter-grain slippage and rotation [14; 15].

(a)

(b)
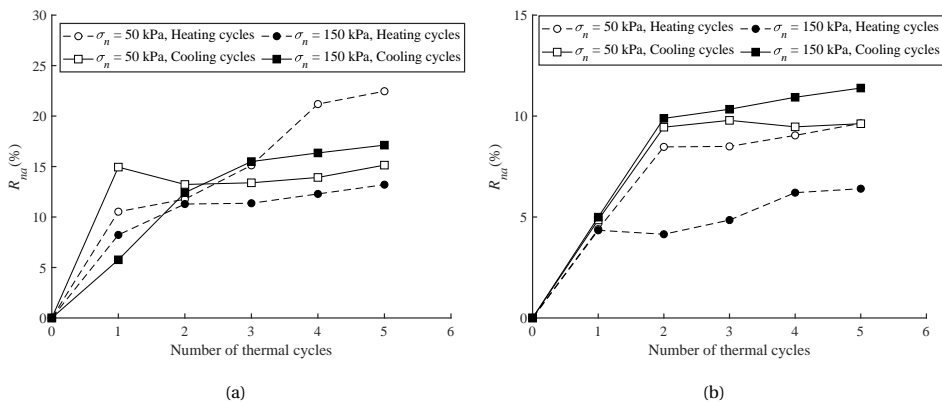
Figure 7.4: R_{na}: (a) clay-concrete interfaces; (b) sand-concrete interfaces
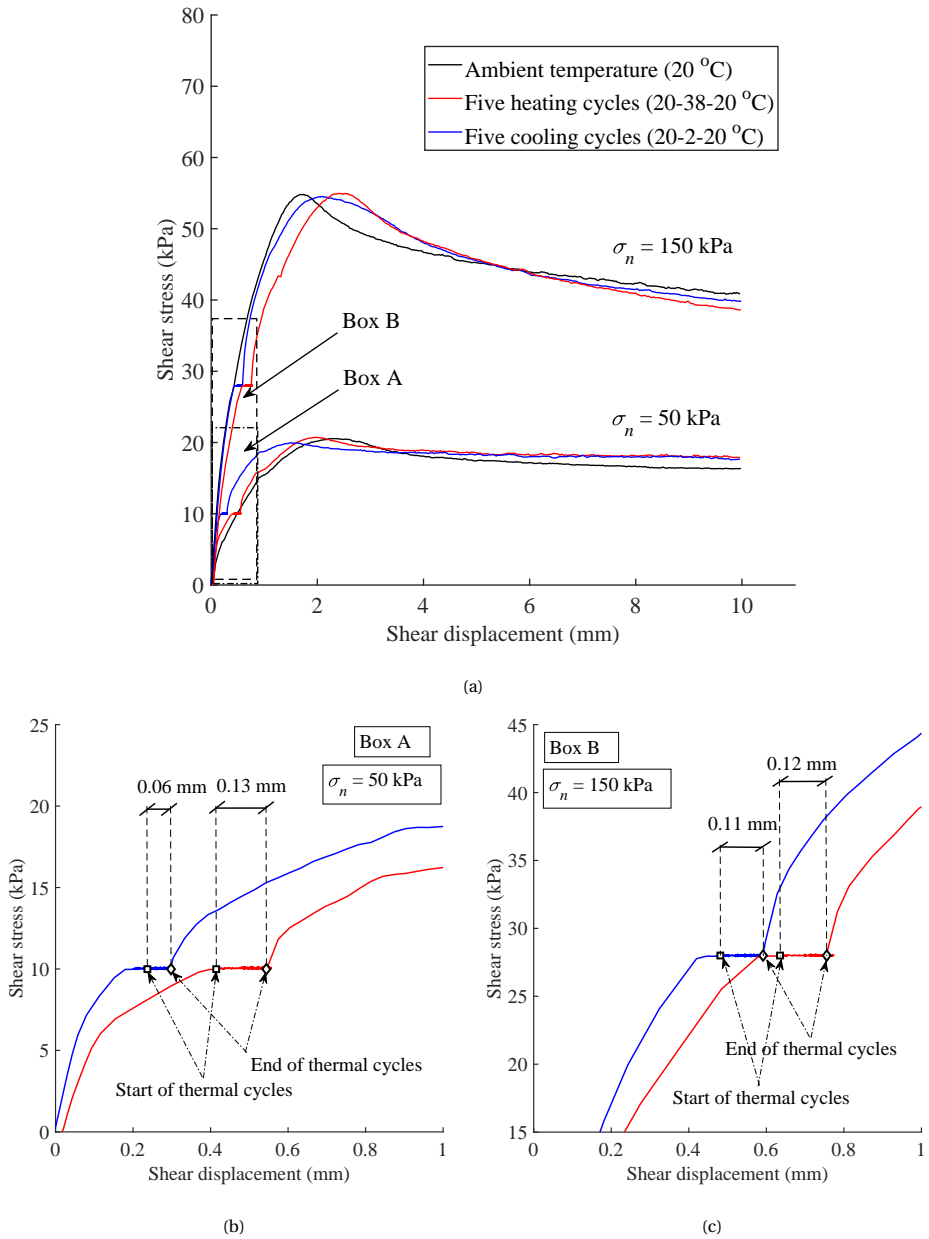
Figure 7.5: Shear stress versus shear displacement of clay-concrete interface: (a) all specimens; (b) magnified box A for the samples at $\sigma_n = 50$ kPa; (c) magnified box B for the samples at $\sigma_n = 150$ kPa
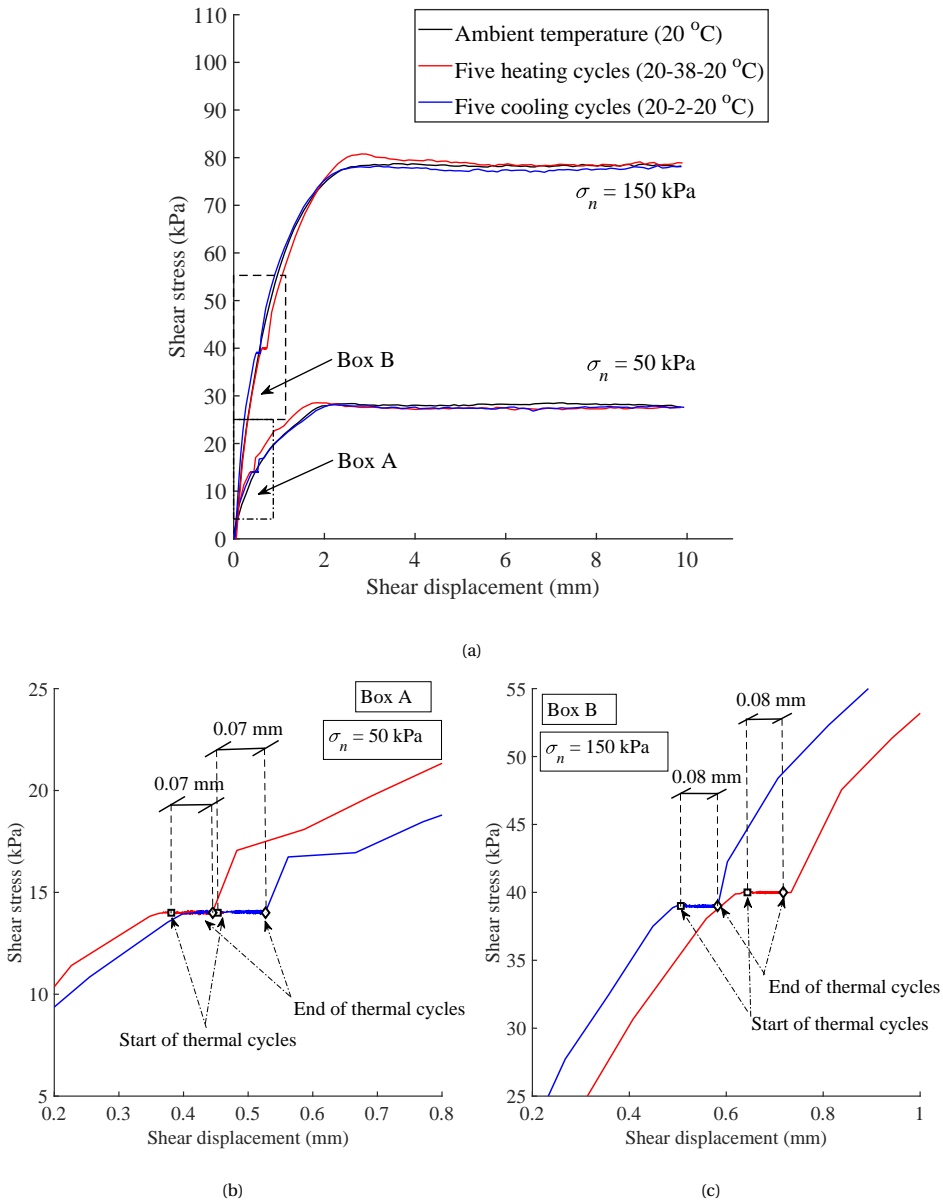
Figure 7.6: Shear stress versus shear displacement of sand-concrete interface: (a) all specimens; (b) magnified box A for the samples at $\sigma_n = 50$ kPa; (c) magnified box B for the samples at $\sigma_n = 150$ kPa

When the temperature changes at the interface level, due to governing thermome-chanical mechanisms (e.g. development of disjoining pressures for clayey soils and thermal expansion of particles and water for sandy soils), the macro-size pores in the fraction of the material associated with weak force chains may collapse. Consequently, the thermodynamically stable state of the soil can be prone to a thermodynamically unstable state. At the thermodynamically unstable state caused by heating, soil particles rotate and reorient temporarily (mostly in the fraction associated with weak force chains), which results in the observed evolution of shear displacement. This process continues until soil particles attain a sufficient number of contacts with adjacent particles and sufficient interlocking stresses are mobilised. Consequently, a new thermodynamically stable state is reached. The increase in the interlocking stresses, and in the area and number of contacts between particles, forms a new micro- and macro-mechanical structure inside the soil with macro-size pores reduced in size compared to before thermal loading. After several thermal cycles, the size of the macro-size pores are sufficiently reduced so that they may not be affected by thermal loads, leading to a cessation in shear displacement development which is consistent with the observed experimental results. This mechanism may be the main reason for the observed stiffer behaviour of the shearing after thermal cycles were applied to the soil (Figure 7.5 and Figure 7.6).

7.5. CONCLUSION

To investigate the thermomechanical stress and temperature histories that soils experience at the interface level of thermo-active geo-structures such as energy-piles, a set of experiments were conducted to investigate the coupling effect of shear stress and thermal cycles on the behaviour of soil-concrete interfaces. Samples were sheared to half of the interface's shear strength prior to being subjected to 5 heating/cooling cycles. The results indicated that shear displacements evolved when soil-concrete interfaces were subjected to thermal cycles, although only negligible changes in shear strength were observed. This is an important observation which should be considered in the design procedure of thermo-active structures. The observed temperature-induced shear displacements under constant shear stresses may result in additional and unwanted settlements during the serviceability life-time of these structures, especially for those whose main load-transfer mechanism to the soil and bearing capacity are through skin-friction mobilisation such as floating piles. Although a slight increase of stiffness was observed after thermal cycles under constant shear stresses, due to the newly formed micro- and macro-mechanical structures in the soil, these structures appear to be destroyed by subsequent shearing due to additional loading.

REFERENCES

[1] Di Donna, A., Ferrari, A. and Laloui, L. Experimental investigations of the soil–concrete interface: physical mechanisms, cyclic mobilization, and behaviour at different temperatures. *Canadian Geotechnical Journal*, 53(4):659–672, 2016.

[2] Guo, Y., Golchin, A., Vardon, P. J., Liu, S., Zhang, G. and Hicks, M. A. Supplementary material to "Soil-structure interface behaviour under monotonic and cyclic thermal

loading". *Acta Geotechnica*, 2023.

[3] Li, C., Kong, G., Liu, H. and Abuel-Naga, H. Effect of temperature on behaviour of red clay–structure interface. *Canadian Geotechnical Journal*, 56(1):126–134, 2019.

[4] Maghsoodi, S., Cuisinier, O. and Masrouri, F. Thermal effects on mechanical behaviour of soil–structure interface. *Canadian Geotechnical Journal*, 57(1):32–47, 2020.

[5] Ravera, E., Sutman, M. and Laloui, L. Cyclic thermomechanical response of fine grained soil concrete interface for energy piles applications. *Canadian Geotechnical Journal*, 58(8):1216–1230, 2021.

[6] Vasilescu, A. R., Yin, K., Fauchille, A. L., Kontronis, P., Dano, C., Manirakiza, R. and Gotteland, P. Influence of thermal cycles on the deformation of soil-pile interface in energy piles. In *E3S Web Conference*, 2019.

[7] Yavari, N., Tang, A. M., Pereira, J. M. and Hassen, G. Effect of temperature on the shear strength of soils and the soil–structure interface. *Canadian Geotechnical Journal*, 53(7):1186–1194, 2016.

[8] Yazdani, S., Helwany, S. and Olgun, G. Influence of temperature on soil–pile interface shear strength. *Geomechanics for Energy and the Environment*, 18:69–78, 2019.

[9] Boulon, M. and Foray, P. Physical and numerical simulation of lateral shaft friction along offshore piles in sand. In *Third International Conference on Numerical methods in offshore piling*, pages 127–147, Nantes, 1986.

[10] Russell Coccia, C. J. and McCartney, J. S. A thermo-hydro-mechanical true triaxial cell for evaluation of the impact of anisotropy on thermally induced volume changes in soils. *Geotechnical Testing Journal*, 35(2):103803, 2012.

[11] Vega, A. and McCartney, J. S. Cyclic heating effects on thermal volume change of silt. *Environmental Geotechnics*, 2(5):257–268, 2015.

[12] Houhou, R., Sutman, M., Sadek, S. and Laloui, L. Microstructure observations in compacted clays subjected to thermal loading. *Engineering Geology*, 287:105928, 2021.

[13] Collins, I. F. Elastic/plastic models for soils and sands. *International Journal of Mechanical Sciences*, 47(4-5):493–508, 2005.

[14] Radjai, F., Jean, M., Moreau, J. J. and Roux, S. Force distributions in dense two-dimensional granular systems. *Physical Review Letters*, 77(2):274–277, 1996.

[15] Radjai, F., Wolf, D. E., Jean, M. and Moreau, J. J. Bimodal character of stress transmission in granular packings. *Physical Review Letters*, 80(1):61–64, 1998.

7

8

CONCLUSIONS AND FUTURE WORK

8.1. INTRODUCTION

The short- and long-term performances of thermo-active geo-structures such as energy-piles impose a complex set of mechanical and thermal loads on the soil surrounding the structure. These loads may significantly affect the behaviour of the soil and consequently, may influence the performance of the soil-structure system so that additional safety criteria may need to be considered. The goal of this thesis was to advance insights into the main mechanisms governing the thermomechanical behaviour of soils and soil-interfaces, and to incorporate them in thermomechanical constitutive models which further can be used to develop numerical tools to facilitate studying thermo-active geo-structure applications such as energy-piles. To achieve this goal, thermomechanical constitutive models were developed, a numerical algorithm was proposed to implement the constitutive models in boundary-value solvers, and direct shear tests were conducted to understand the thermomechanical behaviour of soil-structure interfaces. The main conclusions from the core chapters of the thesis (Chapters 2-7) are synthesised in the following section, and these are followed by an overview of potential future research.

8.2. SINGLE SURFACE THERMOMECHANICAL CONSTITUTIVE MODEL FOR FINE-GRAINED SOILS

In Chapter 2, a thermomechanical constitutive model which was developed based on the thermodynamical framework of Hyperplasticity-Hyperelasticity. The model was formulated with the introduction of a Gibbs-type energy potential and a newly proposed rate of dissipation potential. Through using the energy potential, a non-linear thermo-elasticity relationship was derived. The newly proposed rate of dissipation potential resulted in a flexible yield surface which resembles the yield surface proposed by Collins & Hilder [1], but with a simpler formulation (by eliminating shift stress components) and embedded phenomenological temperature effects on the volumetric and shear be-

haviour of fine-grained soils, observed in laboratory-scale tests. Moreover, due to the presence of stress components in the definition of the rate of dissipation potential, a non-associated flow rule was derived, without introducing a plastic potential similar to conventional elasto-plastic constitutive models. All parameters of the model (12 or as low as 10) may be calibrated based on conventional geotechnical laboratory tests. In addition, a descriptive physicochemical micro-scale mechanism was presented to explain how phenomenological thermoemchanical observations can be incorporated in constitutive equations.

The following conclusions were drawn:

- The constitutive model is unconditionally thermodynamically consistent.

- Comparing the predictions using the thermomechanical constitutive model with laboratory test results showed that the model is capable of capturing the majority of thermomechanical volumetric and deviatoric behaviours of soils.

- The proposed constitutive model may not be suitable for boundary-value solvers, such as finite element methods, when numerically implemented using an implicit stress integration algorithm if certain numerical remedies are not considered. This is due to the existence of undesired elastic nuclei and/or domains with erratic gradients. This drawback is addressed in Chapter 3.

- Although the model captures the main thermomechanical behaviour of fine-grained soils, it failed to capture some features such as smooth stress-strain responses and hardening and shakedown behaviour of soils when subjected to heating-cooling cycles. This drawback is addressed in Chapter 6.

8.3. A FLEXIBLE AND ROBUST YIELD FUNCTION FOR GEOMATE-RIALS

Many flexible yield surfaces proposed in literature for geomaterials may not be suitable for boundary-value solvers when using implicit stress integration algorithms. The return mapping numerical algorithm may not be able to return the stress back onto the yield surface when subjected to large strain increments, due to undesired elastic nuclei and/or domains with erratic gradients or divergence. In Chapter 3, a new flexible yield surface was proposed which is non-singular and uniquely defined in meridian stress space. This was achieved by designing and imposing geometrical constraints on the formulation of a quadratic-form yield surface via the roots of the yield surface in meridian stress space. The flexibility of the yield surface was also validated by comparing with experimental data for geomaterials available in literature. It was concluded that the proposed flexible yield surface was suitable and robust for implementing in boundary-value solvers when using implicit stress integration algorithms. This yield surface was further used in Chapter 4 for implementing the thermomechanical model developed in Chapter 2 in a finite-element context, and for developing a two surface/bubble thermomechanical model developed in Chapter 6.

8.4. NUMERICAL IMPLEMENTATION OF THE FLEXIBLE SINGLE YIELD SURFACE THERMOMECHANICAL CONSTITUTIVE MODEL

In Chapter 4, the thermomechanical constitutive model presented in Chapter 2 was modified to include Lode angle dependency and the flexible yield surface proposed in Chapter 3 and generalised in three-dimensional stress space. Then, a numerical algorithm was proposed to implement the thermomechanical constitutive model which consisted of a flexible, Lode angle dependent and temperature-dependent yield surface, non-associated flow rule and non-linear thermo-elasticity relationships, in a boundary-value solver, such as the finite element method, with an implicit stress-integration technique of the *elastic predictor-plastic corrector* type. The numerical algorithm was formed by simultaneously solving the residual equations defined for the state variable (here, strain was considered), the hardening variable (here, the pre-consolidation pressure) and consistency condition. The accuracy, robustness and effectiveness of the algorithm was thoroughly investigated via studying iso-error plots, iteration-stress maps and Gudehus plots. The stress and residuals were also checked and were confirmed to be quadratic. Then, the thermomechanical model was implemented into the DIANA FEA finite element software via a user-defined material model subroutine. Fine-grained soils subjected to various thermomechanical stress paths in triaxal and oedometer tests, when using a wide range of material parameters, were simulated via this algorithm. All simulations were stable and the predicted thermomechanical behaviours were aligned with those observed in the laboratory-scale tests presented in Chapter 2. It was concluded that the numerical algorithm can be used to numerically investigate the thermomechanical behaviour of a thermo-active geo-structure and soil system for various mechanical and thermal load scenarios.

8.5. TWO SURFACE/BUBBLE THERMOMECHANICAL CONSTITUTIVE MODEL FOR FINE-GRAINED SOILS

A two surface/bubble-type thermomechanical model was developed in Chapter 5 to address the shortcomings of the single surface model explained in Section 8.2, which were the incapabilities of simulating smooth stress-strain responses and hardening and shakedown behaviour of fine-grained soils when subjected to thermal cycles. The two surface model was developed by introducing an additional yield surface (inner yield surface) that could translate inside the outer yield surface with a kinematic rule. The model was formulated in accordance with the framework of Hyperelasticity-Hyperplasticity, which ensured that the principles of thermodynamics were unconditionally satisfied. Thus, all constitutive components were derived based on the definition of a Gibbs-type energy potential and a rate of dissipation potential. A new rate of dissipation potential was developed that consisted of three components: (1) the sub-rate of dissipation potential for the inner yield surface, (2) the sub-rate of dissipation potential for the outer yield surface, and (3) the kinematic rule that governs the translation of the inner yield surface. The sub-dissipation potentials of the inner and outer surfaces had similar formulation to the formulation of the flexible yield surface presented in Chapter 3. The kine-

8

matic rule was added to the rate of dissipation by using the concept of thermodynamical constraints and consisted of isothermal and non-isothermal components. Smooth stress-strain responses and progressive elasto-plastic deformations when subjected to mechanical cyclic loads were obtained with the isothermal component of the kinematic rule. With the non-isothermal component of the kinematic rule, the model could predict the state-dependent plastic deformations when subjected to thermal cycles. By comparing experimental data with the predictions made with the thermomechanical model, it was concluded that the model successfully captured the hysteresis cyclic behaviour and thermal shakedown behaviour of fine-grained soils when they are subjected to mechanical cyclic and thermal cyclic loads, respectively.

8.6. THERMOMECHANICAL BEHAVIOUR OF SOIL-STRUCTURE INTERFACE

The effect of temperature with various mechanical boundary conditions and stress levels for soil-concrete interfaces was investigated experimentally via a temperature controlled direct shear apparatus and presented in Chapters 6 and 7. The thermomechanical stress paths were designed to mimic those that a soil-interface may experience during the short- and long-term operation of an energy pile. The main conclusions from these tests were:

- The shear properties such as friction angle of the studied soils (here kaolin clay and Geba sand) were temperature independent.

- Soil-interfaces may experience volume changes (mainly reduction) when subjected to thermal cycles. This thermally-induced volume change depends on the soil type, stress level and thermal load direction and are more pronounced when samples are subjected to cyclic shearing afterwards.

- The cyclic displacements due to annual or daily temperature variations of an energy-pile may significantly influence the shear responses of the soil-interfaces, which can influence the capacity and performance of the soil-pile system.

- Due to the coupling effect of the initial shear stress and thermal cycles, the soil-interface may experience additional shear displacements and therefore settlements.

These findings should be considered in the design procedure of energy-piles as well as in the traditional design consideration of a normal pile.

8.7. RECOMMENDATIONS FOR FURTHER RESEARCH

In this thesis, progress has been made in understanding and quantifying the main mechanisms governing the thermemchanical behaviour of soils, by developing thermomechanical constitutive models and numerical algorithms for boundary-value solvers, and by performing laboratory scale tests on soil-structure interfaces. The findings of this thesis are useful for design and analysing the performance of energy-piles. However, many other aspects should be studied which may lead to a more robust tool that can be used

for thermo-active geo-structure applications. The following recommendations and suggestions may be potential topics for further research.

- The effect of temperature on soil anisotropy can be investigated via laboratory-scale tests and can be implemented in constitutive models via a rotational/kinematic hardening rule in the two surface/bubble thermomechanical constitutive model presented in Chapter 5.

- A numerical algorithm can be developed to implement the two surface/bubble thermomechanical model presented in Chapter 5 in boundary-value solvers with an implicit stress integration technique.

- Thermomechanical interface models can be developed based on the findings of Chapter 6 and Chapter 7. Then, they can be numerically implemented in boundary-value solvers such as finite-element methods.

- The predictive performance of boundary-value solvers coupled with the constitutive models proposed here should be validated via field tests.

- With the use of the thermomechanical constitutive model for soils and soil-interfaces, the performance of thermo-active geo-structures such as energy-piles can be thoroughly studied.

REFERENCES

[1] Collins, I. F. and Hilder, T. A theoretical framework for constructing elastic/plastic constitutive models of triaxial tests. *International Journal for Numerical and Analytical Methods in Geomechanics*, 26(13):1313–1347, 2002.

8

ACKNOWLEDGEMENTS

laid the groundwork for all that I have achieved. Their foundational love and encouragement resonate throughout every page of this thesis.

Each person mentioned—along with the many unmentioned—has been an invaluable part of this transformative chapter of my life. I am profoundly grateful for your impact, and I look forward to carrying your influence into the future as I continue to grow and contribute to the world of research.

Ali Golchin
Delft, October 2023

8

CURRICULUM VITÆ

Ali GOLCHIN

EDUCATION

2017–2023   Ph.D. Candidate in Geotechnical Engineering
Section of Geo-Engineering, Faculty of Civil Engineering and Geosciences
Delft University of Technology, Delft, The Netherlands

2010–2012   Master of Science in Geotechnical Engineering
Department of Civil and Environmental Engineering
Shiraz University of Technology, Shiraz, Iran

2006–2010   Bachelor of Science in Civil Engineering
Department of Civil Engineering
University of Zanjan, Zanjan, Iran

EMPLOYMENT

2022-current	Senior Geotechnical Engineer
	Department of Geo-engineering, Global Engineering
	Boskalis B. V., Papendrecht, The Netherlands
2021-2022	Researcher
	Section of Geo-Engineering, Faculty of Civil Engineering and Geosciences
	Delft University of Technology, Delft, The Netherlands
2017-2023	Ph.D. Researcher
	Section of Geo-Engineering, Faculty of Civil Engineering and Geosciences
	Delft University of Technology, Delft, The Netherlands
2012-2017	Geotechnical Engineer
	Freelancer
	Iran
2011-2012	Research Assistant
	Department of Civil and Environmental Engineering
	Shiraz University of Technology, Shiraz, Iran

ACADEMIC ACTIVITIES

Reviewer	Géotechnique
	Computers and Geotechnics
	Numerical and Analytical Methods in Geomechanics
	Geothermics

LIST OF PUBLICATIONS

JOURNAL PAPERS

8. **Golchin, A.**, Guo, Y., Vardon, P. J., Liu, S., Zhang, G and Hicks, M. A. Shear creep behaviour of soil-structure interfaces under thermal cyclic loading. *Géotechnique Letters,* 13, 1, 2023.

7. Guo, Y., **Golchin, A.**, Hicks, M. A., Liu, S., Zhang, G. and Vardon, P. J. Experimental investigation of soil–structure interface behaviour under monotonic and cyclic thermal loading. *Acta Geotechnica,* Ahead of print, 2023.

6. **Golchin, A.**, Vardon, P. J. and Hicks, M. A. A thermodynamically consistent two surface/bubble thermo-mechanical model considering thermal and mechanical cyclic behaviour of fine-grained soils. *International Journal of Solids and Structures,* 254–255, 111847, 2022.

5. **Golchin, A.**, Vardon, P. J. and Hicks, M. A. A thermo-mechanical constitutive model for fine-grained soils based on thermodynamics. *International Journal of Engineering Science,* 174, 103579, 2022.

4. **Golchin, A.**, Schreppers, G. J., Coombs, W. M., Hicks, M. A. and Vardon, P. J. Numerical implementation of a hyperplastic thermomechanical constitutive model for fine-grained soils based on Gibbs energy potentials. *In preparation.*

3. **Golchin, A.**, Vardon, P. J., Coombs, W. M. and Hicks, M. A. A flexible and robust yield function for geomaterials. *Computer Methods in Applied Mechanics and Engineering,* 387, 114162, 2021.

2. **Golchin, A.** and Lashkari, A. A critical state sand model with elastic–plastic coupling. *International Journal of Solids and Structures,* 51, 2807-2825, 2014.

1. Lashkari, A. and **Golchin, A.** On the influence of elastic–plastic coupling on sands response. *Computers and Geotechnics,* 55, 352-364, 2014.

CONFERENCE AND PROCEEDING PAPERS

6. **Golchin, A.**, Vardon, P. J., Hicks, M. A., Coombs, W. M. and Pantev, I. A. On the Numerical Implementation of a Thermomechanical Hyperplasticity Model for Fine-Grained Soils. *In: Barla, M., Di Donna, A., Sterpi, D. (eds) Challenges and Innovations in Geomechanics. IACMAG 2021. Lecture Notes in Civil Engineering,* 125, 422–429, 2021.

5. **Golchin, A.**, Vardon, P. J. and Hicks, M. A. A thermodynamically based thermo-mechanical model for fine-grained soils. *Proceedings of the XVII ECSMGE-2019. Geotechnical Engineering foundation of the future,* 1-8, 2019.

4. **Golchin, A.**, Vardon, P. J., Hicks, M. A., Pantev, I. A. and Musivand Arzanfudi, M. Energy-piles in the Netherlands: geotechnical behaviour. *European Geothermal Congress 2019,* 1-7, 2019.

3. **Golchin, A.** and Lashkari, A. A critical state sand model with elastic-plastic coupling. *In: Yang, Q., Zhang, JM., Zheng, H., Yao, Y. (eds) Constitutive Modeling of Geomaterials. Springer Series in Geomechanics and Geoengineering., 4-24, 2013*.

2. **Golchin, A.** and Lashkari, A. Study on the influence of elasticity on predictions of elasto-plastic models of granular soils. *20th Annual International Conference on Mechanical Engineering - ISME2012*, 2012.

1. **Golchin, A.** and Lashkari, A. Constitutive equations for the elastic behavior of granular soils with thermodynamics considerations. *9th International Congress on Civil Engineering*, 2012.